The University of Nottingham

UNITED KINGDOM · CHINA · MALAYSIA

A Coupled Lagrangian-Eulerian Framework to model droplet to film interaction with Heat Transfer

Akinola A. Adeniyi

B.Eng.(Ilorin), M.Sc.(London), R.Eng.(COREN)

Thesis submitted to The University of Nottingham

for the degree of Doctor of Philosophy

July 2015

To my family for their wonderful support as ever.

Abstract

In aeroengine applications, oil is used lubricate and cool the bearings as well as cool the structural parts. The high operational speeds break the oil up forming ligaments and droplets. To contain the oil, the bearings are located inside sealed bearing chambers and a positive pressure across the seals is used to contain the oil within the system. The highly rotational flow in the chamber is laden with droplets emanating from the bearings. The droplets travel to the outer bearing chamber walls and form cooling oil films that rotate in the direction of the shaft spin. The used oil is scavenged out via the sump for recycling.

The multiphase flow in aeroengine bearing chambers includes strong interactions between the gas and the liquid, where the liquid can exist in the form of droplets and continuous film. There are other applications, such as spray cooling, that create similar modelling challenges. In spray cooling nozzle atomisation of the coolant creates high speed droplets that eventually form a film on the hot surface being cooled. To model this type of flows, with computational fluid dynamics (CFD), there is a need to be able to account for the multiple impacting droplets and the resulting cooling films. Volume-of-Fluid (VoF) based CFD techniques have been used by researchers to model droplet-film impacts by applying an extremely fine computational mesh to resolve the flow around the droplets and the film. Such methods, because of the computing cost are, however, not practical for applications of interest in this work.

In this work, droplets are not explicitly resolved to a computational mesh, they are represented as point source terms in an unsteady Lagrangian formulation. Representing droplets in Lagrangian formulation, as done here, is not new but the coupling with the continuous phase to form flowing film from user defined source terms and onward tracking of splashing droplets using published correlations are novel. The mass and momentum of the Lagrangian particle are transferred into VoF by adding the source term as a "handover" of mass from the discrete phase to VoF film, in the continuity and momentum equations after interface tracking is done. Heat transfer is achieved by mass averaging of the temperatures in the spread zone equivalent to the spherical droplet. The particle tracking is then stopped and the particle is subsequently removed from the simulation. The method is developed using the ANSYS-Fluent CFD software and formulated using an enhanced VoF technique. The developed technique is validated using a series of simple numerical checks on single Lagrangian droplet-to-film to more complex spray-to-film test cases to check for mass, momentum and heat transfer with reasonably good performance.

The developed sub-model was also tested on two different aeroengine bearing chamber geometries; one representative of a bearing chamber in the AE3007 aeroengine and one representative of a bearing chamber test rig at Karlsruhe Institute of Technology. The AE3007 geometry was used in the experiments of Chandra *et al*. [1, 2] and the KIT geometry by Gorse *et al*. [3]. The AE3007 bearing chamber geometry is somewhat similar to that of the high-pressure/intermediate-pressure (HP-IP) bearing chamber of a 3-spool large civil aircraft. The film thickness results predicted for the AE3007 geometry are over-predicted but similar in trend when compared with experimental measurements. The simulations show film formation and pooling as observed in the experiments. The top

parts of the bearing chamber, generally, show higher heat transfer coefficient results than the lower parts of the chamber where films are typically somewhat thicker.

For the KIT chamber application, there is a good prediction of the film thickness when compared with the experiment. A parametric study of the flow shows that the film thickness increases with the flow rate. At a fixed liquid flowrate, film thickness decreases with increasing shaft speed. The average film temperature increases with a reducing flow rate and increases with shaft speed. This current work presents the development of a useful tool applicable to bearing chamber modelling.

List Of Publications

Published

[1] Akinola A. Adeniyi, Hervé P. Morvan & Kathy A. Simmons, A transient CFD simulation of the flow in a test rig of an aeroengine bearing chamber, GT2014-26399, *Proceedings of the ASME Turbo Expo 2014, D´usseldorf, Germany*, 2014.

[2] Akinola Adeniyi, Hervé Morvan & Kathy Simmons, A Coupled 3-Phase CFD Approach to model Droplets to Film Interaction with Heat Transfer, *2014 UoN High Performance Computing (HPC) user conference, University of Nottingham*, 2014.

[3] Adeniyi, A.A., Morvan, H. & Simmons, K., Droplet-Film Impact Modelling Using a Coupled DPM-VoF Approach, ISABE-2013-1419, *Proceedings of XXI Intl. Symp. on Air Breathing Engines (ISABE 2013), American Inst. of Aeronautics and Astronautics (AIAA), Busan, South Korea*, 2013.

Pending/In review

[1] Akinola A. Adeniyi, Hervé P. Morvan & Kathy Simmons, A DPM-VoF approach for the formation of film from Lagrangian droplets spray with heat transfer in the non-boiling regime, *Int. J. of Heat and Fluid Flow*, XXXX.

[2] Akinola A. Adeniyi, Hervé P. Morvan & Kathy A. Simmons, A COUPLED EULER –LAGRANGE CFD MODELLING OF DROPLETS-TO-FILM, *Int. J. Multph.*, XXXX.

[3] Akinola A. Adeniyi, Hervé P. Morvan & Kathy A. Simmons, Splashing of droplets on an arbitrary free film surface using a coupled Lagrangian-Eulerian (DPM-VoF) technique, *AIP Phy. Rev.*, XXXX.

Posters and Presentations

[1] A.A. Adeniyi, H.P. Morvan & K. Simmons, Bearing Chamber modelling with a DPM-VOF technique, *Nottingham-Surrey UTCs Workshop, Institute for Aerospace Technologies, (IAT), Nottingham*, 13 Mar. 2014.

[2] A.A. Adeniyi, H.P. Morvan & K. Simmons, Progress on a coupled Lagrangian-VOF approach for oil systems applications, *Rolls-Royce UTC QTR, Derby*, 28 Nov. 2013.

[3] Akinola A. Adeniyi, Hervé Morvan & Kathy Simmons, Modelling Heat Transfer within Aero-Engine Bearing Chambers, *Rolls-Royce PhD Day*, 12-13 June 2013.

[4] Akinola A. Adeniyi, Hervé P. Morvan & Kathy A. Simmons, A Coupled Lagrangian - Volume of Fluid Approach to Simulate Aero-engine Bearing Chambers, *Energy & Sustainability Poster Competition, University of Nottingham*, Jan. 2013.

Acknowledgements

I acknowledge God the Almighty for making this a possibility.

This research was carried out at the University Technology Centre (UTC) in Gas Turbine Transmissions Systems at the University of Nottingham with financial support from University of Ilorin ETF/AST&D 2009 award for my tuition and maintenance.

I must also mention financial supports from Rolls-Royce plc, Aerospace Group, Energy & Sustainability Division of The Faculty of Engineering, University of Nottingham, and of course, mainly, by the UTC group. The fundings cover all expenses for my conference attendance in Busan, South-Korea. I was also sponsored on ICEM meshing software training at the ANSYS UK Office in Sheffield. I also wish to say thank you for the provision of the powerful computing resources.

I sincerely acknowledge the contributions, supervision, mentoring, motivation and the many supports from my supervisors, Prof. Hervé Morvan and Dr. Kathy Simmons. I benefited a great deal from their skills, industrial links and experience. Contributions from Prof. Henry Power, my internal examiner, during my first and second year review were very helpful in preparing this thesis. This thesis would not have been complete without the thorough reading and constructive criticism by Prof. John Chew. I got inspirations from Prof. Seamus Garvey.

The UTC has a fantastic team of researchers. I especially acknowledge discussions and contributions from Al Baydu, Piotr Tkaczyk, Turner Adam, De Carvalho Thiago, Natarajan

Arun Prakash, Peduto Davide (KIT), Torsten Sonner (KIT) and Roberto Ovando Martinez (Instituto Tecnológico de la Laguna, Mexico).

The Graduate School is a place to look out for when studying in University of Nottingham. I received a number of useful training from the Grad. school. I was even sponsored for a 3-day Engineering Young Entrepreneur Scheme (*Engineering YES*) competition in Loughborough, for which my team won "Best Team Work Award" in 2011.

I cannot forget the constant *"how many percent more?"* reminder from Lawal Bashir and Komolafe Biola. I must acknowledge Prof. A.A. Adedeji, Prof. Y.A. Jimoh, Prof. J.S. Olorunmaiye, Prof. H.D. Olusegun, Dr. K.R. Ajao, Dr. A.S. Aremu, Dr. Wahab Salami, Dr. T.K. Ajiboye for their wonderful contributions towards making my PhD a possibility. All my friends were very supportive; I want to specially mention Ibrahim Olojoku, Abubakar Mohammed, Muntaka Sirina, Nurudeen Almustapha, Ajibi Michael, Akanmu Olalekan, Oba Abdullahi and others so numerous to list for their support.

I want to acknowledge my family members for their support and solid confidence in me. My parents, Alhaji Mohammed Baba (dad) and Mrs. Idiayat Adunni (mom) are inspirational. My brothers Dr. Suleiman, Ghaly, Abdul-Jeleel, Abdul-Rasaq, Lawyer Ahmed and others.

Finally, I want to specially mention the kind support and understanding of my wife Mrs. Temitope Mariam Adeniyi. Our children Miss Ayomide Azizat, Miss Farida Oyinkansola and Miss Adeola Amira Elizabeth "the PhD baby" born in Nottingham and named after the Queen.

Contents

List of Figures

List of Tables

Nomenclature

A	:	Area:
	:	A_{cell} : of a 2D cell ,
	:	A_{liq} : of liquid phase in a 2D cell , [m^2]
	:	An arbitrary vector, $\overrightarrow{A}$
B	:	Turbulence damping constant [ ]
	:	An arbitrary vector, $\overrightarrow{B}$
$C_{1\epsilon}, C_{2\epsilon}, C_{1\epsilon}$	:	Constants in the turbulence models
C_0, C_1	:	Cell centroids
c, C_g	:	Speed of sound [m/s]
C_D	:	Coefficient of drag [ ]
c_p	:	Specific heat[J/kgK]
D_o	:	Droplet diameter just before impact [m]
D_p	:	Diameter of Langrangian droplet [m]
D_ω, D_ω^+	:	Cross-diffusion terms in the κ-ω model
d_{32}	:	Sauter mean diameter [m]
E	:	Total enthalpy [J/m^2K]
F_1, F_2	:	Blending function in the κ-ω model
F_d	:	Drag force per unit mass on a particle [N/kg]
F_s	:	Surface tension force [N/m^3]
f	:	Frequency of droplet train [Hz]
f_n	:	Nozzle atomisation frequency [Hz]
g, g_i	:	Gravity [m/s^2]
G_κ	:	Production of turbulence kinetic energy
G_b	:	Bouyancy driven production of turbulence kinetic energy
		(film thickness with respect to droplet diameter)

Nomenclature ...

H_ε	:	Heaviside function
H^*, h^*	:	Relative film thickness,
$\bar{h}_f$	:	Mean spray film thickness [m]
h	:	Grid spacing [m]
		Convective heat transfer coefficient [J/m^2K]
h_b	:	Bulk heat tranfer coefficient [W/m^2K]
h_f, h_{film}	:	Film thickness [m]
	:	[subscritical (h_{sub}), supercritical(h_{sup}), free flow (h_0)] [m]
h_{fg}	:	Latent heat of vaporisation [J/kg]
h_t, HTC	:	Heat tranfer coefficient [W/m^2K]
i	:	Index or item number (similar for j, k & n)
J_L	:	Jet length [m]
k	:	Thermal conductivity [W/mK]
K	:	Splash factor
K_B	:	Boltzmann constant [W/m^2K^4]
k_t	:	Turbulent thermal conductivity [W/mK]
m	:	mass [kg]
Δm_p, m_p	:	Mass of a droplet [kg]
M_{fn}	:	Lagrangian equivalent of a continuous mass flow rate [kg]
M_f	:	Mass of bulk of liquid in a cell [kg]
	:	Mass of ejected droplets/film [kg]
M_g	:	Gas molecular weights [kg/mol]

m_s	:	Mass of ejected (secondary droplets) [kg]

Nomenclature ...

N,N_1,N_2	:	Interface normals (vectors)
	:	Count of items (or n)
Δn	:	Cell spacing (m)
N_f	:	Number of splashing droplet fingers
N_s	:	Number of splashing droplets
N_x, N_y, N_z, N	:	Number of nodes
N_{pb}	:	Number of particles released from a nozzle per timestep
N_{1sec}	:	Number of droplets in 1 sec.
P, p	:	Pressure [Pa]
		Droplet impact planar vector [$\overrightarrow{P}$]
q	:	Cell wall heat flux, [W/m^2]
q_a	:	Time and area-averaged wall heat flux, [W/m^2]
Q	:	Flow rate of water, Q_l & air Q_a [kg/s]
$\overrightarrow{r}$	:	Displacement vector
R	:	Universal gas constant [$Jkg^{-1}K^{-1}$]
R_b	:	Radius of bearing chamber [m]
S	:	Source term
SR	:	Scavenge ratio
SR_{in},SR_{out}	:	Region inside/outside a sphere
S_1, S_2	:	A plane or a surface

Nomenclature ...

S^*	:	Relative grid spacing to resolve a DPM droplet to a VoF droplet, D_p/h
S_ρ, S_{α_i}	:	Mass source term [$kgm^{-3}s^{-1}$]
S_{ij}	:	Mean strain rate [$1/s$]
S_ω, S_κ, S_ω	:	Source terms in the turbulence models
S_m	:	Momentum source term [$kgm^{-2}s^{-2}$]
T	:	Temperature [K, ^oC], (T_s, T_1, T_2, T_3, T_i, T_d)
T_{spray}	:	Temperature of spray [K, ^oC]
$Y_\kappa, Y_\epsilon, Y_\omega$	:	Dissipation of κ, ϵ or ω
$\overrightarrow{U}$, $\overrightarrow{u}$	:	Velocity of continuous phase (similar for V, v, W, w) [m/s]
U_o	:	Velocity of droplet particle at impact on a film [m/s]
U_t	:	Threshold velocity to determine splash [m/s]
$\bar{U}_f$	:	Mean film velocity of a spray [m/s]
U_p, V_p, $\vec{V}_{d_0}$	:	Velocity of a droplet particle in the gas phase [m/s]
v_s	:	Superficial velocity [m/s]
V_{wj}	:	Water jet velocity at the exit of the RID device [m/s]
X_i, X_c, X_p	:	3D spatial locations/centroids within the domain

Greek symbols

α	:	Volume fraction
α_p	:	Angle of attack of droplet on a surface [^{o}]
α^*	:	Low Reynolds number correction coefficient in the κ - ω models
α^*_∞	:	Turbulence models constants, and similary for : α_0, α^*_0, α_∞, β_{i1}, β_{i2}, β_i,β^*_∞, ζ, R_β, R_ω
β	:	Mass fraction of liquid absorbed [$\%$]
	:	Coefficient of thermal expansion [K^{-1}]
β_{max}	:	Ratio of maximum to primary droplet diameter
ρ	:	Density [kg/m^3]
σ	:	Surface tension [N/m]
σ_κ, σ_ϵ, σ_ω	:	Turbulent Prandtl number (for κ, ϵ & ω)
$\Gamma_\kappa, \Gamma_\epsilon, \Gamma_\omega$	:	Effective diffusivity of κ, ϵ or ω
Λ	:	Material property, mass diffusivity [m^2/s]
ν	:	Kinematic viscosity [m^2/s]
μ	:	Dynamic viscosity [$Pa.s$]

Greek symbols ...

γ	:	Specific heat ratio
κ	:	Surface curvature [m^{-1}]
κ	:	Turbulent kinetic energy per unit mass [m^2/s^2]
ϵ	:	Turbulence dissipation rate of κ [m^2/s^3]
ε	:	A small distance [m]
θ	:	Mean ejection angle of secondary droplets [^{o}]
	:	Contact angle [^{o}]
τ	:	Wall shear stress [Pa]
ω	:	Inverse time scale of turbulence
Ω	:	Shaft speed [RPM]
Ω_{ij}	:	Mean rate of rotation of a tensor [$1/s$]
Φ	:	Angular rotation/displacement [rad]
ϕ	:	Level set function
		Orientation/angles [^{o}]
$\Psi(t)$	:	Transient transport variable of a fluid (properties)
Ψ	:	Mean transport variable of a fluid (properties)
$\psi'(t)$	:	Stochastic component of $\Psi(t)$
λ_d	:	Droplet spacing length scale [m],
λ^*	:	Relative droplet spacing length scale [],
δ, δ_ε, δ_o	:	Delta function

Subscripts/Superscripts

o,0	:	Before impact
a	:	Air
g	:	Gas
l	:	Liquid, oil or water
s	:	Secondary droplet
d, p	:	Droplet (Primary droplet)
w	:	Wall
$*$	:	Non-dimensional

Table 0: Useful non-dimensional numbers

Number	Expression	Showing/Describing
Bond	$Bo = \frac{\rho g D^2 o}{\sigma}$	Bouyancy to surface tension effect (Same as Eötvös number).
Crater diameter	$D^* = \frac{D}{D_p}$	A measure of the diameter, D, of the crater formed by a droplet of diameter D_p on a film.
Drop impact frequency	$f^* = f\frac{d_o}{U_o}$	Frequency of the train of droplets.
Film thickness	$H^* = \frac{h_f}{d_o}$	Relative film thickness at impact point.
Froude	$Fr = \frac{U_o^2}{g d_o} = \frac{We}{Bo}$	Inertia to gravitational forces.
Laplace	$La = \frac{\rho\sigma D_o}{\mu_l^2} = \frac{Re^2}{We}$	Surface tension to momentum transport ratio.
Nusselt	$Nu = \frac{hL}{k_{eff}}$	Ratio of convective to conductive heat transfer coefficients.
Ohnesorge	$Oh = \frac{\mu_l}{\sqrt{\rho\sigma D_o}} = \frac{\sqrt{We}}{Re}$	Viscous to inertia and surface tension.
Prandtl	$Pr = \frac{c_p \mu}{k}$	Viscous diffusion rate to thermal diffusion rate.
Reynolds	$Re = \frac{\rho D_o U_o}{\mu_l}$	Inertia to viscous forces.
Schmidt	$\frac{\mu}{\rho\Lambda}$	Viscous momentum diffusivity to mass diffusivity.
Surface roughness	$R^* = \frac{Ra}{D_o}$	Surface roughness of the walls, wall roughness, Ra, is often expressed in microns.
Time	$t^* = \tau = t\frac{D_o}{U_o}$	Flow time.
Weber	$We = \frac{\rho D_o U_o^2}{\sigma}$	Inertia to surface tension.

Abbreviation	Full meaning
BC	Boundary Condition
CCFL	Counter-Current Flow Limitation
CFD	Computational Fluid Dynamics
CFL	Courant-Lewy-Friedrich
CV	Control Volume
CLSVoF	Coupled Level Set Volume of Fluid
DLL	Dynamic Linked Library
DNS	Direct Numerical Simulation
DPM	Discrete Phase Model
FG	Film Generator
FBH	Front Bearing Housing
FSM	Fractional-Step Method
FVM	Finite Volume Method
GUI	Graphical User Interface
HI-IP	High-Pressure Intermediate Pressure
HP	High-Pressure
HPC	High Performance Computing; High Performance Computers
HTC	Heat Transfer Coefficient
IAT	Institute for Aerospace Technology
IGB	Internal Gear Box
IP	Intermediate Pressure
KIT	Karlsruhe Institute for Technology
KIT	Karlsruhe Institut für Technologie
LP	Low Pressure
LP-IP-HP	Low Pressure-Intermediate Pressure-High Pressure
LS	Level Set
MAC	Marker-and-Cell
PIC	Particle-In-Cell
PISO	Pressure-Implicit with Splitting of Operators
PLIC	Piecewise Linear Interface Calculation/Construction
RANS	Reynolds-Averaged Navier-Stokes
RID	Rotating Inlet Distributor
SILOET	Strategic Investment in Low-carbon Engine Technology
SIMPLE	Semi-Implicit Method for Pressure-Linked Equations
SIMPLEC	Semi-Implicit Method for Pressure-Linked Equations Consistent
SPH	Spherical Particle Hydrodynamics
SR	Scavenge Ratio
TBH	Tail Bearing Housing
UDF	User-Defined Function
UTC	University Technology Centre
VoF	Volume of Fluid

Chapter 1

Introduction

1.1 Background

Oil finds useful applications in engineering. In aeroengine applications, for example, it is often relied upon to provide lubrication and cooling for the transmissions system. The transmissions system consists of moving parts, such as the bearings, shafts, gears, and static parts of the engine core. In an aero engine, the oil is used in a cycle. From the colder tank, it is pumped to where it is needed for lubrication and cooling, the used oil is scavenged out for filtering, cooling, and further re-use. It is desired that the oil goes through this loop with no part of the oil residing longer than necessary. Longer than necessary residence time will degrade the oil faster and potentially increase chance of coking as a result of the high temperatures. It is known that higher operational temperatures can allow for better efficiencies in aeroengines.

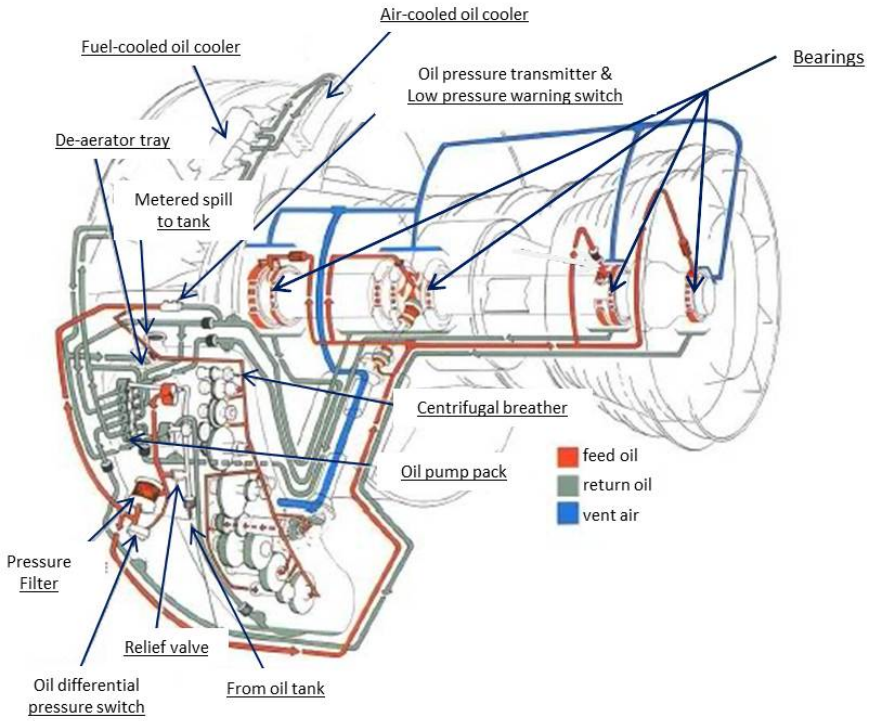

(a) Oil system schematic[4]

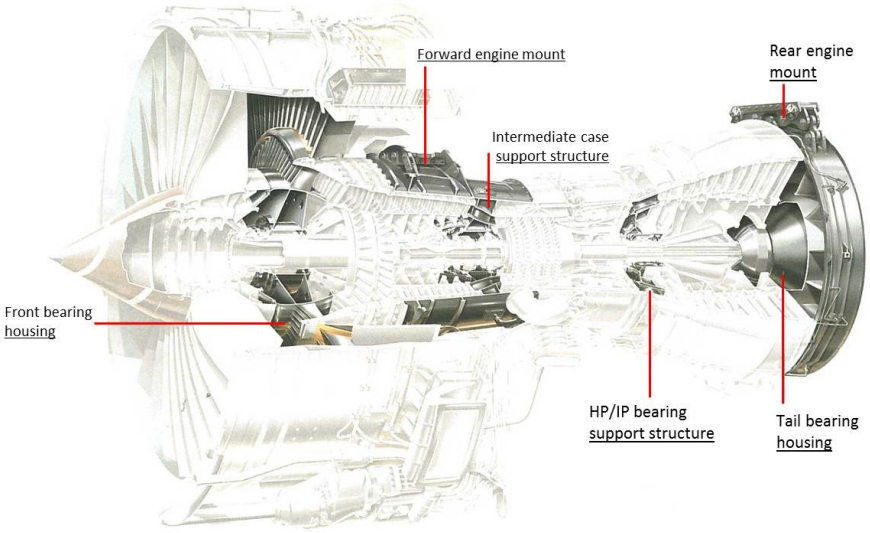

(b) Main support structures & engine mounts on a Trent Engine[5]

Figure 1.1: Aero-Engine Oil System & Engine Mounting illustrations

The aeroengine oil system for a 3-shaft civil aeroengine is schematically illustrated in Figure 1.1a. The shafts are supported on bearings and these bearings are housed in

bearing chambers. For a 3-shaft Trent-style aeroengine, shown in Figure 1.1b, there are typically 4 bearing chambers: the front bearing housing (FBH) at the front of the engine; the internal gearbox (IGB), towards the centre of the engine; the HP-IP[1] bearing chamber also towards the centre of the engine and the tail bearing house (TBH) towards the rear of the engine. Of these the two hottest chambers are those in the middle of the engine. The HP-IP chamber is the smallest and hottest. The IGB is also a hot region and it contains the spiral bevel gear pair used for the auxiliary power offtake, adding additional complexity to the heat management challenge. The oil loop is designed to recycle the oil and as much as possible and the bearing chamber allows the containment and capture of the oil shed. These chambers are typically pressurised to guarantee the oil containment from the bearings.

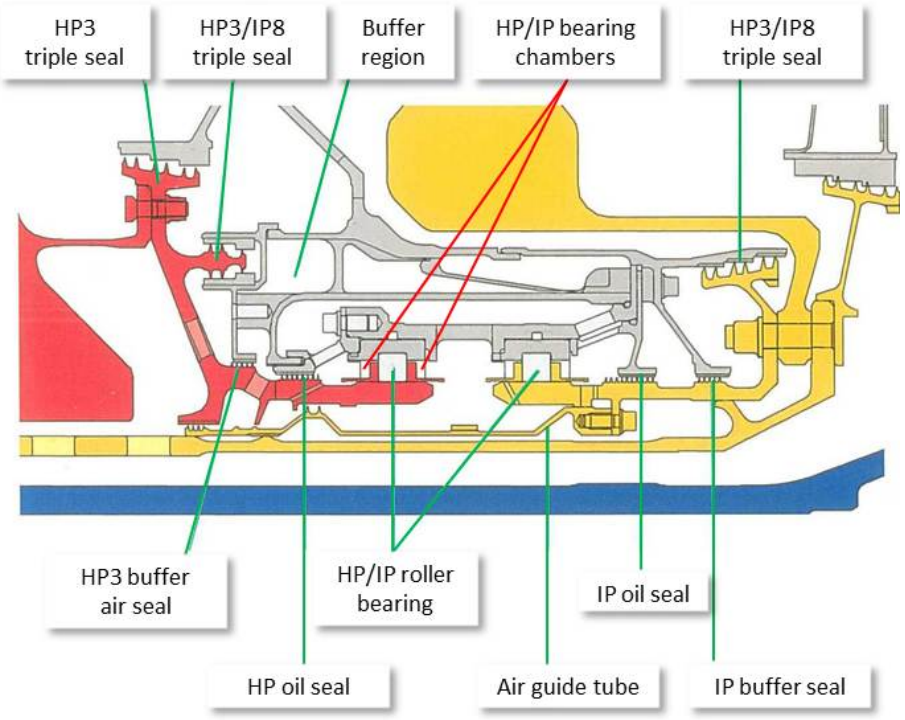

Figure 1.2: Air sealing in the HP-IP hub [5]

[1]HP: High Pressure, LP: Low Pressure, IP: Intermediate Pressure.

Figure 1.2 shows a representation of the HP-IP air/oil sealing structure. To prevent oil escaping from the bearing chambers, air pressurised seals such as labyrinth seals are used to provide a positive pressure into the chamber and thus contain the oil. The oil mainly exits the bearing chamber via the sump but some of the oil exits with the air through *vents*. The oil that exits through such vent needs to be separated from the air, before it can be reused.

In the bearing chambers, the oil can be found in various forms. It can be found as films flowing on the hot wall structures or as fast moving filaments, bubbles (trapped air within a film) and droplets. The oil plays an important role as a coolant for the bearings. It is obvious that an aeroengine oil system is a complex two-phase flow of air and oil. Progress in engineering material technology to support very high temperatures is also pushing the limits for aeroengine design, thus understanding the oil system is critical to the overall engine performance.

1.2 The Challenge

The capability to model fully an aeroengine bearing chamber is highly desirable for an engine designer. Aeroengine bearing chambers present a particular challenge because of the multiphase flow. When doing multiphase flow simulations, there is a difficult challenge deciding how to model the way the fluids interact whilst interchanging mass, momentum and heat. It is not reasonable to assume one representation only for the different fluid phases present. The oil/liquid exists as a continuum when it is a either a flowing film

or as ligaments before eventually breaking up into droplets. The oil droplets in the gas space are another form of existence. Bubbles of gas/air trapped within the oil continuum or the bulk air over the film surface is another form. The film interface is not static and its locations cannot be predetermined. The interface deforms as it moves over arbitrary shapes dictated by properties such as the viscosity, surface tension and density. The various forms of existence of these fluids interchange mass and momentum and sometimes heat. For example, an impingement of a cold droplet into a pool of hot liquid will add mass by mixing and transfer of momentum into the pool the result of which may result into a splash. Also, there will be a local cooling of the film at the impact region. A holistic model of these phenomenon is as complex as it sounds.

The use of CFD techniques, in fluid systems analysis, play a very important role in understanding the problem and making engineering design decisions. Understanding the multiphase flow and heat transfer process within the aeroengine bearing chambers has been a challenge for several years. Most of the bearing chamber related studies have been carried out by experiments, mathematical analyses and CFD simulations. Many of the bearing chamber simulations have been limited to single phase, two-dimensional and mostly isothermal. Some of the studies involve very *detailed* simulation of specific phenomena, such as a single droplet splashing. Despite having very powerful multi-thread High Performance Computing (HPC) facilities, the detailed simulation of the full flow in the bearing chambers is still not computationally feasible.

High speed droplets forming cooling film over hot surfaces exist in many engineering applications, for example in spray-film cooling. The flow in the bearing chambers is even

more complex because of the geometry and the sealing air dynamics.

1.3 Applications

There are a number of applications in which liquid and gas flow together and sometimes with droplet entrainment into the liquid or gas phase. The multiphase scenario of interest in this work involve segregated fluids for which the capture of the gas-liquid interface is key. A significant body of work devoted to this area, both experimentally and numerically, exist. There are a number of *research based* techniques available to individually describe some of the aforementioned interactions between various forms of the liquid, some of the techniques even at an atomic level of resolution. There is still, however, a gap between what can be achieved through detailed simulation of events or phenomena and what can be used practically. The detailed analysis of a droplet impinging on a film creating a splash, for example, shows it is a highly complex process. As complex as the process is, there are models that can be used to simulate it.

A detailed, multiphase and transient simulation of a representative bearing chamber is not currently feasible with available techniques because of the computational overhead. In particular there is a need to bring together developed computational models; this is addressed and presented in the work.

1.3.1 Aero Engine Bearing Chambers

The bearing chamber of an aeroengine can be described simply as a cylinder encasing a portion of a high speed shaft, bearings and other static parts. A major source of heat-to-oil comes from the bearing ball friction; there is also a secondary contribution from the compressor as well as the combustion chamber [6]. Figure 1.3 shows the Rolls-Royce Trent 1000 engine used on the Dreamliner™ (Boeing 787) commercial aircraft. One of the bearing chamber locations, the HP-IP[2] bearing chamber, is indicated in the figure. The surrounding parts of the chamber carry load through the HP turbine exit airflow. This chamber is located in one of the hottest parts of the engine [5]. A section through a Trent engine is shown in Figure 1.4 indicating the rotors and the bearings.

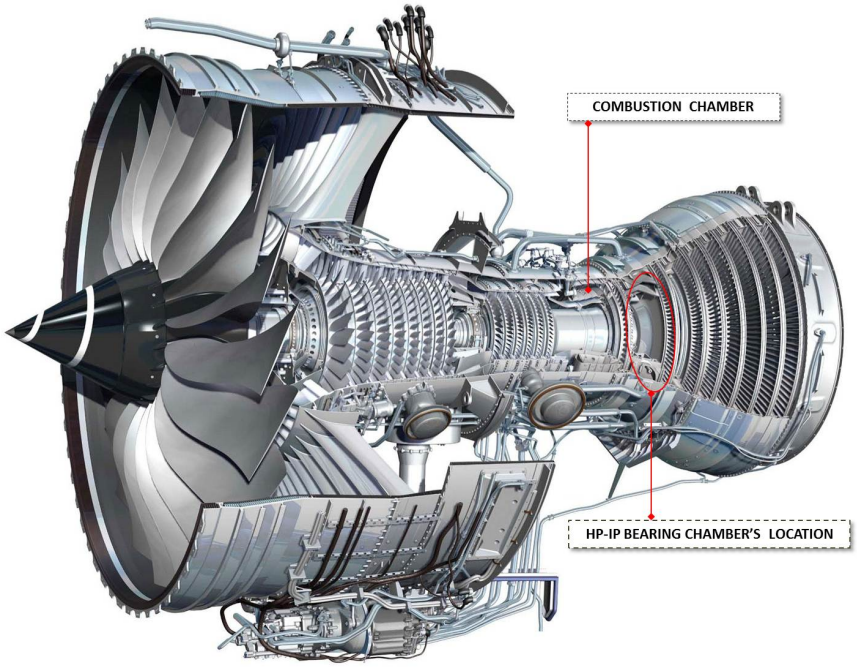

Figure 1.3: A cutaway view of the Rolls-Royce Trent 1000 engine [7]

[2]HP-IP: High-Pressure, Intermediate Pressure.

The closed loop oil system basically consists of the pressure feed & distribution system, a scavenge system and a venting system. The pressure feed & distribution system supply oil to the components. An external gearbox, powered by the HP shaft, drives the oil feed pump, the centrifugal breather and scavenge pumps. The design also includes the oil filter and fuel oil heat exchanger. A complete description of the Rolls-Royce Trent engine oil system can be found in Rolls-Royce publications[5].

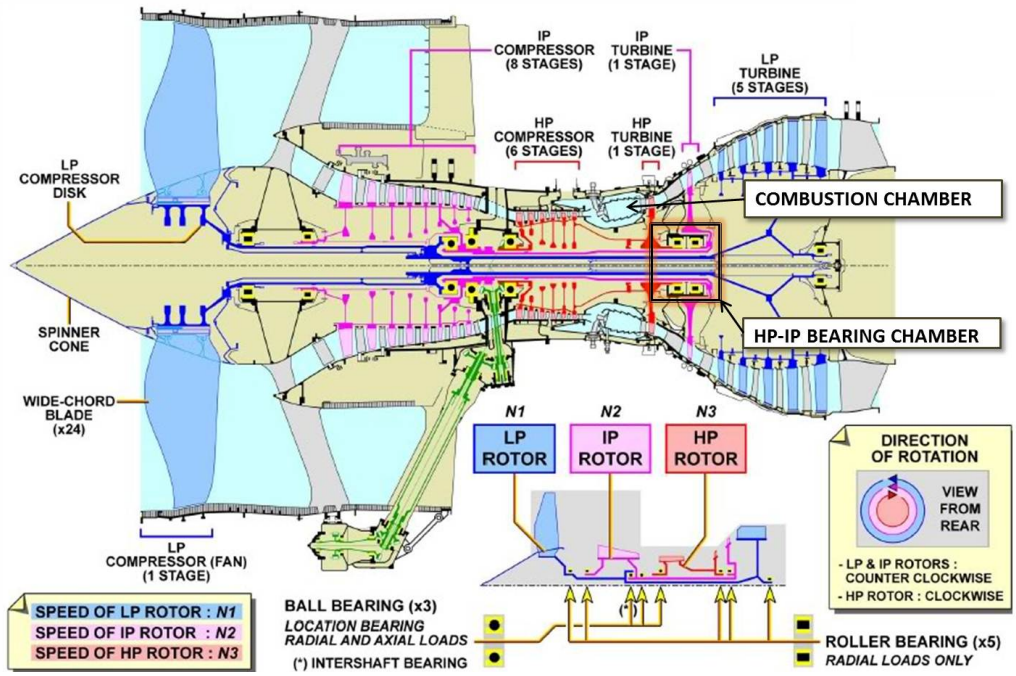

Figure 1.4: Rolls-Royce Trent engine sectional view [4]

The design and modelling of the HP-IP bearing chambers is a challenging feat. This involves a need to understand the oil history in the bearing chamber; the oil feed, film formation and its thickness at the walls, and the heat convection from the hot chamber walls. If the oil does not reach some parts of the chamber it can potentially result in coking of bearing walls; and if the oil is resident longer than necessary, it could lead to

a quicker oil degradation. Figure 1.5 shows a schematic representation of the flow in a representative sector of an HP-IP bearing chamber. The oil breaks up as it lubricates the bearings and travels to the walls to cool the walls. The used oil goes through the scavenge for re-use.

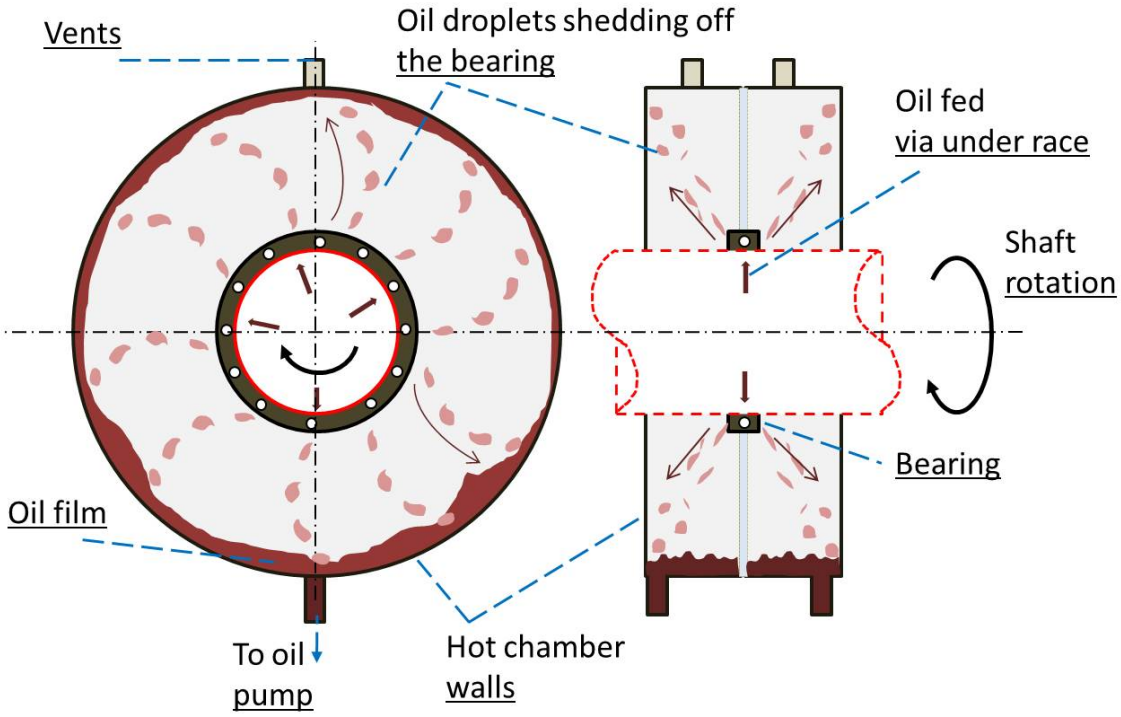

Figure 1.5: A schematic representation of the HP-IP bearing chamber

1.3.2 Other Applications

Spray film cooling is an example of where a sheet of liquid is atomised into tiny droplets that cool a hot surface. In the spray film cooling process, the atomised droplets exit the nozzle and form a thin wall film that convects heat away from the hot surface.

The transport of liquid and gas in pipes is another application where the interaction of

phases is important. Authors, for example, Weisman *et al*. [8] and Coleman [9], classified flow patterns observed in pipes/ducts as stratified wavy flow, bubbly flow, plug flow, and annular flow among others. These classifications were based on the superficial or average velocities[3] of the gas and liquid phases. Of these, the stratified flow pattern [§2.2.1] is of interest in this work.

1.4 The Thesis

Multiphase interaction of fluids is a complex phenomenon. There has been significant progress in Finite Volume Computational Fluid Dynamics (CFD) to model multiphase interaction as a Eulerian mixture of phases. There is also good progress to model discrete phase but little or no work exist to couple the discrete liquid phase with the Eulerian/continuum phase. This thesis focuses on the integration and extension of available CFD models for the interaction of droplets and a film with heat transfer, for which the HP-IP aeroengine bearing chamber is the primary target. In the bearing chamber, the injected oil is thought to break up into high speed droplets that coat the bearing walls in a film that provides cooling to the entire structure. The high speed droplets impact on the film and can splash to produce even smaller droplets. It is possible to model the droplet to film impact process. In finite volume CFD techniques, the fluids are resolved and discretised around a computational mesh and solved with the continuity and Navier-Stokes equations. This is the so called Eulerian approach. This ultimately means that an extremely fine mesh will be required to resolve the flow to the droplet level in the simulations. A heavy com-

[3] Superficial velocity of a given phase of fluid, v_s [m/s], is described as the ratio of the volumetric flow rate of the phase, Q $[m^3/s]$ to the cross-sectional area, A $[m^2]$, $v_s = Q/A$.

putational overhead is involved to an impractical level as the mesh density increases in a CFD simulation.

In this work, the droplets are not discretised to the computational mesh, but taken as Lagrangian particles. The flowing/continuous oil and gas phase representations are described in the Eulerian frameworks. There is a need to couple the Eulerian and Lagrangian phases. The mesh density is focused around the liquid regions and the wall regions of the control volume (domain), based on a technique from the in-house SILOET[4] project of the Nottingham University Technology Centre (UTC) in Gas Turbine Research. This technique, pro-actively, reduces the computational mesh in the domain and thus potentially reduces computational time. The use of a combination of fine and coarse mesh in such a multiphase flow has a price. Detailed physics, such as jetting and splashing, is lost in the coarse regions. The method uses published experimental correlations to predict the splashing droplets and continues to track them as Lagrangian particles.

1.4.1 Specific Objectives

The aim of this work is to develop a technique to model the complex multiphase flow of air and oil flow in the bearing chambers of aeroengines. The specific objectives of the work presented in this thesis are:

- extend existing modelling capabilities by coupling the Lagrangian representation and Eulerian representations of the interacting fluids.

[4]SILOET: Strategic Investment in Low-carbon Engine Technology funded by the Technology Strategy Board.

- validate the developed model against appropriate experimental data from the literature.

- implement the developed model on realistic 3D and non-isothermal aeroengine bearing chamber geometry.

1.4.2 Thesis Overview

This chapter introduces the background to the thesis. The modelling challenges involved were also discussed. There are a number of potential applications for the modelling methodology developed and presented in this thesis. The primary focus of application is the modelling of an aeroengine bearing chamber, but spray-to-film, and oil/gas transport were also introduced as likely immediate applications. This introductory chapter also gives the specific objectives of the work.

In Chapter 2, an overview of relevant literature is presented. There is relevance in free-surface modelling and droplet to film impact research. As the identified primary application of this work is the bearing chamber, a short review of past research work in this area is also presented.

The basic multiphase framework is presented in Chapter 3. This chapter describes the models, the methods and the strategies used to apply these models. It describes the techniques to model turbulent immiscible two-phase flows. The techniques to capture the free interface and interface correction to effect the correct inter-facial momentum transfer are presented.

Chapter 4 presents an extension to the basic multiphase framework discussed in Chapter 3. This extension enables the coupling of the two phases and the two liquid components as discretised in this work. The chapter discusses the coupling, which exists as a result of the so called "source terms" contribution into the Eulerian (continuum) phases. The droplets-film interface tracking algorithm is presented. The Lagrangian droplets can "identify" the arbitrarily shaped film surfaces and the walls in this technique. The splashing model, which is based partly on correlations, is presented.

Whereas Chapter 4 presents the proposal and methodology for modelling droplet interaction of the continuous phases, Chapter 5, presents a number of numerical verifications and validations of the methods. A simple Lagrangian droplet *turning* to an Eulerian droplet, and a simple box fill test demonstrates the conservation of mass between the model. Detailed modelling of crater dynamics demonstrates momentum transfer and data obtained is compared with correlations [10–13]. Basic heat transfer is demonstrated by filling an adiabatic box and compared with an analytical expectations. The complex case of multiple droplets (spray) impacting on a hot wall forming film, is modelled using data from the experiments by Yaqing *et al.* [14]. The capability to create splashing droplets on normal and arbitrary surfaces is also presented. This chapter shows the developed modelling technique to be sufficiently robust and accurate that it can be applied to a bearing chamber geometry with confidence and thus leading into the work of Chapter 6.

In Chapter 6, the developed technique is applied to the geometry of an experimental/research rig (AE3007 geometry) as used by Chandra *et al.* [1, 2]. This test rig comprises an outer stationary cylindrical chamber housing a single rotating shaft from which

droplets are flung via a bespoke rotating inlet distributor (RID) system. The experimental test rig is Perspex and uses water as the working fluid, droplets travel from the RID to, the chamber walls where they form a film that travels under the combined influences of gravity and shear towards the scavenge region. Although the experiment was performed isothermally, some arbitrary temperature boundary conditions were set in the simulation to give some initial non-isothermal results on the three dimensional bearing chamber model. The bearing chamber model also included the pump outlet boundary condition [15] so that scavenge ratios comparable to those investigated experimentally could be applied. A second bearing chamber application is modelled and results compared with the film thickness measurement experiments on the KIT bearing chamber by Gorse *et al*. [3]. Unlike in the simulation of the AE3007 geometry, the boundary conditions for the droplets in KIT geometry are obtained from the experimental measurements from the work of Glahn *et al*. [16] for the same bearing chamber geometry.

A summary and conclusion of the work is presented in Chapter 7. This chapter also includes some recommendations for future work and has a section where the unique contribution to knowledge of this work is clearly summarised. The Appendix sections contain among other things, a documentation (*readme file*) [A.1.0.5] on how to make the developed code available in ANSYS-Fluent otherwise called “hooking” of the user defined functions (UDF). The source code [A.2] is also included.

Chapter 2

Literature Overview

2.1 Overview

This work is concerned with the multiphase flow of liquid and gas for engineering applications. In the target applications, the liquid phase exists as a continuous flowing film and as filaments and droplets impacting or shedding off the free interface of the liquid and gas. This chapter presents a survey into the literature for relevant research work in liquid-gas interface modelling, droplet to film impact dynamics, and in aeroengine bearing chamber applications, the main focus of the developments proposed in this work.

2.2 Free-Surface modelling

Free-surface modelling involves numerically describing the hydrodynamic fields of the gas phase, the liquid phase and the liquid-gas interface [17]. The interface between the gas and the liquid phases is known as a free-surface. The abrupt change of physical properties at the free surface makes the modelling more involved. Several simplifications to flows with sharp interfaces exist; the simplifications often depend on the application of interest.

A simplification is that both the gas and the liquid phases are incompressible; another is that only the gas phase is compressible. Many of the formulations solve the momentum balance by decomposing the flow into bulk phases and implementing numerical jump conditions at the free surface [17]. Navti *et al.* [18] & Caboussat [19], for example, assume that the gas phase is compressible. The pressure in the gas phase is taken to be constant and can be solved with the ideal gas equation. The Navier-Stokes equations [*see* §3.2.2] are solved in the liquid phase. This method has been shown to perform quite well for low Reynolds number and highly viscous flows such as in molten metals [18]. In the two methods mentioned here, the surface tension force is simply balanced at the free-surface with the pressure drop (ΔP) across the interface using the Laplace formulation [20] ($\Delta P = \sigma\kappa$, where σ is the surface tension and κ is the interface curvature).

A generalised analytical solution of free-surface flow is not possible. The techniques developed have all been based on solving a set of non-linear partial differential equations (PDEs). Flows can be solved using the *Lagrangian* or *Eulerian* frameworks [21]. These describe the viewpoints or the observer reference frame.

In the Lagrangian formulations, the local reference frame moves with the fluid flow. In the Eulerian approaches, the reference frame observes the fluid system as it goes through it, otherwise known as a *grid* based method. For the purpose of this thesis, the Lagrangian framework can be considered as imaginary points (observers) or particles embedded within the flow. These two frameworks can be used alone or in combination.

In flows of interest in this work, the approaches can be categorised into Lagrangian, Eulerian-Eulerian and Eulerian-Lagrangian techniques depending on how each phase is treated. In all of these techniques, the fluid system is discretised into representative units or local reference frames. In Euler-Lagrange techniques, both moving and fixed reference frames can be used.

A prominent Lagrangian technique is the so called Smooth Particle Hydrodynamics (SPH) which was originally developed in 1977 by Lucy, and Gingold & Monaghan for nonaxisymetric phenomena in astrophysics [22, 23]. The fluid system is discretised into N interacting spherical particles separated by a smoothing length/kernel; a general equation modelling pressure interactions is used to model their evolution [24–26]. The SPH technique has developed over the years and is getting more attention in multiphase simulation of free-surface applications, such as the *air entrapment* work of Colagrossi & Landrini [26]. Handling realistic fluid properties and complex boundary conditions as well as the computational overhead are still a challenge for the SPH method, it is however, a promising tool for engineering applications; for example, Figure 2.1 shows an SPH simulation of the classical Rayleigh Taylor instability owing to inertia and body forces of two fluids. The heavier fluid (Phase -**A**) is above and the arrow indicates the free-surface separating the

fluids. The model captures instability at the interface that results in the interpenetration of the two fluids.

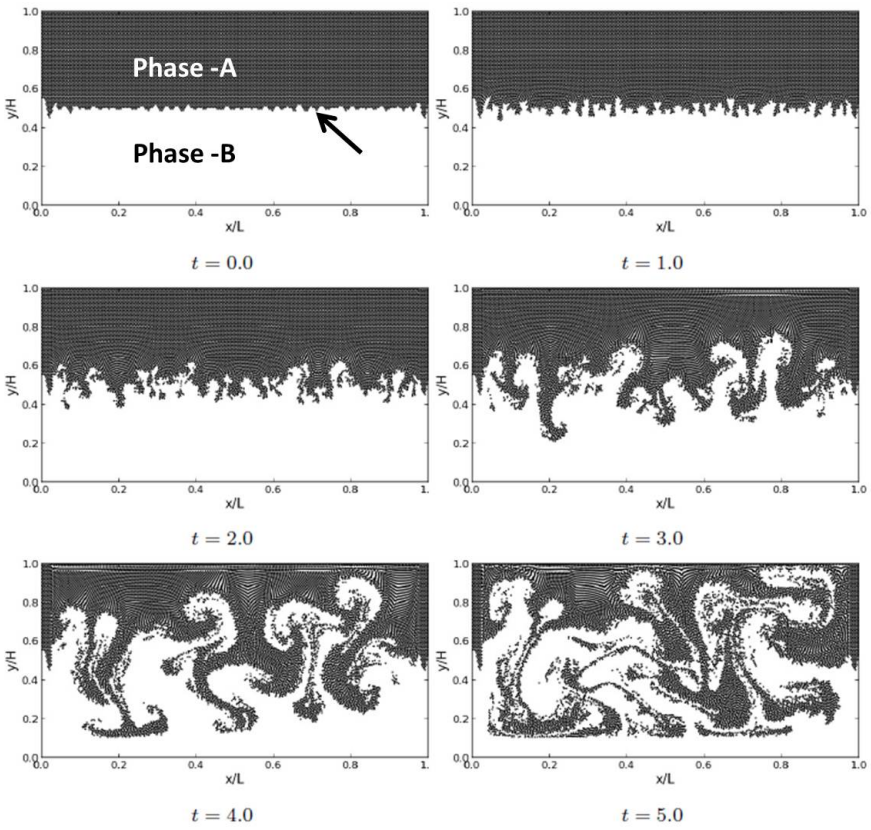

Figure 2.1: An SPH simulation of Rayleigh-Taylor Instability [27]

The Euler-Lagrange technique has been used by a number of authors for modelling free-surface flows [28], such as large bubbles [29, 30] rising in a liquid column. The classical particle in cell (PIC) method of Harlow & Welch [31], where marked (Lagrangian) particles are tracked with the (Eulerian) fluid to determine the free-surface is an Euler-Lagrange technique. In this PIC based method, the Navier-Stokes equations are written in iterative finite-difference form around the fixed grid. The inert/massless particles are placed inside cells with fluid present; the local velocities move the particles and by some

linear interpolation, the coordinates are determined. The free-surface is determined where there are no marker cells. An improved particle marker tracking algorithm to include effects of the surface tension was developed by Popinet & Zaleski [32]. The technique uses a bilinear interpolation scheme for the particle advection and a set of connected cubic polynomials of the particle coordinates to describe the free-surface. Surface marking, like this, makes them particularly good for films forming vortices (Figure 2.2A) or thin bridge(Figure 2.2B) structures [17].

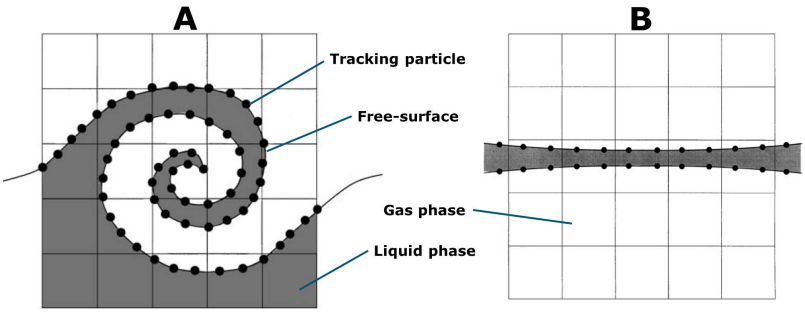

Figure 2.2: Particle in Cell surface markers [17]

The requirement to represent the interface clearly makes free-surface modelling difficult. Fixed grid and moving (deformable) grids are the two types of methods used to treat incompressible/immiscible fluids [32–34]. Boundary discretisation and volume discretisation techniques are generally the two numerical techniques to simulate non-linear free-surface flows [35, 36]. Although all numerical techniques are developed around a mathematical basis, it is worth noting that it is difficult to have a general technique that is all inclusive. The finite volume discretisation techniques are quite robust to handle both inviscid and viscous flows [17, 35]. The finite volume implementation of the governing equations is used by the main commercial solvers (ANSYS-Fluent, ANSYS-CFX, FLOW3D,

STAR-CD and others) [37, 38] and is also available with the major open source codes (OpenFoam [39] and its variants such as *CAE Linux*™[40]). Finite volume methods perform well for simulations that require high memory or processing on parallel machines [41, 42]. ANSYS-Fluent is Rolls-Royce's choice for two-phase flow applications and the work presented in this thesis was conducted using it.

The Volume of Fluid (VoF) method is a homogeneous Eulerian-Eulerian based method used in two-phase simulation of incompressible and immiscible fluids flows with free-surface. The VoF methods trace back to the works of Noh & Woodward [43] and Hirt & Nichols [44]. The VoF technique is rather a "cheap" way to deal with segregated flows. It is known to be more memory efficient than the Harlow & Welch [31] marker-and-cell (MAC) approach, although unphysical results might result with poor choice of spatial discretisation [44]. VoF is a homogeneous approach that assumes a single fluid continuum of varying properties defined by the so called "colour" functions typically defined with the representative phase volume fractions. In the 2D representation, illustrated in Figure 2.3, the volume fraction of the phases present is the ratio of the area integral of the liquid present, A_{liq}, to the cell area, A_{cell} as given in Equation 2.1.

$$\alpha = \frac{A_{\text{liq}}}{A_{\text{cell}}} \tag{2.1}$$

Therefore, cells filled with the liquid phase have a volume fraction, α equal to 1 and cells filled with the gaseous phase have a volume fraction of zero such that free-surface is somewhere in $0 < \alpha < 1$. In the free-surface regions α has values not exactly 1 nor 0.

Therefore, there is still a desire to reconstruct the interface. In early VoF models interface reconstruction was based on a first-order or simple line interface calculations [17, 44] as shown in Figure 2.3B.

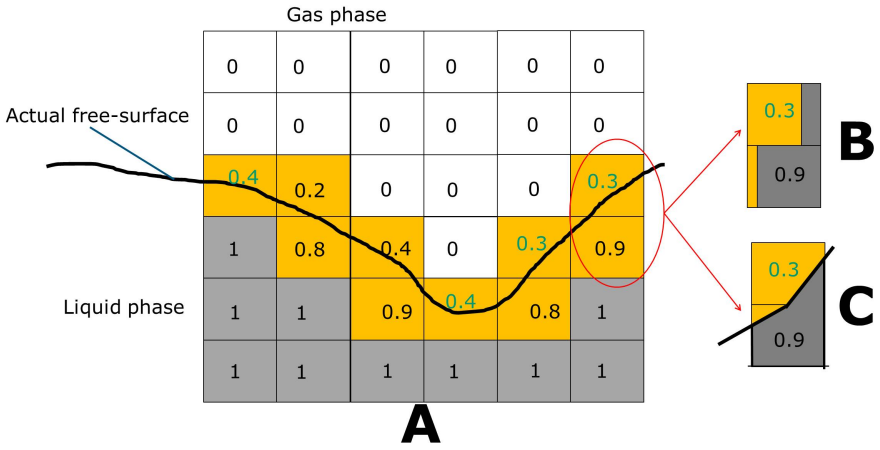

Figure 2.3: VoF free-surface construction

Advancement of the VoF technique to improve the free-surface prediction has been researched over the years. The Piecewise Linear Interface Calculation (PLIC) method, Figure 2.3C was intended to smooth the interface using a joined train of segments [45, 46]. It is known that VoF based methods have good mass conservation properties [34, 47] but the difficulties of interface normal and curvature prediction remain following that surface tension models rely on the local curvature for example. The coupling of the Level Set (LS) function with the VoF method was proposed by Bourlioux [48] in 1995 and was further developed by Sussman & Puckett [34]. The level set function is a signed, smooth and continuous function [§3.2.4.2] advected similarly to the volume fraction equation. Osher & Sethian [49] defined the free-surface at a zero LS iso-surface. Level Set does not on its own have good mass conservation properties [47], the coupling combines the interface

capturing ability of level set and the good mass conservation ability of the VoF method. The surface tension force can be predicted using the continuum surface force models such as the Brackbill model [50]; this model depends on properly capturing the interface curvature. Without properly capturing the interface curvature, the VoF only technique has been noted to over-predict the surface tension force, and this can lead to, undesirable calculation outcomes such as the prediction of unphysical dry out in flows where surface tension forces are important [15].

A promising approach for the extension of the VoF method to compressible multiphase flows is given by Saurel & Abgrall [51]. They employed a system of equations that ensures the closure of partial pressures, surface tension, interface velocity relaxation, and mass transfer with volume fraction evolution *(a technique similar to VoF)*. They presented good results for some supersonic test regimes; these regimes are, however, not relevant to this work. In the kind of applications of interest in this work, the incompressible assumptions will suffice. Free-surface prediction plays a very important role in modelling the flow in the bearing chamber.

2.2.1 Stratified flows

Stratified flows are a special class of free-surface flow resulting from the vertical variation in density of the fluids systems [52]. A flow consisting of layers of two or more fluids with different densities is hereby considered a stratified flow. Figure 2.4 shows a schematic representation of a sectional side view of a horizontal duct where liquid and gas exhibit a stratified flow. In Figure 2.4A, both phases flow in the same direction and this is therefore

known as co-current but in Figure 2.4B, a counter-current stratified flow, the gas phase flows in the opposite direction to the liquid. Figure 2.4C illustrates a phenomenon known as the hydraulic jump.

At a minimal energy level, the liquid will flow out of the channel with a mean thickness h_0, assuming the flow is steady. The behaviour of the liquid depends on the local Froude number, Fr, where $Fr = U_l/\sqrt{gh_f}$ and h_f is the local film thickness. The flow is supercritical when $Fr > 1$ and subcritical when $Fr < 1$. The flow of the liquid from a supercritical flow zone into a sub-critical zone creates a hydraulic jump [52]. A high velocity liquid flowing into a region of slower or stationary pool will create a hydraulic jump. This is seen to occur in the sump region of bearing chamber geometries tested experimentally in the UTC. Counter-current stratified flows are inevitable in some engineering applications for example in a nuclear reactor core cooling process. Counter-current flows are only stable within certain flow regimes known as the *counter current flow limitation* (CCFL) [53, 54].

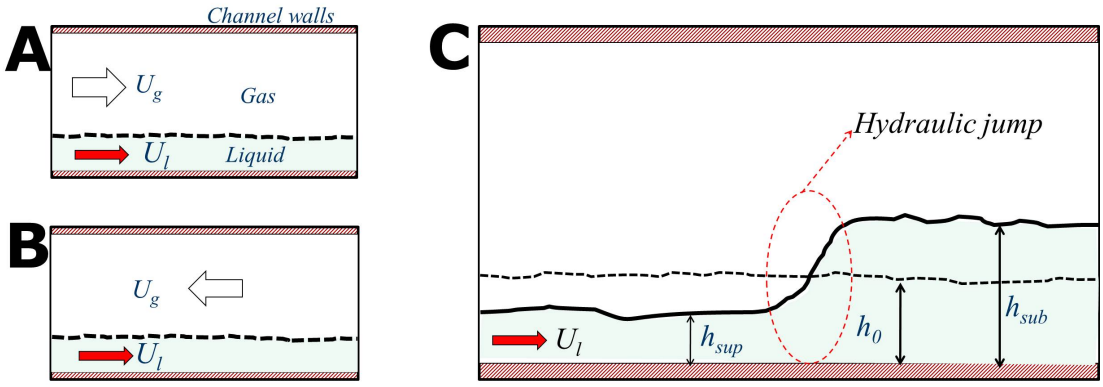

Figure 2.4: Stratified flows

The flow in the bearing chamber is both co-current and shear-driven. Shear driven

flows have the gas phase exerting a shear stress over the surface of the film and the shear may even drive the film flow. For turbulent flows [*see* §3.3], the VoF method needs correction for momentum exchange at the free-surface [53, 55]. There is a huge difference in physical properties and a high velocity gradient at the interface results in numerical noise; very high turbulence is generated in the higher velocity gas phase than in the slower liquid phase. There is a need for correction at the interface in the turbulence model. An approach consists in *approximating* the interface as if it were a wall and creating a near wall damping effect such as proposed by Egorov *et al.* [56]. Vallée *et al.* [53] conducted both experimental and CFD simulation studies of the stratified flow using a VoF technique using the interface damping correction [*see* §3.3.4] with good prediction of the slug pattern as compared with the experiments. Tkaczyk & Morvan [55] investigated and established the validity of this correction for bearing chamber flow regimes.

A stratified flow can be extremely complex. For example, stratified flow past sharp edges may break up into liquid jets and create droplets [57]. Film separation and breakup phenomenon could happen when the film flows past obstacles such as close to sharp angles that may be found in the scavenge offtake or in regions of the bearing chamber where the geometry changes abruptly such as in the recesses. Figure 2.5, shows film separation occurring as a film flow encounters a sharp edge. A number of works exists on flow past sharp bends; Owen & Ryley [58] conducted experiment and numerical analysis of radial stress distribution within a thin film flow around sharp and fixed bend radius and observed that thick films[1], $H^* > 1.06$, are more likely to separate than thin films and the point of separation is at a boundary wall. They defined the non-dimensional film thickness as the

[1] *see* Table 2.1 *for description/notations of film thickness.*

ratio of the film thickness to the curvature ($H^* = h_f/R$).

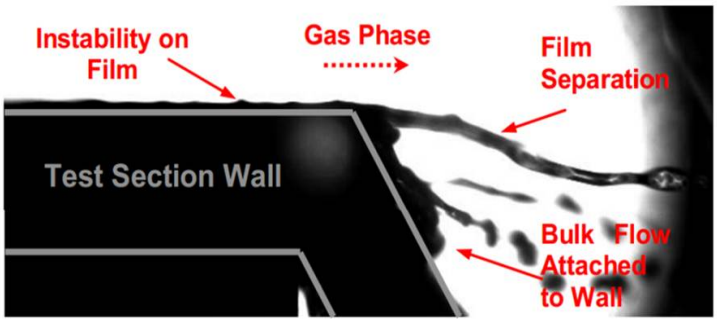

Figure 2.5: Film separation from a sharp bend [57]

In Maroteaux *et al.* [59], film of given thickness separates only after reaching a critical angle defined as a function of the amplitude of film surface perturbation and perturbation growth frequency. Friedrich *et al.*[61] observed that about 90% of the film is separated about corners; but the onset of separation for a thin film attached to a wall [*see* Fig. 2.5] begins at a force ratio of 1, with about 5% of the film separated. The force ratio described as the ratio of the inertia film force to restoring force; this ratio is defined in a complex equation relating the local Weber, Froude, Reynold numbers and the corner angle. The characteristics or sizes of the droplets stripped from the film are, however, not reported and the results limited to rectangular ducts.

An investigation of deforming droplets to film impact in a shear driven flow was reported by Alghoul *et al.* [62] and is schematically represented in Figure 2.6. Both 2D and 3D surface wave patterns were observed. A transition between 2D (rolling) and 3D wave patterns was not distinct but a low film loading creates 2D wave patterns and a high loading creates 3D surface patterns which create secondary droplets. The experiments were performed at low Weber numbers using large droplets, with diameters larger than

$2,400\mu m$. The results showed that the impact process on a static film is different from that of a shear driven film, but the outcome of the impact of spherical droplets in a shear-driven flow is similar to those on static film [62]. In a similar experiment, by Samenfink *et al.* [63], the criteria[2] leading to splashing or deposition was given.

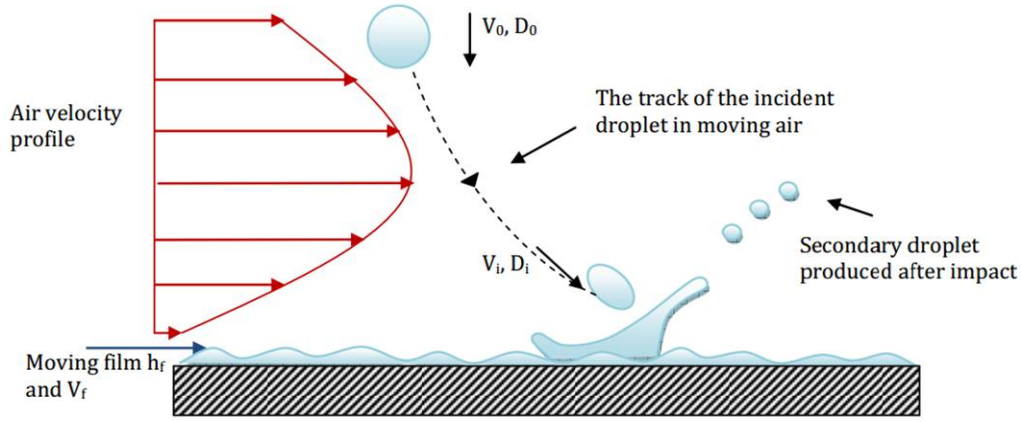

Figure 2.6: Droplets deforming in a shear-driven flow [62]

2.2.2 Inter-facial heat transfer

The gas and the liquid phases are in contact and exchange heat. Inter-facial heat transfer modelling will be important if interphase mass transfer can occur at the free-surface in the form of either condensation or evaporation [64–66]. The VoF technique in its original form cannot handle such mass and heat exchange at the free-surface. There are no simple correlations for inter-phase momentum and heat transfer at the free-surface. Davidson & Rudman [66] presented a VoF based algorithm for inter-facial heat and mass transfer of a droplet rising in a liquid column by partitioning the cells. The energy equation is solved for both phases in the computational cell and properties mass averaged. The technique

[2]Please refer to Table 2.2.

is, however, limited by the its inability to compute highly deformable free-surfaces and lack of validation data. In a similar work by Yang & Mao [67], a 2D Level Set together with mass transport equations across the phases were solved for laminar and buoyancy driven droplet rising in a column. The concentrations of mass compare well with the experimental data [68] of which the model constants were calibrated against.

ANSYS-Fluent offers a mass averaged energy equation without mass transfer at the cells within the free-surface zone for VoF [69]. The conditions at the interface are assumed to be at equilibrium conditions so that simple mass averaging applies. Mass transfer from one phase to the other in the form of evaporation or condensation can be treated as source terms in the transport equations. These source terms can be added or subtracted from the energy equation provided that the mass transfer rate is known [65]. Interphase mass transfer, such as oil vaporisation, has not be implemented in this work.

2.3 Droplet impact outcome

The outcome of droplet impact has been a subject of intensive research for more than a century. Splashing studies date as far back as the 1908 work of Worthington [70]. Splashing is one of the possible outcomes of the impact of a droplet on a surface; it has been observed at high Reynolds and high Weber number impact conditions [13, 71, 72]. Droplet film interaction is a complex phenomenon and depends on a wide range of parameters such as the inertia, surface tension, thermal properties of the impacting liquid and the surface of impact. Yarin [73] generalised the outcomes of the impact of a droplet

on surfaces (*dry or free-surface*) as *stick*, *spread*, *rebound* or *splash*. These scenarios are relevant in this work and are depicted in Figure 2.7.

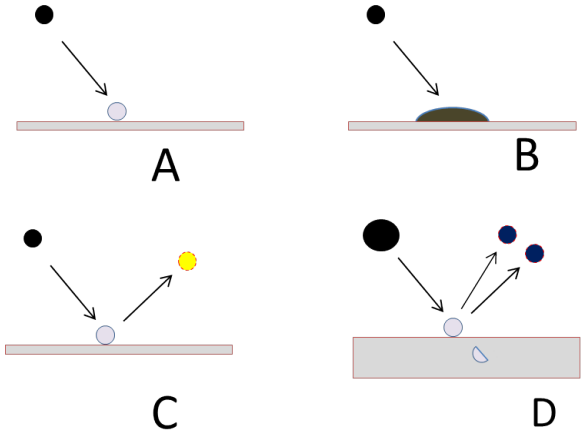

Figure 2.7: Droplet impact outcome (**A** - Stick, **B** - Spread, **C** - Bounce, **D** - Splash)

In Figure 2.7**A**, the droplet sticks to the surface. A surface can be a dry wall or a gas-film interface. Figure 2.7**B** is a case where the droplets spreads [74] on impact to the surface; in Figure 2.7**C**, the droplet bounces [75]. The droplet impact in Figure 2.7**D** creates child droplets in the form of a splash as a result of the impact and accompanied with crater formation. The droplet approaching a surface is regarded as the primary droplet and the splashing droplets are referred to as a child droplets or secondary droplets. This identification is conventionally used in this work; that is, a child droplet becomes a primary droplet as it approaches the film or a wall.

There is a wide body of work on droplet-film studies at different flow regimes. Of the various possible outcomes of droplet impact on films, splashing and sticking are of particular interest to this work because of the high impact energy regime. Bouncing, such as observed on super-hydrophobic surfaces [75] is very unlikely. Bisighini [76] observed other

complex phenomena at selected impact Weber number, such as the *trampoline bounce* and *toroidal bubble* regime; but these are not relevant to the present work. The interest in splashing is not limited to experiments, there are also bodies of work on theoretical and numerical prediction of droplet impact outcome. A number of authors [11, 12, 77] have tried to use direct numerical simulation (DNS) or detailed VoF techniques to study the first few timestep after impact.

Experimental observations in droplet to film impact studies have been based majorly on normal impact and only a few on oblique impact. A normal droplet impact happens when the primary droplet hits a flat surface along a normal vector to the surface. An oblique droplet impact happens when the droplet impacts at a shallow angle relative to the surface. A droplet can impact on a wet or a dry surface. It is common to refer to a film as thin or thick. In droplet film impact studies, relative film thickness or the ratio of film thickness to droplet diameter, H^*, ($H^* = h_f/D_0$, where h_f is the film thickness and D_0 is the droplet diameter at the point of impact.) have been used to characterise the film and impact outcomes. Table 2.1 gives the description of film thickness by authors [12, 13, 71].

Table 2.1: Description of droplet impact surfaces

Film type	Expression	Wall type
Dry wall	$H^* = 0$	Dry wall by definition
Thin-film	$H^* \ll 1$	Pre-wetted wall
Intermediate film	$H^* = 1$	Pre-wetted wall
Thick film/Deep pool	$H^* \gg 1$	Deep pool/pre-wetted wall

This non-dimensional film thickness is conventionally used in this work. This con-

vention is useful as a matter of convenience in programming the droplet interaction with film, for example when checking the droplet impact outcome from published correlations [*see* §4.6.1]. In this work, it is not intended to "finely" resolve the flow physics such as the splashing droplets. To compensate for the lost details such as the splashing droplets, the secondary droplets are determined from published correlations in the relevant or closest regimes. Tables 2.2 & 2.3 give published correlations for different scenarios that could result in droplets *sticking* or *splashing*. Table 2.4 gives correlations useful to predict secondary droplets.

Table 2.4: Published criteria for droplet impact outcome -III

Author	Correlation	Note
Okawa *et al.* [84]	$N_s = 7.84{\cdot}10^{-6} \cdot K^{1.8} \left(H^*\right)^{-0.3}$	Experiment range: $0.0275 < H^* < 68$ N_s = number of secondary droplets.
Mehdizadeh *et al.* [85]	$N_f = 1.14We^{\frac{1}{2}}$	Impact on flat plat, range: $753 < We < 44,520$ $5,500 < Re < 65,000$ $D_p > 550\mu m$ N_f = number of fingers.
Peduto *et al.* [12]	$\theta = 0.015K + 12$ $K = 2100 + 5880(H^*)^{1.44}$ $\frac{V_s}{V_p} = 0.52$; & $M_f = 0.04$	θ = mean ejection angle; V_s/V_p = mean ratio of impact to ejection velocity; M_f = mean mass fraction ejected (oblique impact).
Okawa *et al.* [84]	$M_f = 0.00158e^{0.000486K}$	Experiment range: $0.0275 < H^* < 68$ $0 < \alpha < 10^o$ $K < 1.3 \cdot 10^4$

Droplet impact outcomes depend on the inertia effects and thermal conditions of the droplets and the film pool; most of the experiments in the open literature and in the

Table 2.2: Published criteria for droplet impact outcome -I

Citation	Parameters [a]	Possible outcome	Notes[b]
Yarin[73]	$U_t = 18\left\{\frac{\sigma}{\rho_l}\right\}^{\frac{1}{4}} \times \upsilon^{\frac{1}{8}} f^{\frac{3}{8}}$	if $U_o < U_t$ - SPREADS if $U_o > U_t$ - SPLASHES	On dry wall, where U_t is a threshold velocity and U_o is the impact velocity.
Samenfink *et al.*[63]	$\bar{h}_f \simeq 210\mu m$ $0.5 < H^* < 1.8$ $S_{cd} = \frac{1}{24} Re \times La^{-0.4189}$	if $S_{cd} < 1$ - COALESCENCE. if $S_{cd} = 1$ - Secondary droplets initialisation. if $S_{cd} > 1$ - SPLASHES	Oblique impact, wavy flowing film $(0.56cm^2/s)$
Randy *et al.*[78]	$d_0 = 2.00mm$ *(constant)* $0.1 \leq H^* \leq 1.0$	Thick films inhibit delayed splashing, high surface tension inhibits splashing for thin films or dry surface. Thin films generate either prompt or delayed splashing.	
Cossali *et al.*[71]	$Y = \frac{We \cdot Oh^{-0.4}}{2100 + 5880 \cdot (H^*)^{1.44}}$	if $Y < 1$ -STICKS if $Y > 1$ -SPLASHES	$0.1 < H^* < 1.0$ & $Oh > 7 \cdot 10^{-3}$ -Not valid for pure water where: $H^* > 0.2$ Smoother surfaces or $H^* < 0.02$ form more secondary droplets.

[a] $\bar{h}_f$ = mean film height, La = Laplace's number, Oh =Ohnesorge number, S_{cd} = Schmidt number and We = Weber number.
[b] Please refer to Table 0 on the Nomenclature page for description of non-dimensional numbers.

Table 2.3: Published criteria for droplet impact outcome -II

Citation	Parameters [a]	Possible outcome	Notes
Yarin[73]	$K = We \cdot Oh^{-\frac{2}{5}}$ $K = 2100 + 5880(H^*)^{1.44}$	if $0.1 < H^* < 1.0$ & $Oh > 7 \cdot 10^{-3}$ - SPLASHES if $0.08 \leq H^* \leq 0.14$ & $K \simeq 400$, - SPREADS	A pre-wetted surface. Surface roughness: $R^* = 5 \cdot 10^{-5}$ $0.1 < H^* < 1.0$
ANSYS Fluent [69, 79, 80]	Impact Energy $E^2 = \frac{\rho U_o^2 d_0}{\sigma} \times \left[\frac{1}{min(H^*,1)+\frac{\delta_{bl}}{d_0}}\right]$	if $E^2 > 57.7^2$ - SPLASHES	Film thickness $< 500\mu m$ Number of secondary droplets is pre-set by user. boundary layer thickness, $\delta_{bl} = d_0/\sqrt{Re}$
Vladimir & Heister[81]	$E^2 = \left(\frac{We}{min(H^*,1)+Re^{-0.5}}\right)$	if $E^2 > 57.7^2$, - SPLASHES	$d_0 = 700\mu m, \alpha_p = 50.5^0$ $U_0 = 60.6m/s$ $N_s = \left(\frac{m_s}{m}\right)\left(\frac{d}{d_{32}}\right)^3$ Geometry like the Rolls-Royce AE3007 engine.
Xu *et al.*[82]	Aerodynamic stress ratio:[b] $\frac{\sum_g}{\sum_l} = \sqrt{\gamma M_g} \cdot P \cdot \sqrt{\frac{d_0 \cdot U_0}{4K_B T}} \cdot \frac{\sqrt{\upsilon}}{\sigma}$	if $\frac{\sum_g}{\sum_l} > 0.45$, - SPLASHES	$d_0 = 3.4 \pm 0.1mm$ Pressure,P, range: $0 < P < 80kPa$, $2 < U_0 < 8m/s$ & $\frac{\sum_g}{\sum_l} = \frac{1}{2}\frac{C_g}{U_0}\frac{\rho_g}{\rho} We \cdot Re^{-0.5}$
Mundo *et al.*[83]	$Oh_c \sim \sqrt{\frac{3(1-\cos(\theta)\beta_{max}^2-12)}{Re^2-4.5\beta_{max}^4 Re}}$	if $Oh > Oh_c$ -SPLASHES if $Oh < Oh_c$ -STICKS	$60 < d_0 < 150\mu m$ $4^0 < \alpha_p < 65^0 \mu m$

[a] K_B = Boltzmann constant, γ = ratio of specific heats, M_g = gas molecular weights, C_g = speed of sound in gas, T = Temperature, f = droplet train frequency, d_0 = droplet impact diameter, d_{32} = Sauter-mean diameter, α_p = primary droplet impact angle, m_s = mass of ejected droplet, m = mass of the primary droplet, β_{max} = ratio of maximum to primary droplet diameter, υ = viscosity, σ = surface tension and θ = contact angle.

[b] They concluded that if splashing is required, either or both of pressure and gas properties be increased. In the review by Marengo *et al.* [72] the Xu *et al.*'s[82] approach is said to contradict the hydrodynamic approach.

regimes relevant to this work, however, have been mostly based on inertia effects. There is still much to know about splashing despite the long term study, interest and practical applications of it. For example, there are hardly any published results on the thermal effects of splashing at high speed/energy impact or at oblique angle impact as most of the work has been done at a normal impact angle. The data in Tables 2.2 to 2.4 identify possible outcomes of droplet impact at high Weber and Reynolds number that can be used in combination in a splashing model. The limitation of the experiments to basic impact scenarios limits the splashing model.

2.4 Bearing Chamber flow

Research into multiphase flow for aeroengine bearing chamber applications is an area where the Nottingham UTC, KIT and Rolls-Royce are well experienced and there are a number of outstanding analytical, numerical simulation and experimental works done in this area.

The bearing chamber flow can, in a very simple form, be represented as the flow inside two cylinders (an annular geometry). Flow in annular geometries is not a new field of study, it has been a problem of interest for over a century. Rayleigh for example, in 1916, was interested in the stability of inviscid flow inside concentric layers with no-slip wall conditions [86]. Taylor [86] proposed the conditions for the onset of instability in laminar annular geometry flow, using approximations based on the thinness of the fluid in the annulus gap. There is a vast amount of literature on single phase laminar

[87] or turbulent [88] flows within co-axial cylinders with/without eccentricity[3] [88, 89], inner/outer wall rotations [90], axial flow [91, 92] and even heat transfer from the wall [93], although not all are in regimes relevant or similar to bearing chamber applications; moreso, flow in the bearing chambers is multiphase.

There are a number of fundamental and fairly mathematical works [94–96] on idealised cases and others that are more application specific ones [55, 97, 98] like this current work. In accounting for the two phases, there are generally the thick and the thin film approximations. In the thin-film assumptions (classical lubrication theory), the film thickness is very small compared to the length scale of the geometry; the wall film is generally taken as boundary layer with a prescribed profile and the core flow taken as a single phase flow; while thick film models attempt to resolve both phases. An integral method with an assumed boundary layer profile (thin-film) was proposed by Chew [99] to analyse the flow in a drum partially filled with oil and rotated horizontally forming a rimming flow. Although it was a simplistic 2D thin-film model, there was consideration for surface friction, swirl of the oil at the inlet and heat transfer from the film to the drum. The model was simplified by assuming that axial variations and air-oil interaction are all negligible. The model was validated with experimental data from Wittig *et al.* [100]; although there was no agreement with the level of sensitivity of heat transfer coefficient with speed of rotation but there was a good agreement with film thickness and the mean heat transfer coefficient.

Baxter [94] developed 3D mathematical models for low Reynolds number thin-film

[3] Eccentricity here means whether or not the centers of the annular cyclinders are aligned.

profile for flows over and around cylindrical obstacles as may obtain in specific regions of the bearing chamber; this work provided a good insight to the challenges and physics involved around *awkward* obstacles such as bolts & nuts, it however still needs consideration for important effects such as surface air shear. Williams [95] assumed the bearing chamber system to be isothermal and made of a horizontal cylinder with the inside coated with a film of fluid. The simplified model accounts for surface tension, gravity, rotation and Marangoni forces and formulated dilute distribution of droplets carried in an inviscid airflow. Kay *et al*. [96, 101] is similar, but an improvement, to the work of Williams [95]. It accounted for air-shear and thermal effects as well as the mass flux of the film driving droplets. Quadratic profiles for both velocity and temperature fields in the film depth were assumed. The work is a significant improvement but still limited to thin film rimming flows.

The flow in the bearing is not simply that of oil on the wall and core air; the core flow also contain of oil mostly in the form of droplets. Authors have considered the droplets as discrete particles in motion with the air using Lagrangian formulations [102, 103]. The Lagrangian droplet formulation helps to study gas phase interaction with the droplets. Farrall *et al.* [102] modelled the chamber isothermally and as consisting of three components, the core-air, the oil droplets and the oil film. The vent and scavenge ports were accounted for using an extension of their previously validated 2D film model [98] and reported sensitivity of film thickness and associated bulk-velocities to their choice of boundary conditions. The 2D model [98] describes a continuous, shear driven film in an annular geometry profile. Maqableh [103] worked on simplified bearing chamber geometries in 2D, extending the work of Farrall [98]. The studies included turbulent single phase gas

flow in an annular cylinder. In the work, the ANSYS-CFX Eulerian multiphase technique was employed. The oil and air phases were considered but there was no consideration for the mass of the droplets impacting on the oil film.

The Volume of Fluid (VoF) technique has been used for bearing chamber related studies. Unlike in the thin-film models, the film is not taken as a boundary layer but explicitly resolved as a true film. Young & Chew [104] simplified the flow as a that of a laminar 2D partially filled rotating horizontal drum, at a speed of less than 250 rpm. The simulation was more of a demonstration of the VoF technique for aeroengine applications. The proposed model under-predicted the speed for the film to collapse by around 12% relative to the observations of White & Higgins [105] but interestingly captures the relevant rimming flow. VoF with enhancement has been used in recent studies to study flows in sections of the bearing chamber. Krug [97] recently evaluated the VoF method for application to the KIT aeroengine bearing chamber test rig and concluded it is suitable for the two-phase flow found in the chamber but it is still computationally expensive. The flow of film on the outer wall into the sump of a sector of the AE3007 styled bearing chamber was studied by Tkaczyk & Morvan [55].

One of the challenges of numerical simulation of the aeroengine bearing chamber is boundary conditions for the oil and air inlets. A mass flow inlet into a small sector of the bearing chamber was setup by Krug [97] using a very fine mesh to observe the oil behaviour as it enters the chamber. An adaptive mesh technique to study the oil breakup process as it enters the bearing chamber on a full chamber geometry was illustrated by Crouchez-Pillot & Morvan [106]; there is however a high memory requirement challenge.

The inlet oil boundary condition did not capture the breakup of oil from the ball bearings, for the demonstration purposes it was taken as a continuum of oil breaking up as a result of the air turbulence inside the bearing chamber rather than as being shed off the ball bearings.

Bearing chambers studies have not been limited to theoretical or numerical modelling works. A number of bearing chamber related experiments [16, 100, 107–109] have been performed over 20 years. It is known that the highly rotational environment creates very tiny droplets that escape through the vents. The separation of the tiny droplets, as low as $0.55\mu m$, from the air as observed by Gorse *et al.* [107] was carried out using an experimental breather by Willenborg *et al.* [110]. The experimental rig of Busam *et al.* [108] and the visualisation rigs by Chandra *et al.* [1, 111] have been used to measure a number of parameters, including but not limited to, film thickness, oil residence volume and droplet motion. Pooling was reported on the lower half of the bearing chamber for which gravity was thought to be mostly responsible for the phenomenon [1, 102]. Experiments for shaft speeds ranging from 10,000 to 19,000 revolutions per minute, similar to cruise speeds of commercial aircraft, were carried out. Observation of the flow in the bearing chamber in regimes similar to aero-engine real time operations, were made by Busam *et al.* [108] to describe the bearing chamber flow field. It was described *as rotating film of oil which is interspersed with some gas bubbles and oil droplets in the turbulent regime driving the film circumferentially*. A more recent attempt was made by Kurz & Bauer [112] to predict flow regimes in bearing chambers. Consistent with other authors [1], two major regimes were identified, first of which is at low shaft speeds where gravity dominates the oil driving; and the second regime is where the shaft speed creates enough momentum in the air to

sufficiently drive the film around the chamber. A momentum correlation dependent on the chamber goemetry, shaft speed and oil viscosity was proposed. The critical momentum for regime change could be identified but it does not account for the contributions from the impacting droplets shed from the bearings.

There has not been, to date, any full and transient aero-engine bearing chamber simulation which includes the droplet to film interaction. This is partly because of the memory need of detailed techniques, for example, a detailed simulation of a single droplet splash required over 3 million computation cells [12] but the bearing chamber is laden with thousands of droplets in any single "camera-exposure". In this work, a technique based on simplifying the computational overhead need in the droplet representation of the oil phase is presented. The VoF technique is used in predicting the flowing film and a coupling method is used to account for the interaction of the droplet with the walls and the free-surface.

2.5 Summary

The turbulent flow of gas and liquid is complex to numerically simulate because of the need to account for several features of the flow. The complexity arises from the need to predict the clear separation of the interfaces or resolving the flow to droplets level phase interaction on top of the other flow field parameters. The practical applications of these fluid interaction is found in oil and gas applications, spray-film cooling application, bearing chamber cooling applications among other possibilities.

A number of techniques for predicting free-surface flows and droplet to film impact works have been reviewed in this chapter. A number of authors have measured the outcomes of droplet impact on films and proposed correlations for the outcomes. These existing data sets do not, however, cover all possible impact scenarios likely to occur in an aeroengine bearing chamber, e.g. shallow impacts on fast moving films. In the later part of this thesis, selected correlations in the regimes relevant to the flow are used, as a reference, to predict impact outcomes such as splashing or sticking of the droplets to the film.

Several attempts have been made as reported in the literature, to study the flow in the HP-IP bearing chamber and other similar bearing chambers. To account for the multiphase, annular and highly rotational, flow of air and oil, different models are utilised. Thick/thin film assumptions as well as discrete representation of the droplets in core-air, in different numerical formulations and with their different challenges, have been used over the years. There is, however, still a need to bring many of the proposals together for a practical modelling of the complex flow of the bearing chamber.

Chapter 3

Existing Multiphase Modelling Framework

3.1 Overview

The flow of interest in this work consists of liquid-gas interaction, gas-droplet interaction and droplet-liquid film interaction in a turbulent environment. These individual flow modelling techniques have come of age and have been used as standards in most commercial codes. This work builds around ANSYS-Fluent and the descriptions following apply largely around this commercial code. In this chapter, the basic and relevant models, upon which the next chapter [*see* §4] builds are described. The continuum phases (liquid and gas interaction) are modelled in the Eulerian framework but the droplet representation is made in the Lagrangian framework.

3.2 Eulerian Phase

The multiphase flow of continous fluids can be modelled using a number of techniques. In ANSYS-Fluent, Volume of Fluid (VoF), Mixture and Eulerian models are available. In these approaches, the phases are mathematically represented as continua. This approach for representing the fluids is referred to as the Euler-Euler approach.

The choice of model is determined by the nature of the problem to be solved and the capability of the model. In the Eulerian model, each of the phases share a single pressure but individual momentum and continuity equations are solved for all the phases. The phases are treated as inter penetrating continua. Inter-phase drag coefficients are implemented to couple the phases. This model is used in both *fluid-solid* and *fluid-fluid* flow applications. Risers, bubble columns and particle suspensions are typically modelled with this model.

In the Mixture model, similar to the Eulerian model, the phases are treated as inter-penetrating continua. The Mixture model, however and unlike the Eulerian model, considers the two phases to be a single fluid and solves a single momentum equation. It prescribes the relative velocities for the disperse phases. Like the Eulerian model, it can also be applied to liquid-solid flow applications. It is typically used for modelling applications such as cyclones, bubbly flows and sedimentation.

The VoF technique uses a colour function to represent the phases as volume fraction. VoF assumes a single continuum and solves only one momentum equation [*see* §3.2.4]. VoF is a free-surface tracking technique applied on fixed Eulerian mesh. It is particularly

useful for applications where the position of the free-surface is important, such as in dam break, sloshing, stratified flows and transient bubble tracking.

The three models can handle only one of the phases as compressible, but this can be extended using User Defined Functions (UDFs). In the Eulerian model, Lagrangian particles interact only with the primary phase. This will not be suitable for the problem described in this work.

The finite volume numerical technique described in §3.5.1 is used to solve the governing equations by discretising the fluid domain into finite computational cells [37, 38, 42].

The governing equations as used within ANSYS-Fluent to solve the fluid flow are described in §3.2.1 to §3.4.1. For the work presented in this thesis, the Volume of Fluid technique is considered the most suitable. This work effectively extends the Volume of Fluid technique as an Euler-Euler-Lagrange technique.

3.2.1 Continuity Equation

The continuity equation, Equation (3.1), is a statement of mass conservation within a control volume.

$$\frac{\partial \rho}{\partial t} + \nabla \cdot (\rho \overrightarrow{u}) = 0 \tag{3.1}$$

The flow velocity is $\overrightarrow{u}$. This can be expressed in index or Cartesian vector representations. In the index notation, $\overrightarrow{u} = (u_1, u_2, u_3)^T$ and in the Cartesian vector representation, $\overrightarrow{u} =$

$u_1\hat{i} + u_2\hat{j} + u_3\hat{k}$. The vector components are u_1, u_2 and u_3. $\hat{i}$, $\hat{j}$ and $\hat{k}$ are the Cartesian unit vector components.

The incompressible assumption has been taken in this work, and so Equation (3.1) reduces to Equation (3.2).

$$\nabla \cdot \overrightarrow{u} = 0 \tag{3.2}$$

This assumption is because of the low fluid velocities, the Mach number[1], Ma, is by far less than 1. Therefore, no part of the mass of the continuum is compressed or expands.

3.2.2 Navier-Stokes Equation

The Navier-Stokes equations are given in Equation (3.3). These represent the force balance at each point in the domain. The inertial terms are balanced with the divergence of stress, body forces and other contributory source terms such as $\overrightarrow{S_m}$.

$$\overbrace{\rho\left(\underbrace{\frac{\partial \overrightarrow{u}}{\partial t}}_{\text{unsteady acceleration}} + \underbrace{\nabla \cdot (\overrightarrow{u}\,\overrightarrow{u})}_{\text{convective acceleration}}\right)}^{\text{Inertial terms}} = \overbrace{\underbrace{-\nabla p}_{\text{pressure gradient}} + \underbrace{\nabla \cdot \mu\left[\nabla \overrightarrow{u} + (\nabla \overrightarrow{u})^T\right]}_{\text{viscous forces}}}^{\text{Divergence of stress terms}} \overbrace{- F_s + \underbrace{\rho \overrightarrow{g}}_{\text{gravity}}}^{\text{body forces}} + \underbrace{\overrightarrow{S_m}}_{\text{source term}} \tag{3.3}$$

[1] $Ma = \frac{u}{c}$, ratio of fluid speed, u, to speed of sound, c. A flow is supersonic if $Ma > 1$; subsonic if $Ma < 1$.

where F_s is the surface tension force added as a spatially varying body force and only near the free surface [*see* §3.2.4].

3.2.3 Energy Equation

The energy equation for the multiphase flow is computed as given in Equation (3.4a) and, also, for the VoF technique, mass averaging is done for the energy and temperature as given, respectively, in Equations (3.4b) and (3.4c). E_i for each phase, i to phase n, is based on the specific heat of that phase and the shared temperature. k is the thermal conductivity and S_h is the source term.

$$\frac{\partial}{\partial t}(\rho E) + \nabla \cdot (u(\rho E + p)) = \nabla \cdot (k \nabla T) + S_h \tag{3.4a}$$

$$E = \frac{\sum_{i=1}^{n} \alpha_i \rho_i E_i}{\sum_{i=1}^{n} \alpha_i \rho_i} \tag{3.4b}$$

$$T = \frac{\sum_{i=1}^{n} \alpha_i \rho_i T_i}{\sum_{i=1}^{n} \alpha_i \rho_i} \tag{3.4c}$$

3.2.4 Free-surface tracking

The concept of interface tracking was earlier introduced in §2.2. The computation of the "colour-functions", or volume fraction, α is given in Equation (3.5). From the computation, a volume fraction isosurface with value in the region $0 < \alpha < 1$ identifies the free-surface. The VoF technique alone is not sufficient to describe the free-surface, thus the coupling of VoF with Level Set was introduced [34, 48]. The Level Set method clearly defines the free-surface at a zero isosurface [*see* §3.2.4.2].

3.2.4.1 Volume of Fluid (VoF) - Technique

The VoF technique is essentially solving the continuity equation for the volume fraction of the present phases in the form of Equation (3.5).

$$\frac{1}{\rho_i}\left[\frac{\partial}{\partial t}(\alpha_i\rho_i) + \nabla\cdot(\alpha_i\rho_i\overrightarrow{u}) = S_{\alpha_i} + M_{net}\right] \tag{3.5}$$

where M_{net} is the net mass exchange between the phases such as could exist in the event of evaporation or condensation. Physical phase change is not modelled in this work, thus M_{net} is zero. S_{α_i} is the source term. The primary phase volume fraction is not computed using Equation (3.5), but rather calculated using Equation (3.6); this restriction enforces mass conservation. For a liquid and gas multiphase flow, where the air phase is taken as the primary phase, for example, $\alpha_l = 1 - \alpha_g$.

$$\sum_{i=1}^{n}\alpha_i = 1 \tag{3.6}$$

$$\Lambda = \sum_{i=1}^{n}\Lambda_i\alpha_i \tag{3.7a}$$

$$\rho = \rho_g\alpha_g + \rho_l\alpha_l \tag{3.7b}$$

$$\mu = \mu_g\alpha_g + \mu_l\alpha_l \tag{3.7c}$$

The effective material properties that occur in the transport equations are computed

using the volume fraction average Equation (3.7a) for a given material property Λ in an n-phase system. The density and viscosity, for example, are computed respectively in Equations (3.7b) & (3.7c).

3.2.4.2 Coupled Level Set Volume of Fluid (CLSVoF)

The Level Set (LS) function, ϕ, is advected using Equation (3.8). The Level Set function, ϕ, can take positive and negative values; the interface is described at the zero Level Set and the liquid phase is described with positive Level Set values.

$$\frac{\partial \phi}{\partial t} + \overrightarrow{u} \cdot \nabla \phi = 0 \tag{3.8}$$

The equation will move the zero Level Set exactly as the free-surface motion from the initially known position of the film. The Level Set function is smooth and continuous; this makes it possible to accurately compute the spatial gradients. This capability of the Level Set method provides a good estimation of the interface curvature, Equation (3.9) and in turn the surface tension force, Equation (3.10), required in the Navier-Stokes Equation (3.3).

$$\kappa\left(\phi\right) = \nabla \cdot \frac{\nabla \phi}{|\nabla \phi|}\bigg|_{\phi=0} \tag{3.9}$$

$$F_s = \sigma\kappa\nabla\phi\delta_\varepsilon(\phi) \tag{3.10}$$

where δ_ε [Eqn. 3.11] is a delta function, smoothed over a distance ε, this is by assuming that the interface can be considered as a "thin" fluid region with a thickness ε.

$$\delta_\varepsilon(\phi) = \begin{cases} \frac{1}{2\varepsilon}\left(1 + cos\left(\frac{\pi\phi}{\varepsilon}\right)\right) & \text{if } |\phi| < \varepsilon \\ 0 & otherwise \end{cases} \tag{3.11}$$

where ε is taken as 1.5 times the grid spacing.

In Level Set method [34], the effective density and viscosity of the fluid are calculated using Equations (3.12a) & (3.12b) respectively.

$$\rho = \rho_g + (\rho_l - \rho_g) H_\varepsilon(\phi) \tag{3.12a}$$

$$\mu = \mu_g + (\mu_l - \mu_g) H_\varepsilon(\phi) \tag{3.12b}$$

where $H_\varepsilon(\phi)$ is a smoothed Heaviside function.

$$H_\varepsilon(\phi) = \begin{cases} 0 & \text{if } \phi < -\varepsilon \\ \frac{(\phi+\varepsilon)}{(2\varepsilon)} + \frac{1}{(2\pi)} sin(\frac{\pi\phi}{\varepsilon}) & \text{if } |\phi| \leq \varepsilon \\ 1 & \text{if } \phi > \varepsilon \end{cases} \tag{3.13}$$

Level Set alone is, however, not mass conservative. In the VoF formulation on the other hand, there is discontinuity at the free-surface posing a weakness for the method to compute the spatial gradients. A major strength of the VoF method is its mass conservation ability however. The coupling of both Level Set and the volume of fluid (CLSVoF) methods ensures mass conservation and the ability to capture the free-surface and correctly compute surface tension force.

In Coupled Level Set Volume of Fluid (CLSVoF) method, both the Level Set and volume fractions are used to reconstruct the free-surface using the concept of piecewise linear interface construction (PLIC) [69]. The algorithmic implementation is shown in Figure 3.1, adapted from Nichita [113]. The nature[2] of Equation (3.8) does not guarantee that $|\nabla\phi| = 1$ is always maintained after the solution thus resulting in errors accumulating during the iteration process. The re-initialisation of ϕ every time step is necessary as a result of the errors that will accumulate during the iteration process.

[2]The interface deforms and has uneven profile with a thickness across the interface.

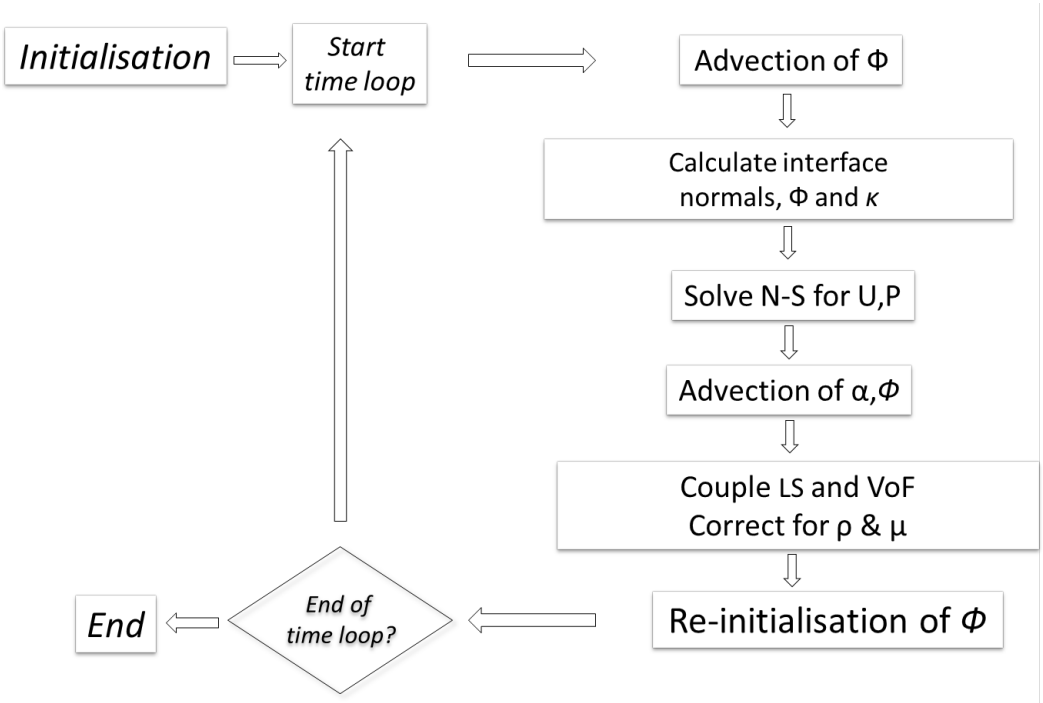

Figure 3.1: Algorithm for implementing CLSVoF [113]

3.3 Modelling Turbulent flows

In turbulent fluid flow, the flow fields fluctuate in a stochastic manner. An approach to "model" the stochastic flow fields, $\psi(t)$, properties is done by decomposing them into two components [37], the mean, Ψ and the stochastic component, $\psi'(t)$. In other words, $\psi(t) = \Psi + \psi'(t)$. For example, the velocity field will be represented as $u = u(t) = U + u'(t)$. Although this is intended to simplify to averaging of flow fields, it introduces further terms to be solved in the continuity, Navier-Stokes equations and any transport equations that may be involved.

The mathematical or algorithmic closure of mean flow equations in a control vol-

ume leads to the turbulence models class known as the Reynolds Average Navier-Stokes (RANS). The RANS technique can be found well discussed in books [37, 42, 69]. The compact index form of the continuity and Reynolds-averaged Navier-Stokes equations are shown, respectively, in Equations (3.14) and (3.15).

$$\frac{\partial(\rho U_i)}{\partial x_i} = S_\rho \tag{3.14}$$

$$\left[\frac{\partial(\rho U_i)}{\partial t} + \frac{\partial(\rho U_i U_j)}{\partial x_j}\right] = -\frac{\partial P}{\partial x_i} + \frac{\partial}{\partial x_j}\left(\mu\frac{\partial U_i}{\partial x_j} - \underbrace{\rho\overline{u_i' u_j'}}_{\text{Reynolds stress tensor}}\right) + S_m \tag{3.15}$$

where S_ρ and S_m are source terms.

Reynolds stress tensor is the new set of unknown introduced. The 1877 Boussinesq hypothesis that Reynolds stresses are proportional to the rate of deformation forms the basis for many of the turbulence models [114, 115]. The proportionality constant or the turbulent viscosity, μ_t is another variable introduced by this simplification, Equation (3.16). The kinematic turbulent viscosity also follows as $\upsilon_t = \mu_t/\rho$.

$$-\rho\overline{u_i' u_j'} = \mu_t\left(\frac{\partial U_i}{\partial x_j} + \frac{\partial U_j}{\partial x_i}\right) \tag{3.16}$$

In an attempt to predict the turbulent viscosity, several “standard” models have been

developed. Such models like the Prandtl‘ mixing length model, Spalart-Allmaras model and the variants of the $\kappa - \epsilon$ and $\kappa - \omega$ models exist. The mixing length model assumes that υ_t is proportional to the length scale. This model can be fine for simple flows where the mixing length scales are known and/or not changing. The Spalart-Allmaras model solves a single conservation equation containing convective and diffusive terms for the production and dissipation of kinematic turbulent viscosity. It is generally known to be good for flows with mild separation or with simple recirculation but not reliable for flows with decaying turbulence or free shear flows.

The $\kappa - \epsilon$ model was proposed by Launder & Spalding [116] in 1974 and it is one of the most used models in industrial applications. It essentially models kinematic turbulent viscosity as proportional to κ^2/ϵ. Where, the flow fields, κ and ϵ are, respectively, the turbulence kinetic energy per mass and dissipation rate of κ. This model further introduces two more equations to be solved for κ and ϵ. The performance is, however, not reliable in flows with large extra strains [37]. The $\kappa - \omega$ models can be thought of, also, as variants of the standard $\kappa - \epsilon$ model. They model turbulent viscosity as $\mu_t = \rho \cdot (\kappa/\omega)$, where ω is an inverse time scale measure of turbulence.

For RANS $\kappa - \epsilon$ based turbulence models, the energy equation is modelled using the

form in Equation (3.17a).

$$\frac{\partial}{\partial t}(\rho E) + \frac{\partial}{\partial x_i}\{U_i(\rho E + p)\} = \frac{\partial}{\partial x_j}\left(k_{eff}\frac{\partial T}{\partial x_j}\right) + S_h \tag{3.17a}$$

$$k_{eff} = k + c_p\mu_t/Pr_t \tag{3.17b}$$

where E is the total energy, k_{eff} is the effective thermal conductivity and Pr_t is the turbulent Prandtl number.

In this work, the (shear-stress transport) SST $k-\omega$ model described in §3.3.3 has been used. For completeness, the standard κ-ϵ and $\kappa-\omega$ models are respectively described in §3.3.1 and §3.3.2.

3.3.1 Standard κ - ϵ turbulence model

The Standard κ-ϵ turbulence model [69, 116] is basically the transport equation for the turbulence kinetic energy, κ, and ϵ, its rate of dissipation. These are expressed in the form, respectively, given in Equations (3.18) and (3.19). ANSYS-Fluent allows user defined functions to describe source terms S_κ and S_ϵ.

$$\frac{\partial}{\partial t}(\rho\kappa) + \frac{\partial}{\partial x_i}(\rho\kappa U_i) = \frac{\partial}{\partial x_j}\left(\Gamma_\kappa\frac{\partial \kappa}{\partial x_j}\right) + G_\kappa + G_b - \rho\epsilon - Y_M + S_\kappa \tag{3.18}$$

$$\frac{\partial}{\partial t}(\rho\epsilon) + \frac{\partial}{\partial x_i}(\rho\epsilon U_i) = \frac{\partial}{\partial x_j}\left(\Gamma_\epsilon \frac{\partial \epsilon}{\partial x_j}\right) + C_{1\epsilon}\frac{\epsilon}{\kappa}(G_\kappa + C_{3\epsilon}G_b) - C_{2\epsilon}\rho\frac{\epsilon^2}{\kappa} + S_\epsilon \quad (3.19)$$

where $\Gamma_\kappa = \left(\mu + \frac{\mu_t}{\sigma_\kappa}\right)$ and $\Gamma_\epsilon = \left(\mu + \frac{\mu_t}{\sigma_\epsilon}\right)$. The turbulent viscosity is modelled as given in Equation (3.20a). G_κ is the production of turbulence kinetic energy modelled using Equation (3.20b). The buoyancy driven generation of the turbulence kinetic energy, G_b, is modelled using Equation (3.20c) and the coefficient of thermal expansion β is given by Equation (3.20d).

$$\mu_t = \rho C_\mu \frac{\kappa^2}{\epsilon} \quad (3.20a)$$

$$G_\kappa = -\rho\overline{u_i' u_j'}\frac{\partial U_j}{\partial x_i} = \mu_t\left(\frac{\partial U_i}{\partial x_j} + \frac{\partial U_j}{\partial x_i}\right)^2 \quad (3.20b)$$

$$G_b = \beta g_i \frac{\mu_t}{Pr_t}\frac{\partial T}{\partial x_i} \quad (3.20c)$$

$$\beta = -\frac{1}{\rho}\left(\frac{\partial \rho}{\partial T}\right)_p \quad (3.20d)$$

$$Y_M = 2\rho M a_t^2 \quad (3.20e)$$

For high turbulent Mach[3] number flows, the effect of compressibility, Y_M, on turbulence is modelled using Equation (3.20e); in incompressible flows this is negligible.

The default model constants [69] are given as $C_{1\epsilon} = 1.44$, $C_{2\epsilon} = 1.92$, $C_\mu = 0.09$,

[3] $Ma_t = \sqrt{\kappa/c^2}$; $c = \sqrt{\gamma RT}$ is the speed of sound.

$\sigma_\kappa = 1.0$, $\sigma_\epsilon = 1.3$, $Pr_t = 0.85$ and g_i is the gravity component in the i^{th} direction.

3.3.2 Standard κ - ω turbulence model

In ANSYS-Fluent, the standard κ-ω model is based on the work of Wilcox [115]. This model employs modification for low-Reynolds number effects, compressibility and shear flow spreading [69]. It is an empirical model for the transport of κ and ω as given, respectively, in Equations (3.21) & (3.22) similar to the κ-ϵ model described in §3.3.1 with the ability to define user defined source terms S_κ and S_ω.

$$\frac{\partial}{\partial t}(\rho\kappa) + \frac{\partial}{\partial x_i}(\rho\kappa U_i) = \frac{\partial}{\partial x_j}\left(\Gamma_\kappa \frac{\partial \kappa}{\partial x_j}\right) + G_\kappa - Y_\kappa + S_\kappa \tag{3.21}$$

$$\frac{\partial}{\partial t}(\rho\omega) + \frac{\partial}{\partial x_i}(\rho\omega U_i) = \frac{\partial}{\partial x_j}\left(\Gamma_\omega \frac{\partial \epsilon}{\partial x_j}\right) + G_\omega - Y_\omega + S_\omega \tag{3.22}$$

where the effective diffusivities, Γ_κ & Γ_ω, are respectively defined by Equations (3.23a) & (3.23b). The turbulent viscosity, μ_t, is a blend of both κ and ω as given by Equation

(3.24a).

$$\Gamma_\kappa = \left(\mu + \frac{\mu_t}{\sigma_\kappa}\right) \tag{3.23a}$$

$$\Gamma_\omega = \left(\mu + \frac{\mu_t}{\sigma_\omega}\right) \tag{3.23b}$$

To correct for low-Reynolds number, the coefficient α^*, Equation (3.24b), damps the turbulent viscosity as a function of the turbulent Reynolds number, Re_t, given by Equation (3.24c). It is easy to see from Equation (3.24d) that this correction approaches unity for high Reynolds numbers.

$$\mu_t = \alpha^* \frac{\rho\kappa}{\omega} \tag{3.24a}$$

$$\alpha^* = \alpha^*_\infty \left(\frac{\alpha^*_0 + \frac{Re_t}{R_\kappa}}{1 + \frac{Re_t}{R_\kappa}}\right) \tag{3.24b}$$

$$Re_t = \frac{\rho\kappa}{\mu\omega} \tag{3.24c}$$

$$\lim_{Re_t \to \infty} \left[\alpha^*_\infty \left(\frac{\alpha^*_0 + \frac{Re_t}{R_\kappa}}{1 + \frac{Re_t}{R_\kappa}}\right)\right] = \alpha^*_\infty = 1 \tag{3.24d}$$

The modelling of the production of κ, G_κ is same as given in Equation (3.20b). The production of ω, G_ω is given by Equation (3.25a). The coefficient α is given Equation

(3.25b).

$$G_\omega = \alpha \frac{\omega}{\kappa} G_\kappa \tag{3.25a}$$

$$\alpha = \frac{\alpha^*_\infty}{\alpha^*} \left(\frac{\alpha_0 + \frac{Re_t}{R_\omega}}{1 + \frac{Re_t}{R_\omega}} \right) \tag{3.25b}$$

The dissipation of κ and ω are modelled using Equations (3.26a) & (3.26b).

$$Y_\kappa = \rho \beta^* f_{\beta 1} \cdot \kappa \omega \tag{3.26a}$$

$$Y_\omega = \rho \beta^* f_{\beta 2} \cdot \omega^2 \tag{3.26b}$$

where the coefficients in Equations (3.26a) & (3.26b) are expressed in Equations (3.27a)

to (3.27g).

$$\beta^* = \beta^*_\infty \left(\frac{4/15 + (Re_t/R_\beta)^4}{1 + (Re_t/R_\beta)^4} \right) \tag{3.27a}$$

$$f_{\beta 1} = \begin{cases} 1 & , \chi_\kappa \leq 0 \\ \frac{1+680\chi_\kappa^2}{1+400\chi_\kappa^2} & , \chi_\kappa > 0 \end{cases} \tag{3.27b}$$

$$\chi_\kappa \equiv \frac{1}{\omega^3} \frac{\partial \kappa}{\partial x_j} \frac{\partial \omega}{\partial x_j} \tag{3.27c}$$

$$f_{\beta 2} = \frac{1 + 70\chi_\omega}{1 + 80\chi_\omega} \tag{3.27d}$$

$$\chi_\omega = \left| \frac{\Omega_{ij}\Omega_{jk}S_{ij}}{(\beta^*_\infty \omega)^3} \right| \tag{3.27e}$$

$$\Omega_{ij} = \frac{1}{2} \left(\frac{\partial U_i}{\partial x_j} - \frac{\partial U_j}{\partial x_i} \right) \tag{3.27f}$$

$$S_{ij} = \frac{1}{2} \left(\frac{\partial U_j}{\partial x_i} + \frac{\partial U_i}{\partial x_j} \right) \tag{3.27g}$$

where Ω_{ij} is the mean rate of rotation of the tensor and S_{ij} is mean strain rate.

The model constants are given as follows; $\alpha^*_\infty = 1$, $\alpha_\infty = 0.52$, $\alpha_0 = \frac{1}{9}$, $\beta^*_\infty = 0.09$, $\beta_i = 0.072$, $\alpha^*_0 = \frac{\beta_i}{3}$, $R_\beta = 8$, $R_\kappa = 6$, $R_\omega = 2.95$, $\sigma_\kappa = 2.0$ and $\sigma_\omega = 2.0$.

3.3.3 SST κ - ω turbulence model

The development of the (shear-stress transport) SST $k - \omega$ model is based on the 1992-1997 work of Menter [38, 117]. It is essentially the hybrid of the $k - \omega$ equations in the near wall region, and the transformation of the original $k - \epsilon$ model in the fully turbulent region far away from the walls.

The transport equations solved in the SST $k-\omega$ model for κ and ω are respectively given in Equations (3.28) & (3.29). Although the transport equations are expressed similarly to the standard $\kappa-\omega$ model further refinements were introduced in ANSYS-Fluent [69]. In the implementation, a "blending" function is used such that it activates the $k-\omega$ close to the surface and $k-\epsilon$ is activated away from the wall. The model constants are different and a damped cross-diffusion derivative term, Equation (3.32), is introduced to the ω equation blending the $\kappa-\epsilon$ and $\kappa-\omega$ models together. A modification of the turbulent viscosity is done to account for turbulent shear stress. The constants are also different from the standard equations.

$$\frac{\partial}{\partial t}(\rho\kappa)+\frac{\partial}{\partial x_i}(\rho\kappa U_i)=\frac{\partial}{\partial x_j}\left(\Gamma_\kappa\frac{\partial\kappa}{\partial x_j}\right)+\widetilde{G_\kappa}-Y_\kappa+S_\kappa \tag{3.28}$$

$$\frac{\partial}{\partial t}(\rho\omega)+\frac{\partial}{\partial x_i}(\rho\omega U_i)=\frac{\partial}{\partial x_j}\left(\Gamma_\omega\frac{\partial\omega}{\partial x_j}\right)+G_\omega-Y_\omega+D_\omega+S_\omega \tag{3.29}$$

The effective diffusivities are defined using Equations (3.23a) & (3.23b), but the turbulent viscosity, μ_t, turbulent Prandtl numbers for κ and ω are, respectively, described in Equations (3.30a) to (3.30c). The coefficients of these equations are described in Equa-

tions (3.31a) to (3.31e).

$$\mu_t = \frac{\rho\kappa}{\omega}\frac{1}{max\left(\frac{1}{\alpha^*}, \frac{SF_2}{\alpha_1\omega}\right)} \tag{3.30a}$$

$$\sigma_\kappa = \frac{1}{F_1/\sigma_{\kappa 1} + (1-F_1)/\sigma_{\kappa 2}} \tag{3.30b}$$

$$\sigma_\omega = \frac{1}{F_1/\sigma_{\omega 1} + (1-F_1)/\sigma_{\omega 2}} \tag{3.30c}$$

$$F_1 = tanh\left(\Phi_1^4\right) \tag{3.31a}$$

$$F_2 = tanh\left(\Phi_2^2\right) \tag{3.31b}$$

$$\Phi_1 = min\left[max\left(\frac{\sqrt{\kappa}}{0.09\omega y}, \frac{500\mu}{\rho y^2\omega}\right), \frac{4\rho\kappa}{\sigma_{\omega 2} D_\omega^+ y^2}\right] \tag{3.31c}$$

$$D_\omega^+ = max\left[2\rho\frac{1}{\sigma_{\omega 2}\frac{1}{\omega}\frac{\partial\kappa}{\partial x_j}\frac{\partial\omega}{\partial x_j}}, 10^{-10}\right] \tag{3.31d}$$

$$\Phi_2 = max\left[2\frac{\sqrt{\kappa}}{0.09\omega y}, \frac{500\mu}{\rho y^2\omega}\right] \tag{3.31e}$$

where S is the strain manitude (Eqn. (3.27g)), F_1 and F_2 are blending functions and y is the distance to the next surface and D_ω^+ is the positive portion of the cross-diffusion term, D_ω, described in Equation (3.32).

$$D_\omega = 2\left(1-F_1\right)\rho\frac{1}{\omega\sigma_{\omega 2}}\frac{\partial\kappa}{\partial x_j}\frac{\partial\omega}{\partial x_j} \tag{3.32}$$

The production of the turbulence kinetic energy, $\widetilde{G_\kappa}$ and the production of ω, G_ω are given by Equations (3.33a) & (3.33b). This formulation is different[4] from the standard $\kappa - \omega$ as seen in the coefficients Equations (3.34a) to (3.34c).

$$\widetilde{G_\kappa} = min\left(G_\kappa, 10\rho\beta^*\kappa\omega\right) \tag{3.33a}$$

$$G_\omega = \frac{\alpha}{\nu_t}\widetilde{G_\kappa} \tag{3.33b}$$

$$\alpha_\infty = F_1\alpha_{\infty 1} + \left(1 - F_1\right)\alpha_{\infty 2} \tag{3.34a}$$

$$\alpha_{\infty 1} = \frac{\beta_{i1}}{\beta^*_\infty} - \frac{\zeta^2}{\sigma_{\omega 1}\sqrt{\beta^*_\infty}} \tag{3.34b}$$

$$\alpha_{\infty 2} = \frac{\beta_{i2}}{\beta^*_\infty} - \frac{\zeta^2}{\sigma_{\omega 2}\sqrt{\beta^*_\infty}} \tag{3.34c}$$

The modelling of the turbulence dissipation term, Y_κ, is modelled using Equation (3.35a) and the dissipation of ω given by (3.35b).

$$Y_\kappa = \rho\beta^*\kappa\omega \tag{3.35a}$$

$$Y_\omega = \rho\beta\omega^2 \tag{3.35b}$$

where $\beta^* = 1$ and $\beta = F_1\beta_{i1} + \left(1 - F_1\right)\beta_{i2}$.

The model constants are $\sigma_{\kappa 1} = 1.176$, $\sigma_{\omega 1} = 2.0$, $\sigma_{\kappa 2} = 1.0$, $\sigma_{\omega 2} = 1.168$, $\alpha_1 = 0.31$,

[4] Unless otherwise described in this section, the terms are the same as those of the standard $\kappa - \omega$.

$\beta_{i1} = 0.075$, $\beta_{i2} = 0.0828$ and $\zeta = 0.41$.

Although the $\kappa - \omega$ model is isotropic, the attractiveness of the SST $k - \omega$ model to this work is because it combines the good near-wall behaviour of the $k - \omega$ model with the robustness and numerical stability of the $k - \epsilon$ models far from the walls. The $\kappa - \omega$ model performs better than $\kappa - \epsilon$ models in modelling stratified flows as a result of the turbulence damping correction introduced by Egorov *et al.* [56] described later in §3.3.4.

3.3.4 Turbulence Damping

The need for the damping correction arises from the fact that there is a big difference in the physical properties of the fluids across the free-surface. The difference manifests as a high difference in turbulence level in the gas and the liquid phases. The damping correction model has been validated by authors (Valle *et al.* [118], Amir *et al.* [119] & Tkaczyk and Morvan [55]) and is only available in the SST $k - \omega$ model for free-surface flows in ANSYS-Fluent 14.5 and subsequent versions. Numerical turbulence damping is introduced by Egorov *et al.* [56] as source term in the ω [Eqn. 3.29] equation. This is expressed as S_ω in Equation (3.36).

$$S_\omega = A_i \Delta n \beta \rho_i \left(\frac{6 \cdot B \mu_i}{\beta \rho_i \Delta n^2} \right)^2 \tag{3.36}$$

where B is a damping constant that can take values from $0 - 100$. The default value in ANSYS-Fluent is 10 and is rather a calibration factor. A_i is the inter-facial area while ρ_i is the density for the phase i. From Egorov *et al.* [56] and the ANSYS-Fluent [69]

implementation, the area is computed as a function of the volume fraction, α_i, as $A_i = 2 \cdot \alpha_i \left|\Delta\alpha_i\right|$. The cell height normal to the free-surface is Δn. β is the model closure coefficient ($\beta = 0.075$).

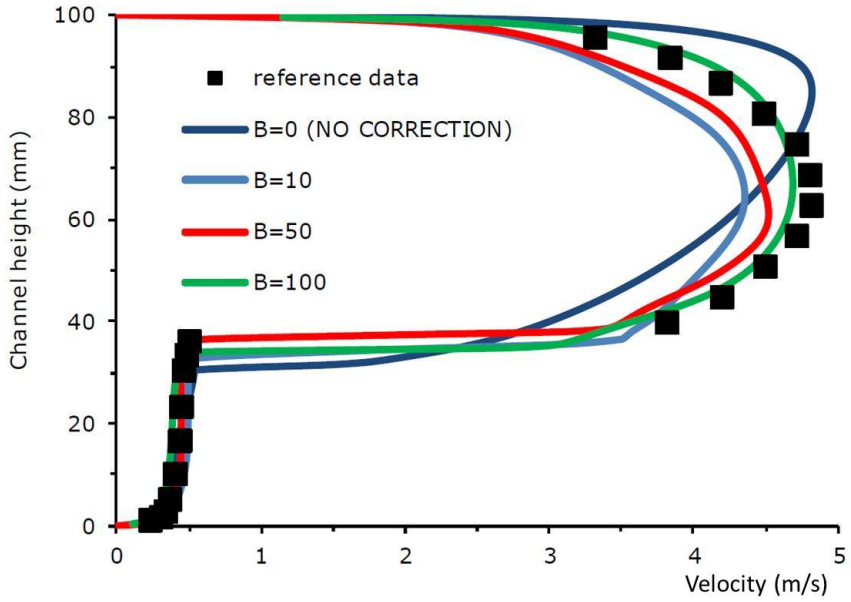

Figure 3.2: Turbulence damping effect [55]

Figure 3.2 shows result from Tkaczyk & Morvan's [55] implementation of the turbulence damping correction. The velocities are measured on a plane downstream of a rectangular duct carrying water film and air in a stratified flow. The film depth is about 40mm and flowing at about 10% of the air velocity.

The value $B = 0$ in the figure is equivalent to the $\kappa - \epsilon$ model implementation. It can be seen that without the correction, there is a numerical "error" at the interface region that propagates into the core flow in the air phase as compared with the experimental data. The value B can therefore be seen as a calibration to the experiment.

3.3.5 Wall treatment

Although a flow may be turbulent, the flow behaviour at the walls is laminar. The flow magnitude increases gradually through the viscous sub-layer, closer to the wall, into the core turbulent regime. For completeness, this section describes the standard treatment of walls in ANSYS-Fluent [69]. y^+ is a non-dimensional distance from the wall boundary as given by Equation (3.37a).

$$y^+ = \frac{\rho u_\tau}{\mu} y \tag{3.37a}$$

$$u_\tau = \sqrt{\frac{\tau_w}{\rho}} \tag{3.37b}$$

where y is a distance measured from the wall, τ_w is the wall shear stress. The viscous sub-layer[69] is in the region where y^+ is below 30.

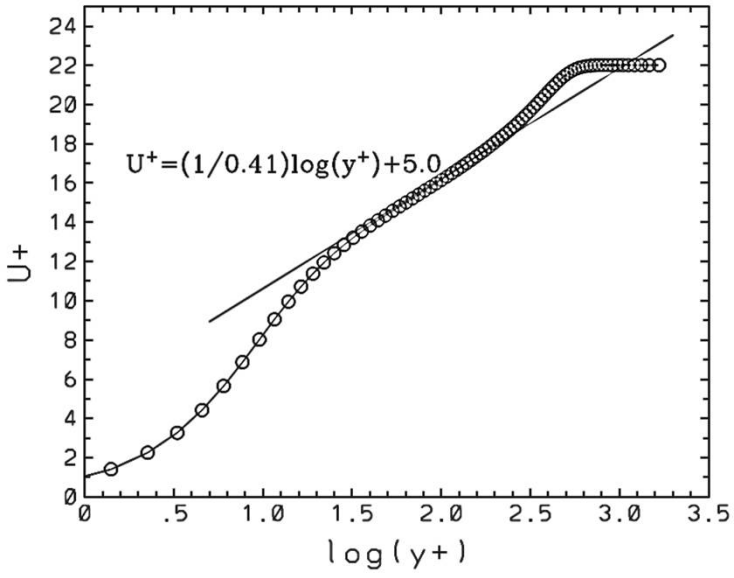

Figure 3.3: Log law [120]

Figure 3.3 shows non-dimensional velocity (U^+) plot against y^+ for flow close to a smooth wall with a no-slip boundary condition. This velocity is normalised with the wall shear stress, τ_w and density ($U^+ = U/\left(\tau_w/\rho\right)$). The circles are experimental points and the solid lines are by curve fitting. The logarithmic law fits well away from the viscous sub-layer.

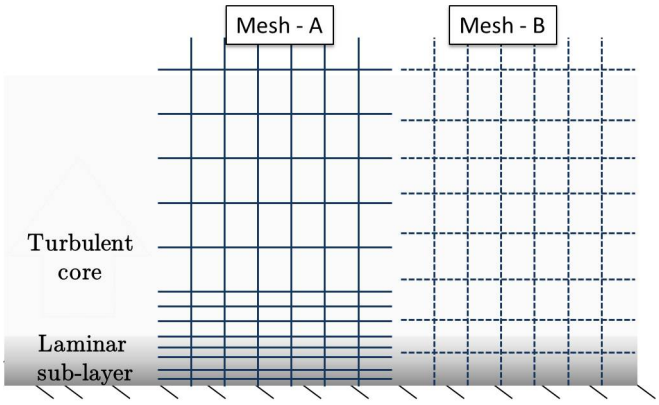

Figure 3.4: Near wall treatment

In ANSYS-Fluent [69], special treatment is used for ω at the walls depending on the mesh. Given the flow in Figure 3.4 where either Mesh A or B is used. Mesh - A is fine and able to resolve flow in the laminar sub-layer to the wall but Mesh -B is not fine enough to resolve it. The viscous layer/region is bridged using wall functions instead of resolving the flow. For fine meshes, the low-Reynolds number boundary conditions apply [*see* §3.3.2 & Equation (3.24b)]. The analytical function approach is used with coarser mesh, where the mesh is not able to resolve the laminar sub-layer and otherwise the appropriate low-Reynolds number boundary conditions apply. The value of ω at the wall or ω_w is given in

Equation (3.38).

$$\omega_w = \frac{\rho\,(u^*)^2}{\mu} \times \begin{cases} \frac{6}{\beta_i (y^+)^2} & \text{Analytical, } y^+ < 30 \\ \frac{1}{\sqrt{\beta^*_\infty}} \frac{du^+_{turb}}{dy^+} & \text{Logarithmic region, } y^+ > 30 \end{cases} \tag{3.38}$$

where $\beta^*_\infty = 0.09$, $\beta_i = 0.072$ and u^* is the non-dimensional friction velocity.

3.4 Lagrangian Phase - Discrete Phase Model (DPM)

A model of a cold droplet moving in a hot stream of high velocity gas needs treatment for aerodynamics, mass transfer and heat transfer. A droplet can be considered as spherical liquid volume held together by surface tension force. The interaction of the droplet with the gas phase, for example, causes deformation as a result of the aerodynamic drag and some liquid may evaporate, thus transferring mass as vapour. The droplet can also cool down in the gas stream if the gas is colder than the droplets. The droplets in the target applications are small *(around* $50 - 1500\ \mu m$*)*. The shape deformation of the droplets is considered negligible and it may be reasonable to assume they maintain a spherical shape because they are small. This non-deformation assumption of the droplets is only for simplicity and could be modified in future development. For a disperse droplet concentration in the fluid domain, the Lagrangian representation could be used, this is the Discrete Phase Model (DPM) in ANSYS Fluent.

Figure 3.5 shows a single droplet in a 3D space moving with a velocity U_p. The actual diameter is given as D_p. A Lagrangian representation, shown as the centre dark dot, of

the whole droplet considers the droplet as a single point, regardless of the actual space occupied by the droplet. The coordinates, $P_{(x,y,z)}$ are obtained from the integration of force per unit mass balance, Equation (3.39).

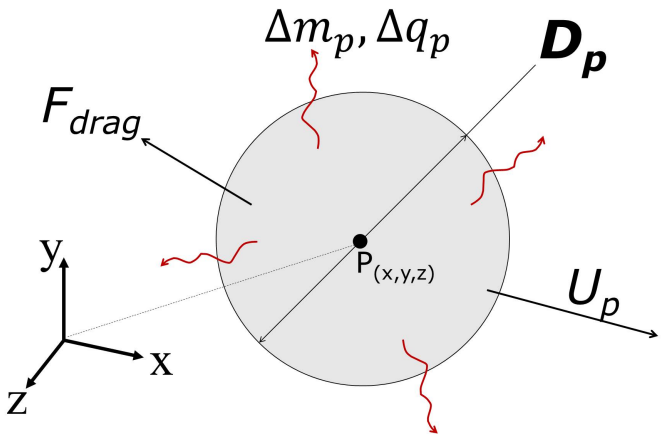

Figure 3.5: DPM in a 3D space

$$\frac{d\overrightarrow{U_p}}{dt} = \underbrace{\overrightarrow{F_D}}_{drag} + \underbrace{\overrightarrow{F}_{otherforces}}_{\text{pressure, virtual mass, bouyancy}} \tag{3.39}$$

The drag force per unit particle mass, $\overrightarrow{F_D}$, is given in Equation (3.40). The Reynolds number of the particle, Re, is estimated as $Re \simeq \frac{\rho_l}{\mu} D_p \left| \overrightarrow{U}_p - \overrightarrow{u} \right|$. The coefficient of drag, C_D, is computed depending on the scenario and can be implemented as a User Defined Function (UDF) in ANSYS-Fluent.

$$\overrightarrow{F_D} = \frac{18\mu}{\rho_l D_p^2} \frac{C_D Re}{24} (\overrightarrow{U}_p - \overrightarrow{u}) \tag{3.40}$$

The droplets are assumed to be non-deforming and behave like hard spheres, an assumption made because of the small sizes of the droplets. The drag coefficient is computed based on the Reynolds number using the Schiller & Naumann [121] correlations as given in Equation (3.41).

$$C_D = \begin{cases} 24\frac{1}{Re}, & Re \leq 1 \\ 24\frac{1}{Re}\left(1 + 0.15Re^{0.68}\right) & 1 < Re < 1000, \\ 0.45, & 1000 \leq Re \leq 3500 \end{cases} \tag{3.41}$$

The energy equation for the Lagrangian particle in the continuous phase whose temperature is T_∞ is given in Equation (3.42).

$$m_p C_p \frac{dT_p}{dt} = \underbrace{hA_p\left(T_\infty - T_p\right)}_{\text{convective heat}} + \underbrace{\frac{dm_p}{dt}h_{fg}}_{\text{evaporative heat}} + \underbrace{A_p\epsilon\sigma\left(T_\infty^4 - T_p^4\right)}_{\text{radiative heat}} \tag{3.42}$$

where the latent heat of evaporation is h_{fg}, σ is the Stefan-Boltzmann constant and ϵ is the emissivity of the surface. In this work, the droplets are non-volatile, travel at very high speeds and travel short distances from shedding to impact, thus limiting the effect of evaporation. Also, considering that the temperature difference between the droplets and the fluids is not extremely wide, or mathematically, $\lim_{T_p \to T_\infty} T_\infty^4 \left\{1 - \left(\frac{T_p}{T_\infty}\right)^4\right\} = 0$. Therefore, both the radiative and evaporative components of Equation (3.42) are assumed negligible.

3.4.1 Eulerian-Phase Coupling

In the implementation of the Lagrangian phase representation of the droplet, when the Lagrangian droplets (DPM particles) do not affect the Eulerian phase but the continuous Eulerian flow fields do affect the DPM particles, it is known as "One-Way Coupling". "Two-way Coupling" is achieved when both the DPM and the Eulerian phases affect each other. In the Two-way Coupling approach, the DPM solution iteration alternates between the Eulerian phase solution iteration until convergence is reached. When coupled, the momentum transfer into the Eulerian phase[5] is expressed in the form given in Equation (3.43).

$$\overrightarrow{F} = \sum \left[\frac{18}{24} \frac{\mu C_D Re}{\rho_l D_p^2} \left(\overrightarrow{U}_p - \overrightarrow{u} \right) + \underbrace{\overrightarrow{F}_{other}}_{\text{other interaction forces}} \right] \dot{m}_p \Delta t \tag{3.43}$$

where $\dot{m}_p$ is the mass flow rate of the particulate phase and Δt is the time step.

3.5 Numerical Method

Although a full review of the numerical techniques available to implement CFD techniques is beyond the scope of this thesis, it is worth briefly summarising what is used here. A detailed description of solvers and techniques have been published widely in books [37, 69]. Moreover, the solution methods and the solution algorithms (solvers) are available for implementation in commercial and major open source solvers.

[5] This can be expressed as S_m in Equation (3.15).

3.5.1 Discretisation

The transport equations can be expressed in the generic form given in Equation (3.44). It obeys generalised conservation principle in the transport of the variable ϕ.

$$\frac{\partial \rho\phi}{\partial t} + \nabla \cdot (\rho\phi\overrightarrow{u}) = \nabla \cdot (\Gamma_\phi \nabla\phi) + S_\phi \tag{3.44}$$

where Γ_ϕ is the diffusion coefficient and the source term per unit volume is S_ϕ.

In Equation (3.44), the temporal term, $\partial(\rho\phi)/\partial t$, accounts for the accumulation of ϕ in the control volume of interest; $\nabla\cdot(\rho\phi\overrightarrow{u})$, the convective term, accounts for the transport of ϕ owing to the existence of the velocity field in it. The diffusion term, $\nabla \cdot (\Gamma_\phi \nabla\phi)$, accounts for the transport of the variable ϕ owing to the gradients while S_ϕ is a source (or sink) term that creates (or destroys) ϕ.

The transport equations are difficult to solve analytically but different kinds of numerical discretisation techniques, such as Finite Difference Method, Finite Element Method, Boundary Element Method, Finite Volume Method, etc could be used [42, 122]. The objective of numerical discretisation is to simplify the governing equations into a system of algebraic equations. Generally, the system of equations obtained by the numerical method can then be applied over the control volume mesh generating a set of linear equations to be solved for the variables.

In Finite Volume Method (FVM) used in ANSYS-Fluent, the transport equation is

integrated about the control volume. The Gauss' divergence theorem is used to reduce the volume integrals of the spatial terms [Eqn. 3.45a] to the surface integrals in the resulting system of equation [Eqn. 3.45b].

$$\int_V \frac{\partial \rho\phi}{\partial t} dV + \int_V \nabla \cdot (\rho\phi \overrightarrow{u})\, dV = \int_V \nabla \cdot (\Gamma_\phi \nabla\phi)\, dV + \int_V S_\phi dV \tag{3.45a}$$

$$\int_V \frac{\partial \rho\phi}{\partial t} dV + \oint \rho\phi u \cdot d\overrightarrow{A} = \oint \Gamma_\phi \nabla\phi \cdot d\overrightarrow{A} + \int_V S_\phi dV \tag{3.45b}$$

where $\overrightarrow{A}$ is the surface area vector, V is the cell volume.

The equivalent numerical discretisation of Equation (3.45b), for a two-dimensional computational cell with N faces is given in Equation (3.46).

$$\frac{\partial \rho\phi}{\partial t} V + \sum_i^N \rho_i \phi_i \overrightarrow{u}_i \cdot \overrightarrow{A}_i = \sum_i^N \Gamma_\phi \nabla\phi_i \cdot d\overrightarrow{A}_i + S_\phi V \tag{3.46}$$

where ϕ_i is the value of ϕ convected through face i, $\nabla\phi_i$ is the gradient of ϕ at face i and, for example, this can be expressed as $\nabla\phi = (\partial\phi/\partial x)\,\hat{i} + (\partial\phi/\partial y)\,\hat{j} + (\partial\phi/\partial z)\,\hat{k}$. The mass flux through face i is given by $\rho_i \overrightarrow{u}_i \cdot \overrightarrow{A}_i$.

Both spatial and temporal discretisation are required for transient solutions as discussed in §3.5.1.1 and §3.5.1.2.

3.5.1.1 Spatial discretisation

In ANSYS Fluent, the values of the scalar ϕ are stored in memory locations corresponding to the centroids C_0 and C_1 shown in Figure 3.6. The figure shows the arbitrary control volume used to illustrate the transport of a scalar quantity ϕ given by Equation (3.45b).

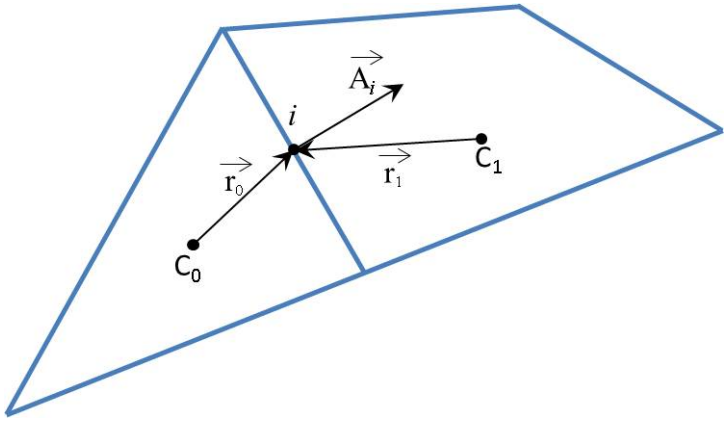

Figure 3.6: Control volume for Scalar Transport Equation [69]

Upwind scheme is used to interpolate for the face values of ϕ_i in Equation (3.46). This implies deriving the scalar from values in the cells upstream/upwind relative to the direction of the normal velocity. There are several spatial upwinding techniques available in ANSYS-Fluent [69]. In this work, the second order upwind has been used for the spatial parts of the transport equations. The second order accurate upwind method is used for the continuity, VoF, momentum, and energy equations. The second-order upwind scheme for the cell-centred solution, $\phi_{i,2}$, about the centroid of the cell as given by Equation (3.47).

$$\phi_{i,2} = \phi + \nabla\phi \cdot \overrightarrow{r} \tag{3.47}$$

where and $\overrightarrow{r}$ is the displacement vector from the upstream cell centroid to the face cen-

troid.

3.5.1.2 Temporal discretisation

The temporal part, $(\partial\rho\phi/\partial t)\,V$, of Equation (3.46), is solved using a numerical integration technique over a time step Δt. The generic temporal PDE in Equation (3.48), can be discretised using backward differencing scheme. Its first order accurate discretisation is given by Equation (3.49a) and a second order accurate discretisation is given by Equation (3.49b).

$$\frac{\partial\phi}{\partial t} = F(\phi) \tag{3.48}$$

$$\frac{\phi_{(t+\Delta t)} - \phi_{(t)}}{\Delta t} = F(\phi) \tag{3.49a}$$

$$\frac{3\phi_{(t+\Delta t)} - 4\phi_{(t)} + \phi_{(t-\Delta t)}}{2\Delta t} = F(\phi) \tag{3.49b}$$

The right hand function, $F(\phi)$, of this discretisation also depends on ϕ which can be evaluated at a time now, t, otherwise referred to as "Explicit time integration" as given by Equation (3.50a). When evaluated in a "future" time, $t + \Delta t$, as given by Equation

(3.50b), it is referred to as "Implicit time integration".

$$\frac{\phi_{(t+\Delta t)} - \phi_{(t)}}{\Delta t} = F\left(\phi_{(t)}\right) \tag{3.50a}$$

$$\frac{\phi_{(t+\Delta t)} - \phi_{(t)}}{\Delta t} = F\left(\phi_{(t+\Delta t)}\right) \tag{3.50b}$$

For solution stability in explicit time integration, the choice of time step (Δt), Equation 3.51b should be made to satisfy the Courant−Friedrichs−Lewy (CFL) number given in Equation 3.51a considering a computational cell with characteristic length ΔX with fluid moving with a velocity $\overrightarrow{u}$.

$$CFL = \frac{|\overrightarrow{u}|}{\left(\frac{\Delta X}{\Delta t}\right)} \tag{3.51a}$$

$$\Delta t \leq \frac{\Delta X}{|\overrightarrow{u}|} \tag{3.51b}$$

The implicit time integration is unconditionally stable with the choice of time step. As shown above, for the explicit time integration, the time step is restrictive but it is useful in capturing transient behaviours. It is also less computationally expensive than the implicit time integration [69].

3.5.2 Solution Algorithm

The numerical solution algorithms for the governing equations in ANSYS-Fluent are often referred to as "Solvers". There are basically two solvers available, the "Pressure-Based Solver" and "Density-Based Solver". The density based solver was originally intended for compressible flows while the pressure based solver was for low-speed incompressible flows [69]. The density based solver, Figure 3.7**A**, solves for all the flow fields, {*pressure, velocity & temperature*}, in a coupled way in all the computational cells at the same time. The velocity field is obtained from the momentum equations while the density is obtained from the continuity equation, but the equation of state is used to determine the pressure.

In the discretised scalar transport equation, [Eqn. 3.46], the scalar variable ϕ is unknown at the cell center and at those of the surrounding neighbour cells. The mesh topology will determine the number of neighbour cells. This is a non-linear system in general and can be expressed in the linear form given by Equation (3.52). For the whole cells in the mesh, this will result in a sparse coefficient matrix system. The linear system is solved using Gauss-Seidel technique in conjunction with an algebraic multigrid (AMG) solver.

$$a_i\phi = \sum_j a_j\phi_j + b \tag{3.52}$$

where the subscripts j point to the neighbour cells and a_i & a_j are the linearised coefficients for ϕ and ϕ_j.

The pressure based solver uses either a segregated algorithm, Figure 3.7**B** or the coupled algorithm, Figure 3.7**C**. In these solvers, a manipulation of the continuity and Navier-Stokes equations is used to solve or "correct" for the pressure field and similar to the density based method, the solution is discretised into computational grids and the system of equations linearised appropriately. In the segregated solver, the flow field variables are solved for one at a time in a sequence. The coupled algorithm solves the same set of variables in a simultaneous manner. The segregated algorithm is known to be more memory efficient although it is slower. It is favoured in this work for its memory efficiency bearing in mind that the volume of computational nodes in a typical geometry can be in order of millions.

The algorithms available in ANSYS-Fluent to couple pressure and velocity are the SIMPLE, SIMPLEC, PISO, Coupled and FSM algorithms. These algorithms are well discussed in books [37, 38, 42, 69]. SIMPLE means *Semi-Implicit Method for Pressure-Linked Equations*, SIMPLEC, an extension of SIMPLE, means SIMPLE -*Consistent*. PISO, extends on SIMPLE and SIMPLEC, means *Pressure-Implicit with Splitting of Operators*. FSM, used in non-iterative time advancement, means *Fractional-Step Method*. The PISO algorithm is favoured in this thesis, over both SIMPLE and SIMPLEC, because it provides better stability to the simulations than the other two. Although the stability issue is not critical with either SIMPLE or SIMPLEC, it is thought to be related with new velocity and fluxes computation in the iteration. They fail to satisfy the momentum balance after the pressure correction equation is solved. The PISO algorithm performs extra corrections [37, 69].

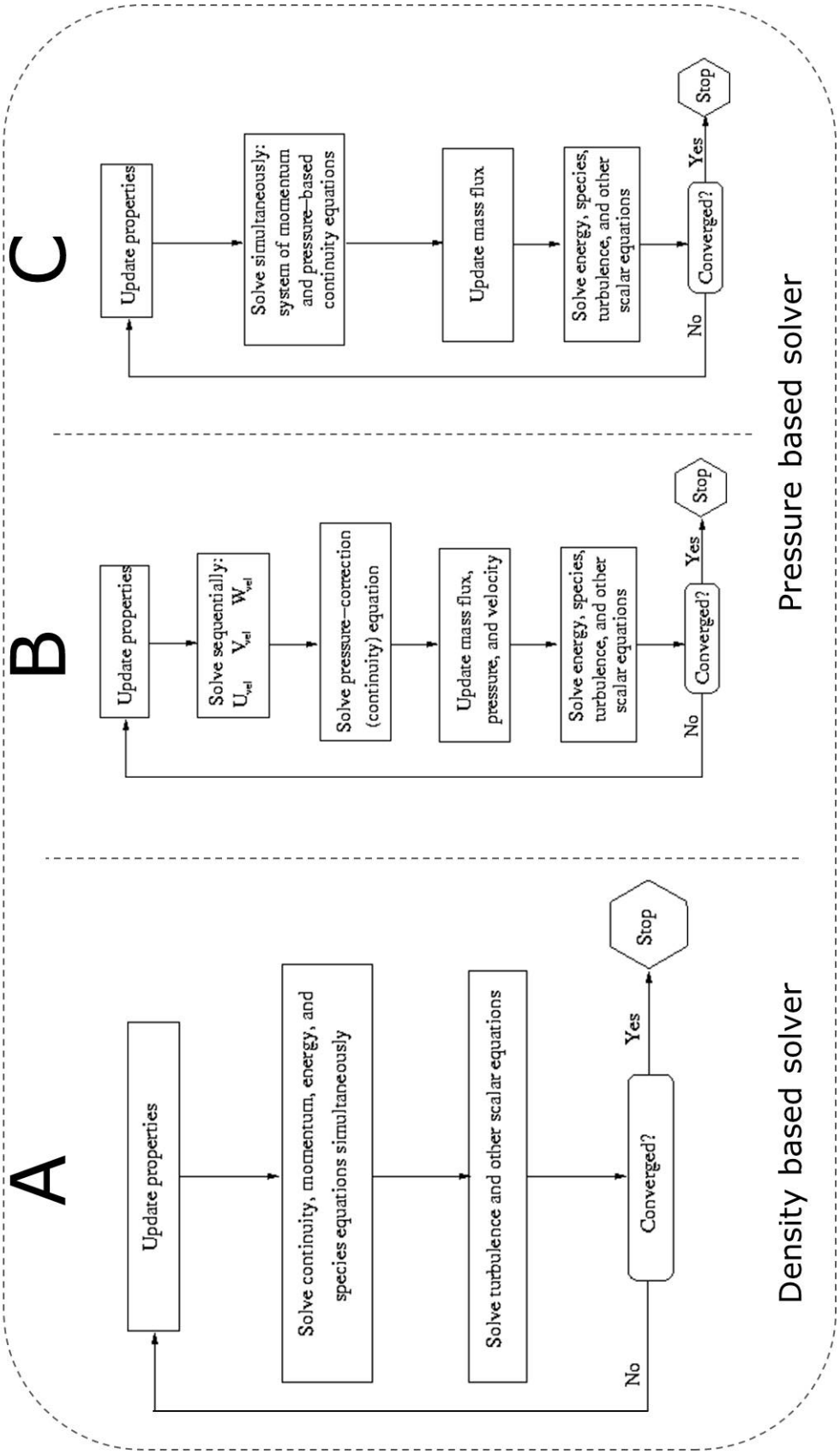

Figure 3.7: CFD Solvers [69]

3.6 Adopted Modelling Strategy

A combination of the modelling techniques is required for the kind of problem described in this thesis. The Volume of Fluid (VoF) with the Level Set enhancement is considered most suitable. This is because it can handle deforming complex free-surface. The combination of the enhanced VoF technique with the turbulence damping strategy provides the opportunity to handle shear driven and turbulent stratified flow. The two-way coupling tracking ability of Lagrangian droplets (DPM) makes its combination with the Eulerian CLSVoF attractive. The stability of the combined model is good with the PISO solver. A second order discretisation for the spatial terms and first order accurate explicit time integration for the temporal terms are required for numerical stability of the solution. The solution of transient partial differential equations is also limited by the Courant−Friedrichs− Lewy (CFL) condition [*see Eqn.* 3.51a]. This requirement means the small time steps are required for stability. The possibility of combining or further enhancing the models is described in the next chapter [§4].

3.7 Summary

In this chapter the mathematical and computational basics for doing multiphase flow simulations have been discussed.

The fluid system in a multiphase system can be represented as separate mixtures coupled mathematically or can be represented numerically as a single fluid identified using

colour function. The free-surface can be tracked using the volume fraction of the fluids present. To solve for the flow fields, the continuity and Navier-Stokes equations are solved. For turbulent flows, the averaged Reynolds equations can be used to simplify the equation systems. The simplification further introduces more complications that need development of turbulent models. For stratified type flows, corrections are required, and available, to compute more accurate propagation of momentum at the free-surface. For disperse droplets, the Lagrangian technique is available to model droplet to gas interaction.

In ANSYS-Fluent, there are robust numerical techniques available and the relevant solution strategies have been identified. The enhanced free-surface Volume of Fluid method combined with the Lagrangian droplet tracking are the identified candidates, and further work will be based them in this thesis.

Chapter 4

The DPM-VoF Model : *A Coupled Framework for Gas-Droplet-Film Interaction with Heat Transfer*

4.1 Overview

The modelling of droplet interaction with the gas and the liquid film using a coupled Lagrangian-Eulerian approach is proposed in this chapter. This is new, in particular in the context of an aeroengine application where it enables a better description of the oil flow in the bearing chamber. In the bearing chamber, the flow consists of high speed filaments and disperse oil droplets interacting with the gas and flowing film, with the latter formed as a result of oil droplets accumulating on the chamber outer wall. Although the oil

is introduced into the chamber in a continuous form, the highly rotational environment breaks some of it up into high speed droplets and probably many of the droplets are shed by the bearings. The oil is fed at a lower temperature than the chamber and so provides cooling.

In Chapter 3, the basic modelling approaches applicable individually for the interaction of the air and oil phases were presented. The coupling of the Lagrangian droplet representation (DPM, in ANSYS-Fluent) with the gas phase was also presented. A novel extension of the DPM coupling accounting for the droplet to liquid (film) interaction is proposed here. There are significant limitations associated with the droplet-liquid interaction as currently formulated in commercially available codes when the droplets are represented by the discrete phase model and the work presented in this thesis provides a formulation where the interaction is far closer to that found in the physical situation.

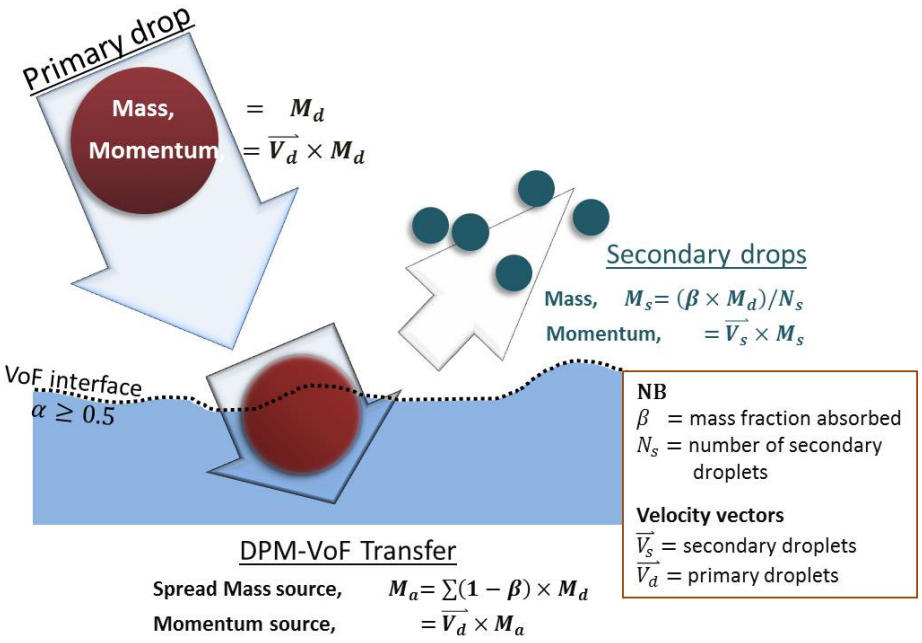

Figure 4.1: The DPM-VoF Concept

The proposal in this work is schematically shown in Figure 4.1. The primary droplet, mass M_d, approaches the gas-liquid interface (dashed line) with a velocity, V_d, the impact of which can lead to splashing (formation of secondary drops). In the model formulation the droplets are still treated as DPM particles (all the mass and momentum located at a single point) but the interaction with the liquid phase is far more physically representative. In the physical situation, when a droplet impacts on a film, mass and momentum are added to the film and if there is a temperature difference then energy is transferred and a new equilibrium is established. Over some impact parameter ranges the impact event can result in smaller droplets being splashed back into the gaseous phase.

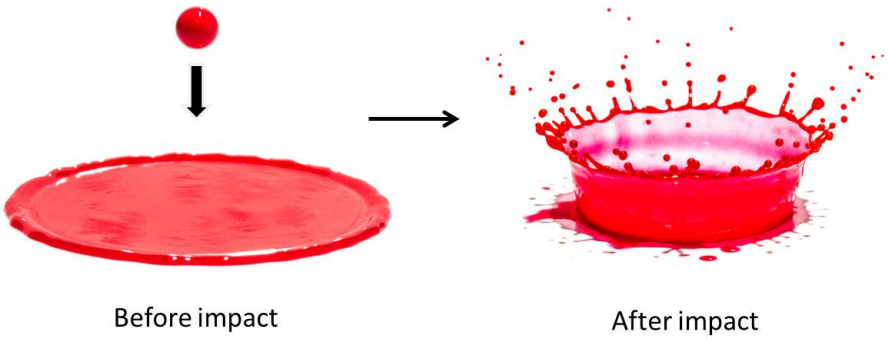

Figure 4.2: Impacting droplet photograph [123]

An example of this type of droplet-film impact is shown in Figure 4.2 where the droplet impact results in a crown being formed and smaller droplets being shed from the crown. Here a fraction of the mass of the impacting droplet goes into the splashing droplets with the remainder (from mass conservation) going into the film. In the model developed and presented in this thesis droplets travel through the gas phase are represented using a Lagrangian framework (DPM). At the point of interaction with the film interface the impact conditions are used to generate an impact outcome including the

mass fraction that splashes, the size(s) of the droplets splashed and their velocities. These splashed droplets, as they move through the gas phase, are represented using a discrete phase model.

Figure 4.3 shows how the DPM-VoF concept of Figure 4.1 is implemented. The dashed boxes represent different computational *modules*.

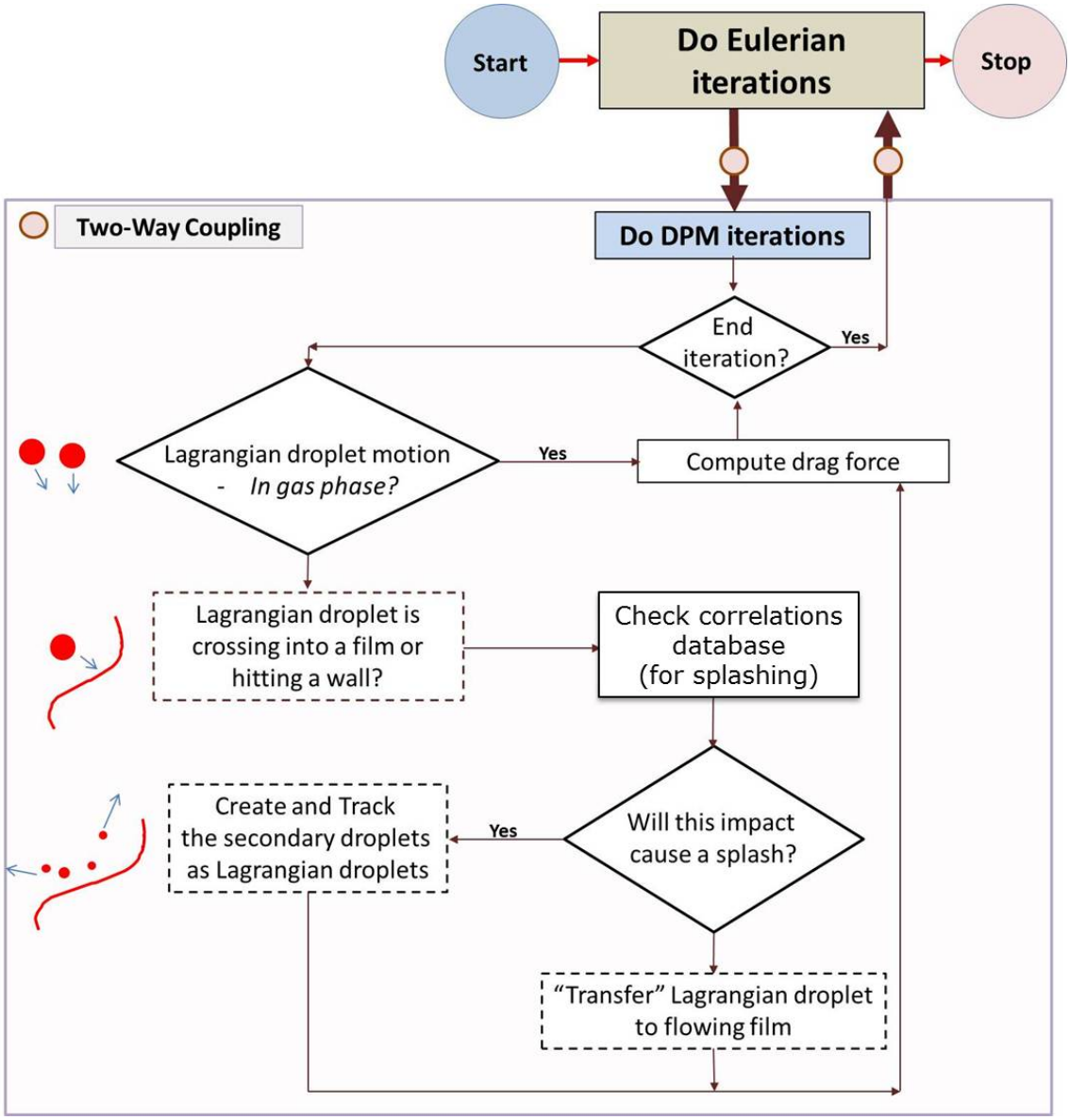

Figure 4.3: Droplet impact and tracking: DPM-VoF Concept

4.2 DPM-VoF Gas phase drag

The coupling of Lagrangian droplet with the gas phase implementation, [*see* §3.4], is done through a User Defined Function (UDF). The effects of interference drag experienced by a droplet trailing behind another droplet are assumed neglible. Kaka & Zhi-yong [124] did numerical simulation to compare drag coefficient of two close spheres with that of a single sphere each of diameter D_s. Their results shows that the drag coefficient ratio of two spheres to that of only one sphere is between about $\pm 5\%$; for $Re > 500$ and when spaced over $5 \times D_s$. It is, therefore, considered safe to do no further calibration on the ANSYS-Fluent standard drag coefficient in the implementation of this work.

4.3 DPM-VoF Mass Transfer

The transfer of mass from the DPM to the VoF phase is achieved by managing source terms into the VoF Equation (3.5) and simultaneously interrupting the particle tracking. Exchange of mass from the Lagrangian droplet particle, mass M_p, (in kg), to the Eulerian VoF phase takes effect when one of two things happens:

(a)

the DPM particles passes into a liquid region. The test for this is related to cell volume fraction and typically the droplet will be said to be interacting with the film interface when the liquid volume fraction in the cell is greater than or equal to 0.5[1].

[1] In ANSYS Fluent 14.5 used in this work, the LS "macro" is not available; this dictates the use of C_VOF as a guage instead of LS.

(b)

when the droplet interacts with a solid surface in such a way that the outcome leaves some or all of the droplet liquid on the surface. In this case a film can be initiated from droplet impacts.

The interface tracking implementation ensures the model works for any arbitrary surfaces [*see* §4.6]. The mass source term (in kg/sm^3) created by this "handover" of DPM to VoF is given in Equation (4.1). This novel exchange of droplets from its Lagrangian representation is responsible for film formation, as seen in the next chapters.

$$S_\rho = \frac{\rho_i}{\rho_l}\frac{M_p}{\Delta t}\frac{1}{V_{cell}}\delta_o \tag{4.1}$$

with the phase source determined using:

$$\rho_i = \begin{cases} -\rho_g & \textit{for gas phase} \\ +\rho_l & \textit{for liquid source} \end{cases} \tag{4.2}$$

where the current computational cell volume is V_{cell} in m^3 and δ_o is a top hat function as given in Equation (4.4).

DPM tracking was originally intended for scenarios where the particle sizes are low in concentration and relatively smaller than the cell. It is common to employ fine mesh density at the interface and sometimes throughout the film to better resolve the film and the interface. It was also shown by Tkaczyk & Morvan [55] that there is a minimum requirement for the number of cells required in the film to achieve a given resolution in

the profile in the interface region. With the technique developed and presented in this thesis, it is possible for the mesh size and particle size to become comparable in size especially close to the walls.

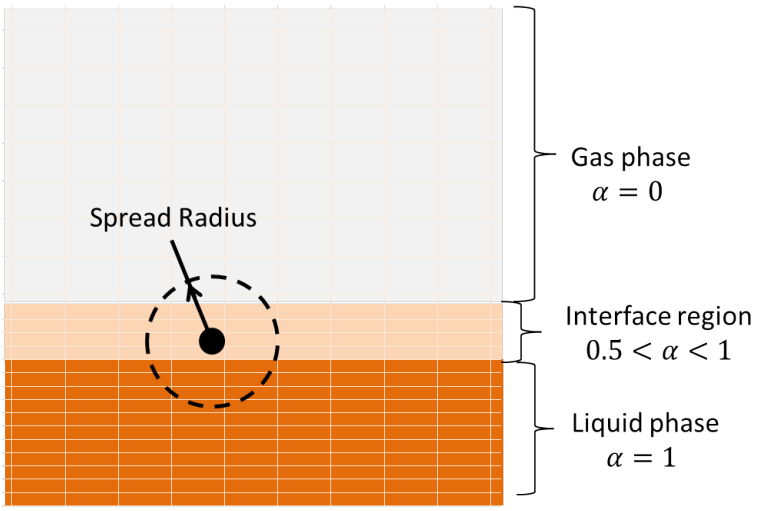

Figure 4.4: Mass source spread sphere

Figure 4.4 shows a schematic representation of a DPM particle, given as the small darker dot, in a cell where the liquid volume fraction is just above 0.5; the level set zero isosurface can be used to identify the interface location within this *interface region*.

As the droplet travels in the solution domain, it is even possible that the droplet volume becomes, on some occasions, larger than the current cell volume. This therefore implies that the mass of the droplet will not "fit" the cell, violating the DPM basic assumptions and the incompressibilty principle. In situations where the droplet size is bigger than the cell, the mass source term is distributed to a "Spread Radius" zone, as indicated in Figure 4.4. This zone represents the actual spherical volume an actual droplet will occupy and as shown for that instance is larger than the current cell. The liquid source

term represents the mass of liquid phase that is supposed to be occupied in the zone if the droplet were not a DPM particle. It should be noted that a mass of an equal volume of the gas should be taken out from that zone, this is achieved as indicated by Equation (4.2). If the whole mass source is added into only the central cell (without spreading the source terms), large residuals are observed because the incompressibility assumptions is clearly violated, thereby causing unphysical velocity and pressure jump. On the other hand, experience has shown that, instability issues might be experienced if the mass is spread over too many cells.

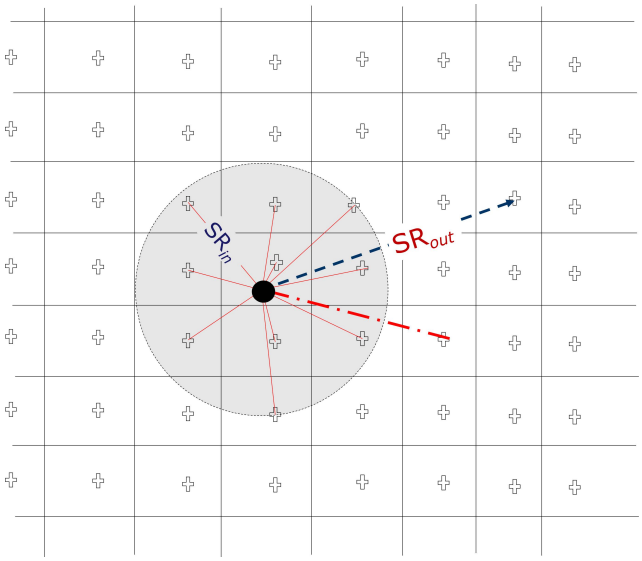

Figure 4.5: Scan zone: from impact point to the centroids

The proposed algorithm involves locating and marking the neigbour cells of the cell where the DPM particle is currently located before distributing the source terms. The centroids, $X_c(x, y, z)$, of the cells in domain are used as reference for each cell while the current position, $X_p(x, y, z)$, of the particle is known. These are, respectively, represented as position vectors $\overrightarrow{X}_c$ and $\overrightarrow{X}_p$. The distances from the particle positions to the cell cen-

troids, R_{SR} given by Equation (4.3), determine if the cell falls inside or outside of the region where source terms are required. The white crosses in Figure 4.5 represent the cell centroids and the current particle position is represented with the dark dot.

$$R_{SR} = \left| \vec{X}_c - \vec{X}_p \right| \tag{4.3}$$

Inside SR_{in}, source terms are added; outside of the zone, SR_{out}, no source term is added. A cell is considered to be in SR_{out} when $R_{SR} > 0.5D_p$. This is used to describe the top hat function δ_o, Equation (4.4), used to determine where the source terms are to be added.

$$\delta_o = \begin{cases} 1 & \textit{if } \frac{R_{SR}}{0.5D_p} \leq 1 \\ 0 & \textit{Out of range} \end{cases} \tag{4.4}$$

It should be noted that real droplets are not spherical all the times as assumed in DPM formulations; upon the DPM turning into VoF film, it is expected to start to deform. There is no special consideration for the curvature of the droplets, the CLSVoF function [*see* 3.2.4.2] and surface tension is relied upon to handle the shape. The marking ensures the correct mass source is added to enforce mass conservation.

4.4 DPM-VoF Momentum Transfer

The momentum of the DPM particle is transferred into the VoF film based on the Lagrangian solution of the particle velocity vector, $\overrightarrow{U}_p$ and the mass source term, S_ρ, earlier described [*see* §4.3]. In Figure 4.1, the fraction of mass splashed is taken off before adding the source terms, if any. The momentum source is transferred into the Navier-Stokes equations and follows simply as given in Equation (4.5).

$$\overrightarrow{S}_M = S_\rho \overrightarrow{U}_p \delta_o \tag{4.5}$$

4.5 DPM-VoF Heat Transfer

The energy equation solution of the DPM particle gives the temperature of a droplet. The droplet is assumed to mix adiabatically and instantly at the impact and the splashing droplets assume the temperature of the film. The temperature, T_i, in each of the VoF cells at the impact locations are approximated as a mass average of the DPM temperature, T_d, and the temperature, T_f, of the fluid. The representative mass of the fluid in the current cell during the scan described in §4.3, M_f, is obtained from the product of the volume fraction, density and the current cell volume, $M_f = \alpha \rho V_{cell}$. Equation (4.6) gives the temperature of the cell at the impact zone.

$$T_i = \frac{M_f T_f + M_d T_d}{M_f + M_d} \tag{4.6}$$

4.6 Interface Tracking & Splashing

An important aspect of the DPM-VoF technique is identifying the free-surface. This is interface tracking. The droplet-position requires interface tracking to continually identify the film or walls. The position, X_p, of the DPM droplet and the computational cell volume's liquid volume fraction, α, is used. Where a droplet crosses into any isosurface with $\alpha > 0.5$, for example, the droplet is taken to be at the free-surface; and the source term modules are initiated once these conditions are met. A UDF code scans the cell faces and determines if a cell volume has a wall bounded face, Figure 4.6. DPM-VoF is initiated in any cell that has a wall-bounded face. The interface normal on the isosurface relative to the incoming primary droplet will determine the splashing direction.

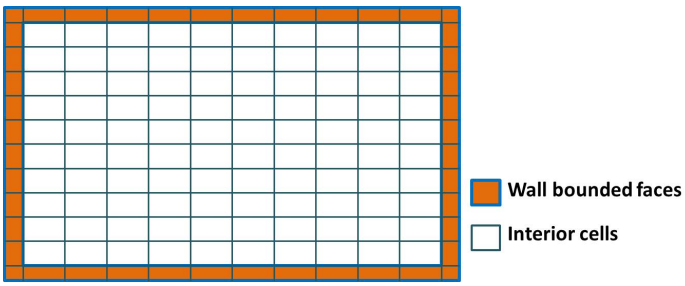

Figure 4.6: Interior and Wall bounded cells faces

4.6.1 Splashing

The droplet-film impact experiment from Roisman & Tropea [125] shown in Figure 4.7 illustrates a normal and an oblique splash. The image in Figure 4.7**(A)** is for a normal droplet impact and Figure 4.7**(B)** is for a primary droplet impact at an oblique angle to the impact surface. A corresponding detailed numerical resolution of the primary and

secondary droplets as undertaken by Peduto *et al.* [12] is shown in Figure 4.8. These simulations required computational grids of the order of 3 million cells.

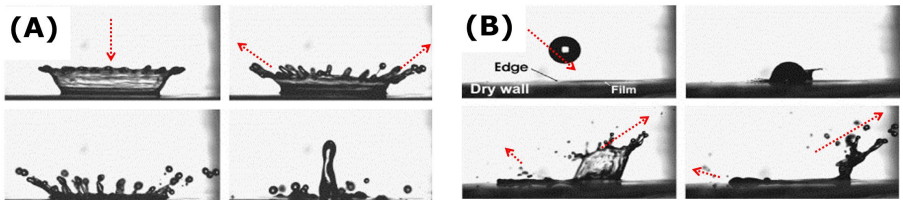

Figure 4.7: Splash from normal, **(A)** and oblique **(B)** droplets impact [125]

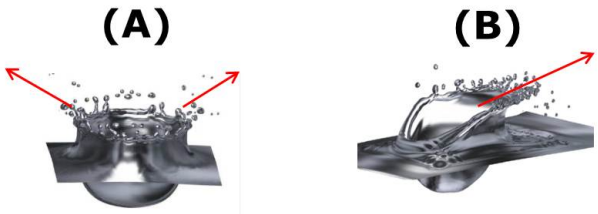

Figure 4.8: Detailed VoF Simulation for Normal **(A)** & Oblique **(B)** impacts [12]

The work of Peduto *et al.* [12], illustrated in Figure 4.8, shows that it is possible to model droplet-film impact directly if a very large number of cells is used. However, for modelling a practical flow situation in which there are many droplets impacts, such meshes are extremely impractical. In the currently developed DPM-VoF model, the simplification of the splash is obtained by assuming that at impact the free-surface is momentarily "hard" and "flat" at the point of impact serving as a "bouncing" plane for the computation of the direction cosines and position vector of the centre of the secondary droplets' distribution. The position vector of the splash ring centre makes it possible to compute the spatial orientation of the secondary droplets (droplets **A**). Figure 4.9 shows the geometric technique applied to model the emerging secondary droplets as Lagrangian particles. The velocity of impact, V_p, and the mean velocity, V_s, of the secondary droplets are obtainable from published correlations. For example, Table 2.2 lists possible outcomes for different impact

conditions.

In the code implementation in this work and based on relavant regimes, the correlations in Table 4.1 have been used.

Table 4.1: Selected Correlations Employed in Splashing

Parameter /Action	Correlation/Criteria	Notes
K	$K_1 = We \cdot Oh^{-2/5}$ $K = 20100 + 5880\,(H^*)^{1.44}$	Definitions from Yarin [73].
SPLASH	$0.08 \leq H^*$ & $K \approx 400$	Yarin [73]
SPLASH	$H^* < 0.08$ & $K \geq 400$	If $K < 400$ droplet STICKS
SPLASH	$H^* \geq 0.14$ & $K_1/K > 1$	If $K_1/K \leq 1$ droplet STICKS, Cossali *et al.* [71].
N_s	$7.84 \times 10^{-6} K^{1.8}\,(H^*)^{-0.3}$	Experiment tested in the range: $0.0275 < H^* < 68$; $0 < \alpha_p < 10^o$, Okawa *et al.* [84].
θ	$0.015K + 12$	Mean angle of secondary droplets ejected from the impact plane [12, 126, 127], with evenly spaced cusps.
β	≈ 0.04	Mass fraction absorbed [126].
β	$= 0.00156e^{0.000486K}$	Experiment range: $0.0275 < H^* < 68$; $0 < \alpha < 10^o$, not valid when $K > 1.3 \times 10^4$ [84].
V_s	$0.52 \times V_p$	Mean speed of ejected secondary droplets [126].
J_L	$\approx 0.57\frac{D_p}{2}$	Jet length [73].

Although these are limited, for example, there are no known correlations for droplets splashing in moving films, where the film flow is turbulent or a moving film on a curved surface. Thus the closest correlation that matches would be used from data where the relative film thickness and other parameters are similar. Column 2, in Table 4.1, shows the criteria calculated or checked against at impact points to determine the action taken in column 1 based on the definitions in column 3. If an impact is determined to create secondary droplets, the number of secondary droplets, N_s, the mean ejection angle, θ, the mass fraction absorbed from the primary droplet, β as well as the mean speed of the splashing droplets, V_s and the jet length, J_L are calculated using column 2.

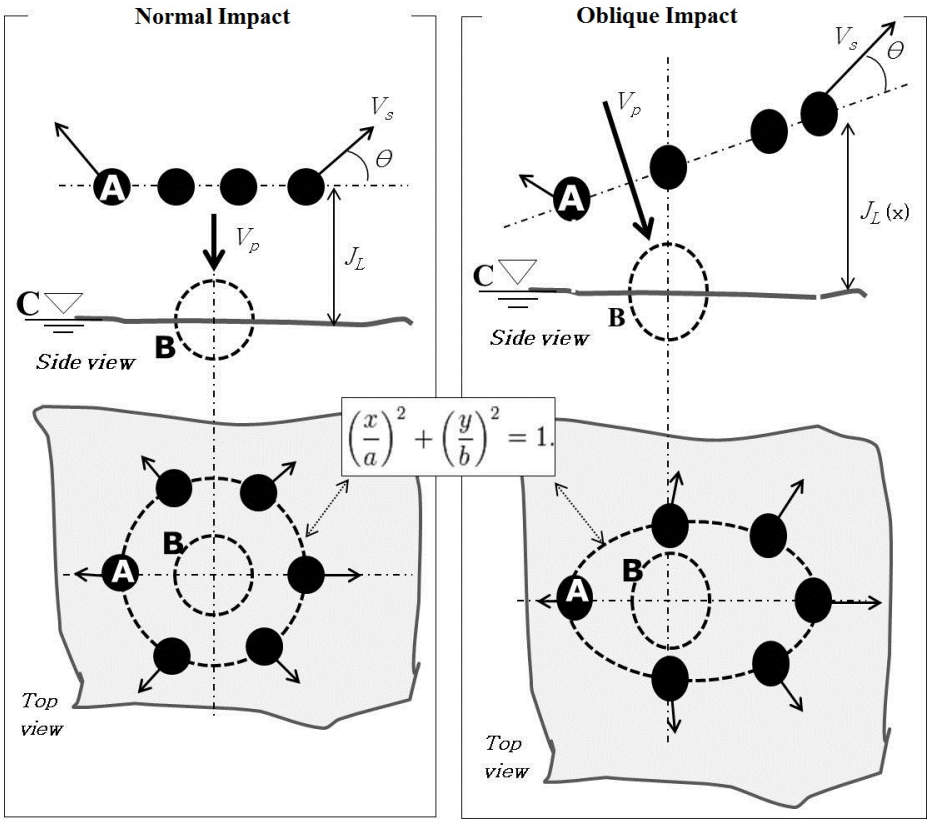

Figure 4.9: DPM-VoF Splash Model

The secondary droplets are created at the end of the impact time step. The position above the free-surface for the creation of the secondary droplets is defined here as the jet length, J_L.

In Figure 4.9, the primary droplet impacts at the free-surface, **C**, at a point **B** to create secondary droplets at **A**. The distribution of the secondary droplets follows an almost elliptical distribution in an oblique impact as shown by the work of Peduto *et al.* [12] & Roisman and Tropea [125] and illustrated by Figures 4.7 & 4.8.

The generation of secondary droplets in the VoF to DPM model occurs a few micro seconds earlier than what the reality is. The start points are also only approximate as well, but from a practical point of view, it is not unrealistic to make such an approximation in the development stages of the model. Layers of complexity can be added as the modelling approach is refined and developed. In the model presented here, the secondary droplets' spatial positions can be represented as a circular ring with a diameter equal to the crown diameter[2] at a chosen time step further down the simulation flow time.

To create a plane of splashing droplet particles, consider a primary droplet impacting on a free surface S_1 at a point P_1 as shown in Figure 4.10. The side and top views are shown. The normal of the splash plane, N_2, is considered to be parallel to the impact normal[3], N_1.

[2]Crown diameter-time evolution curve (Figure 5.10) or equation (Equation 5.2) can be used to estimate this diameter.

[3]The normal, Equation 4.7a, is computed from the level set function based on the Brackbill *et al.* [50] continuum surface force model, Equation 4.7b. An alternative proposal for the improvement of the normal computation technique is proposed by Bohacek [128].

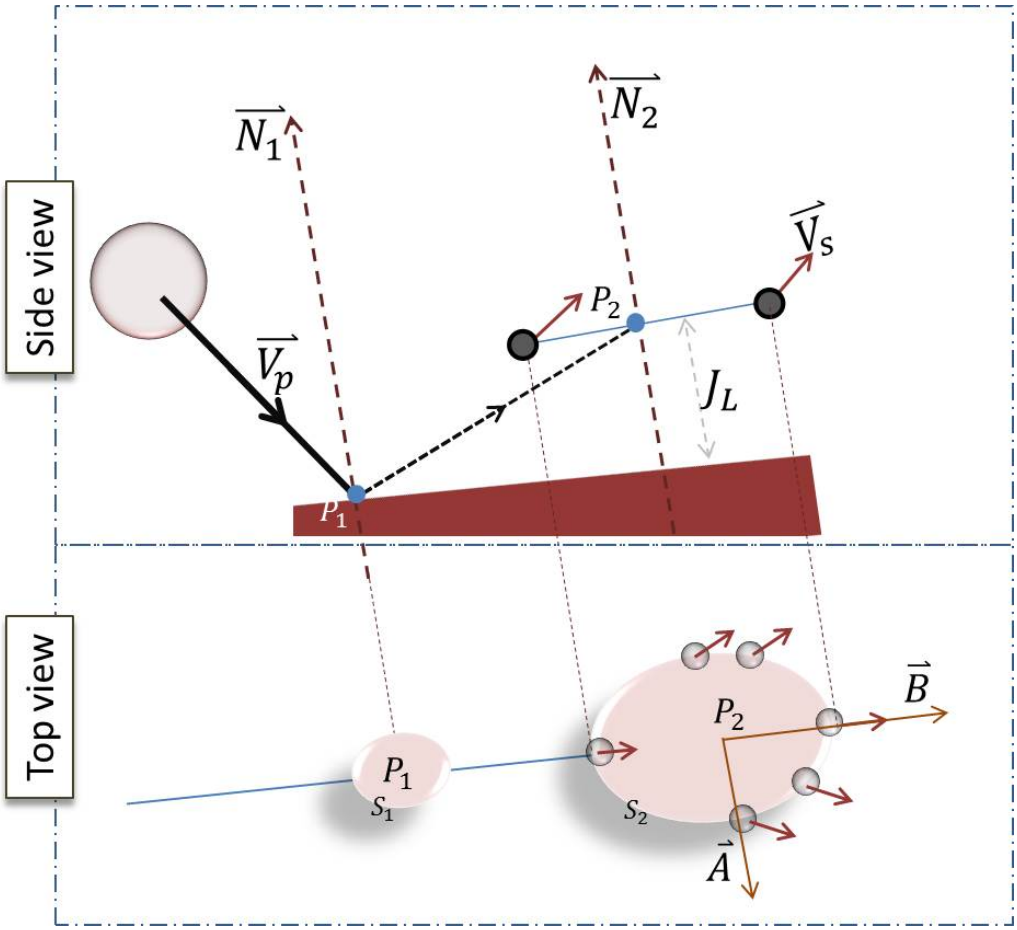

Figure 4.10: Secondary droplet initiation plane

The spatial locations, $X_{i[j]}$, of the secondary droplets are predicted from the geometric equation of the plane S_2 whose centre is a position vector, P_2 [Eqn. 4.7d]. Plane S_2 on Figure 4.11, is a great circle on a sphere whose diameter, $(2 \times r)$, is the same as the crown diameter of the splash.

Equations(4.7a) - (4.7f) are obtained using simple vector manipulations[4] of Figure 4.10.

$$\| \overrightarrow{N} \| = \| \overrightarrow{N_1} \| = \| \overrightarrow{N_2} \|$$

$$= n_1 \underline{i} + n_2 \underline{j} + n_3 \underline{k} \tag{4.7a}$$

$$= \| \nabla \phi \| \tag{4.7b}$$

$$\overrightarrow{V_s} = \| \overrightarrow{V_p} - 2 \left(\overrightarrow{V_p} \cdot \overrightarrow{N_1} \right) \overrightarrow{N_1} \| \tag{4.7c}$$

$$\overrightarrow{P_2} = \overrightarrow{P_1} + J_L \left(\overrightarrow{V_s} \right) \tag{4.7d}$$

$$\overrightarrow{A} = \overrightarrow{V_s} \times \| \overrightarrow{N_1} \| \tag{4.7e}$$

$$\overrightarrow{B} = \overrightarrow{A} \times \| \overrightarrow{N_1} \| \tag{4.7f}$$

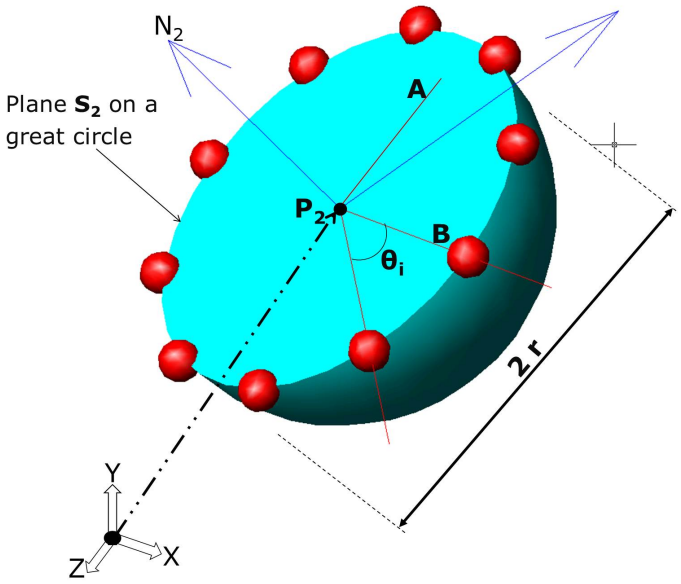

Figure 4.11: DPM-VoF splash plane circle

[4]The double modulus sign operator on a vector here is used to mean computing the unit vector of the vector.

The initiation jet length[5], J_L is taken as $1.5 \times D_p$, as a first approximation. The interface normal is computed in the cell where the DPM particle crosses into the free surface or wall boundary. The magnitude of the velocity vector of the secondary particles is taken from correlations but the directions are obtained from the unit vector of the reflection vector V_s in Equation 4.7c. $\overrightarrow{A}$ and $\overrightarrow{B}$ (Equations (4.7e) & (4.7f) respectively) are any two perpendicular unit vectors in the plane of the splash. The radial distribution of the droplet is clearly stochastic and not known a priori. This stochastic distribution can be implemented into Equation (4.8) which is a parametric equation of a ring on a sphere.

$$X_{i[j]} = P_{2[j]} + rcos\left(\theta_i\right) A_{[j]} + rsin\left(\theta_i\right) B_{[j]} \tag{4.8}$$

The number of droplets are spread evenly on the ring, but the start point, θ_s, uses a random angle from 0 to $\frac{\pi}{4}$. The values of θ_i from θ_s to $2\pi + \theta_s$, are put into Equation (4.8), to get the spatial orientations, $X_{i[j]}$, for a secondary droplet number i of a total of N splashed children. The ring radius, r, is fixed here, but can be adjusted to give an elliptical children *ring* shape as is seen in Figure 4.9**B**. Here, j represents the j^{th} component of the n Cartesian coordinates.

It should be noted that the droplets can be randomly distributed on an area within two concentric circles rather than exactly on the ring described. This is schematically illustrated in Figure 4.12. The region can be obtained by manipulating the radius, r, to be between radii of the two concentric dashed circles. This is subject to availability of data;

[5]Yarin [73] shows a linear growth rate for the jet length, h, with the crown diameter, r as $dh/dr = 0.57$.

the turbulent nature of the target application makes this an “unnecessary complication”.

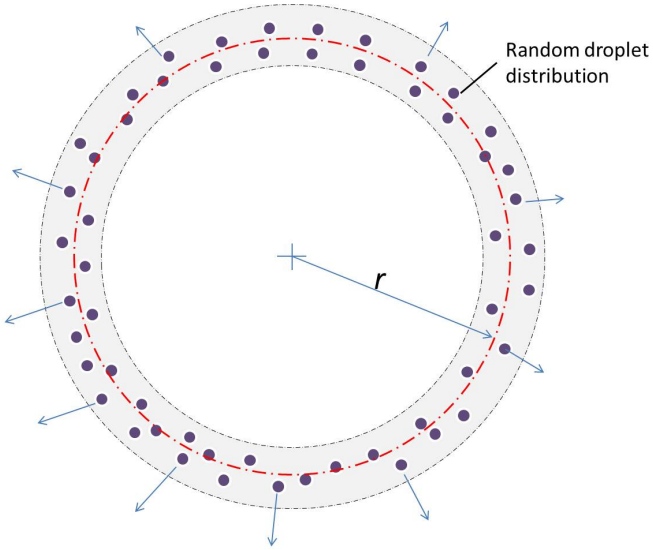

Figure 4.12: Alternative secondary droplets distribution

4.6.2 Film depth search

Most of the correlations depend on the relative film depth, H^*, at the impact point [*see* Table 2.2]. For a simple experiment setup, the film thickness and the droplet diameter can be pre-planned. In a real application environment, the average droplet sizes, D_p, might be known but the film thickness and structure at the impact point are not known a priori. A simple algorithm for computing a “false film depth” is proposed here. A scan is made for the presence of film about an imaginary scan sphere whose maximum radius is equivalent to a “thick film” depth relative to the droplet as shown in Figure 4.13. The scan radius (R_s) is based on the distance from the DPM impact position vector, P, on a free surface to the cell centroids, C.

The Lagrangian particle is represented with the dark dot at the centre of the concen-

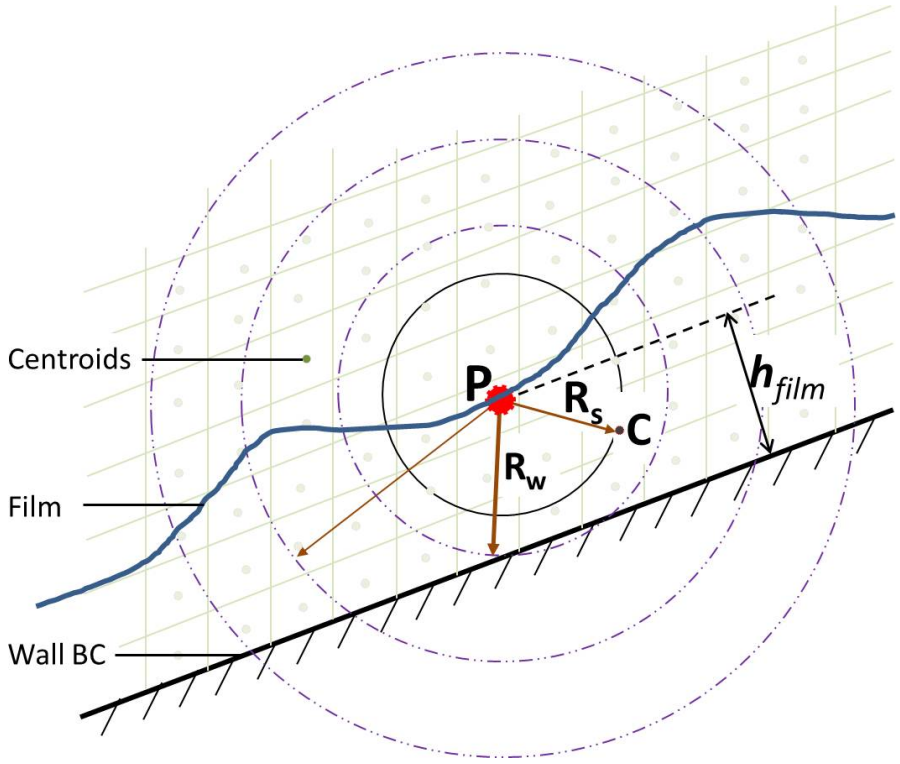

Figure 4.13: DPM-VoF film thickness scan

tric circles shown. The actual droplet diameter is the first (solid) circle. For deep pools, there is no need for scanning the whole film depth, thereby potentially saving computational time. A maximum scan radius is set to, say, $2 \times D_p$. If film is found and there is no wall boundary in the zone, the film is presumed to be a thick film and the thick film correlations apply. If a wall boundary is reached during the scanning, the "scan loop"[6] is stopped and the relative film thickness is computed as the distance from the impact to the point where the wall BC is found. The film depth therefore gets a new definition, $H^* = D_p/PC$, to be used as the relative film thickness in place of $H^* = h_{film}/D_p$ in determining the impact outcome. The closest correlation match from data where the relative film thickness is similar is used along side other parameters.

[6] In ANSYS-Fluent, there is a provision to identify each cell during iteration loop with a *begin_c_loop*. UDF. This loop is used to do the scan on top the solution iteration loop.

4.7 Implementation Algorithm

The numerical implementation described in this chapter is built in ANSYS-Fluent as shown in Figure 4.14. The DPM-VoF code is attached/"hooked" as a compiled UDF[7] and runs as shown in the flowchart. Table 4.2 gives the different modules [*see Appendix* §A.2 - §A.1] and where to "hook" them in the ANSYS-Fluent GUI(graphical user interface).

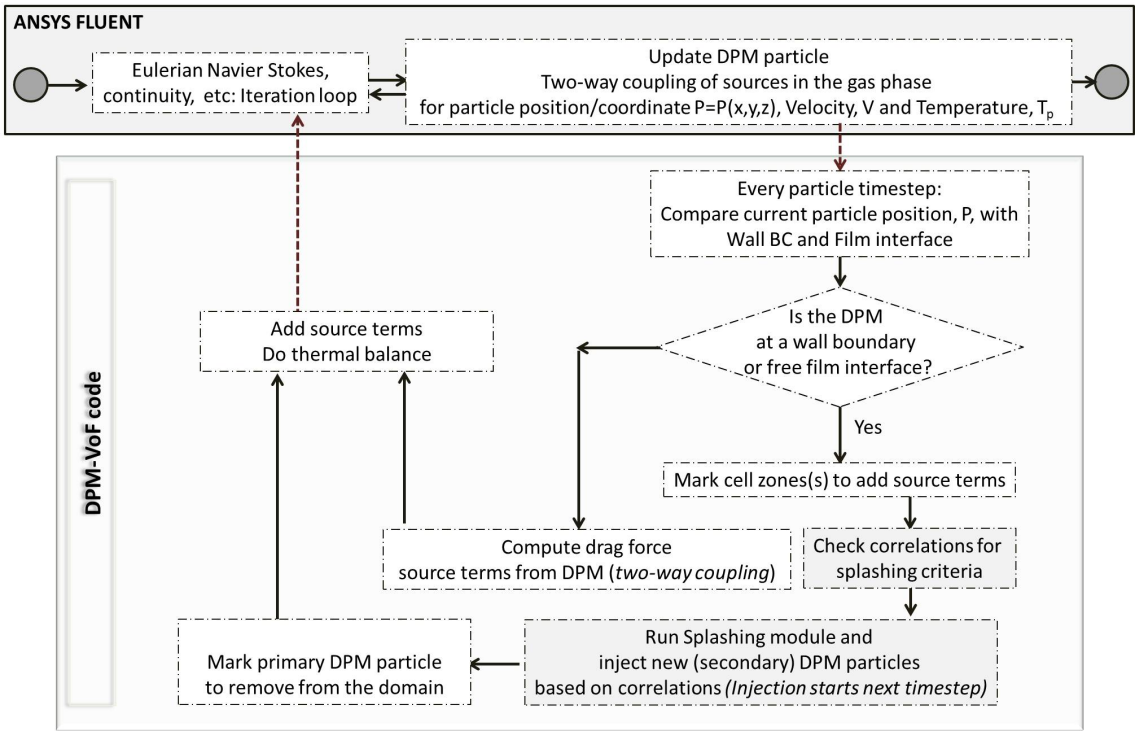

Figure 4.14: The DPM-VoF Implementation

4.7.0.1 Setting up DPM Injection

Droplet injection in the developed model uses the ANSYS-Fluent DPM model. In the ANSYS-Fluent DPM model, *injectors* are used to inject droplets into the control volume

[7] In ANSYS-Fluent, UDF codes can be compiled and the modules will be available dynamically (dll) by loading *libudf*.

based on the initial conditions defined by the user. There are several possible injectors in ANSYS-Fluent; such as *single*, *group*, *cone*, *file*, etc. These are standardised and set up in the graphical user interface to help the user describe the initial conditions of the particles as shown in Figure 4.15. The UDF tab can be used to perform extra user define routines. This is, for example, used to implement the splashing model described in §4.6.1 and the RID model described in §6.2.1.3. The "file injector" gives the description of each individual droplet giving the user a good flexibility to manipulate the droplets.

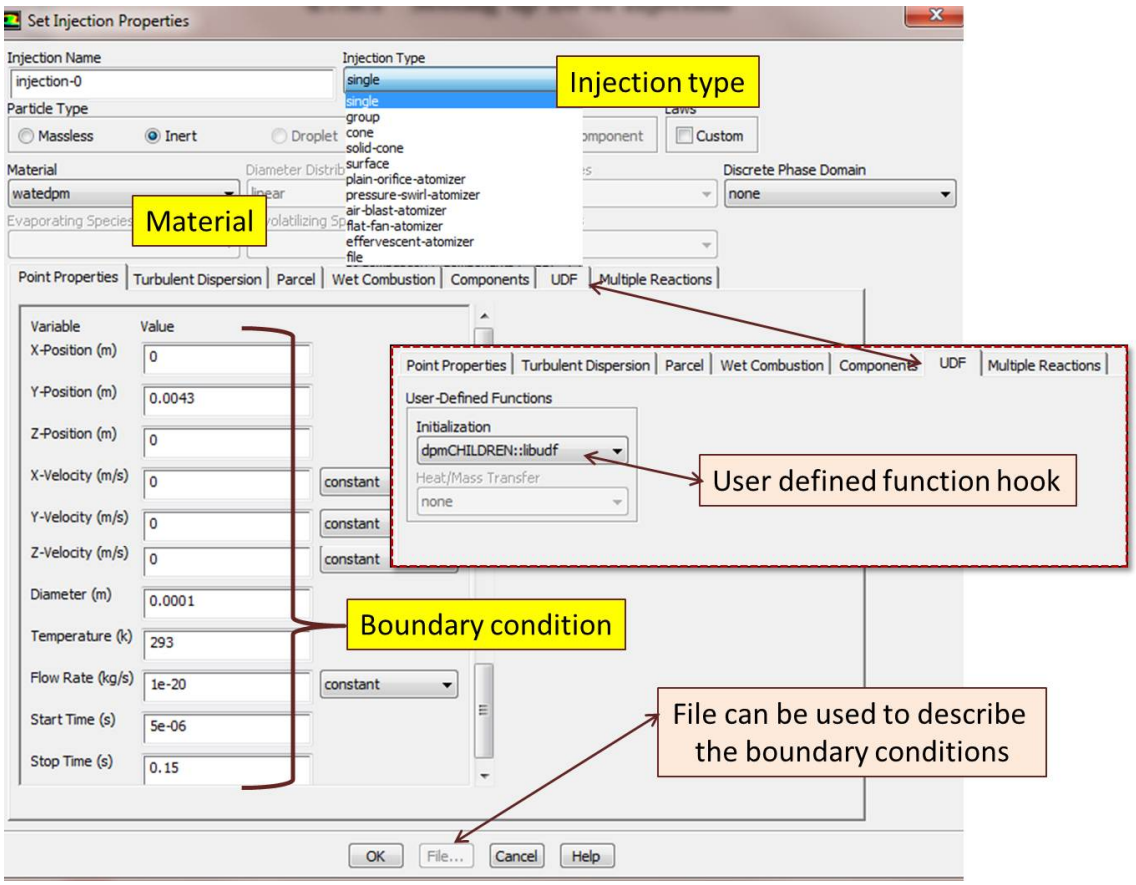

Figure 4.15: DPM setup in ANSYS-Fluent (GUI)

In ANSYS-Fluent, the injection file is created as a plain text file. The format and heading of the injection file is: ((x y z u v w diameter temperature mass-flow) name);

for example the lines below, saved as text file, say *try.inj*, will inject into the domain, 2 droplets each of $50\mu m$ diameter with velocities of $0.5m/s$ from the two different locations (-0.5,0,0)mm and (0.5,0,0)mm at a flow rate of $3g/s$ and $340K$.

- - - - - - - *Save as try.inj and attach to the DPM panel*
((x y z u v w diameter temperature mass-flow) name)
((-0.5E-3 0.0 0.0 0.5 0.0 0.0 50.E-6 340.0 3.0E-3) injector1)
((0.5E-3 0.0 0.0 -0.5 0.0 0.0 50.E-6 340.0 3.0E-3) injector2)
- - - - - - - - - *This is the end of the injection file*

In the DPM-VoF model, the droplets are tracked at the VoF timestep but the droplets are not injected every VoF timestep. By default in ANSYS-Fluent, the flow rate specified gives the mass of DPM injected every timestep. For example, by the default settings, if a mass flow rate of $10^{-3}kg/s$ is specified and the timestep is $1ms$, the mass of DPM injected will be $10^{-3} \times 10^{-3}kg$ or $1\mu g$ every timestep if tracking at the VoF timestep. Therefore, the mass flow rate to specify is the ratio of the mass of the droplet to the VoF timestep.

Other than for a *single injector* that injects only one DPM particle at a time, the standard ANSYS-Fluent injectors (cone, group, file etc) can and typically will inject more than one DPM particle at a time. The droplets are injected at the beginning of each DPM timestep. A droplet injector injects N_d $(N_d \geq 1)$ number of droplets at a time, otherwise called a *batch* of droplets in this thesis. This batch release of DPM droplets/particles is a standard practice in ANSYS Fluent and the number of DPM particle/parcels is released every timestep specified. In this work, although the DPM particles are tracked at the VoF timestep the release frequency is changed in the UDF so as not to release droplets every VoF timestep but based on an artificial atomisation frequency, F_n. Atomisation frequency,

as used throughout in this thesis, refers to the frequency at which DPM droplets are injected into the domain. For example, the injectors wait to inject after every $1/\left(F_n \Delta t\right)$ of the VoF timestep (Δt). For injectors where the number of droplets in a batch to inject are specified, such as from a *surface injector*, the DPM mass flow rate, $\dot{M}_p$, to specify in the GUI is $\dot{M}_p = N_d \times M_d \times F_n$; where M_d is mass of one droplet and N_d is the number of droplets in that batch.

In the standard DPM model setup the injectors are set up manually. This is a problem for tracking the secondary droplets since the locations of the secondary droplets cannot be predetermined until there is an impact. Therefore, a set of *dummy* DPM injectors are used. The dummy injectors are blank injectors and do not inject anything into the domain. They "wait" for a splash to occur, after the splash, their initial conditions are set corresponding to those of the splashing droplets. It should be noted that injectors are not droplets, they only serve as a way to create droplets in the domain. Once the droplets are in the domain they can interact as if they are from the same source; the injectors can be placed at different locations as desired and based on the problem.

These *dummy* injectors serve as "waiters" expecting to inject at any moment. To distinguish among them, the primary droplet injectors are called "mother injectors" and the dummy injectors are called "children injectors". About 10 children injectors are setup to inject inside the domain[8]. As a rule of thumb, the number of injectors will be more than the number of process threads, for example when running on 8-cores, 10 or more dummy injectors will suffice. A memory location is set to hold the initial conditions of

[8] If the injection positions (coordinates) are outside of the fluid domain, ANSYS-Fluent will not track the droplets not even by using a UDF to set the desired positions.

Table 4.2: The DPM-VoF modules and their functions

Module name	ANSYS-Fluent Tab	Function
dpm_drag_virtual	Drag Law	Computes the drag coeffient of the particles
vof_drag_trap	DPM ▷ Boundary Cond. Function (For walls)	Creates film at walls/Splash
vof_dpm_Z_momentum	Cell-zone Source Terms ▷ Z-Momentum	Momentum source in Z-direction
vof_dpm_Y_momentum	Cell-zone Source Terms ▷ Y-Momentum	Momentum source in Y-direction
vof_dpm_X_momentum	Cell-zone Source Terms ▷ X-Momentum	Momentum source in X-direction
vof_dpm_Energy	Cell-zone Source Terms ▷ Energy	Mixing temperature
vof_liquid_src	Cell-zone Source Terms ▷ liquid phase ▷ Mass source	Creates VoF film
vof_gas_src	Cell-zone Source Terms ▷ gas phase ▷ Mass source	Removes gas before adding liquid
dpmCHILDREN	Set Injection Properties ▷ UDF ▷ Initialization	Creates splashing droplets, rotates droplets with RID position [§6.2.1.2]
Cleanup_DPM	UDF Function hooks ▷ Adjust	Removes droplets not required before next iteration starts
Init_Child_Injectors	UDF Function hooks ▷ Initialization	Creates the droplets for tracking
InterfaceNormals	UDF Function hooks ▷ Adjust	Computes interface normal for interface tracking
src_reseter	UDF Function hooks ▷ Execute at End	Frees up memory
NewCaseResetInjectors	UDF Function hooks ▷ Read Case	Resets the injectors based on a new case file
NewDataResetInjectors	UDF Function hooks ▷ Read data	Resets the injectors based on a new data file loaded

the splashing droplets. These override the initial conditions of the children injectors, thus creating the new "boundary conditions". The memory location is checked every iteration to ensure that all the splashed droplets are tracked. With this technique, even the splashed droplets can end up creating further children. A limit is created for the maximum number of splash per impact in the UDF, to prevent memory leak tracking too many droplets. For example, it is assumed that any single droplet impact should not create more than 50 droplets[9]. Once the DPM is in the control volume, the tracking ensues following the standard tracking.

4.8 Summary

In this chapter, a modelling approach is described that represents a considerable enhancement to existing coupled Lagarangian-Eulerian modelling techniques. Using the developed approach it is possible to model a two-phase flow consisting of liquid film, liquid droplets and a gas phase. The oil droplets are represented as Lagrangian particles behaving as if they are disperse *solid spheres* travelling in air. The two phase flow is therefore represented as a gas phase and two components in the liquid phase each with its own numerical representation. This will from here onwards be referred to as "three-numerical phases". Upon the droplets crossing into any part of the control volume with flowing film or a wall boundary condition, the droplets are *transferred* into the Eulerian VoF film as source terms in the continuity and Navier-Stokes equations.

[9]The limiting constant ID is MAX_NO_OF_DROPS_PER_SPLASH and this can be increased if necessary.

The standard energy equation solutions are relied upon to provide the temperatures of the film and the droplets at the impact point. The impact is assumed to be adiabatic with mixing occurring instantly such that the mass averaging of the temperatures of the droplet and representative fluids present is solved at the impact point.

Consideration was also given to the geometric size of the impacting droplet relative to the computational cells. A spreading of the source terms is made across a "Spread Zone" determined by the actual diameter of the droplet.

A method to enable the modelling of splashing of a primary droplet to form secondary droplets was also proposed and developed. The initial conditions for the splashing droplets, such as the velocity magnitude, number of drops and diameters of the secondary droplets are based on the predictions from published correlations. The impact conditions are compared to the available published criteria. The orientations of the splashing droplets are computed using the impact normals and some geometric and vector manipulations. The temperature of the splashing droplets was assumed to be the temperature of the film before mixing.

Since experimental correlations cannot cover the whole range of possibilities, it is reasonable to use the most similar correlations for the experimental conditions that are available. For example, there are no known correlations for droplets splashing in moving film, where the film flow is turbulent or a moving film on a curved surface. It is suggested that the closest correlation match would be from data where the relative film thickness and other parameters are similar.

The implemented code is found to be stable in spite of the “extra load” of these novel contributions on top of the standard Lagrangian-Eulerian formulation. The DPM-VoF method developed and presented in this chapter has been applied and the results can be seen in Chapters §5 & §6.

Chapter 5

Validating the DPM-VoF Model

5.1 Overview

In this chapter the validity and performance of the proposed sub-models is investigated through their application in a number of simplified test cases. This is regarded as a necessary step before moving to the target application of an aeroengine bearing chamber. The tests involve exchange/transfer of mass, momentum and energy (heat) from the Lagrangian droplet representation (*i.e. DPM particle*) with the film which is represented with the Eulerian VoF formulation. They also provide the opportunity for qualitative validation.

5.2 Single droplet: Conversion of DPM droplet representation into VoF droplet representation

In this basic set up, a single DPM droplet is injected at the centre of an empty box. The diameter, D_p, of the droplet is $1000\mu m$. The box is a cube with a width $15 \times D_p$. In this test, four different mesh resolution setups are used. The meshes resolve the droplet by a spacing S^* $(= D_p/h)$ in the zones indicated on Figure 5.1 with the mesh becoming coarser away from the droplet as shown; where h is the grid spacing in the droplet zone. The S^* cases tested are respectively 50, 25, 10 and 5.

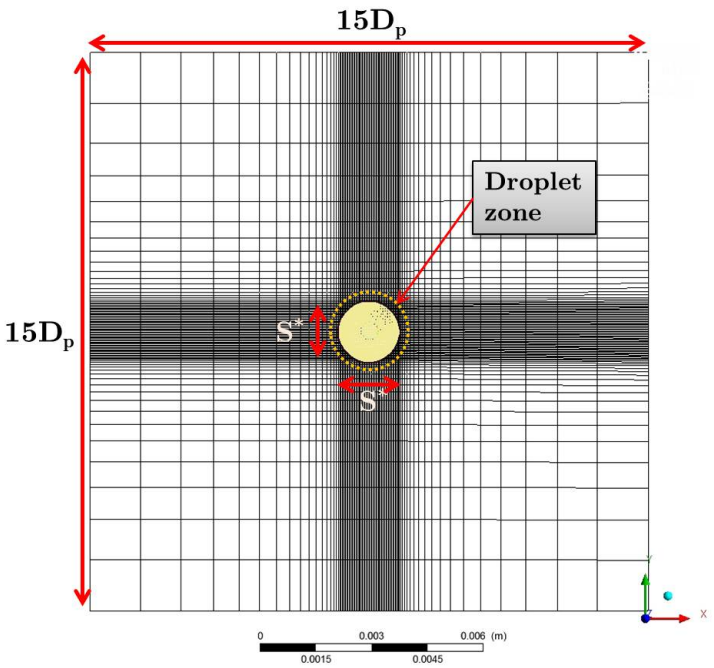

Figure 5.1: Mesh used for single droplet DPM-VoF test case

Figure 5.1 shows that the mesh is only fine in the zone of interest; the expansion of the mesh into the coarse regions increase in a geometric progression ratio of 1.2, a

recommended practice for mesh growth rate when variable mesh spacing is used [69]. Resolving[1] everywhere with equal grid spacing as obtained in the droplet zone is not necessary for this test. The zero level set iso-surfaces in Figures 5.2a to 5.2d show the conversions to the VoF droplets for the four levels of refinements.

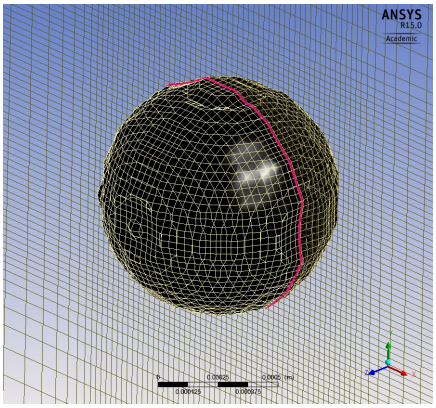

(a) $S^* = 50$, DPM turns VoF

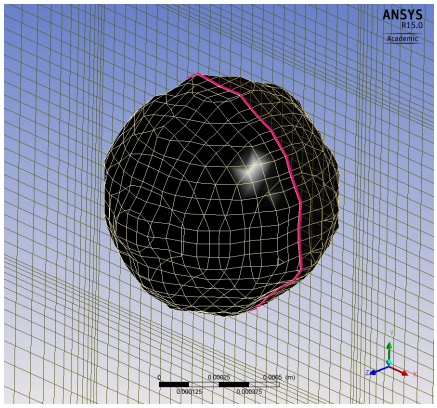

(b) $S^* = 25$, DPM turns VoF

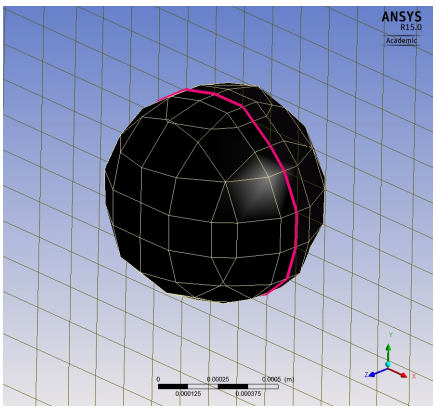

(c) $S^* = 10$, DPM turns VoF

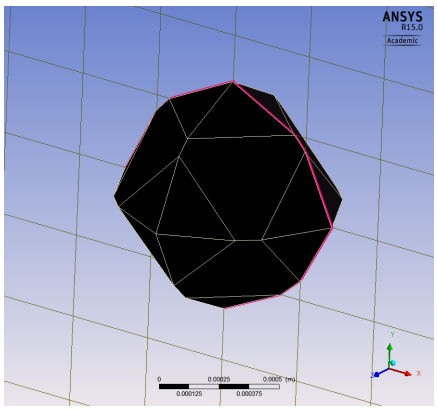

(d) $S^* = 5$, DPM turns VoF

Figure 5.2: Single DPM droplet turns VOF

[1]The case $S^* = 50$, for example, will require about $(15D_p/h)^3 = (15D_p/(D_p/S^*))^3 = (15 \times 50)^3 = 421,875,000$ cells!

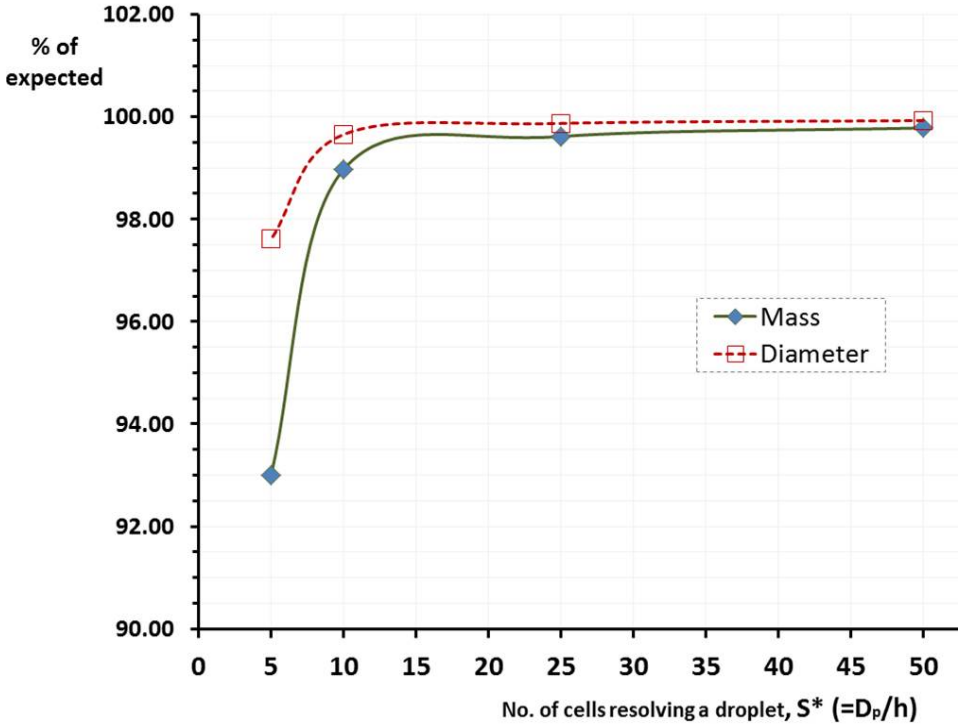

Figure 5.3: DPM-VoF Single droplet: Mesh resolution/mass conservation

Figure 5.3 shows the efficacy of conversion from the DPM droplet to the VoF droplet against the mesh resolution of the droplets. This shows that the "loss in mass" is a result of the inability to resolve the droplet to a mesh by a coarser mesh. The finer the mesh, the better the resolution of the droplet free-surface; it is, however, worth remembering that the number of cells required to resolve the droplet is actually $(S^*)^3$. The "mass loss" can be estimated from $100\left(1-(R/R_e)^3\right)$, where R is the radius of the iso-surface and R_e is the expected radius of the resulting VoF droplet. A resolution, S^*, higher than 10 yields mass conservation over 99.6% in this single droplet test. From this simple test, a rule of thumb can be prescribed for mesh spacing in the wall regions to be of the order $S^* > 10$; i.e. the mesh spacing to be a tenth of the mean droplet sizes, so that the first sets of DPM droplets landing on a dry wall can be resolved.

5.3 Simple box fill with a Single Droplet Train (Mass conservation check)

In this basic test, a train of DPM droplets is injected into a box, as schematically shown in Figure 5.4a. The flow rate is specified for the Lagrangian droplet stream and expected to fill the box to a height, h.

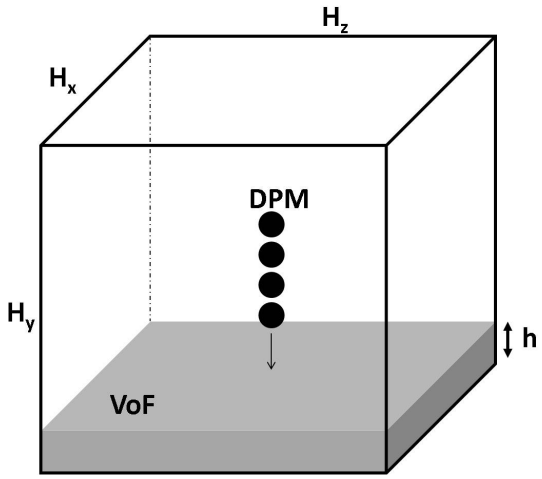

(a) Box fill setup schematic

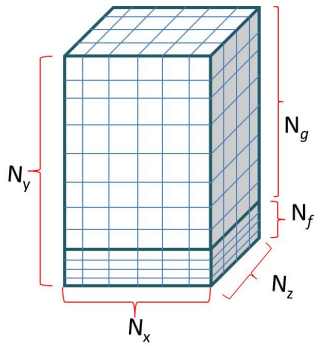

(b) Schematic of mesh setup for the box

Figure 5.4: DPM-VoF: Simple box fill setup

Particles with a density of $1000kg/m^3$ are injected into an initially dry box of volume $12 \times 12 \times 20mm$. The mesh setup is such that it is refined close to where the film is

expected, Figure 5.4b.

The number of nodes (N_x, N_y, N_z) used for mesh dependence studies is shown in Table 5.1. The number of nodes in the film region, N_f, and in the gas, N_g, and those of the box dimensions are varied. The number of nodes in the region where the film is expected are chosen to be able to resolve the film when filled to the height but not sufficient to resolve each droplet as previously done in §5.2 because it is not practical to do so.

Table 5.1: Box mesh dependence case setup

CASE	N_f	Total number of nodes	N_x	N_y	N_z
$MSH-1$	15	$14,625$	15	50	15
$MSH-2$	25	$104,125$	35	60	35
$MSH-3$	40	$300,000$	50	80	50

The target fill level, h, is $1.2mm$ for all the cases described in Table 5.2. The mass of the liquid expected is $172.8mg$ in $1sec$. The droplets are injected at a spacing of $5 \times D_p$ between each injection[2]. In this simulation, the VoF timestep, ΔT, is $1\mu sec$ to limit the Courant number to less than 1. The convergence criteria set for all the equations is 10^{-4}.

Table 5.2: Box case setup

D_p, $[\mu m]$	H_x^*	H_f^*	Number of droplets	Droplet injection frequency[a], $F_d[Hz]$
150	80	8.0	$97,785$	$1,333$
500	24	2.4	$2,641$	400
800	15	1.5	645	250

[a]Please refer to §4.7.0.1 for more on setting up DPM injection.
H_x^* and H_f^* are respectively the box width and target film depth relative to the droplet diameter, D_p

A mesh dependence study is done by comparing the volume of the film in the geome-

[2]Injection frequency, F_d, can be determined from $V = F_d\lambda$, where $\lambda = 5 \times D_p$ and $V = 1m/s$.

try after it settles down with the expected volume of water ($17.3 \times 10^{-6} m^3$) in the box after $1sec$. The results for Meshes $MSH-1$, $MSH-2$, $MSH-3$ given in Table 5.1, for the $800\mu m$ droplet, are smaller than the correct value by 8.5%, 1.6% and 1.49% respectively. With VoF, the finer the mesh, the better the ability to capture the film.

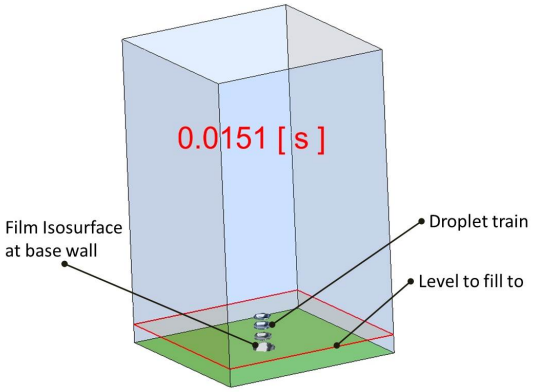

(a) The droplet train and film

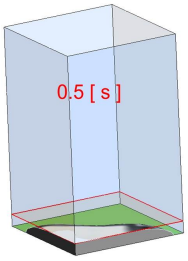

(b) $800\mu m$, $0.5sec.$

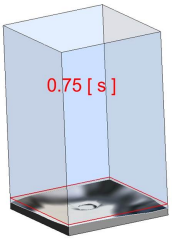

(c) $800\mu m$, $0.75sec.$

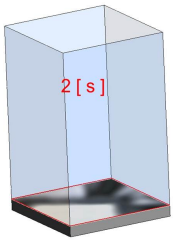

(d) $800\mu m$, $2.0sec.$

Figure 5.5: DPM-VoF: Simple box fill results $800\mu m$ diameter droplet

As the box was initially dry, there was some error capturing the first set of droplets landing but this gets better as the film accumulates to a level where the mesh can resolve the film. This is demonstrated in §5.4 where the film can already be resolved before the droplets are injected. The film grew from *no-film at all* to relative thicknesses, H_f^*, 1.5, 2.4 and 8.0 in the 3 cases, where $H_f^* = h/D_p$. The qualitative film formation is shown in Figure 5.5 for a stream of $800\mu m$ droplets filling the box to the marked level. As the

film continues to form in the box (Fig. 5.5b), they collect together under the influence of surface tension and move about in the box from one side to the other.

5.4 Simple box fill with Multiple Droplet Trains (Mass conservation check)

This is a simple extension of the previous case [§5.3] to test capability for multiple droplets in a domain. In this case, batches of droplets with equal diameters of $260\mu m$ are released into a box already partially filled with water. This physically represents a box being filled from a spray.

Figure 5.6 shows the schematic of the box, H_0 is the initial level of the film before injection starts, the filling is done by the DPM droplets with the simulation duration and fill rate such that at the end of the simulation there should be liquid in the VoF representation up to a level of $2 \times H_0$; Figure 5.7 shows the mesh setup for this case.

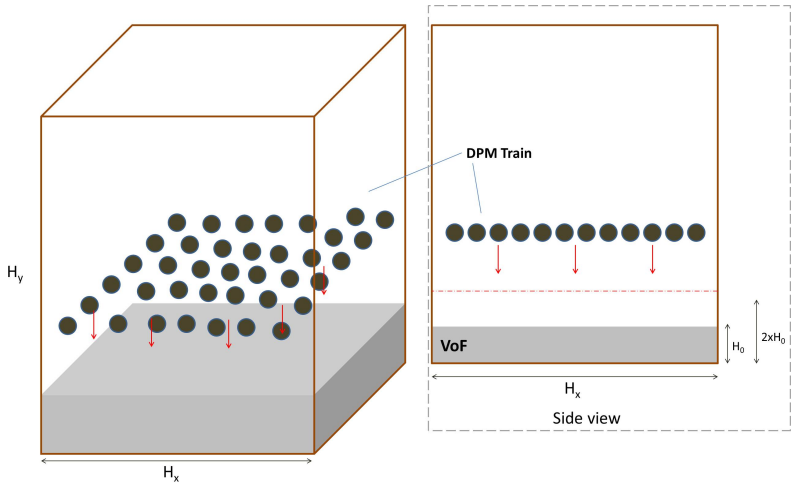

Figure 5.6: DPM-VoF: Schematic of a Train of Multiple Droplets

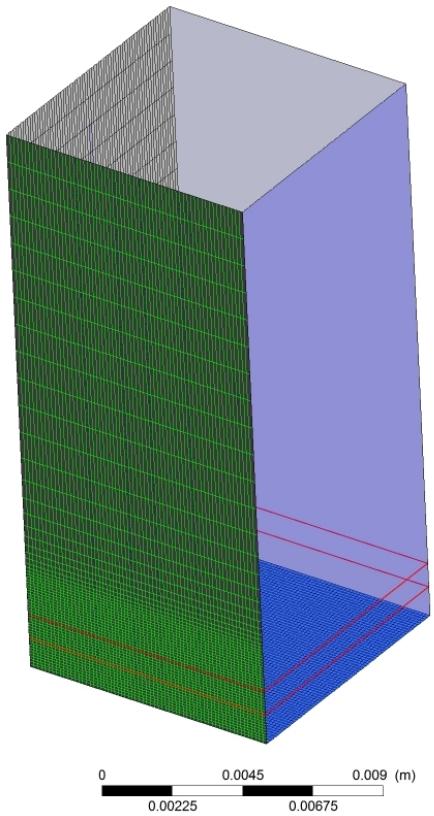

Figure 5.7: Mesh for the Multiple Droplet Train Setup

By the setup given in Table 5.3, the film is expected to fill to $2 \times H_0$ after $1.3sec$. The number of nodes in the region where the film is *expected*, is higher than those in the gas region and two mesh densities are evaluated. In the film region there are 25 and 35 nodes in the vertical direction; these correspond to grid spacing[3], S^*, of about 2.0 and 2.5. According to the criteria set down in [55] both these meshes are fine enough to resolve the film. The finer and coarser meshes contain 30,625 cells and 260,130 cells respectively.

The volume[4] of the liquid present in the domain is computed using Equation (5.1).

[3]The grid spacing described in terms of the approaching droplet, $S^* = D_p/h$. $S^* > 1$ means the droplet is larger than the current cell.

[4]This is the built-in ANSYS CFD-POST function $Volume\_Int$.

The starting volume is $86.260 \times 10^{-9} m^3$ and the expected final volume is $172.520 \times 10^{-9} m^3$; the final volume computed using the finer mesh is $172.544 \times 10^{-9} m^3$, representing 0.013% difference; the coarser mesh with 25 nodes in the film gave a difference of 0.025%.

$$V_{int} = \int \alpha \, dV = \sum_{i}^{N} \alpha^{[i]} V_{\text{cell}}^{[i]} \tag{5.1}$$

where $\alpha^{[i]}$ and $V_{\text{cell}}^{[i]}$ are respectively the volume fraction (α) and the computational cell volume of cell number i of the total of N cells in the domain.

Table 5.3: Train of multiple droplets case setup

Item	Value
Diameter of DPM droplets, D_p	$260\mu m$
Release frequency of droplet batch, F_n	$76.9Hz$
Droplet speed	$0.1m/s$
GUI Mass rate	$920.28\mu g/s$
Box (square) base width, H_x	$50 \times D_p$
Box height, H_y	$75 \times D_p$
Initial film level, H_0	$1.089mm$
Droplets spacing in a batch	$4 \times D_p$
Height from the base with fine mesh	$3.5mm$
Number of droplets in 1 batch	100 (10×10)
Total number of batches of droplets	10

Figure 5.8 shows the transient film formation. The two red marks show the level to fill from and to fill to. This qualitatively shows the mass conversion; with only Figure 5.8c showing the droplets forming the film.

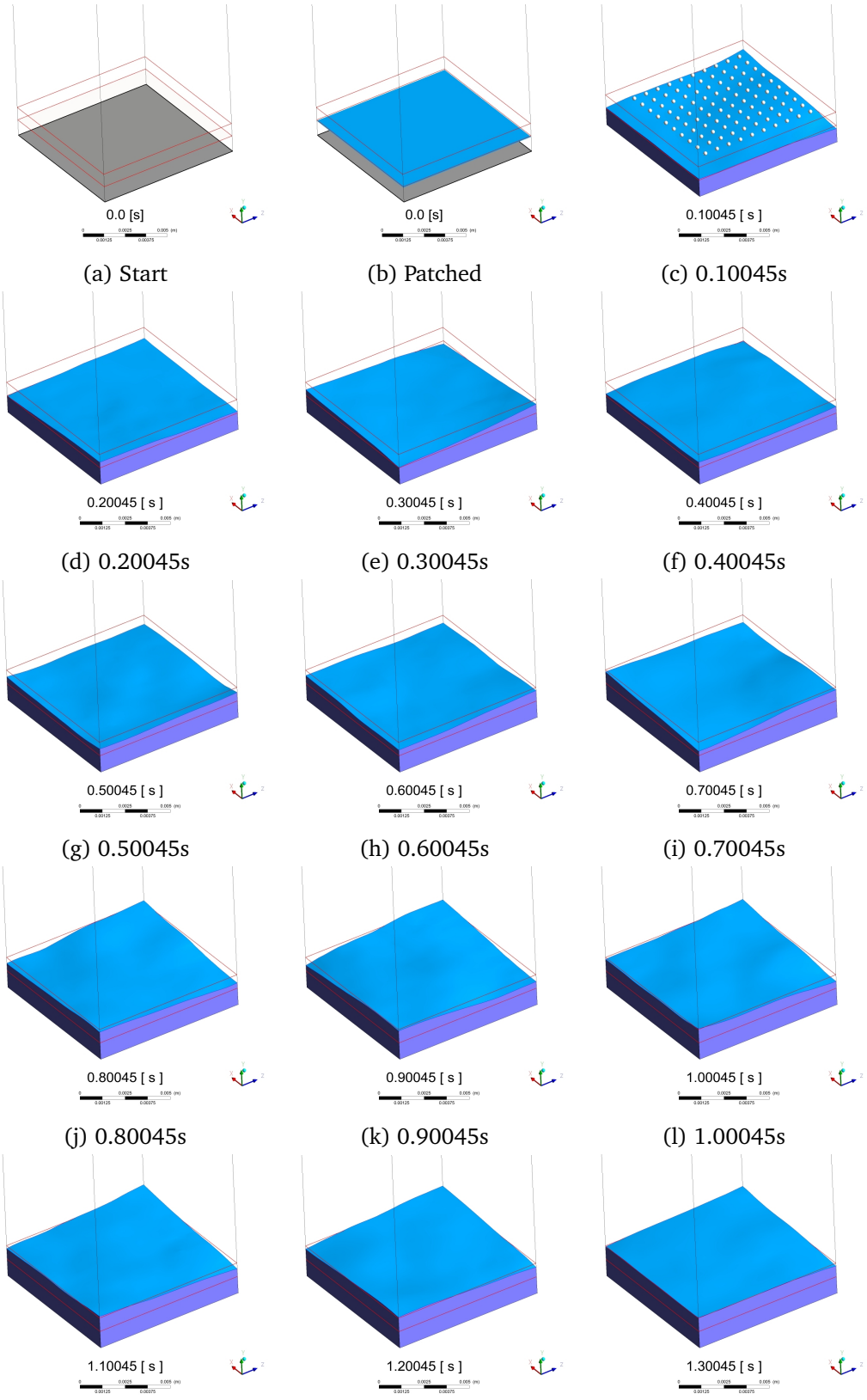

(a) Start (b) Patched (c) 0.10045s

(d) 0.20045s (e) 0.30045s (f) 0.40045s

(g) 0.50045s (h) 0.60045s (i) 0.70045s

(j) 0.80045s (k) 0.90045s (l) 1.00045s

(m) 1.10045s (n) 1.20045s (o) 1.30045s

Figure 5.8: DPM-VoF: Simple multiple droplet box fill results

5.5 Crater dynamics (Momentum conservation)

After impact of droplets on a free-surface, a crater is formed depending on the impinging impact parameters. Capturing the crater diameter evolution in the early evolution times provides a test of the model's momentum transfer abilities. With a fine mesh that is capable of resolving the droplets, it is possible to capture the full crater dynamics [11, 12]. The work of Rieber & Frohn[11] and Peduto *et al.*[12] illustrates this but such simulations are very costly however, and currently not really viable for a full bearing chamber simulation.

5.5.1 Normal Impacts

If the DPM-VoF technique is applied on a normal impact and is able to capture crater diameter evolution well, it will validate mass and momentum transfer from DPM to VoF and this is investigated in the following test case. The setup, schematically represented in Figure 5.9, is a box with a square base, H_x. The setup shows the DPM particle approaching a film of thickness h, the white crater shapes give an impression of the evolution.

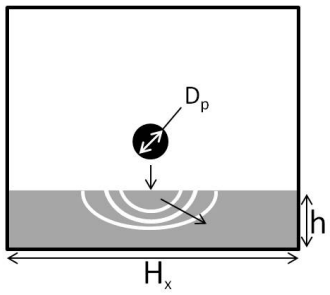

Figure 5.9: DPM-VoF: Crater dynamics test

The crater diameter is measured from the point of impact. The geometry sizes and

the fluid properties are the same as the ones in Peduto *et al.* [12]. The setup details are given in Table 5.4. The dimensionless film thickness parameters used are based on Rieber & Frohn [11], Peduto *et al.* [12] and Cossali *et al.* [13].

Table 5.4: Crater dynamics setup details.

H^*	We	Oh[a]	K	Re	$U_o(m/s)$	H_x/D_p	ρ_l/ρ_g	μ_l/μ_g
0.116	250	0.00141	3,454	11,216	2.70	8.0	997	40
1	328	0.00218	3,806	8,806	2.87	12.1	997	66
2	345	0.00218	4,003	9,469	2.95	12.1	997	66
4.5	737	0.00218	8,552	12,450	4.31	12.1	997	66

[a]Please refer to Nomenclature for the non-dimensional numbers.

A generalisation of the crown rim evolution, as suggested by Cossali *et al.* [13], is given in Equation 5.2 where n is approximately 0.5. The constant C as proposed in Yarin & Weiss [10] is such that it is dependent on the initial film thickness, with $C = (2/3H^*)^{0.25}$. X is the crater width and the droplet diameter at impact is D_p. $T^*\,(= tU_o/D_p)$ is the non-dimensional time and T_o^* is a time shifting constant.

$$D^* = \frac{X}{D_p} = C\,(T^* - T_o^*)^n \tag{5.2}$$

The crater dynamics experiments for a normal impact of a single droplet on a known film thickness are presented in Figure 5.10 using the previous mesh structure in §5.3 and $350,000$ cells in total. The film thicknesses fall into *thin* and *thick* categories (as defined in terms of the droplet and film height relative sizes in Table 2.1). The thin film results ($H^* = 0.116$), are from detailed simulations work of Rieber & Frohn [11], and the thick film experimental data is that of Cossali *et al.* [13], as used in Peduto *et al.* [12].

The experimental points are not connected with curves. The correlations, from Yarin & Weiss [10] and Equation 5.2, are given with the dashed lines. The solid lines are results from the developed DPM-VoF model (matched in colours with the corresponding experimental data points).

Neither the published correlations nor the DPM-VoF model exactly match the experimental data points for all conditions, but follow a similar pattern. It can be seen that the thin film crater growth rate is higher than those of the thick films.

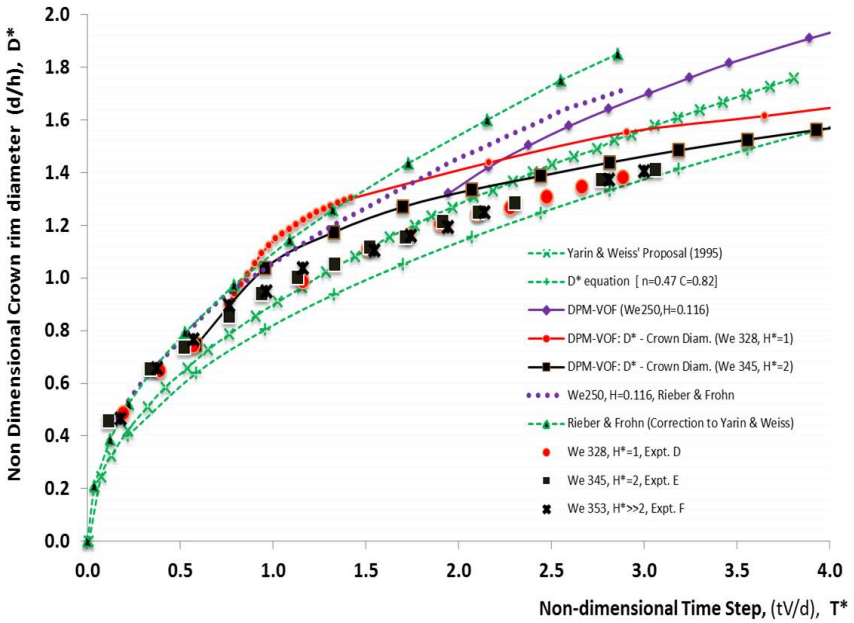

Figure 5.10: Crater evolution

The mean deviations of the simulated D^* from the corresponding reference experimental data points are estimated using Equation 5.3. The deviations are estimated as

4.3%, 15.0% and 8.1% respectively for the relative thickness values of 0.116, 1 and 2.

$$L_2 = 100 \times \sqrt{\frac{\sum_i^N \{D^*_{e_i} - D^*_i\}^2}{\sum_i^N (D^*_{e_i})^2}} \tag{5.3}$$

where $D^*_{e_i}$ is the experimental D^* measured at a point i and D^*_i is corresponding CFD data and N is the total number of points.

5.5.2 Oblique impacts

After normal impacts oblique impacts should also be considered as many of the droplet-film impacts in a bearing chamber are likely to be oblique. A qualitative result of an oblique impact is shown in Figure 5.11c based on the setup of Figure 5.11a. The impact angle is 41^o to the impact surface for the droplet impacting at a Weber number of 283 and the image can be compared directly to the corresponding experimenatal one from the experimental work of Okawa *et al.* [84], Figure 5.11b. The "ship's prow" structure observed at $0.5ms$ and $1.0ms$ are shown for the experiment and the DPM-VoF simulation. Figures 5.11d & 5.11e show sectional views, of the DPM-VoF results in Figure 5.11c, through the impact point and showing the formation of the "ship's prow" shape.

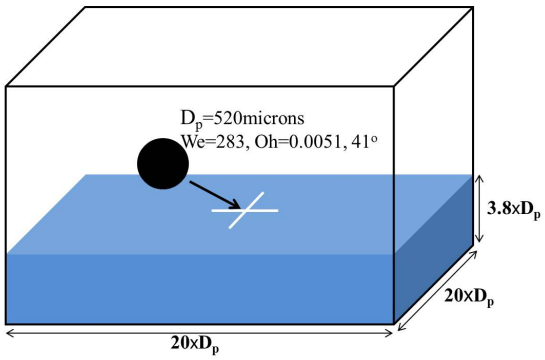

(a) Oblique angle impact: The setup

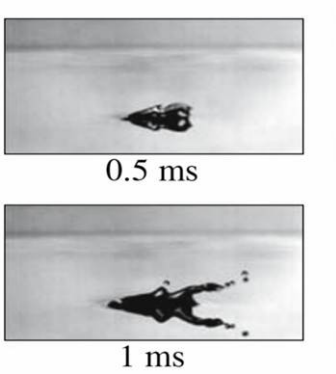

(b) Oblique impact, Okawa *et al.* [84]

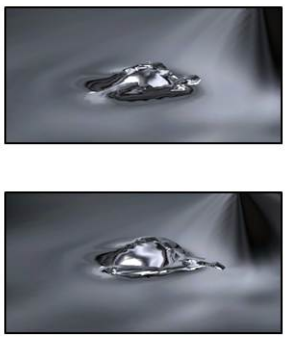

(c) DPM-VoF result

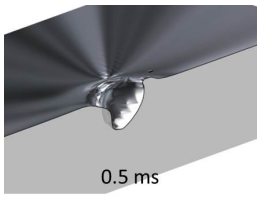

(d) Sectional view of 0.5ms (*see* Fig. 5.11c)

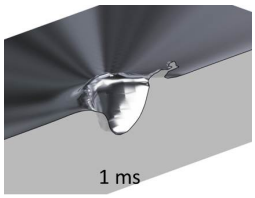

(e) Sectional view of 1ms (*see* Fig. 5.11c)

Figure 5.11: DPM-VoF: Oblique angle droplet impact on film

5.5.3 Crown splashing

Figure 5.12 shows a visual for a normal droplet impact on a film. The DPM-VoF technique is of course not able to “resolve” the splashing droplets and other fine details such as the lamella. This is because the mesh is only fine in the film region.

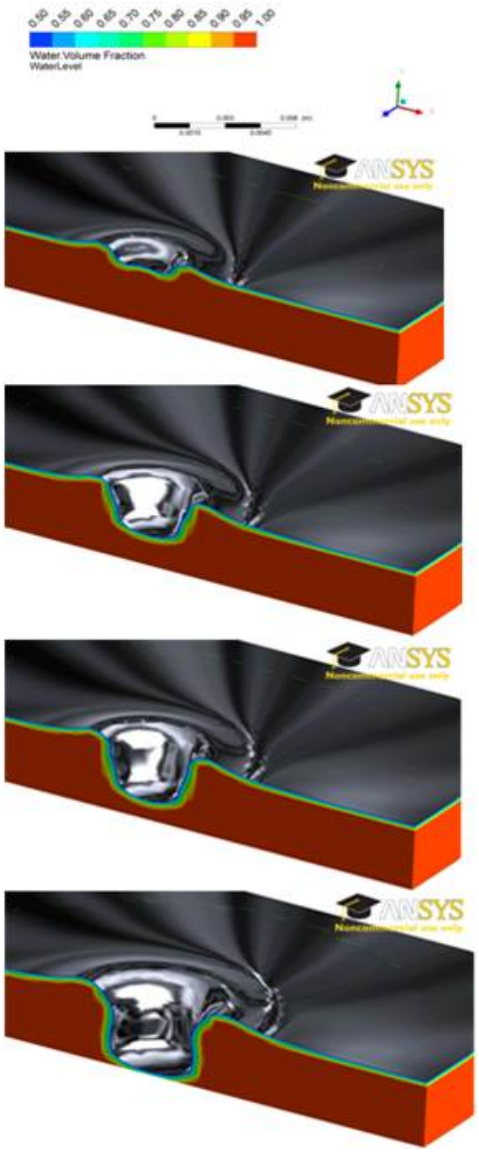

Figure 5.12: A visual impression of a normal crater evolution

Figure 5.13a shows a highly resolved droplet impact at a Weber number of 737, from Peduto *et al.* [12], on a thick film and the DPM-VoF equivalent, Figure 5.13b.

(a) Normal impact [12]: We 737

(b) DPM-VoF normal impact: We 737

Figure 5.13: Highly resolved and DPM-VoF normal impact

It can be argued that it is a rather unfair comparison as the DPM-VoF used about 350,000 computational cells here, or about a 10th of the 3 million cells used by Peduto *et al.* [12]. It is, however, not the intention of the DPM-VoF technique to resolve to very fine details, as it is intended that splashing droplets are specified by correlations and computed as Lagrangian droplets for onward tracking after the impact(*see* §5.8).

5.6 Simple Heat Transfer Checks

5.6.1 Single droplet: Core Temperature as DPM turns VoF

In this section, a very basic test is carried out to check energy exchange from DPM droplet to the VoF droplet. The single droplet case in §5.2 is revisited but now as an adiabatic box. The air temperature before injection is $300K$ and the $1000\mu m$ diameter droplet has a temperature of $350K$.

The core temperature of the VoF droplet at conversion is expected to be the same as the DPM droplet's temperature. Figures 5.14a to 5.14d show the core temperatures of the different mesh resolutions. The droplet iso-surface is given as mesh and the contour is on a plane through the centre of the droplet.

Table 5.5: Single droplet: DPM to VoF Droplet's Temperature

Droplet zone mesh resolution, S^*	VoF droplet Core Temperature, K	$\%$ of Expected
50	349.8	99.95
25	349.8	99.93
10	347.4	99.25
5	344.8	98.50

The mean core temperatures and the accuracy of conversion are given in Table 5.5. This table shows that with a resolution of $S^* > 10$, a conversion of 99.25% is achieved. The accuracies are of the same trend as the ability to resolve the free-surface of the droplets.

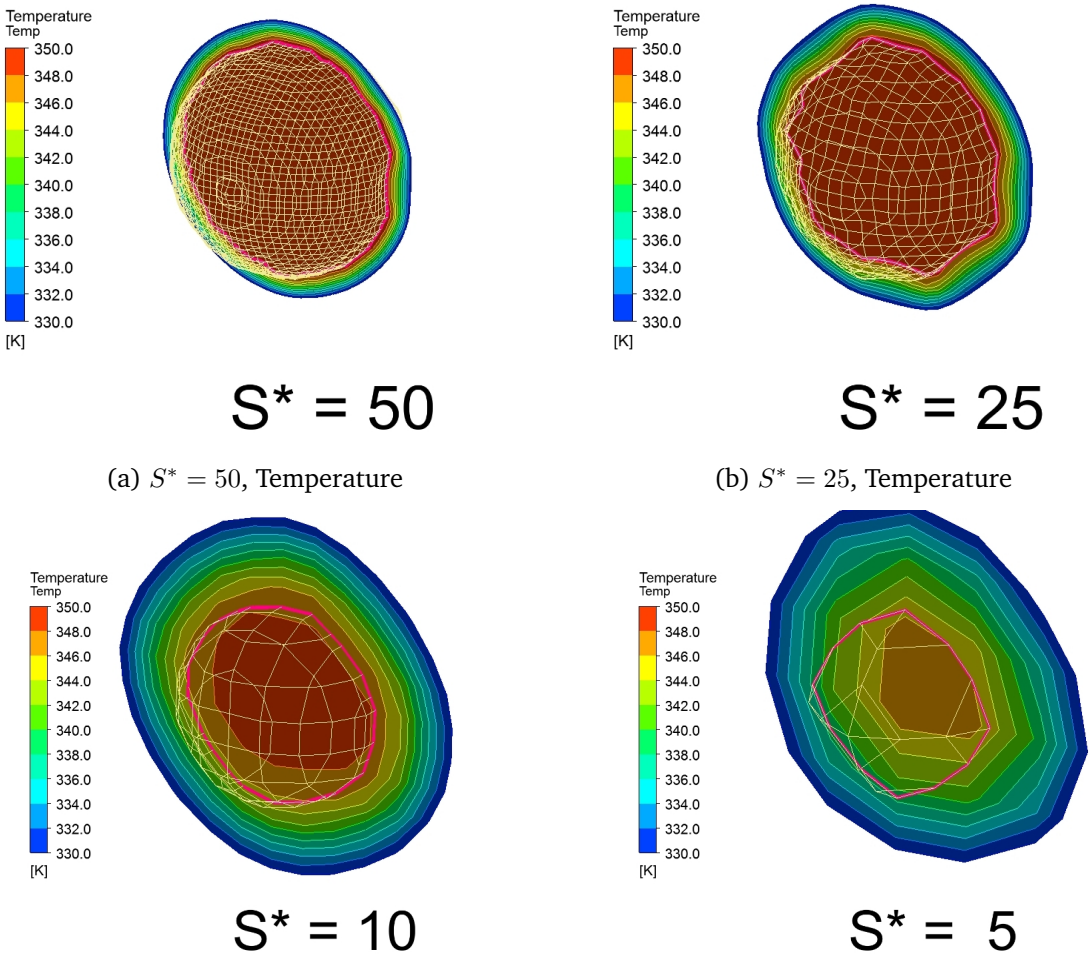

(a) $S^* = 50$, Temperature

(b) $S^* = 25$, Temperature

(c) $S^* = 10$, Temperature

(d) $S^* = 5$, Temperature

Figure 5.14: Single DPM droplet turns VoF - Core Temperature

5.6.2 Single droplet: Impact on a hot wall

A numerical test involving a single droplet impacting on a hot dry wall is used to check for boundedness of the thermal solution using the mesh setup in 5.3. Figure 5.15 shows a cold droplet injected at a temperature T_{drop} to impact on a hot surface in the *spread regime*

[*see* Table 2.2]. At the instance of hitting the wall, the DPM to VoF module *vof_drag_trap*[5] is activated at the wall boundary condition.

The DPM turns to Eulerian VoF liquid and spreads over the wall which is at a wall temperature, T_{wall}. The droplet is naturally expected to heat-up or cool down towards the wall temperature. The DPM-VoF is bounded within T_{drop} and T_{wall} as expected. Figure 5.15b shows the evolution result of a $500\mu m$ droplet at a temperature of $320K$ hitting the wall at $400K$. The temperature does not fall below the initial droplet temperature, $320K$, and did not exceed the wall temperature of $400K$.

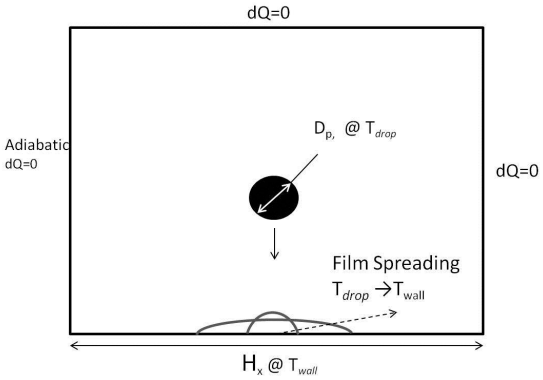

(a) Single droplet setup

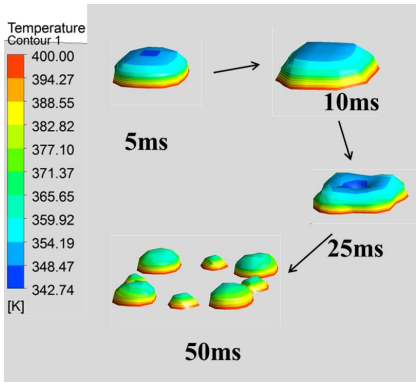

(b) Temperature evolution

Figure 5.15: Single droplet impact boundedness test

[5] see Table 4.2.

5.6.3 Simple Adiabatic box fill

The box-fill simulation [§5.3] is revisited from an energy perspective. The boundary conditions, now, were set as an adiabatic wall and the film level was $1.5mm$ and the internal temperature of both the air and liquid inside were at $500K$. The DPM droplet injection is setup to fill the level to $2.5mm$ similar to §5.3 but with the temperature of DPM droplets injected at $300K$.

An asymptotic (by a first approximation) solution to the described setup can be found by assuming that all the energy from the incoming droplet stream is absorbed by the initial film; so that after a very long time ($10sec$ say), the film cools down to the mass averaged temperatures of the droplets and the original film in the box. From the setup, the ratio of the mass of the film in the box to the injected droplets, M_f/M_d, is 1.5 given that the density of the droplets is the same as that of the film originally in the box before injection of the droplets. Equation 5.4 gives the final temperature a long time after mixing. In this simplified equation, there is no consideration for other types of energy transfer such as radiation or convection with the gas.

$$T_\infty = \lim_{t\to\infty} \left\{ \frac{\frac{M_f}{M_d} T_f\,(t) + T_d}{1 + \frac{M_f}{M_d}} \right\} \simeq 420K \tag{5.4}$$

The box wall temperature after $18s$ is given in Figure 5.16. This is long after steady state is reached. The mass averaged temperature of the domain is about $416K$ (0.95%

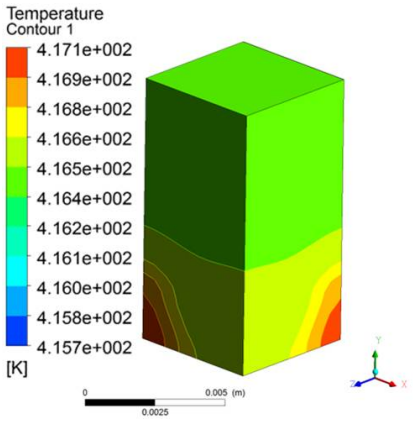

Figure 5.16: Cold droplet injection into an adiabatic box containing hot fluid

off). It is expected to be lower than $420K$ because the gas phase was not considered in Equation 5.4 but this was solved in the energy equation. The results are therefore considered physically acceptable.

5.7 DPM-VoF: Spray Film Cooling Test Case

A spray from a nozzle may consist of hundreds of thousands of small droplets of liquid. The droplets are formed (or atomised) by an interaction of the gas and a sheet of the liquid continuum in the nozzle. Atomisation of a liquid creates a high surface to volume ratio which serves to provide a better cooling on the hot surfaces. Results from the spray cooling experiments of Oliphant *et al.* [129] show that sprays can provide the same heat transfer rate at lower mass flux as a continuum jet of liquid impingement. With a nozzle, the droplet diameters are not equal as is found with a mono-disperse droplet generator. Experimental measurements [130, 131] show that the droplet diameters from a pneumatic nozzle follow some statistical distribution with a wide range of droplet sizes. This range is

often represented using the Sauter mean diameter [132, 133]. The Sauter mean diameter, d_{32}, represents the diameter with the same volume to surface area as the whole spray.

The process of heat transfer in spray cooling is complex because of the several possible mechanisms involved. The droplets interact with the surrounding gas and neighbour droplets before impact on the free-surface or on the hot wall. Some of the droplets may even vaporise before impact. The atomised droplets may form a continuum of film after impact on the wall or mix with the flowing liquid film. Depending on the fluid impact properties and the wall temperature, nucleate boiling and evaporation of the wall film might also occur.

The film thickness and its distribution are very important variables of interest to researchers [134–136] in spray-film studies, but not all their findings and setup are necessarily consistent. It is difficult to measure film thickness and temperature experimentally under a spray. The differences in experimental conditions or parameters such as wall roughness, working fluid's wettability [137], nozzle setup [134, 135] to achieve stagnation or to avoid film pooling might also be responsible for the inconsistency in film thickness distributions under their sprays. Most of the published works have considered spray film cooling in the boiling regime [138] or with sub-cooling [134]. In this thesis the work of Yaqing *et al*. [14] is chosen for comparison because it was done in the non-boiling regime and there are velocity measurements suitable for the DPM-VoF model.

Film formation simulation is important because the film is primarily responsible for conveying the heat away from the hot surface. To apply the DPM-VoF technique, the sprayed droplets are considered as Lagrangian particles in the gas phase; upon the droplets

hitting a wall or a film surface, the model creates the film from source terms informed from the Lagrangian phase as described in §4.3. The data of Yaqing *et al.* [14] present a simpler validation case also for the DPM-VoF technique. This is because of the reduced complexity of the spray mechanism in the non-boiling regime. Although film thickness was not measured in the experiment, the heat flux measurements provide a good validation data for this work. Evaporation is still bound to occur in the non-boiling regime but to a lesser extent. This work does not provide the complete solution to spray film modelling but it will provide a better insight for application to multiple droplets to film impact research.

5.7.1 Spray-Film: DPM-VoF setup

Figure 5.17 shows the DPM-VoF schematic representation of spray-film characteristics of a nozzle. A review of nozzle atomisation process by Schmidt [139] shows it is a very complex process and the outcome depends on several parameters. For simplicity, it is assumed that the droplets are fully atomised at the nozzle exit and that a "batch" of droplets are released at a time from the nozzle. It is assumed that there are N number droplets in a batch. It has been considered that the frequency of release of a batch of droplets from the nozzle is f_n. In other words, every $1/f_n$ sec., N number droplets of mass M_{fn} are released from the nozzle consistently over the spray time [*see §4.7.0.1*].

The spacing length scale, λ_d, of each batch is expressed as an integer multiple of the mean droplet diameter, D_p. A relative droplet spacing, $\lambda^* (= \lambda_d/D_p)$, of 10 is considered reasonable and has been used in this work.

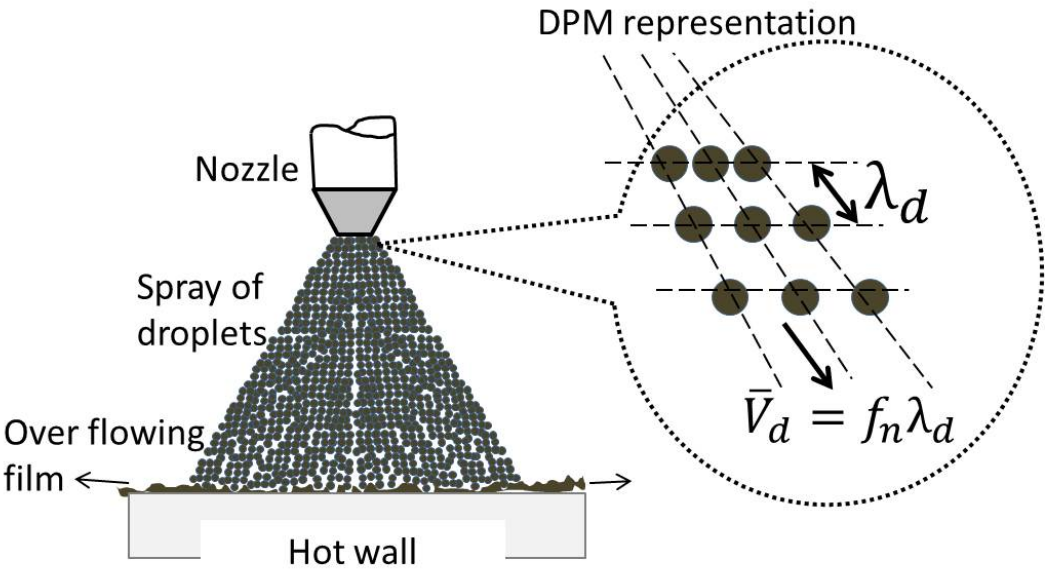

(a) The nozzle film

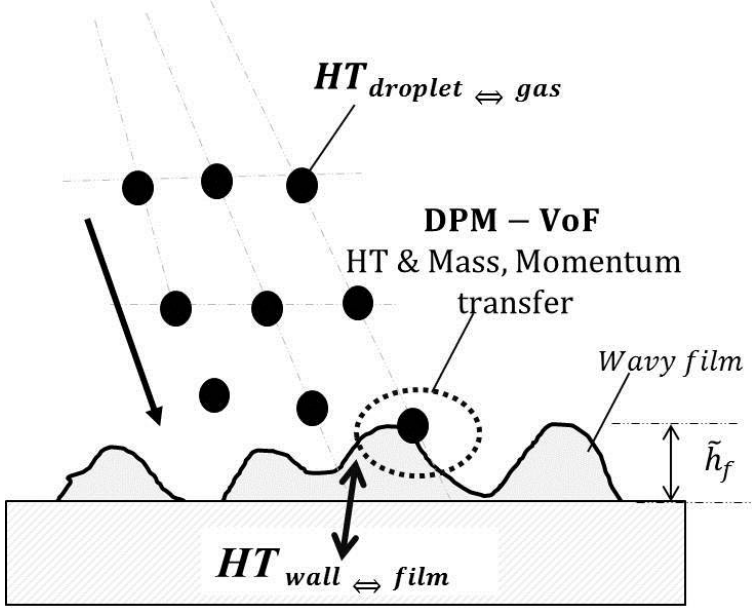

(b) Closeup at the wall

Figure 5.17: Schematic of a nozzle spray with DPM-VoF

The mean velocity, $\bar{V}_d$, frequency, f_n and spacing, λ^* can be mathematically balanced to suit the nozzle continuum mass flow rate such that the mass of a batch of N droplets, M_{fn}, is met as given in Equation 5.5.

$$M_{fn} = \frac{\pi}{6}\rho \sum_{i=1}^{N} D_{p_i}^3 \tag{5.5}$$

An open loop flow system at atmospheric pressure was used in the experimental setup of Yaqing *et al.* [14] as shown in Figure 5.18. The data acquisition system records the thermal measurements. The characteristics of the droplets were measured using a Dantec Phase Doppler Particle Analyser (PDPA).

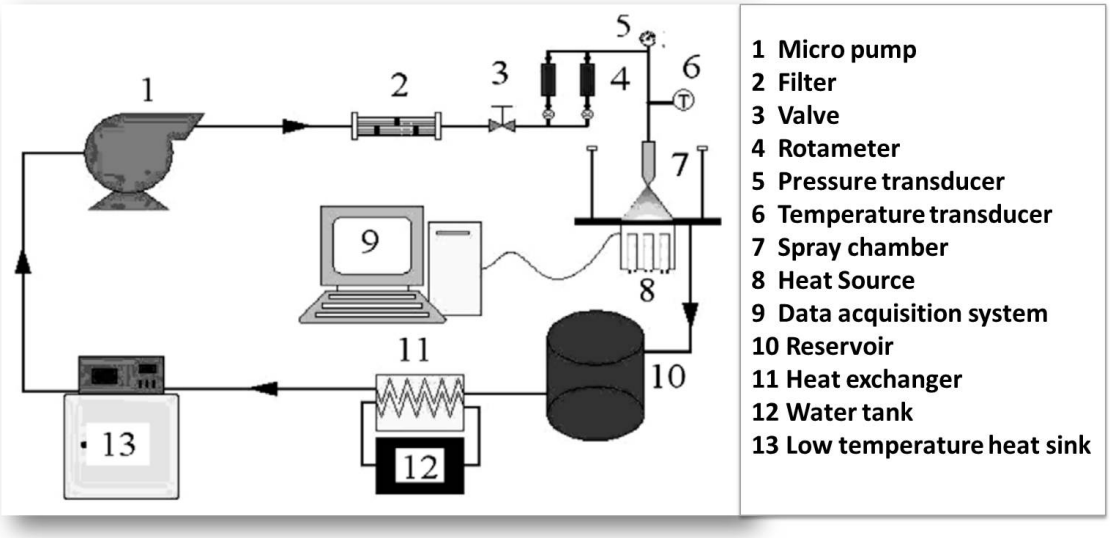

Figure 5.18: Spray-film Experiment Setup, Yaqing *et al.* [14]

The PDPA readings give the Sauter mean diameters and the velocities of the droplets. Water is used as the working fluid and it is supplied to the 60^o cone-spray nozzle from the low temperature heat sink which cools the working fluid in the loop. The working fluid is

pumped through the filter to ensure that there are no impurities in it. The heater surface or hot plate is made of a $10mm \times 10mm$ copper block with a thermal conductivity (k) of $401W/mK$.

The one dimensional Fourier law of heat conduction was used with the temperature measurements from the equispaced thermocouples placed under the hot plate and above the cartridge heaters to predict the surface temperature, T_s, and heat flux. From Figure 5.19, the heat flux and surface temperature can be estimated by solving Equation (5.6).

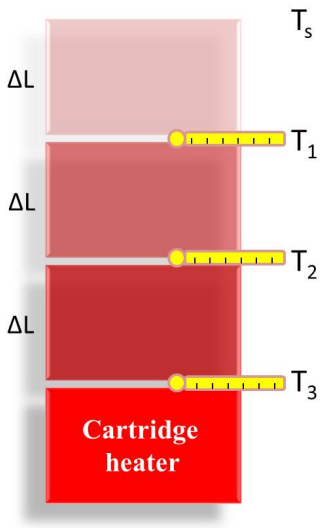

Figure 5.19: Experimental estimation of Heat Flux and Wall Surface Temperature

$$q = k \cdot \frac{T_1 - T_s}{\Delta L} = k \cdot \frac{T_2 - T_1}{\Delta L} = k \cdot \frac{T_3 - T_2}{\Delta L} \tag{5.6}$$

where q is the estimated heat flux, ΔL is the spacing between the thermocouples and T_1, T_2 and T_3 are the mean temperatures recorded at the separations between the thermocou-

ples put inside the heated block.

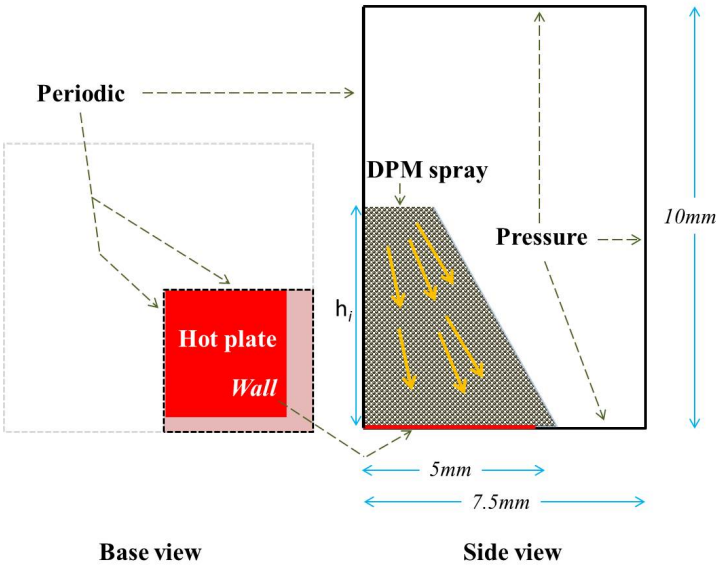

(a) DPM-VoF: Spray-film setup (with the boundary conditions)

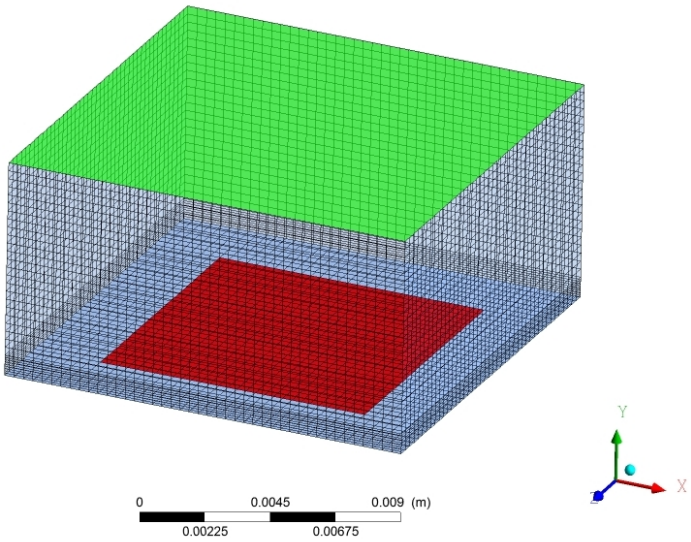

(b) DPM-VoF: Spray-film mesh (mirrored to show fully)

Figure 5.20: DPM-VoF: Spray-film Geometry and Mesh

The schematic representation in Figure 5.20a shows the CFD setup used. A quarter of the geometry is modelled as the geometry is symmetric about x and z axes. In the

simulation, the characteristics, such as the Sauter mean diameters and the mean velocities, of the spray at a height, (h_i), of $4.8mm$ above the heater surface from the experiment are used as the boundary condition for the DPM droplets.

The hexahedral mesh used is given in Figure 5.20b. Computational meshes of about $25,000$ cells were used. The mesh density is finer closer to the hot surface and the wall y^+ is about 12 and there is a minimum of 10 cells in the *film* region. With this mesh, the S^* is between about 1.12 and 1.25.

Table 5.6: Spray film setup: DPM-VoF

Case	$T_w\ ^oC$ [a]	$D_p\ (\mu m)$	Mass flux (kg/m^2s)	$V_n\ (m/s)$ [b]	$F_n\ (kHz)$ [c]	N_{dp}	N_{1sec} [d] $\times 10^6$
249a	40						
249b	64	90	24.9	13.0	14	453	6.54
249c	85						
181a	40	95	18.1	12.0	13	320	4.04
181b	64						
157a	40	100	15.7	11.0	11	273	3.00

[a] T_w, is the wall temperature.
[b] V_n is the nozzle mean velocity.
[c] F_n is the nozzle atomisation frequency.
[d] N_{1sec} is the number of droplets in 1 sec.

The mass fluxes indicated in Table[6] 5.6 are based on the hot plate area. The temperature of the droplets when they leave the nozzle is 19.9^oC or $293.1K$ and the temperatures of the wall takes different values for the different cases as given in Table 5.6. The densities of water (ρ_w) and air (ρ_a) are, respectively, $998kg/m^3$ and $1.25kg/m^3$ and the surface tension is $72.8mN/m$. The viscosities for water (μ_w) and air (μ_a) are, respectively, taken as $10^{-3}Pa.s$ and $10^{-5}Pa.s$. The mass flux, based on the area of the hot plate is used

[6] Note: case names are appended with alphabets *a*, *b* and *c* which, respectively, refer to the temperatures 40, 64 and 85^{o}C.

to obtain the mass flow rate for each case. The number of droplets in a batch of nozzle release, given in Table 5.6, is estimated by balancing the mass flow rate, the expected number of droplets as given by Equation (5.7).

$$N_{pb} = \frac{M_f \times A}{\left(\rho \frac{\pi}{6} D_p^3\right) F_n} \tag{5.7}$$

where N_{pb} is the number of droplets released in an atomisation, M_f is the mass flux (kg/m^2s) and A is the hot plate surface area and F_n is the frequency of release of a batch of DPM particles (nozzle atomisation frequency).

The Reynolds numbers at the nozzle region $\left(Re = \rho_a \bar{V}_d N_{pb} D_p / \mu_a\right)$ are between $(3.76 - 6.62) \times 10^4$. The overall massflow and energy imbalances are have not been monitored in this simulation. The convergence criteria for the residuals are of the order of 10^{-4} and the solution method follows from §3.5.

5.7.2 Spray-Film: Results

In the simulations, the DPM droplets hit the hot plate and form the VoF film as shown in Figure 5.21. The simulated mean film thicknesses for the three different mass fluxes are shown in Figure 5.22 with the error bars showing the deviation from the means.

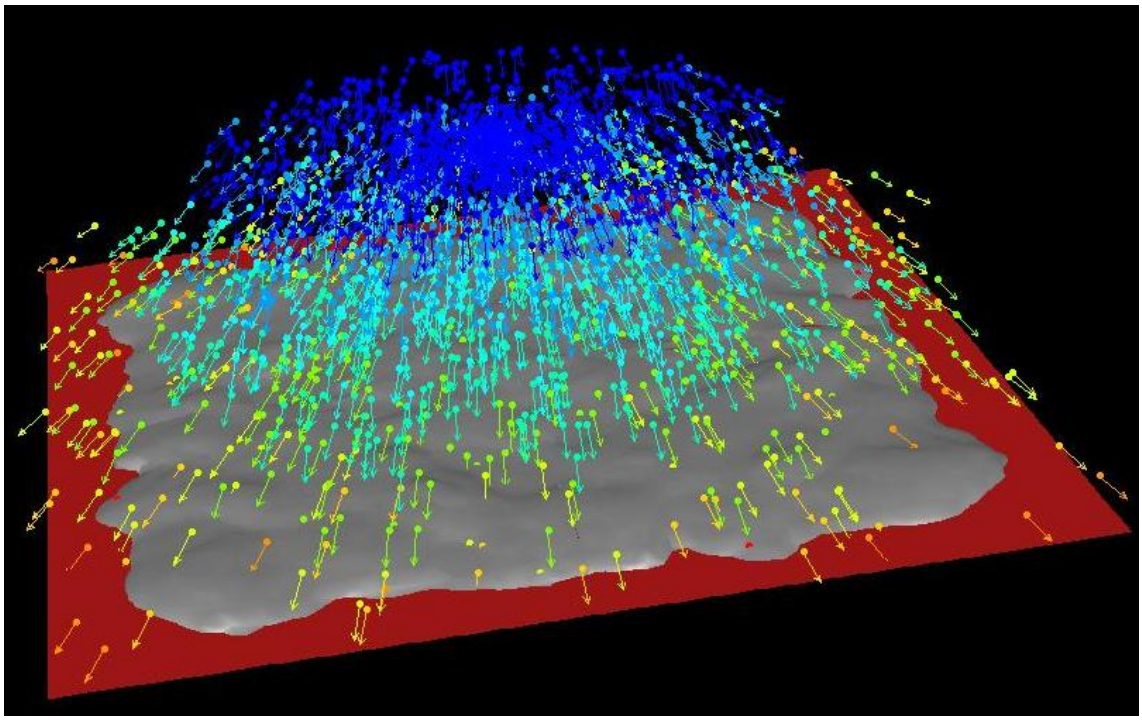

Figure 5.21: DPM-VoF: Spray-film Showing DPM and VoF Film on the hot plate

These are the timed averaged values of the film thickness taken at five planar locations, X from the centre of the plate after steady state has been reached. In this simulation, the film thickness values range from about $180\mu m$ to $226\mu m$. It is seen that the film is generally thicker at the centre of the hot plate. The film thickness increases with an increasing mass flux and the film thickness is more uniformly distributed at the highest spray flux of $24.9kg/m^2s$. The film flow Reynolds numbers[7], (Re_f), are about 450, 470, and 480, respectively for the fluxes 24.9, 18.1 and $15.7kg/m^2s$.

[7] $Re_f = \rho_w \bar{H}_f \bar{U}_f / \mu_w$, where $\bar{H}_f$ is the film mean thickness and $\bar{U}$ is the mean film speed.

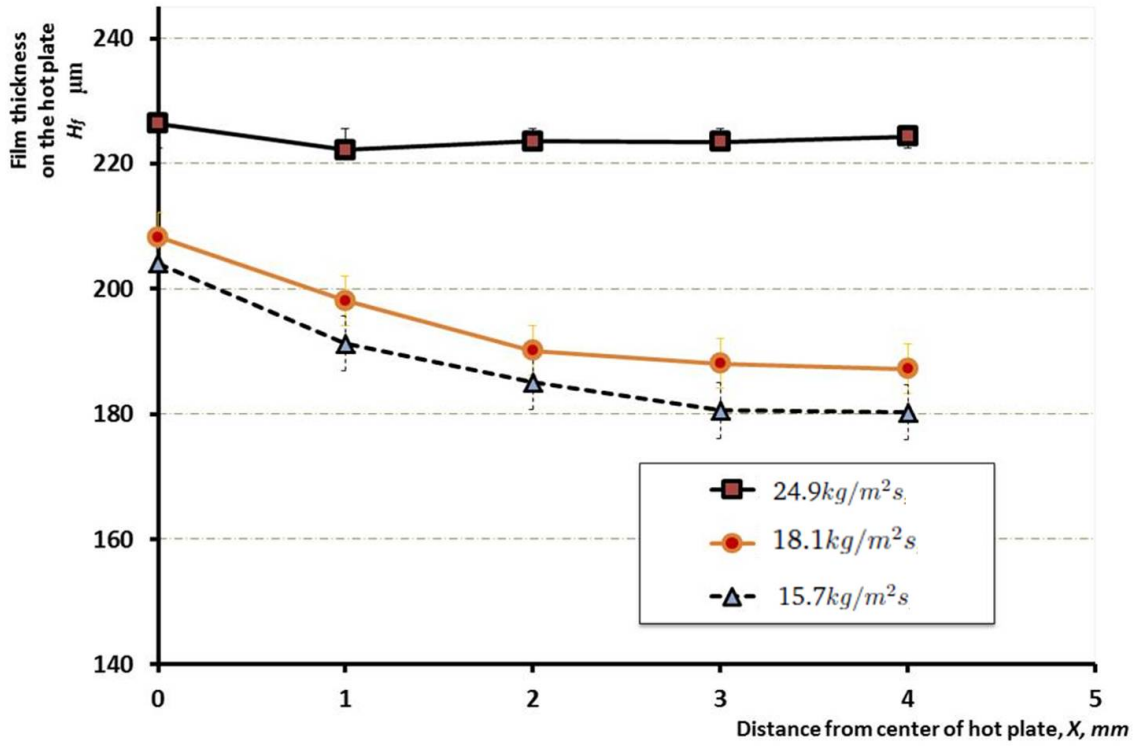

Figure 5.22: DPM-VoF: Spray-film thickness

For a fixed wall temperature, T_w, the wall heat flux, q, is calculated in ANSYS-Fluent using Equation (5.8). The heat transfer coefficient h_t is calculated based on the local flow field condition as described by the law of the wall for temperature using the analogy between heat and momentum transfer [69]. The average heat flux over the hot plate surface is plotted in Figure 5.23 as a function of time.

$$q = h_t \cdot (T_w - T_{sf}) \tag{5.8}$$

where T_{sf} is the local fluid temperature, computed in the first cell next to the wall.

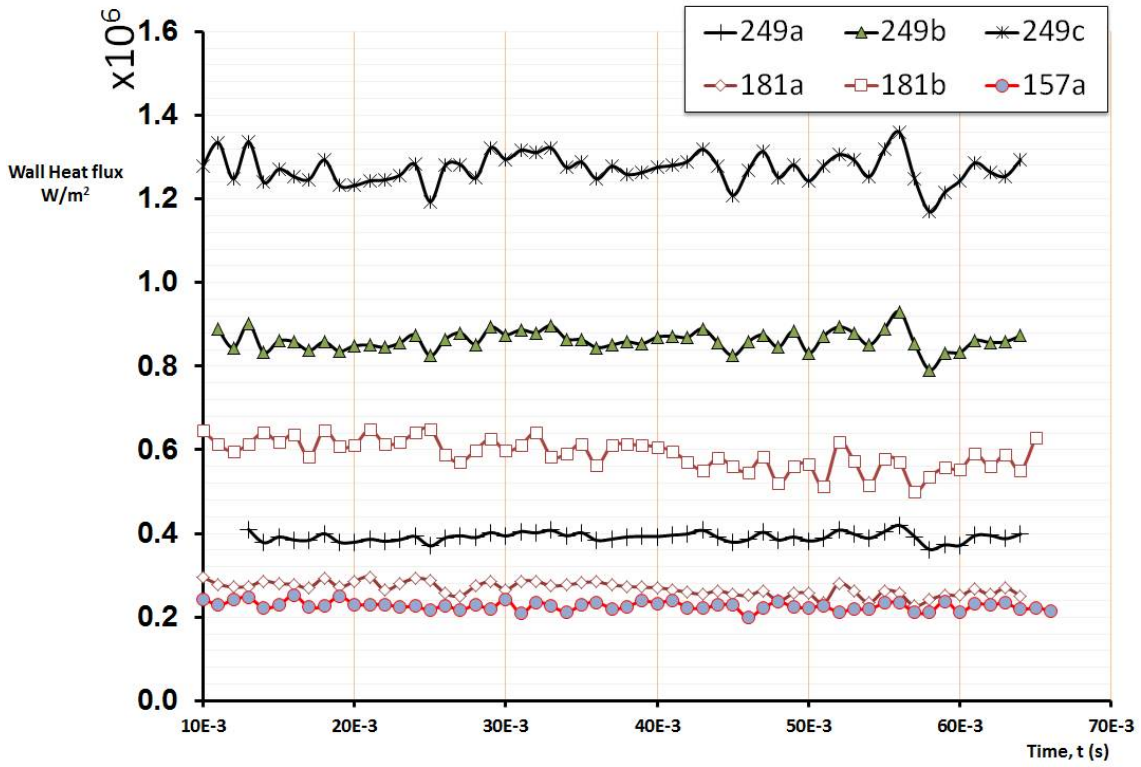

Figure 5.23: DPM-VoF: Spray-film Heat Flux
Note: case names are appended with alphabets a, b and c which, respectively, refer to the temperatures 40, 64 and 85°C; the names also show the spray fluxes; 249, 181 and 157 correspond, respectively, to the fluxes 24.9, 18.1 *and* $15.7 kg/m^2 s$.

In order to compare to the experimental data a bulk heat transfer coefficient for heat transfer between spray and the hot wall is calculated. This is given by Equation (5.9) where q_a is the area-averaged flux over the surface, averaged over the time period shown in Figure 5.23.

$$h_b = \frac{q_a}{(T_w - T_{spray})} \tag{5.9}$$

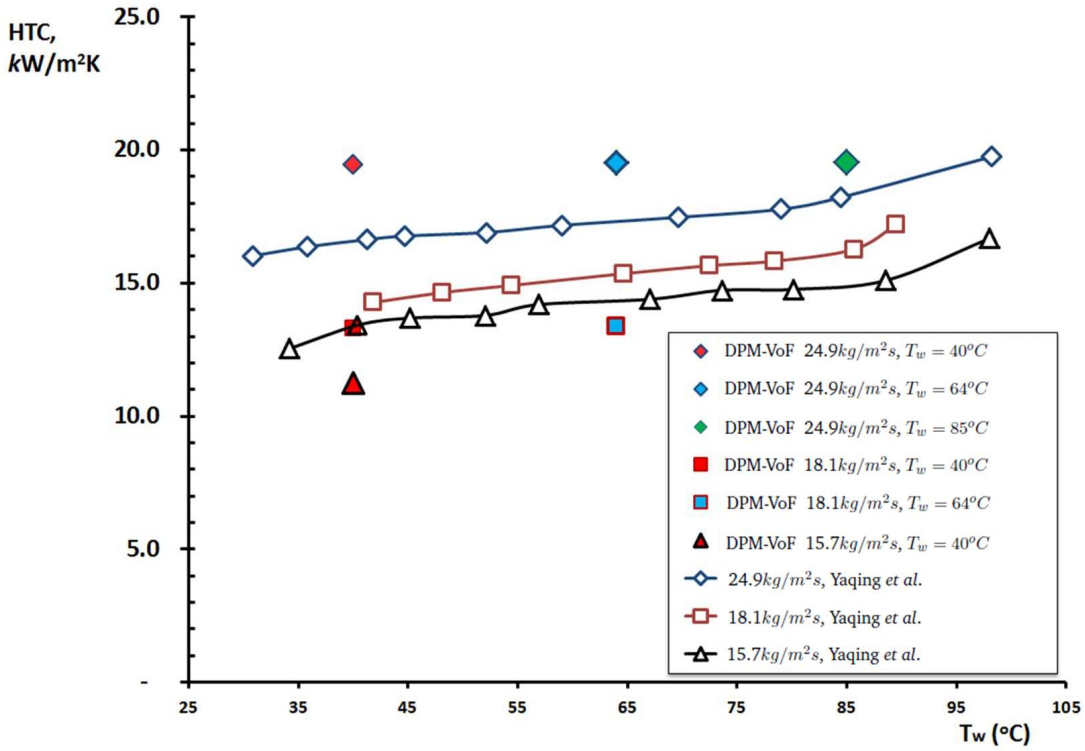

Figure 5.24: DPM-VoF: Spray-film Heat Transfer Coefficient

The wall heat fluxes for the six different cases (given in Table 5.6) are shown in Figure 5.23. This figure shows that for higher spray mass flux and higher wall temperature there is a higher heat flux. These observations are consistent with the experimental observation. The *157a* and *181a* cases are similar in flux and wall temperature and are also similar in wall heat fluxes.

Yaqing *et al.* [14] estimated the instrumentation error contribution to the experimental values for the HTC as $\pm 6\%$. In the DPM-VoF simulations, the mean deviations of the HTC from the experimental measurements is 12.2%. The error range is between 6.8% and 16.8%. The results show a good average prediction with the DPM-VoF technique.

5.8 Splashing demonstration

The impact of a droplet at a high momentum may create lots of even smaller droplets. In practical applications of droplet to film impact, the splashing droplets are also important. This section demonstrates the splashing technique proposed in §4.6.1. Figure 5.25 shows results from the detailed simulation of Rieber & Frohn [11], **A** and the DPM-VoF splashing, **B**. The droplet impact Weber number is 598 on the film with a thickness, h^*, of 0.116. The droplet at A_1/B_1 is just before impact on the free-surface. The detailed simulation required about 32.8 million computational cells while the DPM-VoF has been done on only about 0.5 million computational cells. The detailed simulation is able to capture lots of details and a wide distribution of droplet sizes. The DPM-VoF technique, with that small number of cells, is not able to capture the full cusp and filament disintegration to droplets but the experimental correlations were used to predict the number and diameters of droplets in the splash.

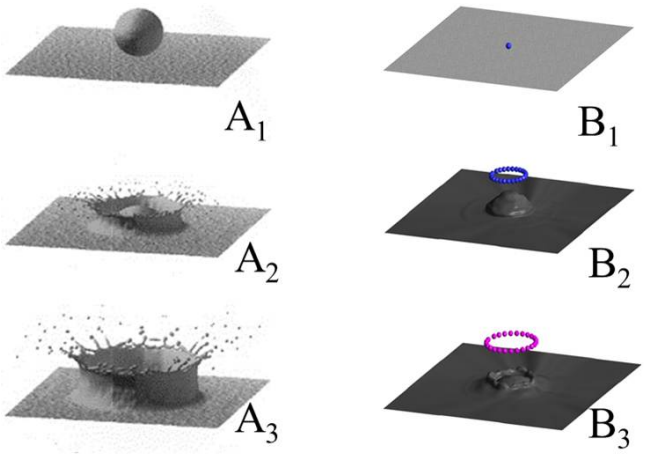

Figure 5.25: Normal impact: **A:** Detailed simulation [11] **B:** DPM-VoF

Mean diameter from correlations has been used for the splashing droplets. The impacting droplet, at B_1, is seen as a Lagrangian particle. The crater is formed as a result of the impact momentum source. A close up look at the DPM-VoF impact is shown in Figure 5.26.

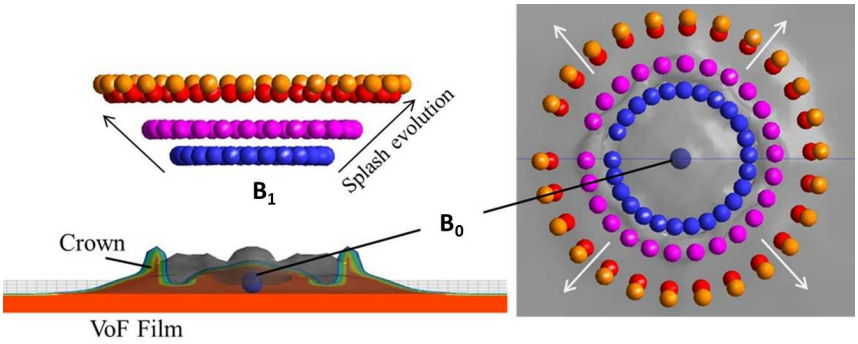

Figure 5.26: DPM-VoF: Normal splashing evolution -*frozen in timesteps*

The droplets have been shown in a time-frozen frame to give an impression of the relative locations. The primary droplet impacts at B_0 and the splashing crown starts at B_1. The crown and the secondary droplets positions grow radially outwards. To demonstrate splashing, the secondary droplets are generated using the splashing technique described in §4.6.1; the interface position is detected and the number of secondary droplets are estimated based on the Weber and the Ohnesorge numbers. The film cross section is also shown, after source term exchanges.

Of key interest to this work is the ability of the droplets to track/identify the free film interface and identify wall boundaries. The (*large*) primary droplet in Figure 5.27 impacts at an oblique angle on an arbitrary curved film interface.

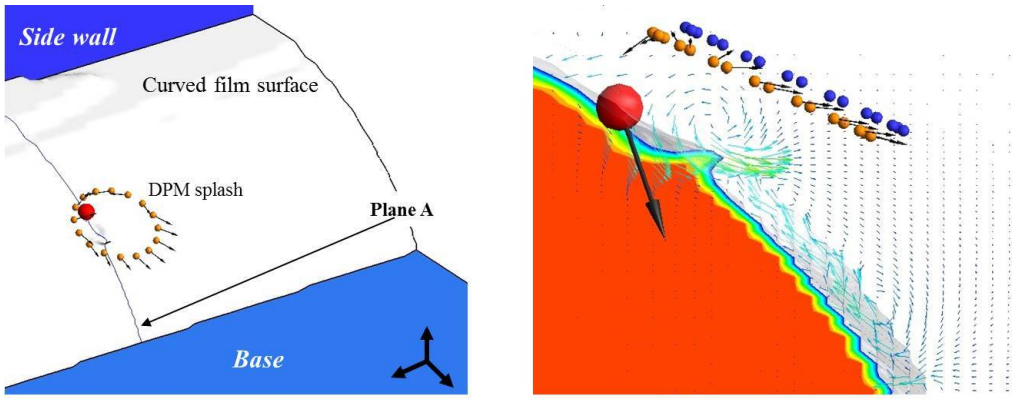

Figure 5.27: DPM-VoF: Oblique splashing on an arbitrary film interface

Experimental correlations do not exist for splashing of droplets on impact on films on curved walls. The algorithm detects the interface normal at the point of impact and generates the secondary droplets based on correlations for impact on flat film surfaces. For the shown case, Figure 5.27, the impact Weber number is 350 and the Reynolds number is $6,175$ and Ohnesorge number is 0.00303. For a similar impact parameter but impacting on a *thick* flat film, the correlations will predict about 16 droplets. The film depth searched "sees" a *thick* film. The film deformation forms the ship's prow structure [84] and deforms in the expected direction.

5.9 Summary

This chapter presented a number of simple to more complex, and application type tests and results for the DPM-VoF technique proposed in chapter 4 for the simulation of droplet to film interaction. The methods exploit the Lagrangian DPM framework to track the

droplets without resolving explicitly the droplets because of their relatively small sizes, often less than $1000\mu m$ diameter in the target applications. To test the proposed model, several basic to more complex cases were used.

A very basic mass conservation test was done by checking a single Lagrangian droplet turning into an Eulerian VoF droplet. To resolve the droplets in VoF, mesh resolutions spaced a fraction of the droplet diameter were used. To resolve a single droplet, a 10^{th} of the droplet diameter, in grid spacing, or lower gives a mass conservation over 99.6%. This sort of resolution in the whole domain is obviously too computationally expensive; but for the DPM-VoF model, such spacings in the wall/film regions provide guidance on the mesh resolutions likely to be required at the wall regions.

The *simple box fill test* was used to demonstrate mass conservation by injecting a single stream of droplets in the Lagrangian form to fill the box to a given level in the VoF form at less than 1.5% error. A further stream of multiple droplets stream were injected into a partially filled box to double the initial volume. By using a mesh that could sufficiently resolve the film in regions where film is expected, the DPM-VoF technique captures mass to less than 0.1% error. The momentum conservation of the technique was checked with crater evolution and compared with published correlations. Momentum transfer capability was found to be within 10% of published correlations (on the basis of crater evolution).

The thermal boundedness of the solution proposed was tested using the single droplet turning into a VoF droplet. With mesh resolution of a 10^{th} of the droplet diameter and better, the computation returned a droplet temperature within 0.8% of the expected temperature. Further, a test of a droplet impacting on a hot wall was done and the temperature

of the film formed did not go beyond bounds. A further simple test was done by repeating the box fill test as a problem of cold and hot fluids mixing in an adiabatic box.

A more application type test was done using spray-film heat transfer setup in the non-boiling regime without consideration for evaporation. The deviation of the heat transfer coefficient from published experimentally measured value is about 12.2%. Splashing after the impact of a primary droplet onto an arbitrary film surface was also demonstrated.

The sparsely distributed droplets forming film on some walls is a challenge from the CFD modelling point of view. The ability to track the free-surface regardless of the impact location is particular useful for an environment like the bearing chamber as will be shown next in chapter 6. A major contribution of this thesis is that in a problem with multiple droplets and film interaction, mesh density can be finer at the walls and the film regions of the domain and potentially reducing computational overhead needed to fully resolve the entire flow. The DPM-VoF model is, therefore, a very practical method for droplet to film interaction. However, it does not attempt to replace detailed simulations in droplet to film interactions.

Chapter 6

Application to Aero-Engine Bearing Geometry

6.1 Overview

A brief description of the bearing chamber flow problem, in §1.1 & §1.3.1, has illustrated the challenges that could be faced in attempting to model such a complex system. The oil enters the chamber from the bearing in the form of sheets, filaments and droplets shedding off the bearings; but these droplets are also formed from the breakup of the film caused by surface instability. These droplets travel and eventually impact on walls and other structures. As this happens mass, momentum and energy (heat) are exchanged with wall films. To study the bearing chamber phenomenon, experimental rigs are used. A visualisation rig that attempts to *simulate* the flow inside the bearing, such as shown in

Figure 6.1, can be used to study inside the bearing chamber.

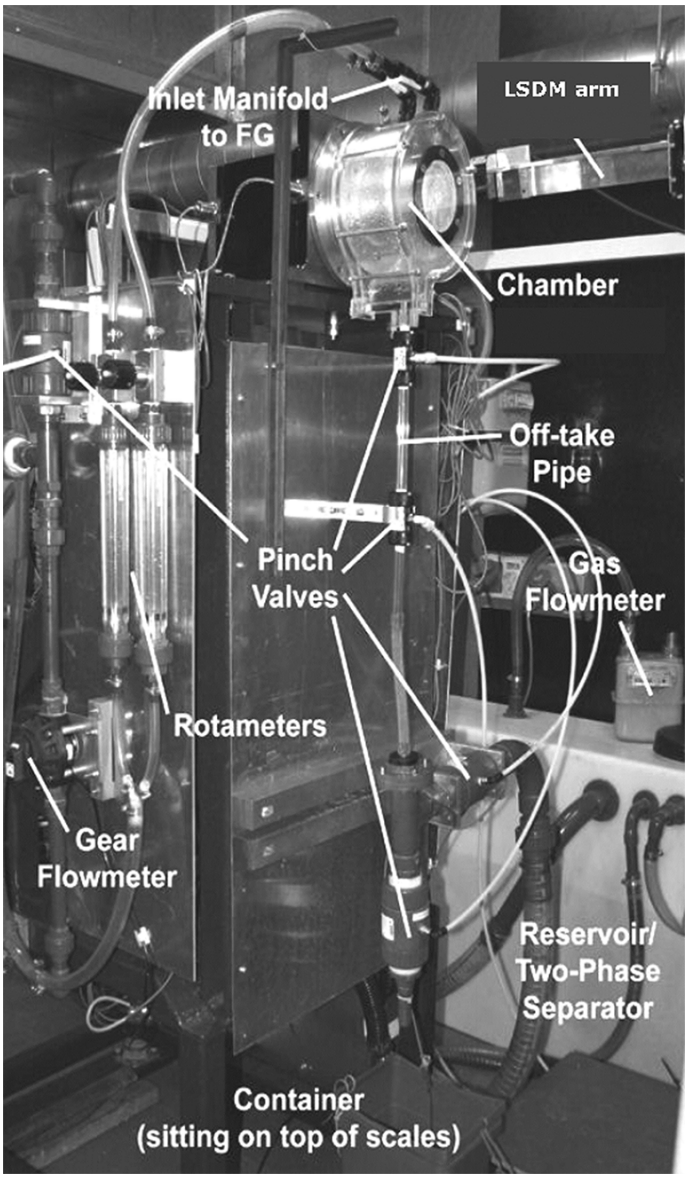

Figure 6.1: Bearing chamber experimental rig [140]

In this chapter, the developed DPM-VoF methodology is applied to two different bearing chamber configurations [CASE 1: §6.2 & CASE 2: §6.3]; the first of which is a visualisation rig and the other is a more *engine realistic* rig. The visualisation rig uses water as its working fluid and does not have bearings that break the working fluid up; rather the film

is *generated* to simulate what happens to the oil as it enters into the chamber, as seen later in §6.2.1. The second configuration operates like an engine and has bearings lubricated with engine oil and has bearing chambers of different geometric configurations.

6.2 CASE 1: The AE3007 Bearing Chamber

The *Nottingham Transmissions UTC* conducts experimental and modelling work to understand the complex flow in aeroengine bearing chambers. As part of this work Chandra *et al*. [1, 2] developed an experimental test facility that could be used to investigate test geometries representative of elements of aeroengine bearing chambers. Figure 6.2 shows one test geometry mounted on the rig, which operates at ambient conditions and shaft speeds up to 15,000 rpm. The rig has good visual access and in addition numerical experimental data for residence volume and film thickness has also been obtained. One of the configurations investigated on the rig, the "curved wall deep sump" was investigated over a number of geometric variants, as reported in [141, 142]. The baseline curved wall deep sump is similar to that found on the AE3007 geometry.

Experiments were conducted on the rig to investigate liquid/gas removal from the bearing chamber for a variety of liquid flowrates, shaft speeds and scavenge ratios (scavenge ratio is the ratio of total volume at chamber exit to volume of supplied liquid and is typically around 4 in normal engine operation).

Water was used as the working fluid in the experiments because of its similar properties, such as density and viscosity, at room temperature with the properties of aeroengine

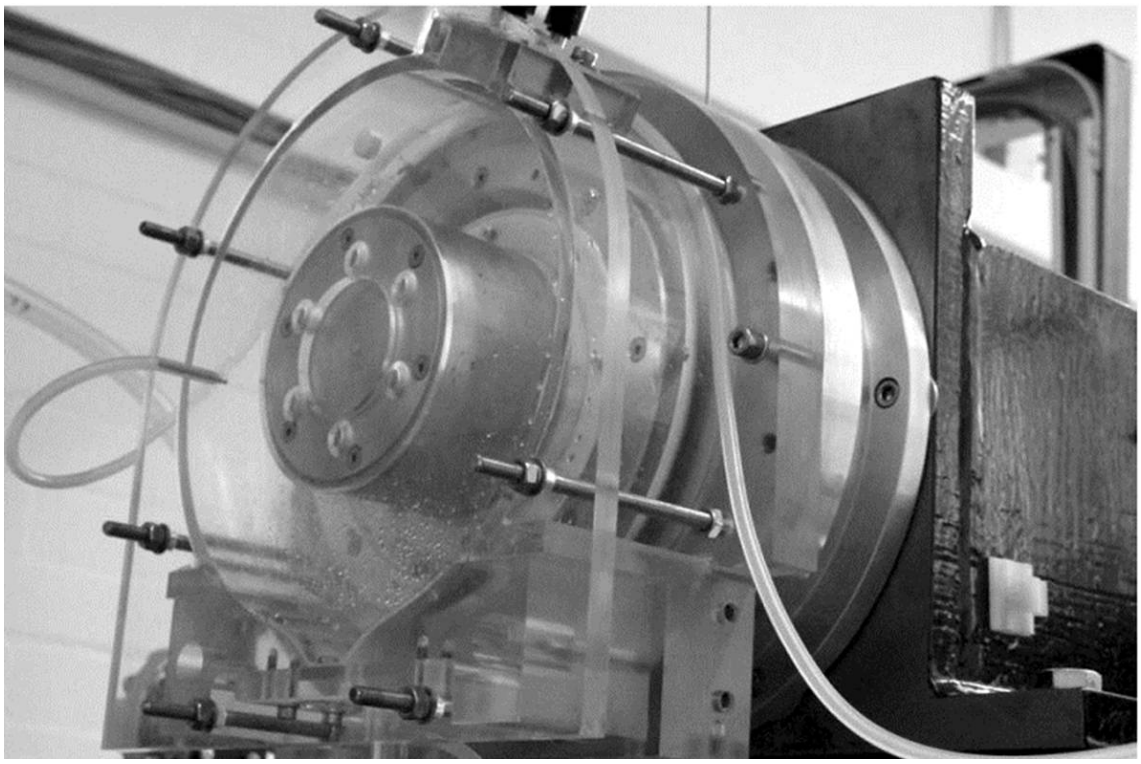

Figure 6.2: Bearing chamber with Perspex see-through wall

bearing chamber oil (*see* Mobil Jet Oil II) at operating conditions.

The baseline AE3007 geometry as tested on the Nottingham UTC test rig was modelled using the capability developed in this thesis. The properties used in the simulation are given in Table 6.1.

Table 6.1: Water and air properties for simulation

Description	Values
Density (water) $[kg/m^3]$	1,000
(air)$[kg/m^3]$	1.24
Dynamic viscosity (water)$[kg/ms]$	100.30×10^{-5}
(air)$[kg/ms]$	2.21×10^{-5}
Surface tension $[N/m]$	0.0728

The experimental test chamber included a vent on the front face that maintained the pressure in the chamber at approximately atmospheric. The scavenging of water from the

chamber is achieved by connecting a gear pump to the offtake region. The scavenge ratio (SR) given by Equation 6.1, defines the ratio of the total exit volume flow rate to the inlet water flow rate.

$$SR = \frac{Q_o + Q_a}{Q_o} \tag{6.1}$$

where Q_o is the flow rate (kg/s) of water and Q_a is the flow rate (kg/s) of air.

6.2.1 Film Generation

To experimentally replicate the bearing chamber flow such that the wall film can be studied, there is a need to be able to introduce the working fluid into the bearing chamber. Chandra *et al*. [1, 2] attempted to reduce the complexity by using two different inlet devices. The devices are the Film Generator (FG) and the Rotating Inlet Distributor (RID). Either the FG or the RID is used at a time, they are not combined in these experiments. Only the RID is of interest in this work but the FG is described for completeness.

6.2.1.1 Film Generator -FG

The Film Generator experimentally simulates film formation at the walls of the bearing chamber by directly creating film at the wall.

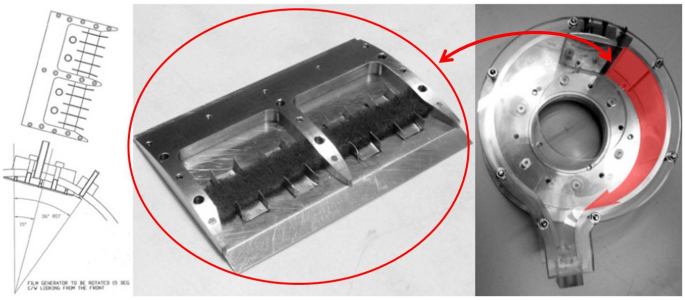

(a) FG Device [140]

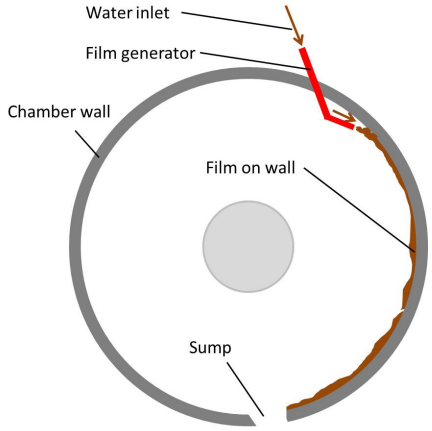

(b) FG Schematic
(Showing it injecting water at the bearing wall)

Figure 6.3: Film Generator

Figure 6.3 shows a representation of a film generator. The CFD simulation of the flow with a Film Generator was done by Tkaczyk & Morvan [55]. It can be immediately seen that this technique is limited to forming film on only one section of the wall. This technique can however create film of uniform thickness at the walls.

6.2.1.2 Rotating Inlet Distributor - RID

The RID can be thought of as a rotating cylinder with a number of holes on its outer surface, Figure 6.4b.

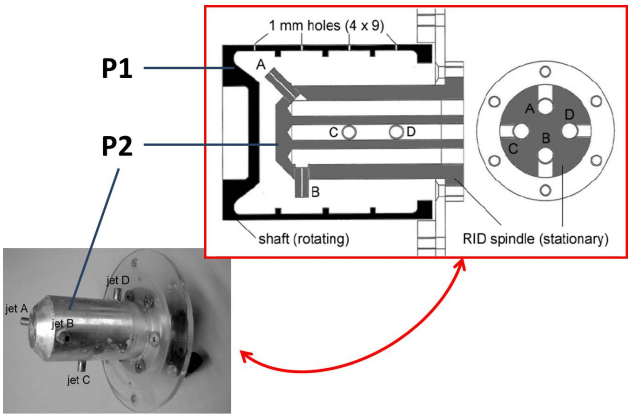

(a) Rotating Inlet Distributor - RID [140]

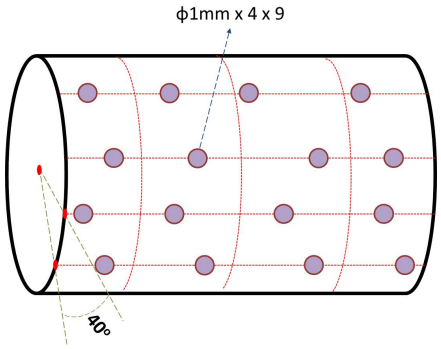

(b) RID wall schematic showing **P1** in Figure 6.4a

Figure 6.4: Rotating Inlet Distributor setup

Pumping water inside the cavity formed by the cylinder (shown in Figure 6.4a) forces the liquid to exit into the chamber via the outer holes in the form of atomised droplets. The cylinder outer wall rotates and represents the shaft going through the engine chamber. Figure 6.4a shows the RID together with details of its internal parts, and in particular jets **A**,**B**,**C**, and **D** that bring the water into the RID cavity.

The $1mm$ diameter holes are randomly distributed in the axial direction, one per section, on the rotating cylinder wall[1] of the RID, but uniformly spaced 40°, Figure 6.4b. With the RID, water is introduced into the bearing chamber in the form of droplets, as if

[1]The photograph inset in Figure 6.4a does not show the cover with the holes.

shedding off the high speed shaft. This working fluid introduction approach results in a film which forms along the entire wall of the test chamber, unlike with the FG approach which only leads to a film upstream of the deeper sump.

6.2.1.3 DPM-VoF Model of the RID

To create the DPM-VoF boundary condition for the RID, the schematic shown in Figure 6.5 is used. The RID encases the shaft. Water is fed into the volume between the shaft and walls of the RID. The *random* holes behave like nozzles to generating droplets of water as it exits the device. The radial component of velocity of the droplets exiting from the holes can be estimated from the continuity for a continuous feed of water into the RID chamber. The tangential component is estimated to be a fraction of the shaft linear speed.

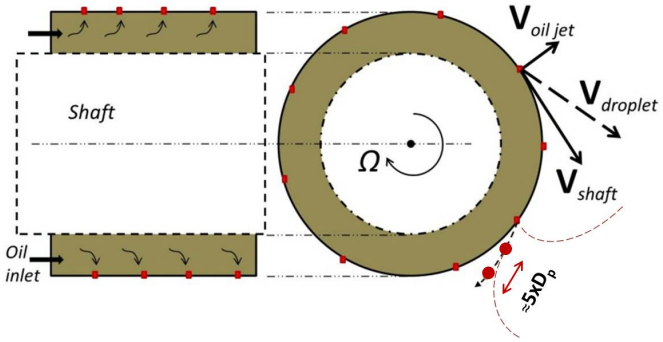

Figure 6.5: RID droplet formation schematic

If the shaft is stationary, the radial component of velocity at which the pumped water leaves the holes can be obtained from Equation 6.2; where $\dot{M}_{RID}$ is the feed rate, in kg/s,

of the water into the RID chamber and A_h is the area of each of the N holes.

$$V_{wj} = \frac{1}{N}\frac{\dot{M}_{RID}}{\rho A_h} \tag{6.2}$$

The droplets initial velocities, $\vec{V}_{d_0}$, can be estimated from the vector components of the shaft tangential components (V_s) and the water jet velocity (V_{wj}). There can be an axial component to the droplet velocity, Equation 6.3, for example if there is significant axial air flow but; although this is possible, no axial movement of the shaft has been considered here.

$$\vec{V}_{d_0} = V_{wj}\hat{i} + V_s\hat{j} + 0\hat{k} \tag{6.3}$$

In the DPM-VoF injection setup, the droplets are not injected directly from the surface of the shaft. The droplets are injected from about $5 \times D_p$ as shown in Figure 6.6 and spread[2] every 5 droplet diameters($5 \times D_p$), between injection.

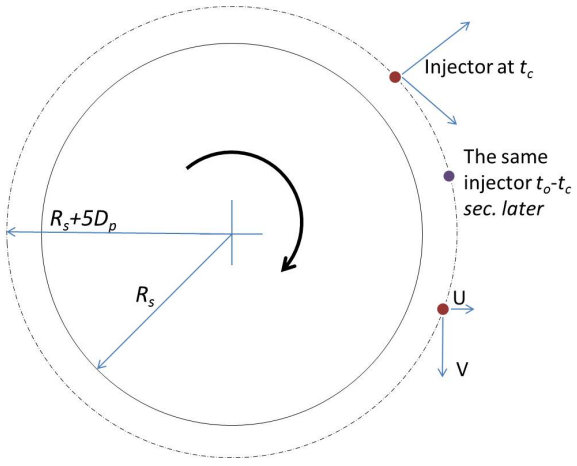

Figure 6.6: RID injector motion

[2]The interference drag between particles is considered negligible with this spacing [143], thus considered a reasonable guide to the arbitrary spacing.

The injectors move with the rotation of the shaft as it will in the experiment, using Equations 6.4a to 6.4e.

$$\Phi = \frac{2\pi}{60} \times \Omega \{t_o - t_c\} \tag{6.4a}$$

$$x = x_o \cos(\Phi) + y_o \sin(\Phi) \tag{6.4b}$$

$$y = y_o \cos(\Phi) - x_o \sin(\Phi) \tag{6.4c}$$

$$U = U_o \cos(\Phi) + V_o \sin(\Phi) \tag{6.4d}$$

$$V = -U_o \sin(\Phi) + V_o \cos(\Phi) \tag{6.4e}$$

where Ω is the shaft speed in RPM, t_o is the starting time for injection based on the specified frequency of injection and t_c is the current time step in seconds, Φ is the angular rotation of the shaft in radians. The previous location of the particle is at (x_o,y_o,z_o) and (x,y,z) is the location the injector is moved to. The velocity vector is also rotated from (U_o,V_o,W_o) to (U,V,W) but the magnitude of the vector remains the same as in the initial condition.

There was no experimental measurement of droplet properties in Chandra *et al.* [1, 2]. Glahn *et al.* [144] studied the disintegration of droplets from a similarly rotating rim arrangement. From the work, it can be seen that there is a rapid reduction in V_{d_0}, in the radial direction outward from the shaft. An attempt was made by Glahn *et al.* [144] to correlate the relative droplet velocity to the rim speed as a logarithmic function of the droplet Weber number. The speed of the droplets was less than 50% of the rim speed. Therefore a reduction factor is required in the velocities of the droplet initialisation.

6.2.2 The AE3007 Bearing Chamber Geometry

The representative CFD geometry[3] of the AE3007 test geometry used by Chandra *et al* [1, 2] is shown in Figure 6.7. The CFD geometry has a shaft diameter of $100mm$, the outer wall diameter is $200mm$ and the length of the shaft section is $100mm$. The diameter of the offtake pipe is $10mm$ and its center is $25mm$ from the wall. The breadth of the sump is $27.4mm$ and of the same width as the shaft [2]. The pump diameter is $30mm$ and $100mm$ long.

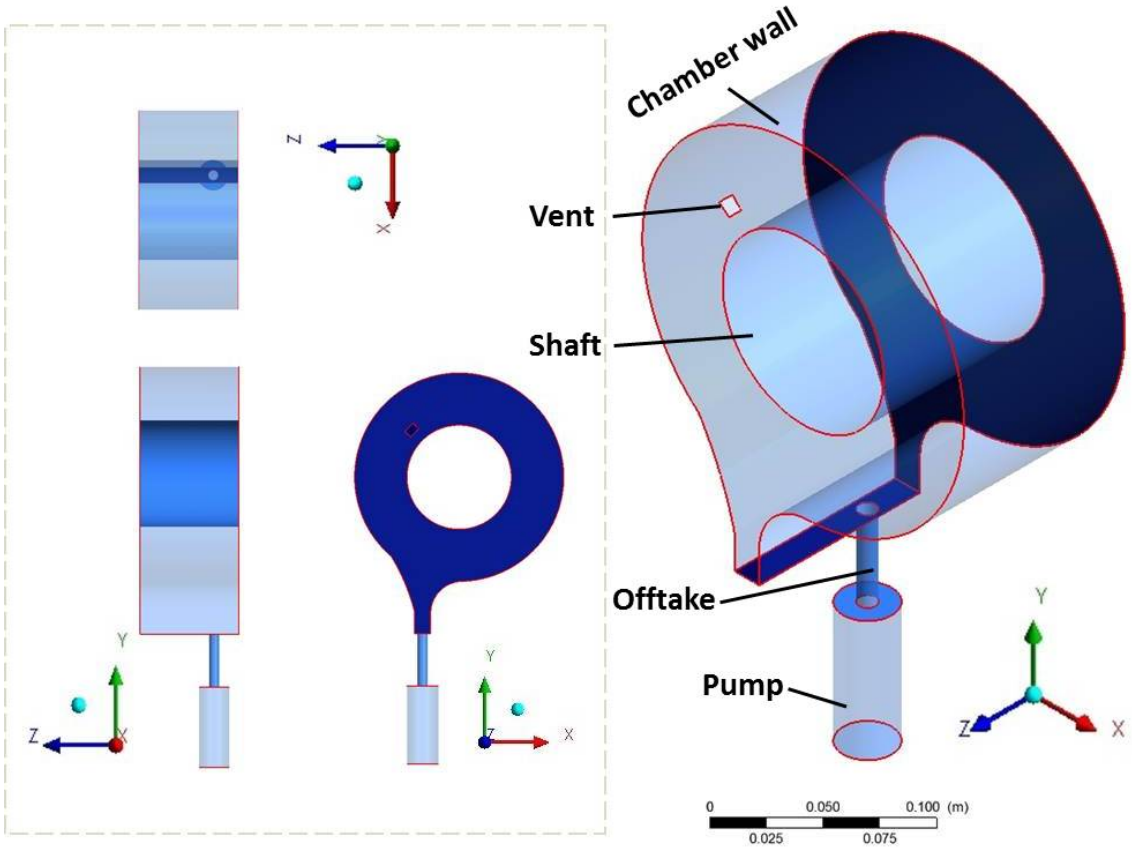

Figure 6.7: Simulated bearing chamber geometry

[3]Please refer to Figure 6.12 for the boundary conditions.

A mixture of water and air goes through the offtake pipe as implied in the definition of scavenge ratio. In ANSYS-Fluent it is possible to specify a mass flow rate boundary for a mixture of air and water. It is, however, not possible to know how much of each of the phases are present at the offtake every time. This, therefore, means that the mass flow boundary condition will not be suitable. To simulate the effect of pumping at a given scavenge ratio, a larger diameter cylinder is attached at the end of the off-take port, an idea from the work reported in Robinson [15].

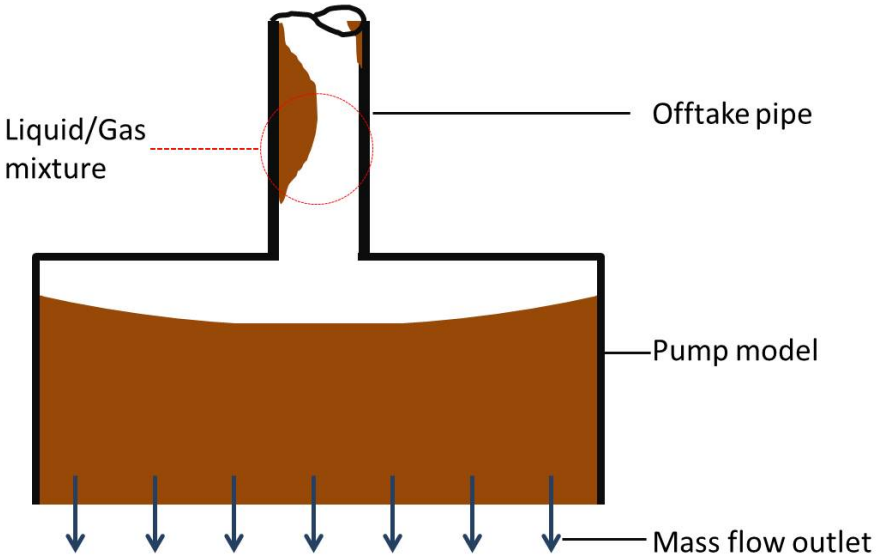

Figure 6.8: CFD Pump Model

To achieve the pumping, the pump part is preset with an initial amount of water and the mass flow rate is set using Equation 6.1. A schematic representation of the *pump model* is shown in Figure 6.8. This is similar to "priming" before starting a centrifugal water pump. Krug [97] validated the pump technique for bearing chamber applications.

6.2.3 AE3007 Bearing Chamber Mesh

Figure 6.9 shows the mesh used in the simulations. It is a structured/hexahedral mesh of about 1 million computational nodes. This builds on the guidelines for meshing the bearing chamber from the work by Tkaczyk & Morvan [55] and Sonner *et al.* [145]. The mesh density is higher closer to the walls to be able to resolve the film.

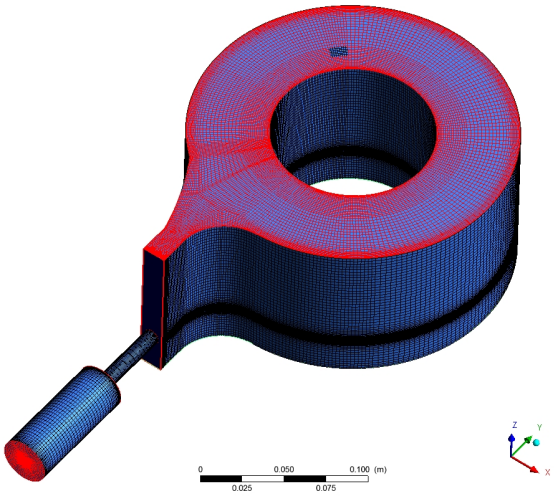

Figure 6.9: Simulated bearing chamber hexahedral mesh

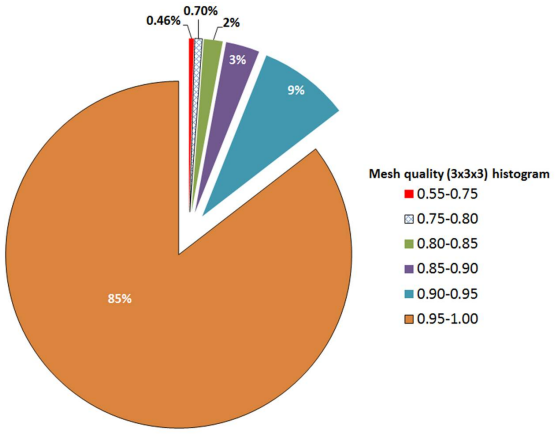

Figure 6.10: Mesh quality histogram [146]

The mesh quality calculated in ANSYS-ICEM is given in Figure 6.10. Mesh regions with quality close to 1 are of high quality and those with quality less than 0.5 are not recommended; for good results, mesh quality should be above 0.5 [146].

A mesh growth factor of 1.2 is used at the walls. At the walls, y^+ is ensured to satisfy $y^+ < 30$ [*see* 3.3.5]. To make the structured mesh, the control volume is split into logical building blocks, Figure 6.11 in ANSYS-ICEM. The O-grid meshing technique [146] is used for the cylindrical parts such as the pump exit, offtake pipe and the shaft.

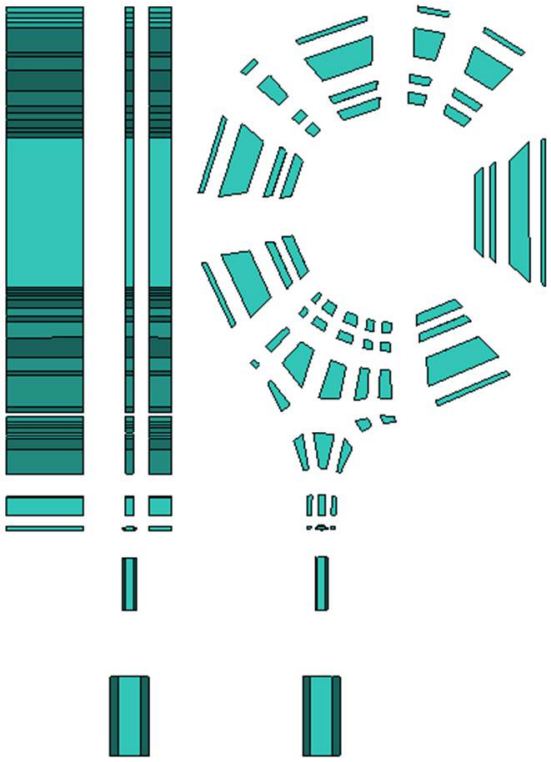

Figure 6.11: Hexa-blocking layout for the bearing chamber

6.2.4 Boundary conditions

The boundary conditions are summarised in Figure 6.12. The vent is kept at 0 bar relative pressure. The pump exit is a mass flow outlet and everywhere else is a wall. All walls are stationary except for the shaft which is a rotating wall boundary. The water inflow into the chamber is achieved using droplets in the DPM representation injected inside the domain from the shaft surface as described in §6.2.1.3. The simulations were carried out at $10,000$ and $15,000RPM$ for selected scavenge ratios of 1.1, 2.0 and 4.0 as given in Table 6.2. The droplets diameters, $\bar{D}_p$, although arbitrary, are chosen to be similar in size to the RID exit holes. The mean velocities of the droplets are taken as 60% of the shaft speeds; these are, respectively, $31.45m/s$ and $47.21m/s$ for the $10,000$ and $15,000$ rpm shaft speeds. For the thermal boundary conditions, water droplets are injected at 60^oC and the wall is kept at the 120^oC. Again, these are arbitrary as the experiments [1, 2] were done isothermally. The offtake region is assumed to be exposed to the atmosphere and wall heat transfer coefficient of $10W/m^2K$ is assumed.

Table 6.2: AE3007 Geometry case setup

Case Name	Shaft speed, [RPM]	SR	$\bar{D}_p$ [μm]	Water flow rate [l/min]	Droplet injection frequency, F_d[kHz]
$10KSR1.1$	$10,000$	1.1	800	8	40
$10KSR4.0$	$10,000$	4.0	800	12	26
$15KSR2$	$15,000$	2.0	600	16	110

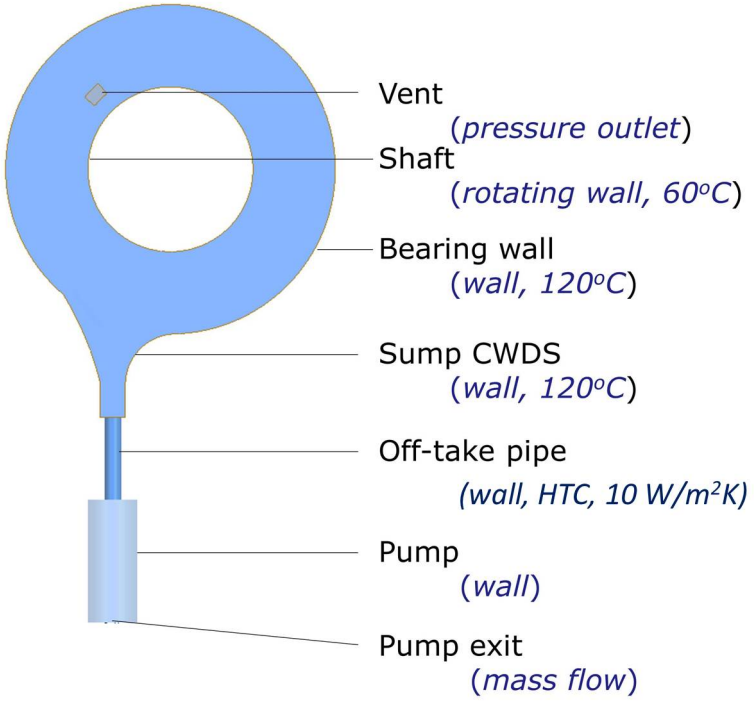

Figure 6.12: Boundary conditions for the AE3007 bearing chamber geometry

6.2.5 AE3007 bearing chamber reference orientation

The orientation used here, as in Chandra *et al.* [2] and Tkaczyk & Morvan [55], to refer to the bearing chamber wall locations follows as shown in Figure 6.13. The shaft speed is clockwise and 3 o'clock is the reference angle zero. The angular positions are taken in a counter-clockwise orientation. Angles 330^o, 0^o, 30^o and 60^o, respectively, fall on the "right side" while angles 120^o, 150^o, 180^o and 210^o fall on the "left side" of the chamber. The axial positions, $Z^* = Z/Z_w$, of the chamber is from -0.5 to 0.5 such that the "middle" of the chamber falls on $Z^* = 0$, where Z_w is the width of the chamber.

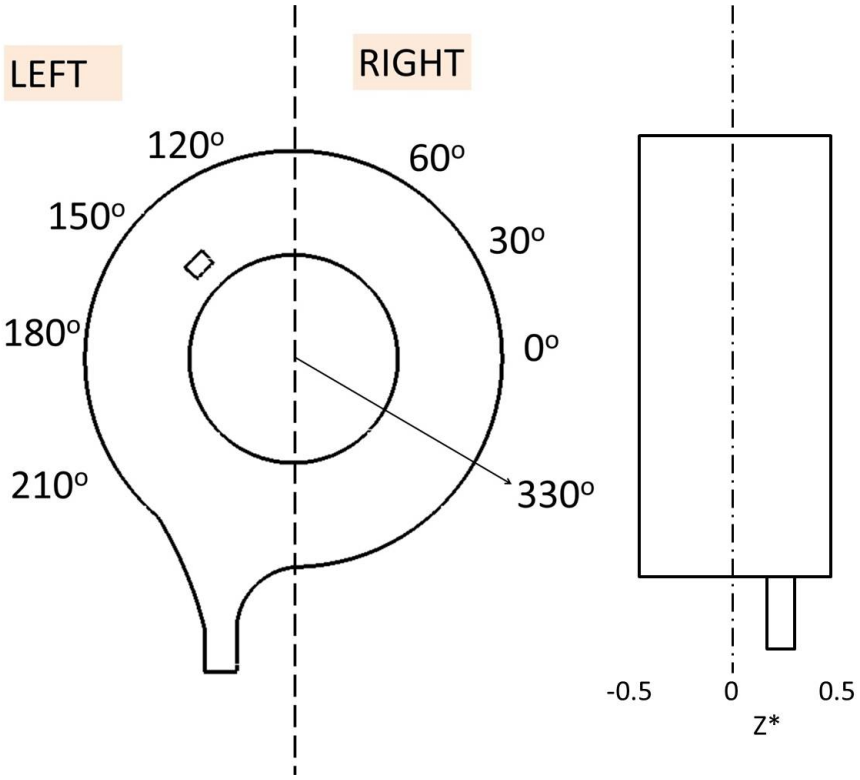

Figure 6.13: AE3007 bearing chamber reference orientation

6.2.6 The Solution method

The boundary conditions, solution method and convergence criteria are set in ANSYS-Fluent. The solution method builds on the existing solution strategy for a bearing chamber [55]. The $\kappa - \omega\,(SST)$ turbulence model [§3.3.3] is used. The Volume of Fluid (VoF) method is used as the multiphase model. The time step is of the order of $1\mu s$ to ensure the CFL [§3.5.1] is maintained below 1. The convergence criteria for all the equations is 10^{-4} or lower for the iteration residuals.

The developed method was implemented using user defined functions (UDF[4]) imple-

[4] *see Appendix* §A.2 - §A.1 for the codes.

mented in ANSYS-Fluent version 14.5 [69]. The UDFs codes are compiled, loaded and implemented based on the algorithm described in §4.7. The simulations were carried out with computational nodes of the order of 1 million. The S^* are in the range 1.6 to 2.2 for the cases. The parallel solver on the University of Nottingham HPC [147] with 24 cores per simulation used. The run time is approximately $30ms$ of the flow per week (of computation), involving up to $120,000$ droplets at a time.

6.2.7 CASE 1: Results and Discussions

Results of the application of the model to the selected bearing chamber are presented here for film formation, film thickness and heat transfer coefficient at the bearing walls for the $10,000$ and $15,000RPM$ shaft speeds setup for comparison against Chandra *et al* [2].

6.2.7.1 Droplets loading pattern

There are a total of 36 "injection" locations on the RID. An instantaneous full droplet loading in the chamber is shown in Figure 6.14 consisting of about $120,000$ droplets.

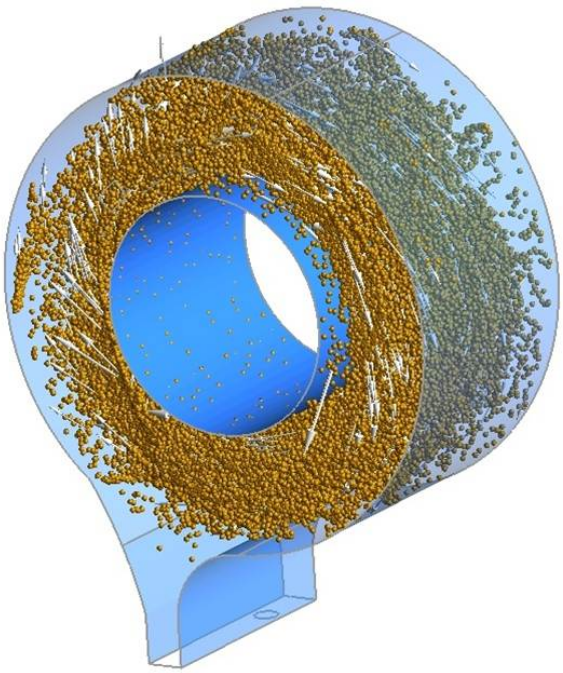

Figure 6.14: An instantaneous loading of droplets in the chamber

Figures 6.15a to 6.15d show an instantaneous droplets' pattern from four randomly selected holes/injectors at $10,000$ rpm. The concentric circles represent the shaft and the outer bearing wall. The small circles represent the droplets' positions. The solid blue droplets, in each of the figures, close to the shaft region are the droplets injected that instance. The red solid droplets (close to the outer bearing walls) have stayed the longest time in the chamber at the instance. The 3D windage (or air motion) affects the pattern of the droplets stochastically. The patterns can be seen to be a roughly spiral following behind the high speed shaft.

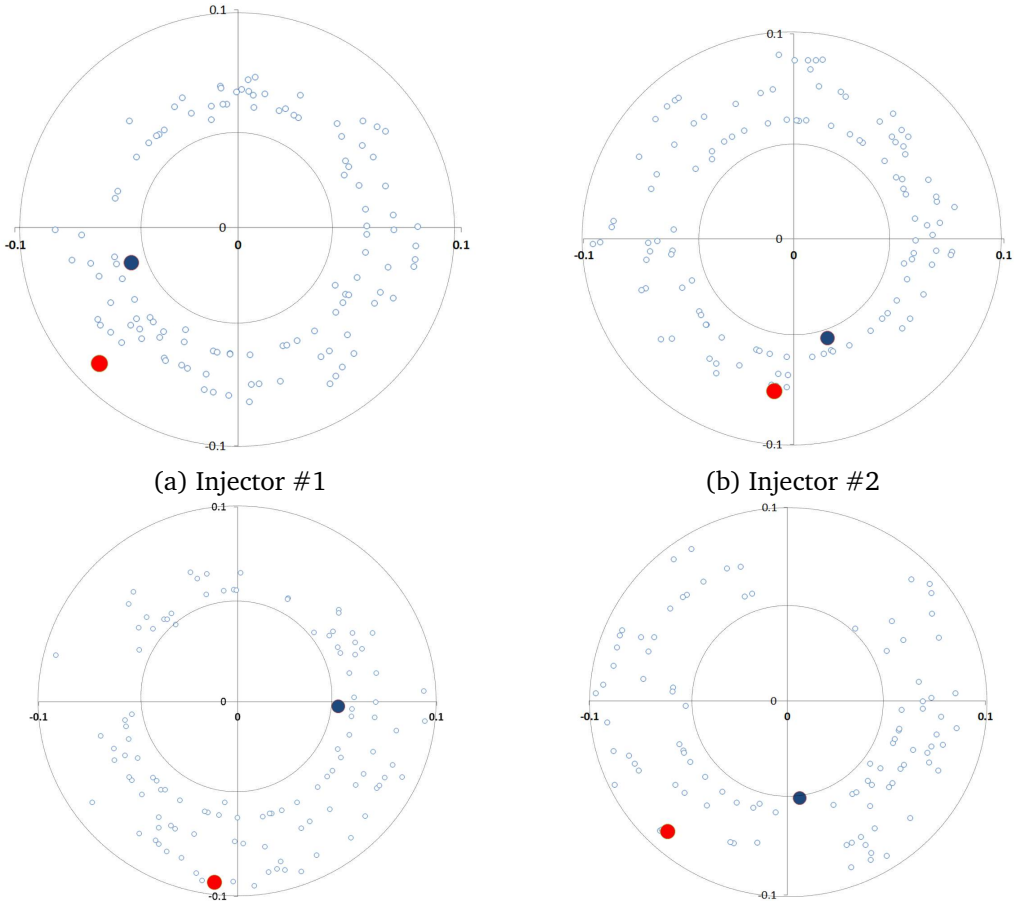

(a) Injector #1 (b) Injector #2

(c) Injector #3 (d) Injector #4

Figure 6.15: Droplets emanating from four random holes of the RID

6.2.7.2 Qualitative chamber film formation

The simulations start by running air only (single phase) for some time to ensure stability of the solution. The pump model is then initialised with water similar to what would happen when an engine is started from rest. At about $5ms$ in Figure 6.16, the arrow shows the initialised water level in the sump area of the initially dry chamber. The pump part is filled with the liquid phase below the indicated level; the isosurface shows the liquid-gas free-surface.

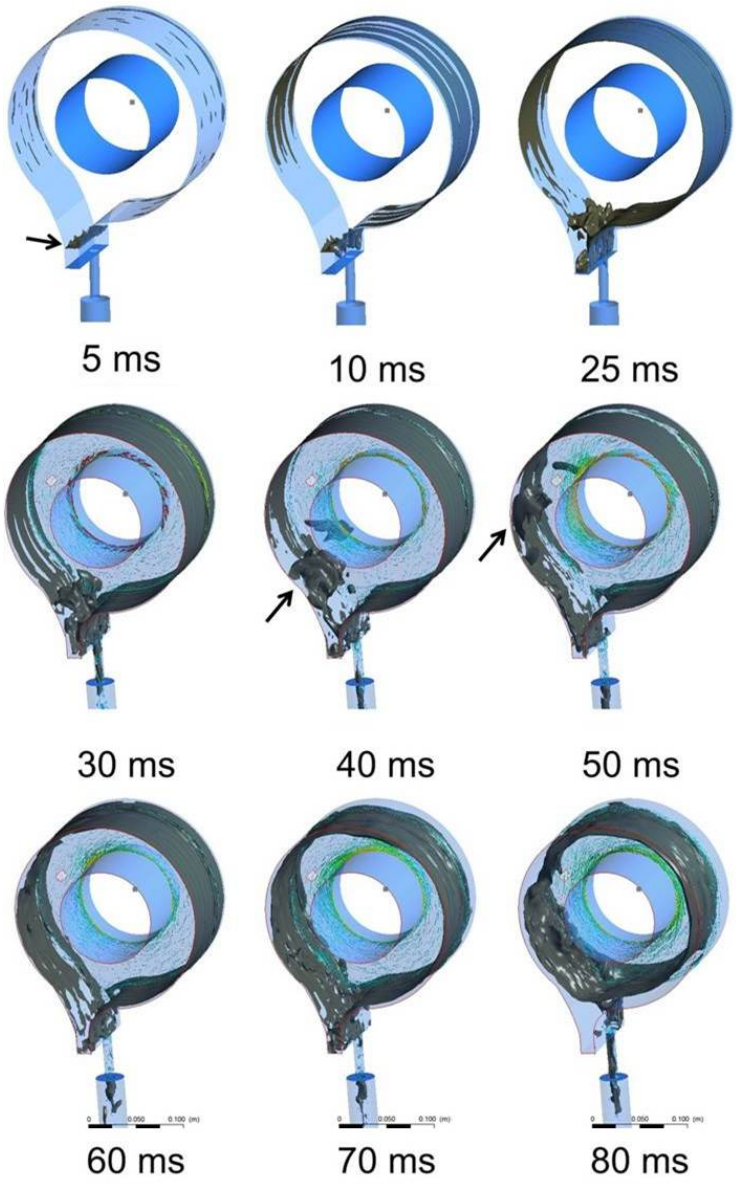

Figure 6.16: Transient formation of film at a shaft speed of $10,000RPM$, inflow rate of $12l/min$, scavenge ratio of 4, 0.2 volume fraction isosurface

The VoF film that is formed on the bearing chamber outer wall is the result of the DPM collection into the VoF model. The film grows and plunges into the sump creating a bulk splash that is noticed after $25ms$. This bulk of film travels along the bearing walls in the windage direction and evens out with the wall film. The offtake pipe can be seen

to be injesting some air as expected. This is indicated by the presence of the isosurface in the offtake and pump regions from $30ms$ of the flow. It should be noted that the droplets (DPM) are not shown in Figure 6.16, only the continuous phases have been shown; the droplet loading has been previously shown in Figure 6.14.

The film distribution is clearly a three dimensional problem. Figure 6.17 shows a cutaway view of the $10,000RPM$ shaft speed at a flow rate of $12l/min$. It shows qualitatively the film surface wave pattern inside the bearing chamber. There is a pooling of the film in the sump region similar to experimental observations in Chandra *et al*. [2]. The rotation and sloshing of the film at the walls makes it look thicker at the walls. The sloshing is, although, less pronounced for the $15,000RPM$ shaft speed. The film can be seen to be occasionally reaching back to the shaft region as a result of the sloshing. The oblique cutaway view at $140 - 144ms$ in Figure 6.17 shows that the film can look very thick at the walls but towards the middle of the chamber, the wall film is thin. The film on the bearing walls is more uniformly distributed in the $15,000RPM$ case as seen in Figure 6.18 but thinner than the $10,000RPM$ shaft speeds.

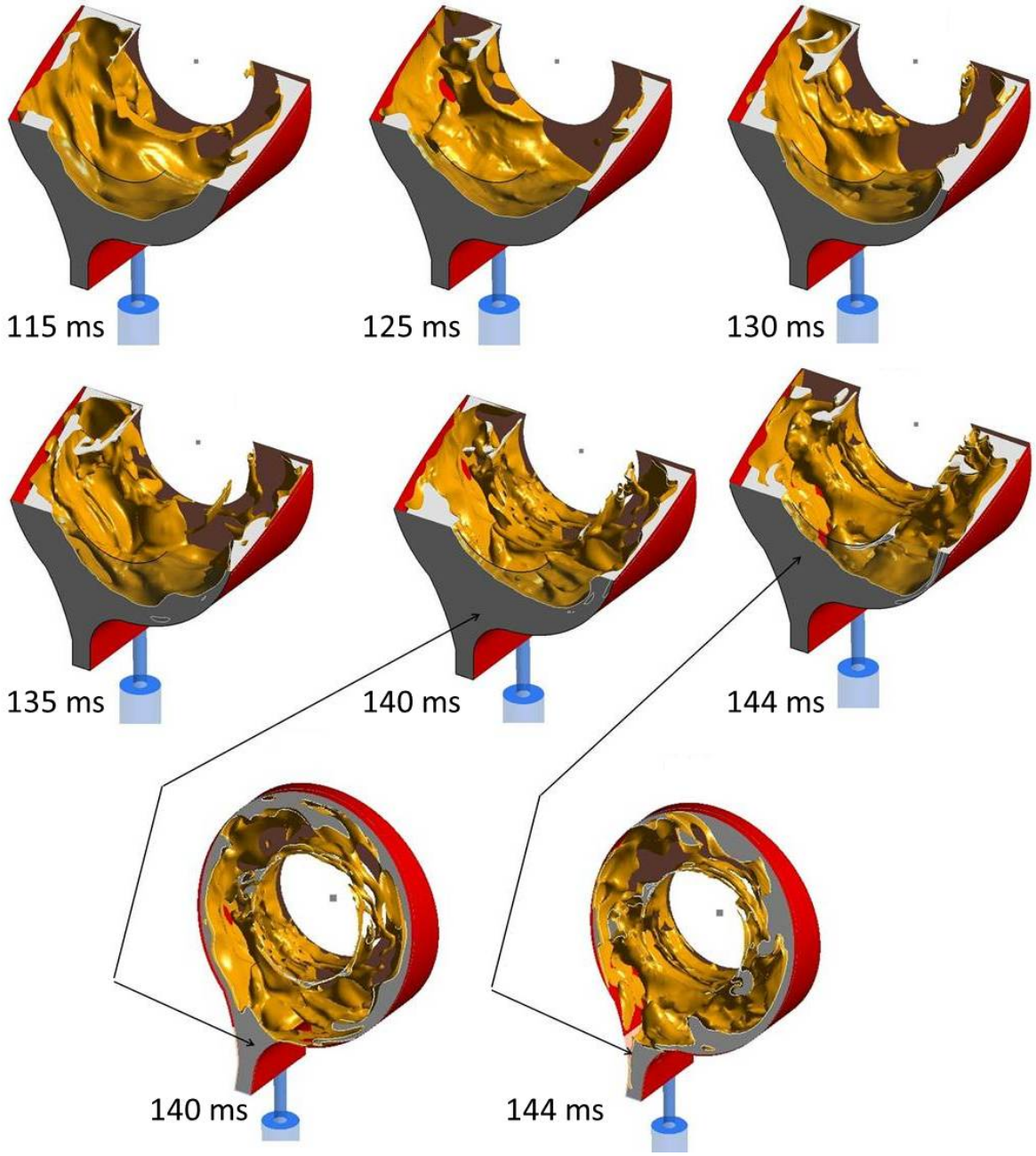

Figure 6.17: Sectional view of the sump region showing 3D pooling for the $10,000RPM$ shaft speed, inflow rate of $12l/min$, scavenge ratio of 4.0 and 0.2 isosurface

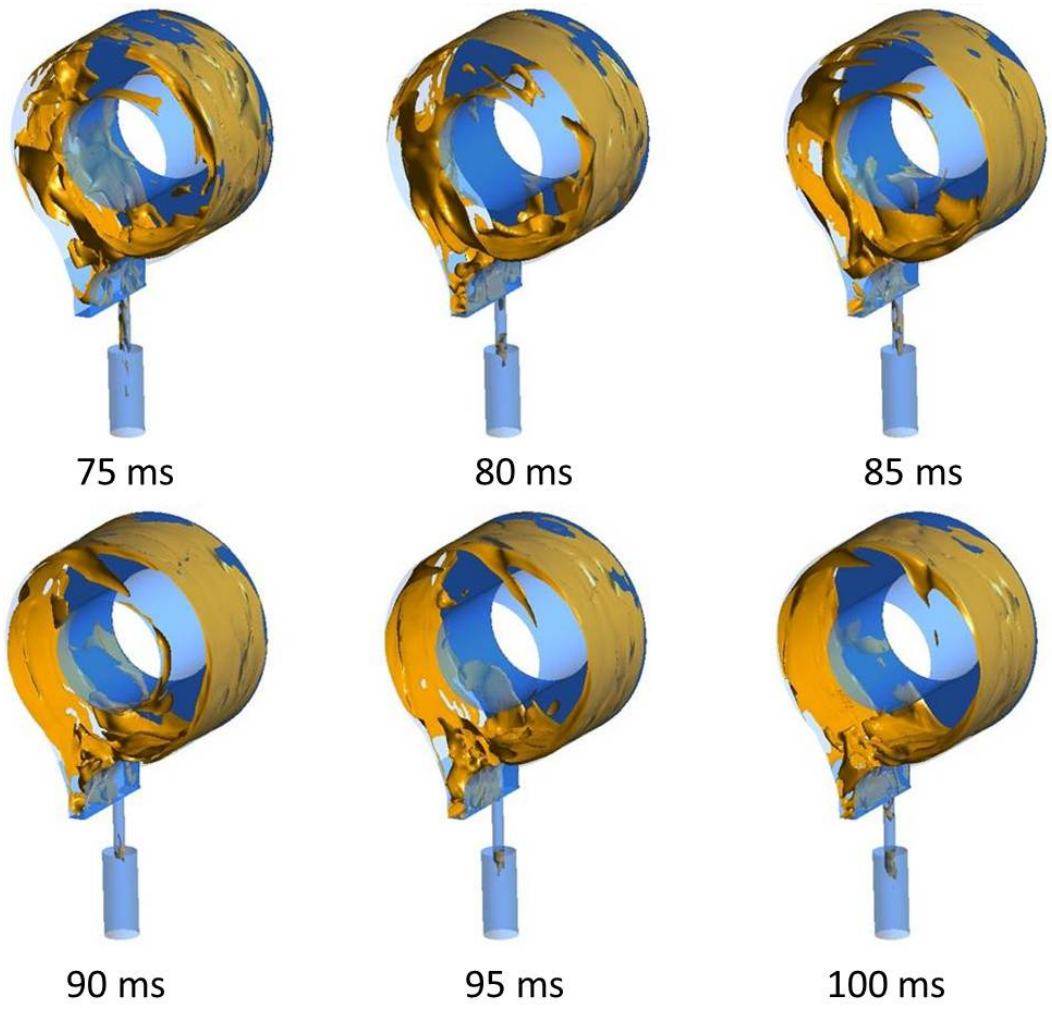

Figure 6.18: Transient formation of film at a shaft speed of $15,000RPM$, inflow rate of $16l/min$, scavenge ratio of 2, and 0.2 volume fraction isosurface

6.2.7.3 Film thickness measurement

The film thickness measurements are taken on a plane across the chamber width at the angular locations described in §6.2.5. The film thickness fluctuates over any given measurement plane. The measurement of the relative film thickness[5], H^*, is taken between

[5]Film thickness, H_{film} , is normalised with the bearing chamber radius, R_b, as done in Chandra *et al.* [140] such that $\left(H^* = \frac{1}{R_b} H_{film}\right)$

-0.45 and 0.45 on the Z^* plane [*see Fig.* 6.13]. This represents a 90% coverage of the chamber width, Z_w. A time averaged film thickness, H^*, against the angular positions are shown in Figure 6.19 for the DPM-VoF computations for the cases given in Table 6.2.

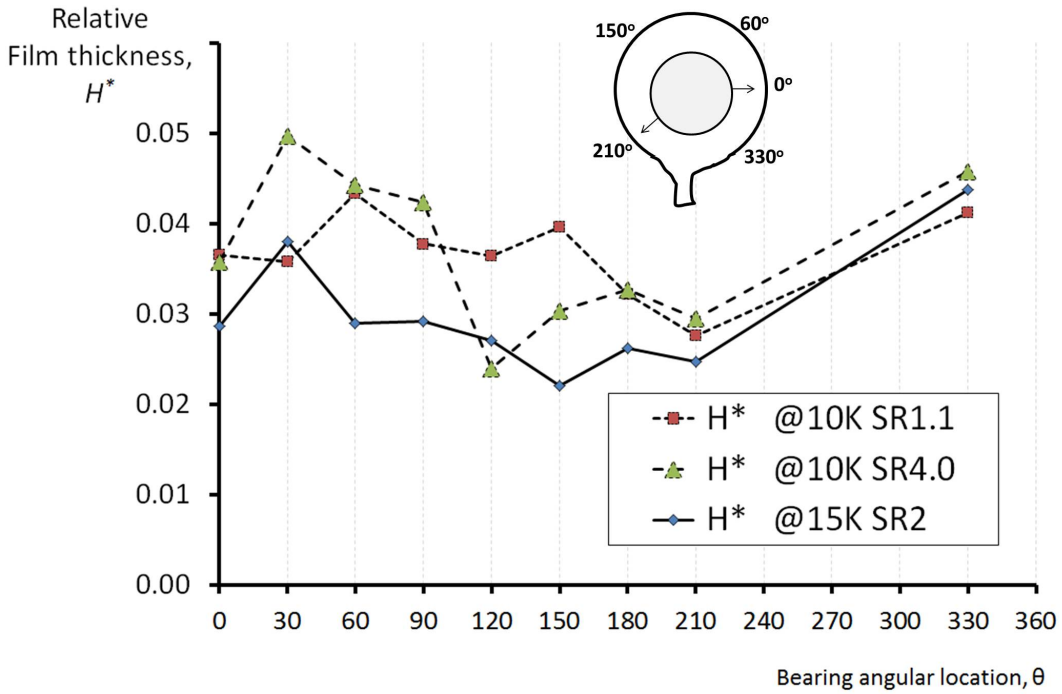

Figure 6.19: Average wall film thickness at angular positions

The fluctuations of the time averaged film thickness about the mean is about ± 0.0005. It is clear that film is relatively thinner for the $15,000 RPM$ shaft overall, as expected. The film thickness pattern is similar for the $10,000 RPM$ shaft speeds. The "right side" (*or gravity side*) of the bearing is generally thicker than the "left side" of the bearing too. There is no strong link of the scavenge ratio variation on the film thickness.

The experimental, relative film thickness, measurements in Chandra *et al.* [2] gave a mean value of $H^* = 0.0030 \pm 0.0007$. The trends and pattern of the film thickness observed in the simulations are similar to the experiments of Chandra *et al.* [1, 2] but the

thickness is being over predicted by the simulation. This may be caused by the uncertainty of the droplet sizes as used in the RID boundary condition for this bearing chamber. There has not been any measurement of the droplet size or distribution for this chamber setup with the RID. The guessed mean droplet diameter values have been chosen to be close the diameters of the holes of the RID. An experimental investigation of the droplet breakup from the RID will therefore form a good dataset. This motivates the simulations in section §6.3 which uses measurements from experimental measurements of droplet sizes.

6.2.7.4 Heat Transfer Coefficient

For the constant wall temperature, T_w, boundary condition specified, the local heat transfer coefficient, h_t, is calculated by solving Equation[6] (5.8).

The heat transfer coefficient calculated at the walls (in ANSYS CFD Post) of the bearing chamber is shown at randomly selected times in Figure 6.20. The heat transfer coefficient is generally higher towards the top region of the chamber. The variation of heat transfer coefficient on the bearing chamber wall surface is as a result of the transient film thickness variation on the wall as the film rotates with the shaft speed. The variation in magnitude of the heat transfer coefficient on the surface is large and also transient. This variation is captured with the error bars in the time averaged result of the surface average heat transfer coefficients in Figure 6.21.

[6] Equation (5.8) is $q = h_t \cdot (T_w - T_{sf})$
where T_{sf} is the local fluid temperature in the first cell next to the bearing chamber wall.

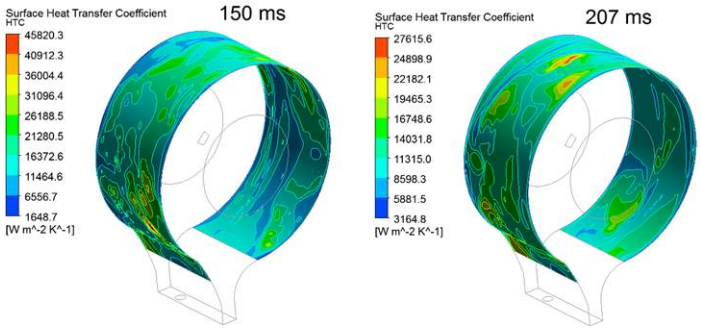

(a) $10,000RPM$ @SR1.1

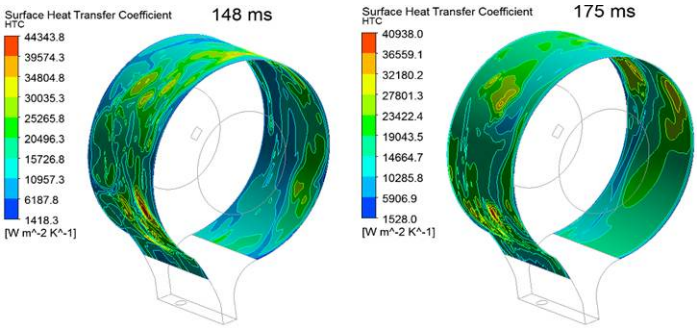

(b) $10,000RPM$ @SR4.0

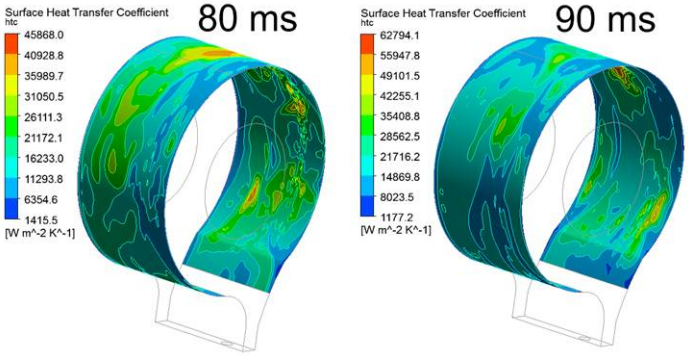

(c) $15,000RPM$ @SR4.0

Figure 6.20: Surface heat transfer coefficient on the bearing walls.

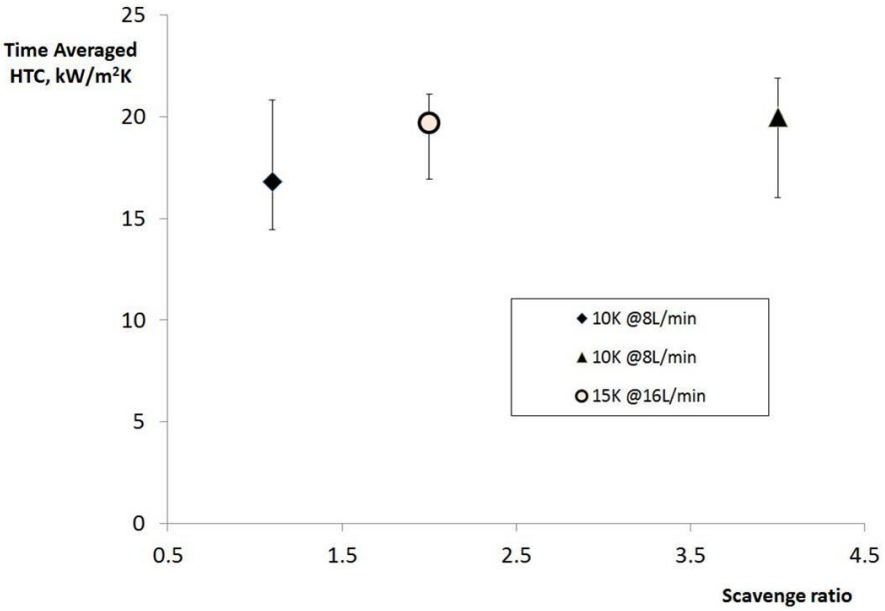

Figure 6.21: Time averaged heat transfer coefficient

The time averaged heat transfer coefficient on the bearing walls is given in Figure 6.21. The average heat transfer coefficient is similar for the $15,000RPM$, $16l/min$, SR 2.0 and $10,000RPM$, $8l/min$, SR 4.0. The gaps in the averages of the heat transfer coefficient is as a result of the fluctuating wall film thickness since local film temperatures will vary with film thickness.

6.3 CASE 2: The KIT Bearing Chamber

This section presents the application and results of the proposed DPM-VoF method to the bearing chamber experiments of Gorse *et al.* [3]. The roller bearings generate the oil droplets from the lubricant supply. Table 6.3 gives the properties of the fluid used in the simulation. The characteristic of the droplets were measured in the experiment of Glahn

et al. [16, 144].

Table 6.3: Oil[a] and air properties for simulation

Description	Values
Density (oil) $[kg/m^3]$	929.5
(air)$[kg/m^3]$	1.24
Dynamic viscosity (oil)$[kg/ms]$	4.83×10^{-3}
(air)$[kg/ms]$	0.0221×10^{-3}
Surface tension $[mN/m]$	24.5

[a]Mobil Oil II [97]

Figure 6.22 shows the experimental rig. It is showing a co-axial sectional view. The oil droplets from the bearings go into both the vented chamber I and II. The simulation reported here applies to Chamber I.

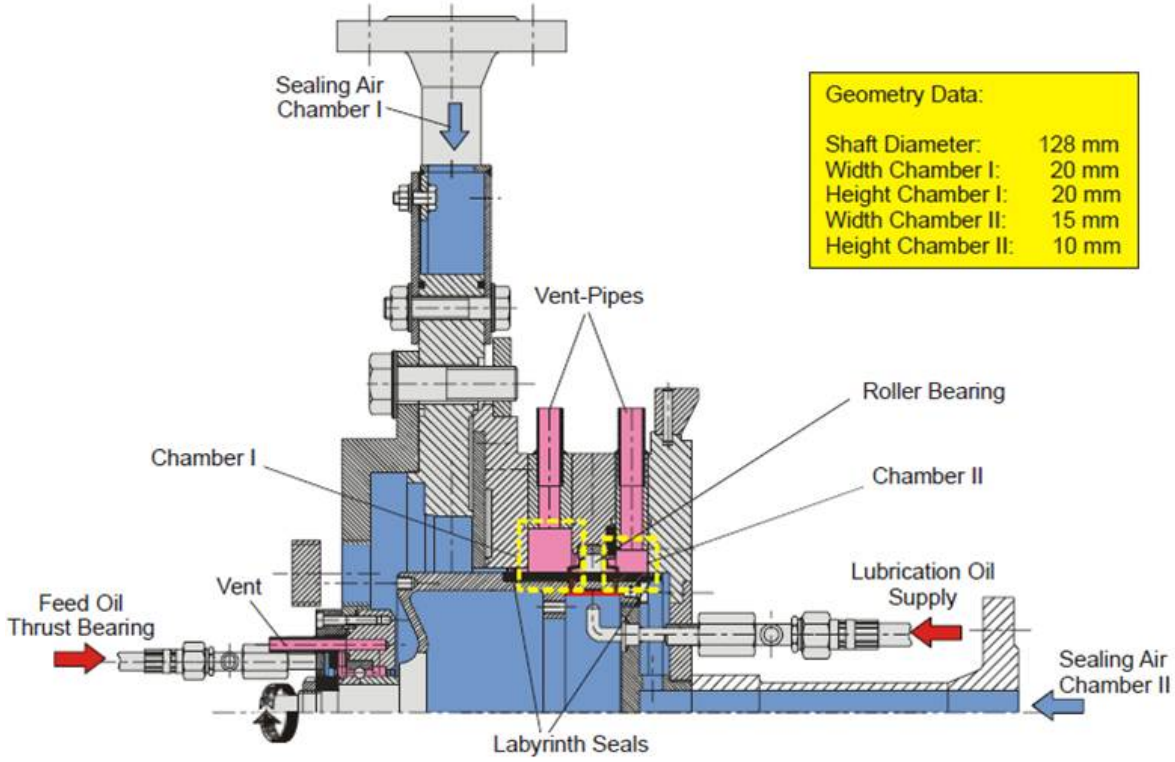

Figure 6.22: The KIT Bearing Chamber Test rig [3]

6.3.1 The KIT Bearing Chamber Geometry

The chamber is simplified to Figure 6.23 for the CFD simulations. The shaft diameter is $128mm$. The width and height of this chamber are, respectively, 15 and $10mm$. The labyrinth seals are $2.5mm$ wide. The diameters of the top and bottom vents are both $10mm$. The vents are aligned axially in the middle. The vent pipes are $15mm$ long and extend to the atmosphere.

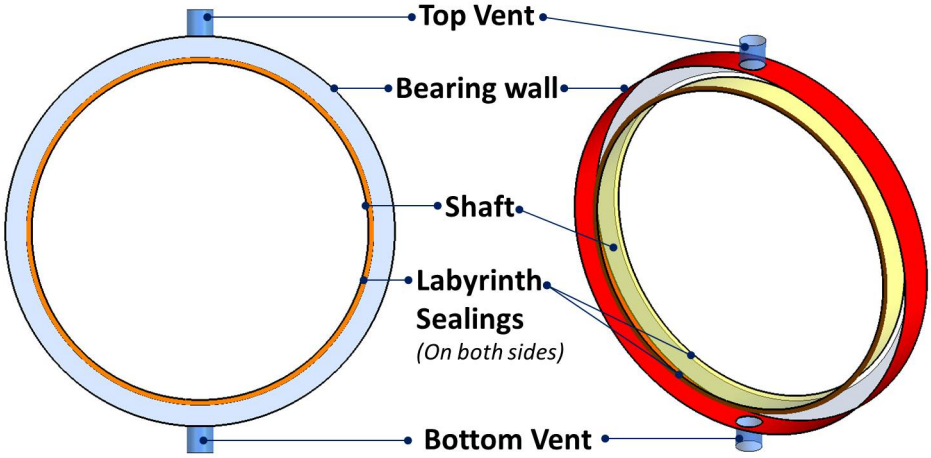

Figure 6.23: The KIT Chamber I - Schematic

6.3.2 KIT Mesh

Figure 6.24 shows the structured/hexahedral mesh used. It consists of about 1.2 million cells. This builds on the suggested mesh requirements at the walls [§5] for film and the mesh dependence studies by Sonner *et al.* [145]; such that y^+ satisfies $y^+ < 30$ and the near wall mesh blocking has a minimum of 10 vertices. The $S^*$are between 1.9 and 2.1.

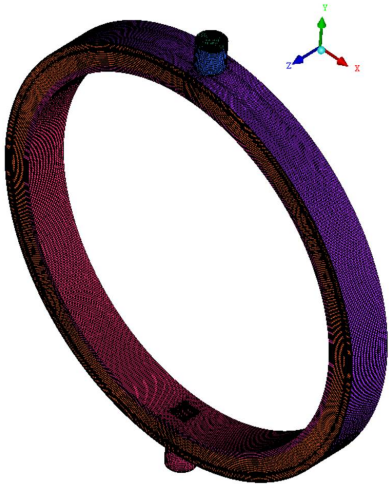

Figure 6.24: The KIT Bearing Chamber Mesh

These conditions ensures film resolution and good heat transfer capture. The cylindrical shapes require using the O-grid technique [146]. The Hexa-blocking strategy for the mesh is given in Figure 6.25. O-grid can be seen in the pipes. The solid shaft O-ring is subtracted to get the cylindrical orientation shown.

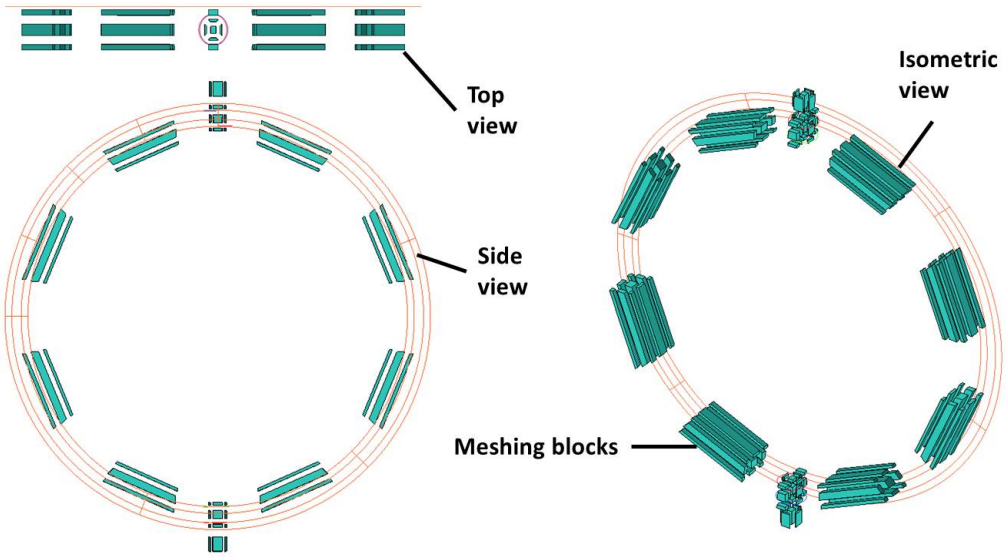

Figure 6.25: The KIT Chamber Hexa-blocking

6.3.3 Boundary conditions

In all the cases, the mass flow rate of air into the chamber through the labyrinth seals is $5g/s$. The droplets with a mean diameter, $\bar{D}_p$, are injected as Lagrangian/DPM particles at radial locations $R_s + 5 \times \bar{D}_p$ from the center of shaft with radius R_s. The injection follows the rotating RID technique earlier described [§6.2.1.3]. The mean droplet sizes given in Table 6.4 are based on the experiments of Glahn *et al.* [16]. The measured diameters range from about 50 to $500\mu m$. The RID injection positions move with the shaft speed and time as given in the developed UDF.

The injection file [*see* §4.7.0.1] is created for each case to match the flow rates. The vents are open to the atmosphere. The shaft temperature is taken to be the same as those of the droplets.

Table 6.4: RID Boundary Condition for the KIT Configuration

CASE Ref.	Shaft speed (RPM)	Oil flow rate (L/hr)	$\bar{D}_p\ \mu m$	Oil droplets speed (m/s)	DPM Frequency (kHz)[a]
N16Q150	$16,000$	150	180	12.04	13
N16Q100	$16,000$	100	150	12.04	16
N16Q050	$16,000$	50	150	14.04	19
N08Q100	$8,000$	100	180	7.16	8
N04Q100	$4,000$	100	200	4.27	4

[a]This is the frequency of injection of the DPM particles into the domain.

The no-slip stationary walls of the chamber are initially dry and at $433K$. The droplets are injected at a temperature of $373K$ and run until steady results are reached. The thermal values are arbitrary but are used to demonstrate and study heat transfer effects not done in the experiment of Gorse *et al.* [3]. Table 6.4 gives the cases simulated for this

chamber configuration.

6.3.4 The bearing chamber reference/notation

To refer to the measurements made in the bearing chamber, the geometric orientation follows from Figure 6.26. The shaft rotates clockwise and 6 o'clock is the reference angle zero.

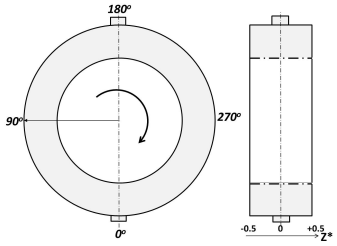

Figure 6.26: KIT bearing chamber reference orientation

The angular positions are taken in a clockwise orientation. Angles, ϕ, between 0^o and 180^o are on the "left side" of the bearing chamber. Angles between 180^o and 360^o fall on the "right side" while angles 0^o and 180^o are, respectively, at the bottom and top vents. The axial positions, $Z^* = Z/Z_w$, of the chamber is from -0.5 to 0.5 such that the "middle" of the chamber falls on $Z^* = 0$, where Z_w is the width of the chamber.

6.3.5 CASE 2: Results and Discussions

The results presented are for the film thickness measurements for the different shaft speeds and oil flow rates. The average film velocities, temperatures and heat transfer coefficients at the bearing walls are also presented.

(a) An instantaneous droplet loading

(b) Wall film: $4,000RPM$, @ $100l/hr$

(c) Wall film: $8,000RPM$, @ $100l/hr$

(d) Wall film: $16,000RPM$, @ $50l/hr$

(e) Wall film: $16,000RPM$, @ $100l/hr$

(f) Wall film: $16,000RPM$, @ $150l/hr$

Figure 6.27: KIT bearing chamber droplet-film formation

6.3.5.1 Film formation

An instantaneous droplet loading in the domain is shown in Figure 6.27a. There are about $25,000$-$40,000$ droplets in the domain in an instance. The droplets form the films qualitatively shown in Figures 6.27b to 6.27f. Parametric analyses of the film for the different setup are given in the next section [§6.3.5.2].

6.3.5.2 Film thickness measurements

The film thickness predictions from the DPM-VoF model application to the KIT bearing chamber are plotted along the bearing chamber walls and compared with the experiment of Gorse *et al.* [3] in Figures 6.28 & 6.29.

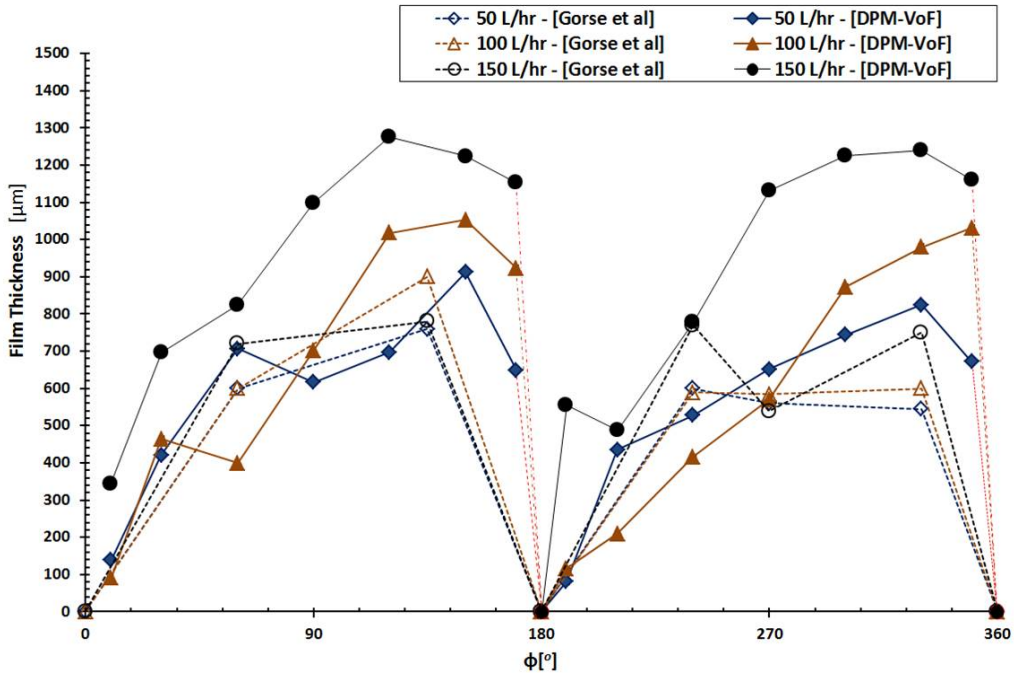

Figure 6.28: Effect of flow rate on film thickness (16,000 RPM)

There are vents at positions 0, 180 and 360^o; the vent position 360^o is the same as 0^o. There are no measurements at these exact positions, the values are only taken as zero at the vents. The solid lines and solid markers are the results from the simulation. The equivalent dashed lines and the hollow markers are of the experiment.

Figure 6.28 shows the effect of flow rate on film thickness. The film thickess generally increases with the flow rate in the bearing chamber. As in the experiment, the film thickness measurements are below $1,500\mu m$. Hydraulic jump can be noticed before the film reaches the vents. The film exits both vents and the thickness is highest before the exits, in the $90 - 180^o$ & $270 - 360^o$ quadrants of the chamber.

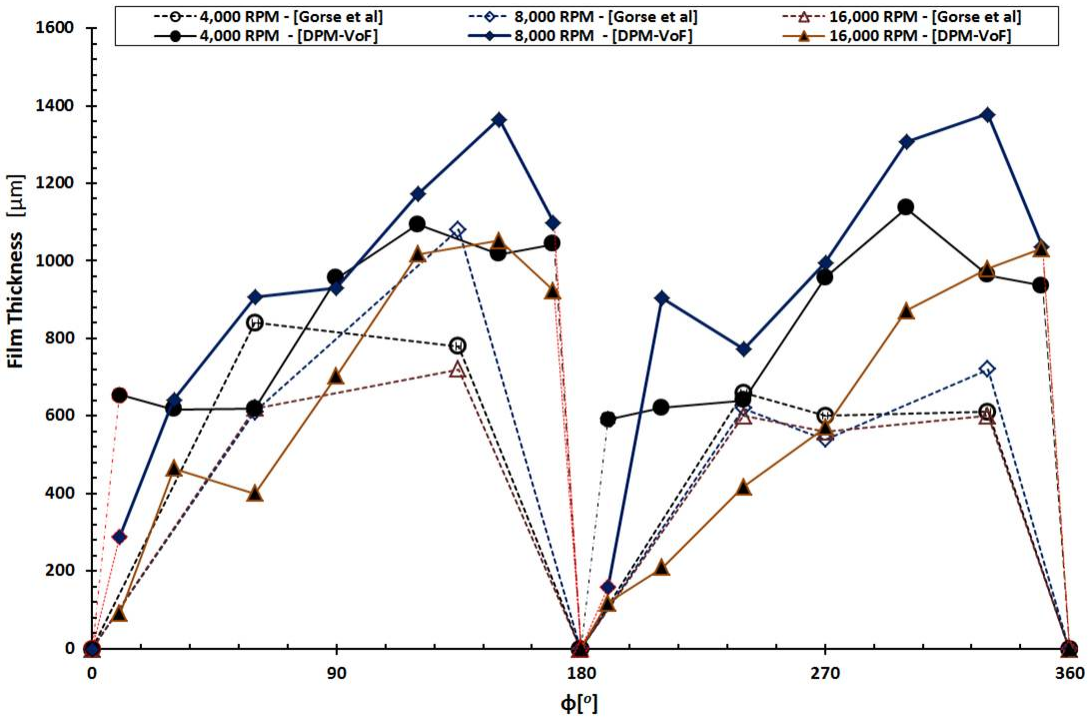

Figure 6.29: Effect of shaft speed on film thickness (100 l/hr)

Figure 6.29 shows the effect of shaft speed at the same flow rate on film thickness at

oil flow rate of 100 l/hr. The film thickness at $16,000RPM$ and $150l/hr$ are similar to the thickness at $4,000RPM$ and $100l/hr$.

Film pooling before the vents occurs at all the shaft speeds. The effect of gravity is pronounced even at $16,000RPM$; the film is thinner in the top right corner of the chamber before getting thicker at bottom vent exit. The results also show that the film thickness is not symmetric about the center of the chamber. Over-prediction of twice in magnitudes can be seen close to the vents. However, the results are generally comparable with the experiment of Gorse *et al*. [3] with about 8.7% over-prediction in the mean film thickness.

6.3.5.3 Average film temperature

For easy reading of Figures 6.30, 6.31 and 6.33, the case name convention are such that the shaft RPM and the flow rates are given; for example, "N04Q100" means 4,000 RPM at 100 litre/hour oil flow rate. Note also the arrangement in increasing orders of shaft speed and by flow rates.

The average film temperatures in the bearing chamber from the computational model are shown in Figure 6.30. The wall temperature is at $433K$ and the liquid temperature is $373K$. The $50l/hr$, increased the highest, at 1.9% rise in the cooling liquid temperature. The lowest temperature rise of 0.05% is at $4,000RPM$. The liquid temperature rose 0.2% and 0.6%, respectively at $8,000RPM$ and $16,000RPM$ at a flow rate of $100l/hr$. The temperature rise of the liquid is 0.4% at $16,000RPM$ at a flow rate of $150l/hr$.

It can be seen that the highest film temperature was obtained at the lowest flow rate,

$50l/hr$. At a fixed flow rate the film temperature increases with an increasing shaft speed. At a fixed shaft speed, the film temperature reduces with an increasing flow rate.

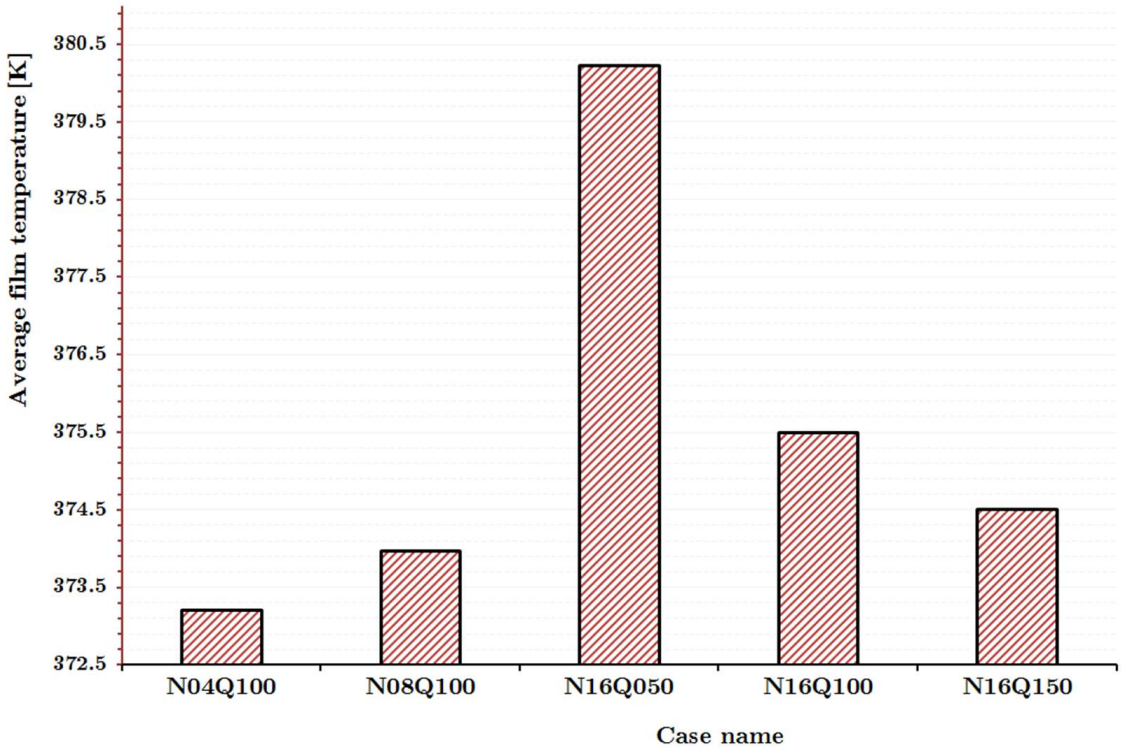

Figure 6.30: Average film temperature

The average film velocities are shown in Figure 6.31. The film velocities increase with the shaft speed and the volumetric flow rates and consequently have effect on the wall heat transfer coefficient.

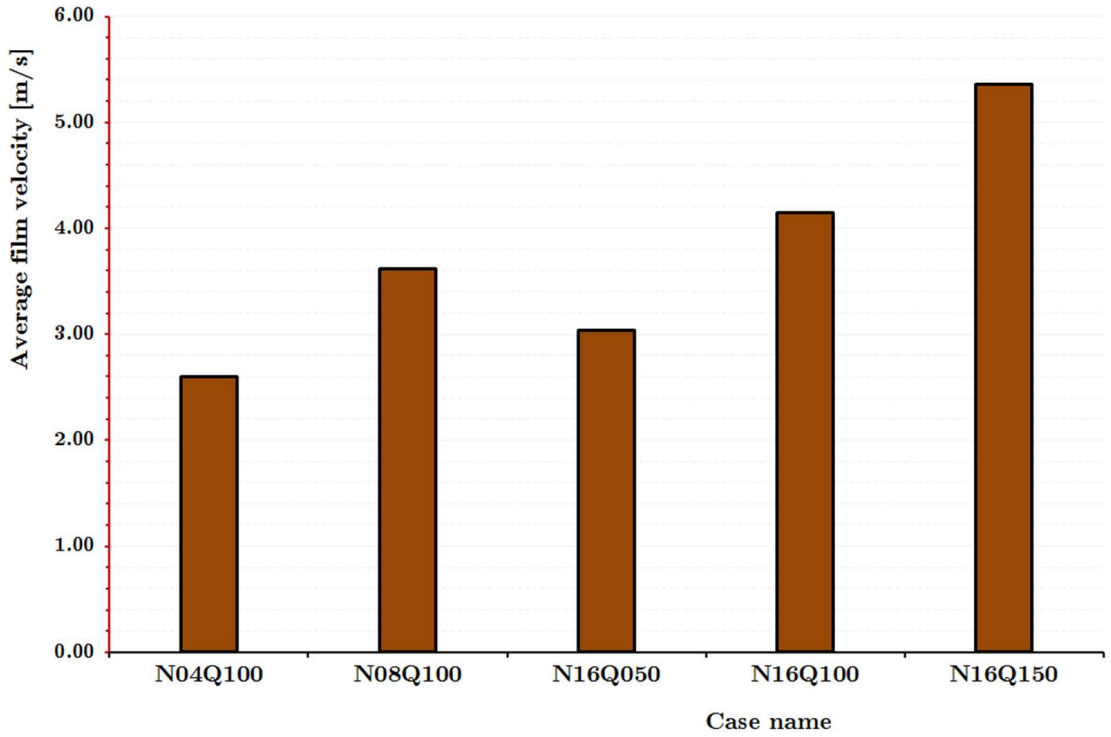

Figure 6.31: Average film velocity

6.3.5.4 Average wall heat transfer coefficient

The surface heat transfer coefficient [*see* §6.2.7.4] distribution on the bearing wall for the different cases are shown in Figures 6.32a-6.32e. The region of low heat transfer coefficients have thinner film coverage. The distribution of the heat transfer coefficient, as seen in the contours, is well spread across the bearing surface. The time averaged values of the surface average heat transfer coefficient (HTC) at the bearing wall for the different cases are shown in Figure 6.33. The wall heat transfer coefficient reduces with an increasing shaft speed at the same flow rate. For a fixed shaft speed, the heat transfer coefficient increase with the flow rate.

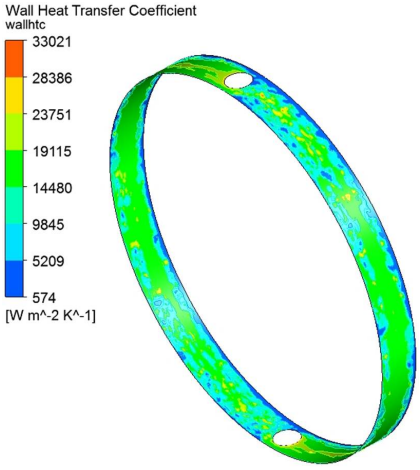

(a) HTC: $16,000RPM$ @ $50l/hr$

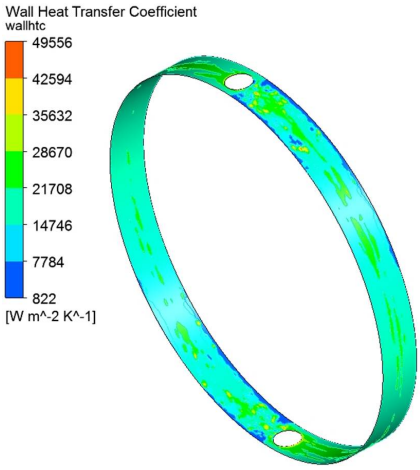

(b) HTC: $16,000RPM$ @ $100l/hr$

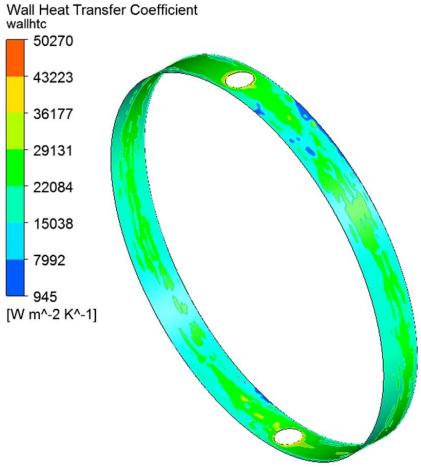

(c) HTC: $16,000RPM$ @ $50l/hr$

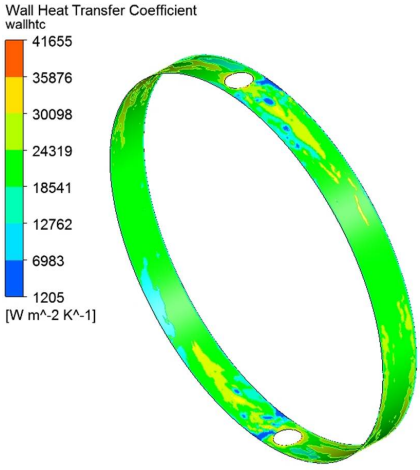

(d) HTC: $8,000RPM$ @ $100l/hr$

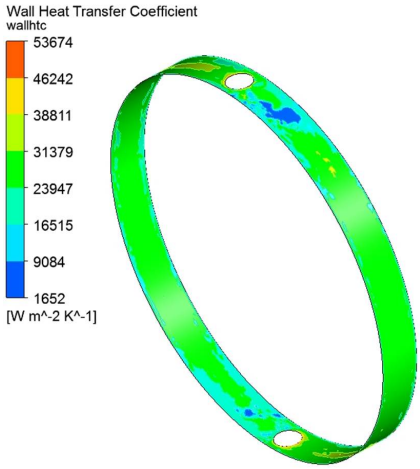

(e) HTC: $4,000RPM$ @ $100l/hr$

Figure 6.32: KIT bearing chamber wall heat transfer coefficient

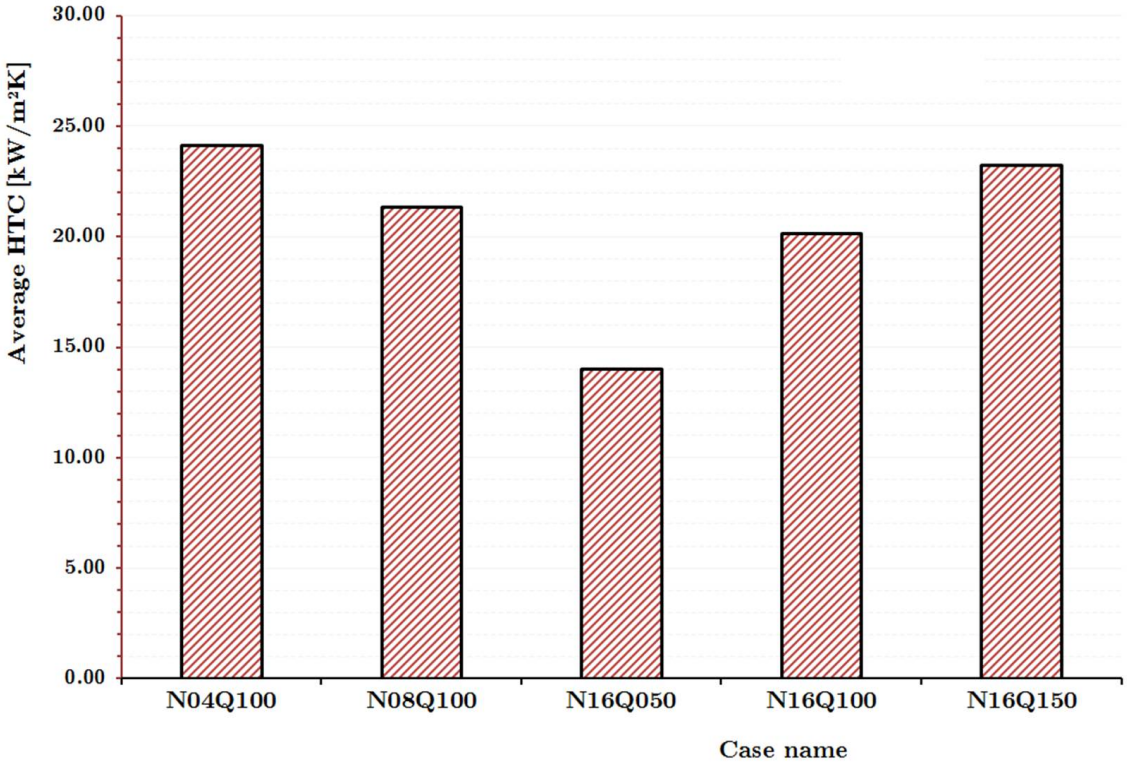

Figure 6.33: Average wall heat transfer coefficient

From these simulations, it can be seen that a higher flow rate is desirable for better heat transfer at high shaft speeds. Since shaft speeds depend on the engine operating conditions and higher lubricant pumping rate has a negative signature on the overall efficiency of the engine, there is a need for an optimal analysis for selecting the appropriate flow rate to match an engine speed. Comparing the flow rate at $150l/hr$ with that at $100l/hr$ (33% flow rate reduction) and at $50l/hr$ (67% flow rate reduction), the heat transfer coefficients reduced, respectively, by about 13% and 40%; the film temperatures consequently increased, respectively, by about $1K$ and $6K$.

6.4 Summary

In this chapter, the validated DPM-VoF methodology was applied [*see* §5] to the flow in two different aeroengine bearing chamber rigs. The Nottingham UTC experimental rig uses water and air as the working fluids and is operated at atmospheric conditions. In the test rig investigating a chamber geometry relevant to the AE3007 aeroengine the rig simulates the droplet breakup from the roller bearings by using the Rotating Inlet Distributor (RID). The chamber has a curved wall deep sump design for the collection of the lubricant. The KIT bearing chamber has oil-lubricated roller bearings that breakup the lubricant continuum to droplets and other forms before entering the bearing chamber areas. The chamber flow is complex to model because of the combined interactions, and the mathematical representation of the present multiphase fluids.

The simulations were carried out using 24 cores per simulation on the University of Nottingham HPC at an average rate of about $30ms$ per week and may involve up to 100 thousand droplets at a time. This is still a significant computational time, however, for this order of simulation, it is a significant progress compared to a computing approach where individual droplets are fully resolved using a VoF approach. The overall massflow and energy imbalances were not monitored in the simulations.

For the first bearing chamber case (AE3007 geometry), the diameters of the droplets released from RID were not measured in the experiment. The values used were taken to be similar in magnitudes with the hole diameter. The film thickness pattern in the bearing is similar for the shaft speeds and delivery volume rates investigated. The film is thicker as

it approaches the scavenge compared to after the scavenge. The film thickness is similar for the same flow rate even at different scavenge ratios. Pooling was observed in the sump regions. The film thickness computed were ten times out in magnitude compared with the experimental measurements. The droplet diameters used in the simulation of the second bearing chamber (KIT geometry) are employed from the experimental observation of the same chamber from an earlier experiment. In this test and at locations close to the vents, the film thickness were over-predicted in magnitudes twice the experimental values. The mean film thickness values are over by around 8.7%; the many uncertainties in the choice of boundary conditions for the RID model as the droplet diameters is thought to be responsible for these.

A parametric study of the flow shows that the film thickness increases with the flow rate. The film thickness increases with reducing shaft speed for same flow rate. The film thickness increases as the film approaches the top and bottom vents. Although the experiment was done isothermal, the thermal boundary conditions given in the simulations show that average film temperature increases with reducing flow rate and increases with shaft speed. The heat transfer coefficient results show that higher flow rates provide better heat transfer at higher shaft speeds. The simulations show that reducing flow rates by 33% and 67% resulted respectively in 13% and 40% reductions in heat transfer coefficients and amounted to average film temperature rise of $1K$ and $6K$.

It is clear that the developed DPM-VoF methodology provides a method for meaningful computations to be carried out on bearing chamber geometries. With good boundary condition data representative results can be obtained providing insight beyond what can

readily be experimentally measured/observed. This approach provides engine designers with a computational design tool that will yield useful data in a timeframe perhaps longer than desired but not inconsistent with engine design timeframes.

Chapter 7

Conclusion

7.1 Main Achievements

In this thesis, a framework was developed for modelling of droplet to film interaction. The focus applications are such as those involving multiple droplets and a continuum of film and gas in a turbulent environment. There are no comprehensive or practical models that can handle this class of multiphase flows in the open literature. An overview of literature in Chapter 2 reveals that the modelling challenge comes majorly from the mathematical representation of the interacting fluids. A close up look at the fluids shows an interaction of gas and liquid; however, it will immediately be clear that the liquid phase presents itself in two forms; as droplets and a continuum of film or ligaments. The problem is further complicated with heat transfer phenomena. In the Finite Volume CFD Method, a computational mesh is required to capture the fluid flow; obviously a very fine mesh

would be required if the full details of the flow at the droplet level were to be resolved given that the diameters of the droplets in such flows are typically far less than $2000\mu m$ and that they are present in hundreds of thousands in number. This is computationally expensive and the state of the art CFD modelling techniques are currently not feasible for target applications like bearing chamber flows or spray-film cooling because of the computational overhead.

In this work, existing multiphase modelling techniques were combined, linked and developed in a novel way leading to a low cost CFD solution for realistic applications that involve droplet-film formation with heat transfer. The "building block" modelling approaches of discrete phase modelling and volume-of-fluid are presented and described in Chapter 3. In Chapter 4 the new methodology for combining and linking these two models is developed and presented. The droplets are tracked as Lagrangian point particles "holding" the droplet history in the gas phase. The Lagrangian droplet representation is otherwise called the DPM phase. The DPM phase is essentially a third numerical phase. This technique, however, creates a challenge of transporting conservatively the mass, momentum and energy between the two numerical liquid phases. Upon the impact of the DPM droplets on a free film surface or a wall boundary, they are coupled into the Eulerian phase using source terms. With this method, fine mesh density is only used close to the walls and the free interface regions; relatively coarse mesh density is used in the gas phase thus significantly reducing the computational overhead. An algorithm was also developed to track droplets at a free-surface and correspondingly determine and track splashing droplets. The algorithm uses published correlation to determine splashing components and the absorbed components based on the balance of mass of the splashing

droplets.

The developed model was tested using simple validations for mass, momentum and heat transfer and this is presented in Chapter 5. Several basic tests were done for mass conservation check for the Lagrangian droplets turning to Eulerian VoF film and the accuracy ranged around 0.1 & 1.5% depending on how the film region is resolved. When a droplet impacts on a film, the consequence of momentum transfer is the crater evolution that follows it. This indirect check for momentum conservation is impressive when compared with published crater evolution results. The crater evolution simulations compare well with published correlations and this is within 9.4%. A validation of the work with the spray cooling experimental work of Yaqing *et al.* [14], in Chapter 5, shows good results. The deviation of the heat transfer coefficient from experimental averages is about 12.2%. For good results, the aim should be that the region where the film is most expected in the domain should be refined sufficiently to capture the film; 10 cells or more are recommended in the film region.

An application of the model to two realistic bearing chamber geometries (test rig at Nottingham representative of a chamber in the AE3007 engine and a test rig at KIT representative of a chamber on a BR7 series engine: AE3007 [2] & KIT [3] geometries) was done. In an engine, the bearings are lubricated with oil; the bearing motion breaks the lubricant up into sheets and droplets. The droplets travel to the bearing chamber walls and provide cooling of the structures before collection of the oil via the sumps. The AE3007 rig setup simulated droplets formation from a Rotating Inlet Distributor (RID). The RID is a cylinder with randomly distributed holes. Pumping water into the RID cavity and

rotating it at the shaft speed simulates droplet breakup from the bearings/shaft region. In the DPM-VoF simulations of the AE3007 geometry, the mean droplet size was taken to be close to the diameter of the holes in the RID. The KIT bearing chamber has a roller bearing with under-race feed and the oil is ejected into the chamber as film and droplets. The KIT bearing chamber has vents where the oil and air exit. The droplet diameters for the DPM-VoF simulations are based on a previous published experiment [16] on the same geometry.

For the AE3007 geometry, the simulations show film formation and pooling as observed in the experiments. Heat transfer coefficients (HTCs), based on an estimated but representative choice of thermal boundary conditions, were calculated. The top parts of the bearing chamber, generally, show higher HTC results than the lower parts of the chamber. The film thickness results are overpredicted but similar in trend when compared with experimental measurements. A parametric study of the flow shows that the film thickness increases with the flow rate. The film thickness increase with reducing shaft speed for same flow rate. The film thickness increases as the film approaches the top and bottom vents. The average film temperature increases with reducing flow rate and increases with shaft speed. The heat transfer coefficient results show that higher flow rates provide better heat tranfer at higher shaft speeds.

Initial boundary conditions for the DPM-VoF model may be obtained from experiments measuring the mean temperatures, droplet distributions and velocities of the droplets. These boundary conditions can be similarly obtained from detailed simulations, for example, a detailed simulation of droplet breakup from the bearings or the RID can serve as

input for the model for a bearing chamber application.

This model can also find potential application in simulating the flow past the blades of a micro wind turbine in the rain or any such similar application where the effect of the film on the surface might be of interest. The model is, however, at best an approximation because fine details are lost to coarse grid, but results in the "region" of interest are quite good and can be useful for taking engineering decisions. The stability of the method is good considering the high Reynolds and/or Weber numbers that can be involved in a bearing chamber flow for example. The spreading of source terms can help prevent divergence during iteration. The extent of spreading source term should be limited as the solution can become unstable; for example spreading source terms over more than 20 cells is not recommended.

7.2 Contributions to knowledge

The work presented in this thesis makes a significant contribution to modelling capability for situations where there is droplet-film interaction arising from large numbers of droplets. Examples include modelling aeroengine bearing chambers and spray cooling situations. It is posible to model such situations using VoF alone but only at the expense of huge computational meshes. The developed approach linking DPM to VoF provides a viable approach of adequate accuracy for bearing chamber design. The work demonstrates the ability to couple Lagrangian and Eulerian phases. The presented work develops and implements an approach to use also employed existing correlations to recreate splashing

droplets from high Reynolds and Weber number impact and creates splashing components in a Lagrangian representation. As future experimental or computational correlations become available they can easily be added into the existing capability.

Prior to the work presented in this thesis, there has never been a full simulation of the complex flow in a bearing chamber, this work has been able to show flow in a bearing chamber and gave insight into the heat transfer coefficient. The presented work also shows clearly the way data from the developed model can be used to provide insight into bearing chamber design.

7.3 Future Work

For a bearing chamber application, there is a need to do a detailed simulation of the droplet breakup process from the shaft. The detailed simulation will give the droplet size distribution, velocities and perhaps the thermal properties. This will be useful to inform more correctly the boundary conditions for the developed Lagrangian-Eulerian model. This simplified model has not considered the effect of physical phase changes like evaporation which is worth consideration in a future work. The fluid properties such as density and viscosity have been assumed to be constant, although it is clearly possible to include non-constant properties in future models.

There is need to develop a more efficient cell zone scanning macro in ANSYS-Fluent. Currently, scanning relies on the built-in "*begin_c_loop*" macro that actually scans through the control volume instead of a *marked region*. Such a macro would be used at impact

points and the diameter to scan would simply be passed as *value* to such macro.

Algorithms that can reduce simulation time are definitely important, an investigation into the possibility of using different timesteps per phase might potentially improve simulation time.

References

[1] B. Chandra, K. Simmons, and S. Pickering, "Parametric Study of Shallow AE3007 Sump," tech. rep., UTC in Gas Turbine Transmission, The University of Nottingham, UK, 2012. JF24/BC/04.

[2] B. Chandra, K. Simmons, and S. Pickering, "Experimental Bearing Chamber Scavenge: Comparison of Sump Designs - AE3007 (INDY), BR725, TP400," tech. rep., UTC in Gas Turbine Transmission, The University of Nottingham, UK, 2012. JF24/BC/03.

[3] P. Gorse, S. Busam, and K. Dullenkopf, "Influence of Operating Condition and Geometry on the Oil Film Thickness in Aeroengine Bearing Chambers," *Journal of Engineering for Gas Turbines and Power*, vol. 128, pp. 103–110, 2006.

[4] Airliners.NET, "Trent engine." www.airliners.net Accessed: Jul, 2014.

[5] Rolls-Royce, *The Jet Engine*. Rolls-Royce plc, London, 2005.

[6] H. Streifinger, "Fuel/oil system thermal management in aircraft turbine engines,"

RTO AVT Symposium on Design Principles and Methods for Aircraft Gas Turbine Engines, Toulouse, France, vol. 15, May 11 1998.

[7] Rolls Royce Plc, "Trent-1000 engine." www.rolls-royce.com Accessed: Jul, 2013.

[8] J. Weisman, D. Duncan, J. Gibson, and T. Crawford, "Effects of fluid properties and pipe diameter on two-phase flow patterns in horizontal lines," *International Journal of Multiphase Flow*, pp. 437–462, 1979.

[9] W. John and C. S. Garimella, "Characterization of two-phase flow patterns in small diameter round and rectangular tubes," *International Journal of Heat and Mass Transfer*, vol. 42, no. 15, pp. 2869–2881, 1999.

[10] A. Yarin and D. Weiss, "Impact of drops on solid surfaces: self-similar capillary waves, and splashing as a new type of kinematic discontinuity," *Journal of Fluid Mechanics*, vol. 283, pp. 141–173, 1995.

[11] M. Rieber and A. Frohn, "A numerical study on the mechanism of splashing," *International Journal of Heat and Fluid Flow*, vol. 20, pp. 455–461, 1999.

[12] D. Peduto, R. Koch, H. Morvan, K. Dullenkopf, and H.-J. Bauer, "Numerical studies of single drop impact onto a plane shallow and deep liquid pool," in *ILASS -Europe 2011, 24th Annual Conference on Liquid Atomization and Spray Systems, Estoril, Portugal*, 2011.

[13] G. Cossali, M. Marengo, A. Coghe, and S. Zhdanov, "The role of time in single drop splash on thin film," *Experiments in Fluids*, vol. 36, pp. 888–900, 2004.

[14] W. Yaqing, L. Minghou, L. Dong, K. X., and C. Yiliang, "Experimental study on the effects of spray inclination on water spray cooling performance in non-boiling regime," *Experimental Thermal and Fluid Science*, vol. 34, no. 7, pp. 933–942, 2010.

[15] A. Robinson, *Computational investigation into offtake flows with application to gas turbine bearing chambers*. PhD thesis, The University of Nottingham, 2010.

[16] A. Glahn, M. Kurreck, M. Willmann, and S. Wittig, "Feasibility Study on Oil Droplet Flow Investigations Inside Aero Engine Bearing Chambers - PDPA Techniques in Combination With Numerical Approaches," *Journal of engineering for gas turbines and power*, vol. 118, pp. 749–755, 1996.

[17] R. Scardovelli and S. Zaleski, "Direct Numerical Simulation of Free-Surface and Interfacial Flow," *Annu. Rev. Fluid Mech.*, vol. 31, no. 567-603, 1999.

[18] S. Navti, K. Ravindran, C. Taylor, and R. Lewis, "Finite element modelling of surface tension effects using a Lagrangian-Eulerian kinematic description," *Computer methods in applied mechanics and engineering*, vol. 147, pp. 41–60, 1997.

[19] A. Caboussat, "A numerical method for the simulation of free surface flows with surface tension," *Computers & fluids*, vol. 35, no. 10, pp. 1205–1216, 2006.

[20] L. Landau and E. Lifshitz, *Fluid Mechanics*. Pergamon, New York, 1959.

[21] I. Malcevic and O. Ghattas, "Dynamic-mesh finite element method for lagrangian computational fluid dynamics," *Finite Elements in Analysis and Design*, vol. 38, no. 10, pp. 965–982, 2002.

[22] J. Monaghan, "SMOOTHED PARTICLE HYDRODYNAMICS," *Annual review of astronomy and astrophysics*, vol. 30, pp. 543–74, 1992.

[23] R. Gingold and J. Monaghan, "Smoothed particle hydrodynamics: theory and application to non-spherical stars," *Monthly notices of the royal astronomical society*, vol. 181, pp. 375–89, 1977.

[24] S. Idelsohna, M. Stortia, and E. Oñateb, "Lagrangian formulations to solve free surface incompressible inviscid fluid flows," *Computational Methods in Applied Mechanics and Engineering*, vol. 191, no. 6-7, pp. 583–593, 2001.

[25] C. Hirt, J. Cook, and T. Butler, "A Lagrangian method for calculating the dynamics of an incompressible fluid with free surface," *Journal of Computational Physics*, vol. 5, no. 1, pp. 103–124, 1970.

[26] A. Colagrossi and M. Landrini, "Numerical simulation of interfacial flows by smoothed particle hydrodynamics," *Journal of Computational Physics*, vol. 1, no. 2, pp. 448–475, 2003.

[27] T. Yue, F. Pearce, A. Kruisbrink, H. Morvan, and A. Cliffe, "Numerical Simulation of single and multi-mode Rayleigh Taylor Instability using weakly-compressible Smoothed Particle Hydrodynamics," *Computer & Fluids*, vol. in press.

[28] H. Braess and P. Wriggers, "Arbitrary Lagrangian Eulerian finite element analysis of free surface flow," *Computer Methods in Applied Mechanics and Engineering*, vol. 190, pp. 95–109, 2000.

[29] V. Buwa, D. Deo, and V. Ranade, "Eulerian-Lagrangian simulations of unsteady gas-

liquid flows in bubble columns," *International Journal of Multphase Flow*, vol. 32, pp. 864–885, 2006.

[30] S. Laín, D. Bröder, M. Sommerfeld, and M. Göz, "Modelling hydrodynamics and turbulence in a bubble column using the Euler-Lagrange procedure," *International Journal of Multiphase Flow*, vol. 28, pp. 1381–1407, 2002.

[31] F. Harlow and J. Welch, "Numerical Calculation of Time-Dependent Viscous Incompressible Flow of Fluid with Free Surface," *The Physics of Fluids*, vol. 8, no. 12, pp. 2182–2189, 1965.

[32] S. Popinet and S. Zaleski, "A Front-Tracking Algorithm for Accurate Representation of Surface Tension," *International Journal for Numerical Methods in Fluids*, vol. 30, pp. 775–793, 1999.

[33] D. Gueyffier, J. Li, A. Nadim, R. Scardovelli, and S. Zaleski, "Volume-of-Fluid Interface Tracking with Smoothed Surface Stress Methods for Three-Dimensional Flows," *Journal of Computational Physics*, vol. 152, pp. 423–456, 1999.

[34] M. Sussman and E. Puckett, "A Coupled Level Set and Volume-of-Fluid Method for Computing 3D and Axisymmetric Incompressible Two-Phase Flows," *Journal of Computational Physics*, vol. 162, pp. 301–337, 2000.

[35] W.-t. Tsai and D. K. Yue, "COMPUTATION OF NONLINEAR FREE-SURFACE FLOWS," *Annual review of fluid mechanics*, vol. 28, pp. 249–278, 1996.

[36] H. Power and D. Ingham, "Special issue: application of the {BEM} to interfacial

phenomena," *Engineering Analysis with Boundary Elements*, vol. 28, no. 4, pp. 293 –, 2004. Application of the {BEM} to interfacial phenomena.

[37] H. Versteeg and W. Malalasekera, *An introduction to Computational Fluid Dyanmics: The Finite Volume Method*. Pearson Education Limited, 1995.

[38] H. Versteeg and W. Malalasekera, *An introduction to Computational Fluid Dynamics -The Finite Volume Method Second Edition*. Essex, England: Pearson Prentice Hall, 2007.

[39] OpenFOAM®, "The open source CFD toolbox." www.openfoam.com Accessed: Jan, 2011.

[40] CAELinux®, "CAE Linux." www.caelinux.com Accessed: Jan, 2013.

[41] J. Shang, D. Calahan, and B. Vikstrom, "Performance of a finite volume CEM code on multicomputers," *Computing Systems in Engineering*, vol. 6, no. 3, pp. 241–250, 1995.

[42] S. Patankar, *Numerical heat transfer and fluid flow*. New York:Hemisphere, 1980.

[43] W. Noh and P. Woodward, "SLIC (Simple Line Interface Calculation)," in *Proceedings of the Fifth International Conference on Numerical Methods in Fluid Dynamics June 28 - July 2, 1976 Twente University, Enschede* (A. Vooren and P. Zandbergen, eds.), vol. 59 of *Lecture Notes in Physics*, pp. 330–340, Springer Berlin Heidelberg, 1976.

[44] C. Hirt and B. Nichols, "Volume of Fluid (VoF) Method for the Dynamics of free Boundaries," *Journal of Computational Physics*, vol. 39, pp. 201–225, 1981.

[45] G. Son and N. Hur, "A Coupled level set and Volume-of-Fluid method for the Buoyancy-Driven motion of fluid particles," *Numerical Heat Transfer: Part B: Fundamentals*, vol. 42, no. 6, pp. 523–542, 2002.

[46] M. Meier, G. Yadigaroglu, and B. Smith, "A novel technique for including surface tension in PLIC-VOF methods," *European Journal of Mechanics-B/Fluids*, vol. 21, pp. 61–73, 2002.

[47] Z. Wang, J. Yang, and F. Stern, "Comparison of Particle Level Set and CLSVOF Methods for Interfacial Flows," *46th AIAA Aerospace Sciences Meeting and Exhibit, 7-10 Jan. 2008, Reno, Nevada*.

[48] A. Bourlioux, "A coupled level-set volume of fluid algorithm for tracking material interfaces, Proceedings of the 6th International Symposium on Computational Fluid Dynamics, Lake Tahoe, USA.," 1995.

[49] S. Osher and J. Sethian, "Fronts propagating with curvature-dependent speed: algorithms based on Hamilton-Jacobi formulations," *Journal of Computational Physics*, vol. 79, pp. 12–49, 1988.

[50] J. Brackbill, D. Kothe, and C. Zemach, "A continuum method for modeling surface tension," *Journal of Computational Physics*, vol. 100, no. 2, pp. 335–354, 1992.

[51] R. Saurel and R. Abgrall, "A Multiphase Godunov Method for Compressible Multilfuid and Multiphase Flows," *Journal of Computational Physics*, vol. 150, pp. 425–467, 1999.

[52] R. R. Long, *Film Notes for Stratified Flow*. Educationa Development Center, National Committee for Fluid Mechanics Films, No. 21618, 1970.

[53] C. Vallée, T. Höhne, H.-M. Prasser, and T. Sühnel, "Experimental investigation and CFD simulation of horizontal stratified two-phase flow phenomena," *Nuclear Engineering & Design*, vol. 238, pp. 637–646, 2008.

[54] M. Gargallo, T. Schulenberg, L. Meyer, and E. Laurien, "Counter-current flow limitations during hot leg injection in pressurized water reactors," *Nuclear Engineering and Design*, vol. 235, pp. 785–804, 2005.

[55] P. Tkaczyk and H. Morvan, "SILOET: CFD Modelling Guidelines of Engine Sumps - Oil and Air Flows Simulation of Bearing Chambers & Sumps using an Enhaced Volume of Fluid (VOF) Method, Technical report JF82/PT/06, UTC in Gas Turbine Transmission Systems, The University of Nottingham, UK.," tech. rep., 2012.

[56] Y. Egorov, M. Boucker, A. Martin, S. Pigny, M. Scheuerer, and S. Willemsen, "Validation of CFD codes with PTS-relevant test cases," in *5th Euratom Framework Programme ECORA project*, CONTRACT N^o FIKS-CT-2001-00154, pp. 91–116, 2004.

[57] M. A. Friedrich, *A Seperation Criterion and Non-Intrusive Thickness Measurement Technique for Shear-Driven Films*. PhD thesis, Missouri University of Science and Technology, 2008.

[58] I. Owen and D. Ryley, "The flow of thin liquid films around corners," *International Journal of Multiphase Flow*, vol. 11, no. 1, pp. 51–62, 1984.

[59] F. Maroteaux, D. Llory, J.-F. Coz, and C. Habchi, "Liquid Film Atomization of Wall

Edges - Separation Criterion and Droplets Formation Model," *Journal of Fluid Engineering*, vol. 124, pp. 565–575, 2002.

[60] P. Tkaczyk and H. Morvan, "Film thickness prediction in an annular two-phase flow around c-shaped bend," *Journal of Computational Multiphase Flows*, vol. 3, no. 1, pp. 27–40, 2011.

[61] M. A. Friedrich, H. Lan, J. Wegener, J. Drallmeier, and B. F. Armaly, "A separation criterion with experimental validation for shear-driven films in separated flows," *Journal of Fluids Engineering*, vol. 130, no. 5, p. 051301, 2008.

[62] S. Alghoul, C. Eastwick, and D. Hann, "Experimental investigation of a Single Droplet Interaction with Shear Driven Film," in *ILASS, 23rd Annu. Conf. on Liquid Atomization and Spray Systems, Brno, Czech Republic*, 2010.

[63] W. Samenfink, A. Elsaβer, K. Dullenkopf, and S. Wittig, "Droplet interaction with shear-driven liquid films: analysis of deposition and secondary droplet characteristics," *International Journal of Heat and Fluid Flow*, vol. 20, pp. 462–469, 1999.

[64] I. Chen and G. Kocamustafaogullari, "Condensation heat transfer studies for stratified, cocurrent two-phase flow in horizontal tubes," *International Journal of Heat and Mass Transfer*, vol. 30, no. 6, pp. 1133–1148, 1987.

[65] M. Scheuerer, M. Heitsch, F. Menter, Y. Egorov, I. Toth, *et al.*, "Evaluation of computational fluid dynamic methods for reactor safety analysis (ECORA)," *Nuclear Engrg & Design*, vol. 235, p. 9, 2005.

[66] M. Davidson and M. Rudman, "Volume-of-Fluid Calculation of Heat or Mass Trans-

fer Across Deforming Interfaces in Two-Fluid flow," *Numerical Heat Transfer: Part B: Fundamentals*, vol. 41, no. 3, pp. 291–308, 2002.

[67] C. Yang and Z.-S. Mao, "Numerical simulation of interphase mass transfer with the level set approach," *Chemical Engineering Science*, vol. 60, pp. 2643–2660, 2005.

[68] T. Li, Z. Mao, J. Chen, and W. Fei, "Experimental and numerical investigation of single drop mass transfer in solvent extraction systems with resistance in both phases," *Chinese Journal of Chemical Engineering*, vol. 10, no. 1, pp. 1–14, 2002.

[69] ANSYS, *Fluent 14.5-User Manual*. ANSYS Inc., 2013.

[70] A. Worthington, *A Study of Splashes*. London: Longmans, Green & Co., 1908. http://www.gutenberg.org/files/39831/39831-h/39831-h.htm, Accessed: Jul. 2011.

[71] G. Cossali, A. Coghe, and M. Marengo, "The impact of a single drop on a wetted solid surface," *Experiments in Fluids*, vol. 11, pp. 463–472, 1997.

[72] M. Marengo, A. Carlo, R. Llia V, and T. Cameron, "Drop Collisions with simple and complex surfaces," *Current Opinion in Colloid & Interface Science*, vol. 16, pp. 292–302, 2011.

[73] A. Yarin, "Drop Impact Dynamics: Splashing, Spreading, Receding, Bouncing ...," *The Annual Review of Fluid Mech.*, vol. 38, pp. 159–92, 2006.

[74] S. Schiaffino and A. A. Sonin, "Molten droplet deposition and solidification at low Weber numbers," *Physics of Fluids*, vol. 9, no. 11, pp. 3172–3187, 1997.

[75] R. Riobo, C. Tropea, and M. Marengo, "Outcomes from a drop impact on solid surfaces," *Atomization and Sprays*, vol. 11, no. 2, pp. 155–165, 2001.

[76] A. Bisighini, *Single and Double Drop Impacts onto a Deep and Thick liquid layers*. PhD thesis, Universitá degli Studi di Bergamo, 2009.

[77] B. Edin, P. v. H. Nils, J. Suad, V. R. Llia, and C. Tropea, "Drop impact onto a liquid layer of finite thickness: Dynamics of the cavity evolution," *Physical Review E*, vol. vol 79/036306, pp. pp 1 – 15, 2009.

[78] L. Randy, W. Vander, M. B. Gordon, and D. M. Steven, "Droplets splashing upon films of the same fluid of various depths," *Experiments in Fluids*, vol. vol. 40, pp. pp 33–52, 2006.

[79] C. Bai and A. Gosman, "Mathematical Modelling of Wall Films Formed by Impinging Sprays," *SAE TECHNICAL PAPER SERIES 960626*, 1996.

[80] P. O'Rourke and A. Amsden, "A Spray/Wall Interaction Submodel for the KIVA-3 Wall Film Model," *SAE TECHNICAL PAPER SERIES 2000-01-0271*, 1996.

[81] D. Vladimir and S. D. Heister, "Modeling Oil Flows in Engine Sumps: Drop Dynamics and Wall Impact Simulation," *Journal of Engineering for Gas Turbines and Power*, vol. 128, pp. pp 163–172, 2004.

[82] L. Xu, W. Z. Wendy, and R. N. Sidney, "Drop splashing on a dry smooth surface," *Physical review letters (APS J.)*, vol. 94, no. 18, 2005.

[83] C. Mundo, M. Sommerfeld, and C. Tropea, "Droplet-Wall Collisions: Experimental

Studies of the Deformation and Breakup Process," *International Journal of Multiphase Flow*, vol. 21, no. 2, pp. 151–173, 1995.

[84] T. Okawa, T. Shiraishi, and T. Mori, "Effect of impingement angle on the outcome of single water drop impact onto a plane water surface," *Experiments in Fluids*, vol. 44, pp. 331–339, 2008.

[85] Z. Mehdizadeh, Navid, S. Chandra, and J. Mostaghimi, "Formation of fingers around the edges of a drop hitting a metal plate with high velocity," *Journal of Fluid Mechanics*, vol. 510, pp. 353–373, 2004.

[86] G. Taylor, "Stability of a viscous liquid contained between two rotating cylinders," *Philosophical Transactions of the Royal Society of London. Series A, Containing Papers of a Mathematical or Physical Character*, vol. 223, pp. 289–349, 1923.

[87] T. Kuehn and R. Goldstein, "An experimental and theoretical study of natural convection in the annulus between horizontal concentric cylinders," *Journal of Fluid mechanics*, vol. 74, no. 04, pp. 695–719, 1976.

[88] T. Kuehn and R. Goldstein, "Correlating equations for natural convection heat transfer between horizontal circular cylinders," *International Journal of Heat and Mass Transfer*, vol. 19, no. 10, pp. 1127–1134, 1976.

[89] M. Escudier, P. Oliveira, and F. Pinho, "Fully developed laminar flow of purely viscous non-newtonian liquids through annuli, including the effects of eccentricity and inner-cylinder rotation," *International Journal of Heat and Fluid Flow*, vol. 23, no. 1, pp. 52–73, 2002.

[90] C. Nouar, C. Desaubry, and H. Zenaidi, "Numerical and experimental investigation of thermal convection for a thermodependent herschel-bulkley fluid in an annular duct with rotating inner cylinder," *European Journal of Mechanics-B/Fluids*, vol. 17, no. 6, pp. 875–900, 1998.

[91] S. Gardiner and R. Sabersky, "Heat transfer in an annular gap," *International Journal of Heat and Mass Transfer*, vol. 21, no. 12, pp. 1459 – 1466, 1978.

[92] K. M. Becker and J. Kaye, "Measurements of diabatic flow in an annulus with an inner rotating cylinder," *Journal of Heat Transfer*, vol. 84, no. 2, pp. 97–104, 1962.

[93] A. Quarmby and R. Anand, "Turbulent heat transfer in the thermal entrance region of concentric annuli with uniform wall heat flux," *International Journal of Heat and Mass Transfer*, vol. 13, no. 2, pp. 395–411, 1970.

[94] S. J. Baxter, *Numerical Simulation Of Three-Dimensional Free Surface Film Flow Over Or Around Obstacles On An Inclined Plane*. PhD thesis, The University of Nottingham, 2010.

[95] J. Williams, *Thin film rimming flow subject to droplet impact at the surface*. PhD thesis, The University of Nottingham, 2008.

[96] E. D. Kay, *A depth-averaged model for non-isothermal rimming flow driven at the surface by droplet impact*. PhD thesis, The University of Nottingham, 2013.

[97] M. Krug, *Evaluation of the Volume of Fluid Method for the Numerical Modelling of an Aero Engine Bearing Chamber*. PhD thesis, Karlsruhe Institut für Technologie, 2012.

[98] M. Farrall, *Numerical modelling of two-phase flow in a simplified bearing chmaber*. PhD thesis, The University of Nottingham, 2000.

[99] J. W. Chew, "Analysis of the oil film on the inside surface of an aero-engine bearing chamber housing, 96-GT-300," Presented at the International Gas Turbine and Aeroengine Congress & Exhibition, Birmingham, UK - June 10-13, 1996.

[100] S. Wittig, A. Glahn, and J. Himmelsbach, "Influence of high rotational speeds on heat transfer and oil film thickness in aero-engine bearing chambers," *Journal of engineering for gas turbines and power*, vol. 116, no. 2, pp. 395–401, 1994.

[101] E. Kay, S. Hibberd, and H. Power, "A depth-averaged model for non-isothermal thin-film rimming flow," *International Journal of Heat and Mass Transfer*, vol. 70, no. Complete, pp. 1003–1015, 2014.

[102] M. Farrall, S. Hibberd, K. Simmons, and D. Giddings, "Prediction of air/oil exit flows in a commercial aero-engine bearing chamber.," *Proceedings of the Institution of Mechanical Engineers Part G - Journal of Aerospace Engineering, 220(G3):197-202, 2006*.

[103] A. M. Maqableh, *Computational Study of Multi-Phase Air/Oil Heat Transfer in Aero-Engine Bearing Chambers*. PhD thesis, The University of Nottingham, 2005.

[104] C. Young and J. W. Chew, "Evaluation of the volume of fluid modelling approach for simulation of oil/air system flows," in *ASME Turbo Expo 2005: Power for Land, Sea, and Air*, pp. 1249–1257, American Society of Mechanical Engineers, 2005.

[105] R. White and T. Higgins, "Effect of the fluid properties on condensate behavior," *TAPPI Journal*, vol. 41, no. 2, pp. 71–76, 1958.

[106] A. Crouchez-Pillot and H. Morvan, "CFD Simulation of an Aeroengine Bearing Chamber using an Enhanced Volume of Fluid (VoF) Method, GT2014-26405," ASME Turbo Expo 2014.

[107] D. K. Gorse, P. and H.-J. Bauer, "The effect of airflow across aero-engine roller bearing on oil droplet generation , AIAA Paper No. 2005-1208," Proceedings of the XVII Symposium on Air Breathing Engines, ISABE 2005.

[108] S. Busam, A. Glahn, and S. Wittig, "Internal Bearing Chamber Wall Heat Transfer as a Function of Operating Condition and Chamber Geometry," *ASME Journal of Engineering for Gas Turbines and Power*, vol. 122, pp. 314–320, 2000.

[109] P. Gorse, K. Willenborg, S. Busam, J. Ebner, K. Dullenkopf, and S. Wittig, "3d-lda measurements in an aero-engine bearing chamber," in *ASME Turbo Expo 2003, collocated with the 2003 International Joint Power Generation Conference*, pp. 257–265, American Society of Mechanical Engineers, 2003.

[110] K. Willenborg, M. Klingsporn, S. Tebby, T. Ratcliffe, P. Gorse, K. Dullenkopf, and S. Wittig, "Experimental analysis of air/ oil separator performance," *Journal of Engineering for Gas Turbines and Power*, vol. 130, no. 6, p. 062503, 2008.

[111] B. W. Chandra, *Flow in turbine engine oil sumps*. PhD thesis, Purdue University, Indiana, 2006.

[112] W. Kurz and H.-J. Bauer, "An approach for predicting the flow regime in an aero

engine bearing chamber," in *ASME Turbo Expo 2014: Turbine Technical Conference and Exposition*, American Society of Mechanical Engineers, 2014.

[113] B. A. Nichita, *An Improved CFD Tool to Simulate Adiabatic and Diabatic Two-Phase Flows*. PhD thesis, ÉCOLE POLYTECHNIQUE FÉDÉRALE DE LAUSANNE, 2010.

[114] J. Boussinesq, "Théorie de l'Écoulement tourbillat," *Mem. Prés. Acad. Sci*, vol. 46, no. 23, 1877.

[115] D. Wilcox, *Turbulence Modeling for CFD*. DCW Industries, Inc., 1993.

[116] B. E. Launder and D. B. Spalding, "The numerical computation of turbulent flows," *Computer Methods in Applied Mechanics and Engineering*, vol. 3, no. 2, pp. 269–289, 1974.

[117] F. R. Menter, "Two-Equation Eddy-Viscosity Turbulence Models for Engineering Applications," *AIAA Journal*, vol. 32, no. 8, pp. 1598–1605, 1994.

[118] C. Valle, T. Hohne, Horst-Michael, and T. Suhnel, "Experimental Investigation and CFD simulation of horizontal stratified two-phase flow phenomena," *Nuclear Engineering and Design 238*, pp. 637–646, 2008.

[119] A. H. Amir, K. Dullenkopf, R. Koch, and H.-J. Bauer, "CFD Methods for Shear Driven Liquid Wall Films," vol. PGT201-23532, Proceedings of ASME Turbo Expo 2010: Power for land, Sea and Air GT2010.

[120] T. Craft, *Near-Wall Modelling*. Online Teaching Materials, School of Mech. Aerospace & Civil Engineering, University of Manchester., 2010.

[121] L. Schiller and Z. Naumann, "Z. Ver. Deustsch. Ing.77. 318.," 1935.

[122] Y. Liu, *An Introduction to the Boundary Element Method (BEM) and Its Applications in Engineering*. University of Cincinnati, Ohio, 2013.

[123] Alexi Thomas, "A droplet splash." http://mylightpaintings.com Accessed: Jul, 2012.

[124] M. Kaka and L. Zhi-yong, "Numerical Study on the Drag Coefficients of Sphere and Double Spheres," *Comput. Aided Draft. Des. and Manuf.*, vol. 19, no. 1, pp. 26–35, 2009.

[125] I. Roisman and C. Tropea, "Fluctuating flow in a liquid layer and secondary spray created by an impacting spray," *International Journal of Multiphase Flow*, vol. 31, pp. 179–200, 2005.

[126] D. Peduto, R. Koch, H. Morvan, and J. Banner, H, "Splashing products during single water drop impact onto a deep liquid pool using highspeed shadowgraphy and ptv technique," *UTC/Karlsruhe Institute of Technology (KIT), Germany*, 2012.

[127] D. Kalantari and T. Cameron, "Spray impact onto flat and rigid walls: Empirical characterization and modelling," *International Journal of Multiphase Flow*, vol. 33, pp. 525–544, 2007.

[128] J. Bohacek, "Surface Tension Model for High Viscosity Ratios Implemented in VOF Model," in *ILASS, 23rd Annual Conference on Liquid Atomization and Spray Systems, Brno, Czech Republic*, 2010.

[129] K. Oliphant, B. Webb, and M. McQuay, "An experimental comparison of liquid jet ar-

ray and spray impingement cooling in the non-boiling regime," *Experimental Thermal and Fluid Science*, vol. 18, pp. 1–10, 1998.

[130] J. Gretzinger and W. R. Marshall, "Characteristics of pneumatic atomization," *AIChE Journal*, vol. 7, no. 2, pp. 312–318, 1961.

[131] K. Y. Kim and W. R. Marshall, "Drop-size distributions from pneumatic atomizers," *AIChE Journal*, vol. 17, no. 3, pp. 575–584, 1971.

[132] K. A. Estes and I. Mudawar, "Correlation of sauter mean diameter and critical heat flux for spray cooling of small surfaces," *International Journal of Heat and Mass Transfer*, vol. 38, no. 16, pp. 2985–2996, 1995.

[133] J. Kim, "Spray cooling heat transfer: The state of the art," *International Journal of Heat and Fluid Flow*, vol. 28, pp. 753–767, 2006.

[134] B. Horacek, K. T. Kiger, and J. Kim, "Single nozzle spray cooling heat transfer mechanisms," *International Journal of Heat and Mass Transfer*, vol. 48, pp. 1425–1438, 2004.

[135] E. A. Silk, J. Kim, and K. Kiger, "Spray cooling of enhanced surfaces: Impact of structured surface geometry and spray axis inclination," *International Journal of Heat and Mass Transfer*, vol. 49, no. 25, pp. 4910–4920, 2006.

[136] J. Yang, L. Chow, M. R. Pais, and A. Ito, "Liquid film thickness and topography determination using fresnel diffraction and holography," *Experimental Heat Transfer: A Journal of Thermal Energy Generation, Transport, Storage, and Conversion*, vol. 5:4, pp. 239–252, 1992.

[137] J. yuan Jia, Y. xian Guo, W. dong Wang, and S. rong Zhou, "Modeling and experimental research on spray cooling," in *Semiconductor Thermal Measurement and Management Symposium, 2008. Semi-Therm 2008. Twenty-fourth Annual IEEE*, pp. 118–123, 2008.

[138] W. Jia and H. H. Qua, "Experimental investigation of droplet dynamics and heat transfer in spray cooling," *Experimental Thermal and Fluid Science*, vol. 27, pp. 829–838, 2003.

[139] P. D. Schmidt, *Cavitation in Diesel Fuel Injector Nozzles*. PhD thesis, University of Wisconsin - Madison, 1997.

[140] B. Chandra, K. Simmons, S. Pickering, S. Colliocot, and N. Wiedemann, "Study of gas/liquid behaviour within an aeroengine bearing chamber, GT2012-68753," ASME Expo 2012.

[141] B. Chandra, K. Simmons, and B. Keeler, "Parametric study into the effect of geometric and operational factors on the performance of an idealized aeroengine sump, ISABE Paper No. 2005-1208, 2005,"

[142] K. Simmons and B. Chandra, "Experimental investigation into the performance of shallow aeroengine off-takes," in *ASME Turbo Expo 2014: Turbine Technical Conference and Exposition*, American Society of Mechanical Engineers, 2014.

[143] A. Cheung, B. Tan, K. Hourigan, and M. Thompson, "Interference Drag Between Spherical and Cylinderical Particles in Stokes Flow," 2001.

[144] A. Glahn, M. F. Blair, K. L. Allard, S. Busam, O. Schäfer, and S. Wittig, "Disinte-

gration of oil films emerging from radial holes in a rotating cylinder," *Journal of engineering for gas turbines and power*, vol. 125, no. 4, pp. 1011–1020, 2003.

[145] T. Sonner, P. Davide, A. Adeniyi, and H. Morvan, "Verification and Validation of an Euler-Lagrange method for the Modelling of Drop-to-Film interaction, Technical report UF72/TS/01, UTC in Gas Turbine Transmission Systems, The University of Nottingham, UK.," tech. rep., 2013.

[146] ANSYS, *ICEM 14.5-User Guide*. ANSYS Inc., 2013.

[147] The University of Nottingham, High Performance Computing(HPC) Service, "HPC." https://workspace.nottingham.ac.uk/display/HPC/, Accessed: Feb, 2010.

Appendix A

DPM-VoF Code

A.1 .h files

The following built-in ANSYS-Fluent header files are required.

1. "$udf.h$"
2. "$vof\_surf.h$"
3. "$rp\_defined.h$"
4. "$surface\_facet.h$"
5. "$vof\_dpm\_capture.h$"

The next list of header files are developed in this work.

1. [*see* §A.1.0.6] “sourceterms.h”

2. [*see* §A.1.0.7] “globarvars.h”

3. [*see* §A.1.0.8] “otherfunctions.h”

4. [*see* §A.1.0.5] “readme.h”

The main c file is also appendended: “dpmvof.c”[*see* §A.2].

A.1.0.5 readme.h

The readme file shows how to implement the code.

/readme.h 1

```
/*
READ ME or ADVANCED USER GUIDE
1.)
You must define memory locations
Define>User-Defined>User-Defined Memory
20
 8
------------------------------------------------------------
2.)
Compile the code:
 1 source file .c file:
 Header files
            readme.h
   vof_dpm_capture.h
     surface_facet.h
       sourceterms.h
        rp_defined.h
    otherfunctions.h
        globalvars.h
          vof_surf.h
Library Name:
 libudf
------------------------------------------------------------
3.)
Attaching the source terms:
Cell Zone Conditions:
      (a) Mixture:
          edit>select source terms>Source Terms>
             X momentum source:udf vof_dpm_X_momentum::libudf
             Y momentum source:udf vof_dpm_Y_momentum::libudf
             Z momentum source:udf vof_dpm_Z_momentum::libudf
                 Energy source:    udf vof_dpm_Energy::libudf
      (b) Liquid phase:
          edit>source terms>Source Terms>
             Mass source:udf vof_liquid_src::libudf
      (c) Gas phase: ?not required for 1 cell impact?
          edit>source terms>Source Terms>
                Mass source:udf vof_gas_src::libudf

Function Hooks:
    Initialization:
            Init_Child_Injectors::libudf
    Adjust:
            interfaceNormals::libudf
                 Cleanup_DPM::libudf
    Execute at End:
                 src_reseter::libudf
4)
DPM Model:
 Interaction wiht Continous Phase, Update DPM Source Every Flow Iteration
   Drag Parameters
     Drag Law:
        udf dpm_drag_virtual::libudf

    injection names:
       mother-01, mother-02....etc These are the primary injectors eg use
```

/readme.h 2

```
          mother-01 to mother-05
57        child-01, child-02.....etc Splash created here...eg use child-01 to
          child-15
58      for each injection set the UDF code:
59       UDF>Initialization>
60          dpmCHILDREN::libudf
61
62      change DPM material to same as the Liquid phase after set up
63        Mass rate = mass of 1 dpm /vof time step, if more than 1kg/s expect
          crash! Choose carefully
64
65
66  ------------------------------------------------------------
67  Start injection far off the start of the simulation and after film is introduced
68
69
70
71
72
73
74
75
76
77
78
79
80
81
82
83
84
85
86
87
88
89
90
91  */
```

A.1.0.6 sourceterms.h

See following pages for the code ...

/sourceterms.h 1

```
1   #ifndef _SOURCETERMS_H_
2   #define _SOURCETERMS_H_
3   #include "mem.h"
4   #include "sg.h"
5   #include "vof_dpm_capture.h"
6   #include "surface_facet.h"
7   #include "random.h"
8   #include "rp_defined.h"
9   #include "surf.h"
10  #include "dpm.h"
11  #include "globalvars.h"
12  #include "otherfunctions.h"
13  /*
14  (c)2012
15  A.A. Adeniyi, H.P. Morvan, K.A. Simmons
16  Rolls-Royce UTC Centre for Gas Turbine Research
17  University of Nottingham
18  Nottingham, UK
19
20  */
21
22  /*Change when headers updated*/
23
24  #endif
25
```

A.1.0.7 globarvars.h

See following pages for the code ...

/globalvars.h 1

```
1  /*
2   ------------------------------------------------
3    (c) 2012 A.A. Adeniyi, H.P. Morvan, K.A. Simmons
4        Rolls-Royce UTC in Gas Turbine Research
5        University of Nottingham, Nottingham, UK
6  ------------------------------------------------
7  */
8
9  /*You can change any of the following */
10
11 /* DPM Droplets */
12 #define VOF_FLOW_TIME_STEPS 1.E-6 /* Recommended Flow time step,
13                                    If you change in the GUI, change this to match*/
14 #define MAX_NO_OF_DROPS_PER_SPLASH 50 /*If there are more they are ignored */
15 #define RELEASE_STEP 60.0E-6   /* seconds but use micro-seconds order
16                                   eg 10.E-6 instead of 1.E-5 note the dot
17                                  This is the time between droplet injections
                                    1/Frequency
18                                 mass rate of DPM=mass of dpm/vof time step
19                                 tracking is done at VoF time step
20                                 */
21
22
23 #define SHAFT_SPEED 16000. /*eg 5000 RPM */
24
25
26
27 #define MAX_DROPLET_SPEED 50.  /* 50 m/s is the limit, higher is removed!  */
28
29 /*Some VoF  */
30 /* The Properties of the Fluid should be same on the GUI and below
31   todo: Debug and read from GUI interface values better I think?
32
33  User To do: Use the Correct properties if this line is still present */
34 #define LIQ_RHO 1000.0  /*Liquid or oil phase density */
35
36 #define  surf_ten 0.001 /*Surface tension */
37 #define GAS_MU 1.5e-5    /*Gas phase only, viscosity */
38 #define LIQ_MU 0.001   /*Liquid phase viscosity */
39
40
41 /*PLEASE DO NOT CHANGE BELOW, unless you are sure of what you are doing */
42 #define interface_vof1 0.5
43 #define interface_vof 0.35  /*Exchange at the interface or just before it */
44 #define drywall_vof 0.0000001 /*This is not far from dry */
45
46 /* Depth search size: as DPM approaches a film,
47 determine the pool type by searching a to h*<=SR_star_max
48 h*<1 is a thin film
49 h*>1 is a thick film eg h*=1.2 is a thick film relative to the droplet
50 SR_star is how much into the film to scan
51 */
52 #define SR_STAR_MAX 1.8        /* default h/dp to be called a thick film when
   fixing needed */
53 #define hstar_THIN_FILM 0.4    /* Used as the thin film default value, it is
   calculated,
```

/globalvars.h 2

```
54                                  no need to change*/
55
56
57
58
59
60
61
62
63
64
65  #define ForceTrap 0 /* THIS SHOULD BE 0
66                         unless you know what you are doing
67                         you can change it to 1 */
68  /* Further notes:
69   This is 0 or 1:
70              For correct simulation, it should be 0
71              For the test of DPM turning to VoF it is 1 at x,y,z_dpmTrap
72
73         When testing the Momentum source transfer,
74          basic transfer of DPM to VoF without crossing any interface
75          is allowed. This happens when DPM crosses the position x,y,z_dpmTrap
           below
76          */
77
78  /*The position (x,y,z) below is a point where the DPM crosses
79     and turns to VoF without impacting on a film
80     It is assumed you are testing a droplet
81     moving towards the negative axis of your axis system. This works only if
82              ForceTrap 1
83   (see above), it will not if
84              ForceTrap 0
85   */
86  #define x_dpmTrap 0.
87  #define y_dpmTrap -2.5e-6
88  #define z_dpmTrap 0.
89
90
91
92
93
94
95
96  /*DO NOT CHANGE BELOW AT ALL */
97  #define LIQUID_PHASE_ID 3
98  #define SMALLEST_NUMBER 1.e-15
99  #define LARGEST_NUMBER 1.e9
100 #define SRC_CONST 0.001
101 #define Axis_x 0
102 #define Axis_y 1
103 #define Axis_z 2
104 #define No 0
105 #define Yes 1
106 #define DROP_DEAD -1
107 #define DROP_SPLASHES 1
108 #define DROP_SPREADS 2
```

/globalvars.h 3

```
109  #define DROP_STICKS 3
110  #define DROP_BOUNCES 4
111  #define DROP_SPLASHES_NON_WALL 5
112  #define DROP_SPREADS_NON_WALL 6
113  #define DROP_STICKS_NON_WALL 7
114  #define DROP_BOUNCES_NON_WALL 8
115  #define PI 3.14159
116  #define DPM_THROWN_TO_X 0.13
117  #define DPM_THROWN_TO_Y 0.05
118  #define DPM_THROWN_TO_Z 0.
119
120
121
122  /* DO NOT CHANGE ANYTHING BELOW! */
123  enum
124  {R=Axis_z+1,
125  M,
126  xVel,yVel,zVel,
127  Cp,TEMP2,RE,
128  RHO,
129
130  DIM_SPHERE,
131  };
132   enum
133  {/*xVel,yVel,zVel,*/
134  Rscan=zVel+1,
135  itsWall,
136
137  DIM_SCANNER};
```

A.1.0.8 otherfunctions.h

See following pages for the code ...

/otherfunctions.h 1

```
#ifndef _OTHERFUNCTIONS_H_
#define _OTHERFUNCTIONS_H_
/*
 ------------------------------------------------
  (c) 2012 A.A. Adeniyi, H.P. Morvan, K.A. Simmons
      Rolls-Royce UTC in Gas Turbine Research
      University of Nottingham, Nottingham, UK
-------------------------------------------------
 */

int Number_of_Children(real);
real Ejection_Angle(real);
real Secondary_Drop_Size(real);
real Jet_Length(real);
real Secondary_Drop_Mean_Velocity(real);
real Mass_Fraction_Ejected(real, real,int);
real Mass_Fraction_Ejected_2(real,real);
real Ohnesorg(real);
real ScanRange(real*,real*);

real getCrownWeber(real,real);
real getWeber(real,real,real,real);
real getReynolds(real,real,real,real,real);
real signOf(real);
int IsPositive(real);
int IsNegative(real);
real getMIN(real,real);
real getMAX(real,real);
real getMAXIMUM(real,real);
real getGoodNumber(real);
real getMINIMUM(real,real);
real getMAXIMUM_3Nos(real,real,real);
real getNode_Y1 (cell_t,Thread*);
real getNode_Y2 (cell_t,Thread*);
real getNode_X1 (cell_t,Thread*);
real getNode_X2 (cell_t,Thread*);
real getNode_Z1 (cell_t,Thread*);
real getNode_Z2 (cell_t,Thread*);
real getCell_height_X(cell_t,Thread*);
real getCell_height_Y(cell_t,Thread*);
real getCell_height_Z(cell_t,Thread*);
real getFilmThickness(real*);
real getMagnitude(real*);
real create_splashed_drops_old(Tracked_Particle*,real);
int Not_A_Number(real);
int approximately_equal_to(real,real);
int IsMyNeighbour(cell_t,Thread*,cell_t*,Thread**,int);
/* others July 2012 edited: 26 Nov 2012*/
void computeNormal(cell_t, Thread*, real*);


real childrenInjectionStarts;
#define MAX_NUMBER_OF_CHILD_INJECTORS 500
/*This is a store for secondary droplets at one
    instance in an iteration/timestep
  It is not the same as the number of
```

/otherfunctions.h 2

```
57      dummy Injectors child-0 to child-10 eg attached
58      from the GUI
59      child-0 to n injects physically but its fate is
60      determined by the stored childinjector ie can be
61      killed at birth or set to inject..therefore we can
62      track any secondary drop. The algorithm is such that
63      the childinjector goes in a cycle and marked
64      appropriately for use or not.
65
66      Change LIQ_RHO=997.05; edit 26/Nov/2012 Made a constant in global vars .h */
67    int counter,counter_erg;
68    real energy_source(real);
69    real gas_source(real);
70    real liq_source(real);
71    void freeup_Injector(int);
72    void freeup_All_Injectors();
73    real within_360(real);
74    int radial_pointer(real,int);
75    int find_substring(char *, char *);
76    real create_splashed_drops(Tracked_Particle*, real);
77
78    void Kill_DPM(Tracked_Particle*,Thread*,real);
79    int add_tracked_particle_to_vof(Tracked_Particle*,face_t,Thread*,int,real);
80    int drop_impact_outcome(real,real,real,real);
81    void SpreadMassSource(real*);
82    real SphericalRange(real *,real *);
83    real getSpreadRadiusCorrelation(real);
84    void echo(char[]);
85    struct child_injector_t
86     {int ID; int MotherID;
87      char *injector_name;
88      int injection_kind;
89     /* INJECTION_SURFACE=0,_SINGLE=1,_GROUP=2,_CONE=3 */
90      int free;  int number_of_droplets;
91      real x;  real y;  real z;
92      real u;  real v;  real w; real Rho;
93      real diam;  real mass_flow_rate; real Temp;
94      }  child_injector[MAX_NUMBER_OF_CHILD_INJECTORS];
95
96    int Not_A_Number(real foo)
97    {real f=0.;f=foo;
98    if (f+0.==f) return No; else return Yes;
99    }
100   void Kill_DPM(Tracked_Particle *p, Thread *ct, real massadded)
101   {
102
103   if(P_FLOW_RATE(p)<=0.)
104     CX_Message("****KILL a dead PARTICLE: Continue (Yes/No)? Yes selected \n\n");
105   /* Kill DPM Rountine */
106     MARK_PARTICLE(p, P_FL_REMOVED);
107   /* Mark Identity of this particle for Splash Details
108      DEBUG  */
109         p->state.liquid_fraction = SMALLEST_NUMBER; /*Dead Particles*/
110             p->state.temp=-999;
111                  p->stream_index = -1;
112                   P_FLOW_RATE(p) = 0.;
```

/otherfunctions.h 3

```
113                       P_MASS(p) = 0.;
114                    NV_S(P_VEL(p),=,0.);
115       /*if(massadded>=0) =-1.0 when not the regular call */
116          add_to_dpm_summary(p,FATE_ESCAPED,ct);
117
118     /*
119       if(counter<200)*/
120         CX_Message("\n****DPM Killed (Mass source-%E)\n\n",massadded);
121   }
122
123
124   /* */
125   real getCrownWeber(real Re,real We)
126   {
127   /* The impact of a droplet on film creates as sheet of liquid
128       called crown, the Crown's Weber number is determined as obtained from
129       Zi-Niu W. (2003)  -Prediction of the size distribution of secondary ejected
          droplets
130                          by crown splashing od droplets impinging on a solid wall
131              We_CrownSheet=2(We+12)/[sqrt(9+[2*We(We+12)/Re])+3]
132   */
133   real D;
134   D=SMALLEST_NUMBER;
135   if (Re<=0.)
136      {D=SMALLEST_NUMBER; /*No Division by 0 */}
137   else
138   {
139   D=2*We*(We+12.);
140   D/=Re;
141   D+=9.;
142   D=3.+pow(D,0.5);
143   D=2*(We+12.)/D;
144   }
145   return D;
146   }
147
148   real getWeber(real Rho, real Vel, real L, real surface_tension)
149   { /*########################################*/
150   real v2,weber;
151   /*End variables*/
152     v2=Vel*Vel;
153     weber = Rho * v2 * L/ surface_tension;
154     return weber;
155   }
156   real getReynolds(real Rho, real Vp, real v_cont, real L, real Miu)
157   { /*########################################*/
158     /*########################################*/
159   real Re;
160   /* v_cont = Velocity of the continous fluid
161          Vp = Velocity of particle*/
162   Re=Rho*fabs(Vp-v_cont)*L/Miu;
163   /*CX_Message("Particle Vel=%E  VOF Vel.=%E  Re=%E\n", V,v_cont,Re);*/
164   return Re;
165   }
166   real signOf(real N)
167    { if(N>=0.) return 1.; else return -1.;
```

/otherfunctions.h 4

```
168   }
169  int IsPositive(real N)
170  {if (N>=0.) return Yes; else return No;
171  }
172  int IsNegative(real N)
173  {if (N<=0.) return Yes; else return No;
174  }
175  real getMIN(real x, real y)
176  {/*Like Overiding getMINIMUM */
177   real foo;
178   foo=getMINIMUM(x,y);
179   return foo;
180   }
181  real getMAX(real x, real y)
182  {/*Like Overiding getMAXIMIM */
183   real foo;
184   foo=getMAXIMUM(x,y);
185   return foo;
186   }
187  real getMAXIMUM(real x, real y)
188  {if (x>y) return x; else return y;
189  }
190  real getGoodNumber(real x)
191  {/*If number is too big, it must be some internal bug so return some very small
     number*/
192      if (fabs(x)>=LARGEST_NUMBER) return SMALLEST_NUMBER; else return x;
193  }
194  real getMINIMUM(real x, real y)
195  {   if (x<y) return x; else return y;
196  }
197  real getMAXIMUM_3Nos(real x, real y,real z)
198  {if (z>getMAXIMUM(x,y)) return z; else return getMAXIMUM(x,y);
199  }
200  /* ##########################################################
201   DEBUG THESE ----Use Centroid or Gausian Transformation */
202  real getNode_Y1 (cell_t c, Thread *ct)
203  { /* Y1= The Y coordinate of current cell
204  |----------|y2
205  |   CELL   |
206  |----------|y1
207  */
208          int n, i; real h1,h2;Node *node; i=0;
209  h1=h2=0.;
210  c_node_loop(c, ct, n)
211  {node = C_NODE(c,ct,n);
212      if (i==0) h1=NODE_Y(node);
213          if (h1!=NODE_Y(node)) h2=NODE_Y(node);
214   i++;
215  }
216   return getMINIMUM(h2,h1);
217  }
218  real getNode_Y2 (cell_t c, Thread *ct)
219  { /* Y2 =The Y coordinate of current cell
220  |----------|y2
221  |   CELL   |
222  |----------|y1 */
```

/otherfunctions.h 5

```
223         int n, i; real h1,h2;Node *node; i=0;
224  h1=h2=0.;
225  c_node_loop(c, ct, n)
226  {node = C_NODE(c,ct,n);
227      if (i==0) h1=NODE_Y(node);
228          if (h1!=NODE_Y(node)) h2=NODE_Y(node);
229   i++;
230  }
231   return getMAXIMUM(h2,h1);
232  }
233
234  /* X Coord */
235  real getNode_X1 (cell_t c, Thread *ct)
236  { /* X1= The Y coordinate of current cell
237  |----------|x2
238  |   CELL   |
239  |----------|x1
240  */
241         int n, i; real h1,h2;Node *node; i=0;
242  h1=h2=0.;
243  c_node_loop(c, ct, n)
244  {node = C_NODE(c,ct,n);
245      if (i==0) h1=NODE_X(node);
246          if (h1!=NODE_X(node)) h2=NODE_X(node);
247   i++;
248  }
249   return getMINIMUM(h2,h1);
250  }
251  real getNode_X2 (cell_t c, Thread *ct)
252  { /* X2 =The X coordinate of current cell
253  |----------|X2
254  |   CELL   |
255  |----------|X1 */
256         int n, i; real h1,h2;Node *node; i=0;
257  h1=h2=0.;
258  c_node_loop(c, ct, n)
259  {node = C_NODE(c,ct,n);
260      if (i==0) h1=NODE_X(node);
261          if (h1!=NODE_X(node)) h2=NODE_X(node);
262   i++;
263  }
264   return getMAXIMUM(h2,h1);
265  }
266
267  /* Z Coord*/
268  real getNode_Z1 (cell_t c, Thread *ct)
269  { /* Z1= The Z coordinate of current cell
270  |----------|z2
271  |   CELL   |
272  |----------|z1
273  */
274         int n, i; real h1,h2;Node *node; i=0;
275  h1=h2=0.;
276  c_node_loop(c, ct, n)
277  {node = C_NODE(c,ct,n);
278      if (i==0) h1=NODE_Z(node);
```

/otherfunctions.h 6

```
279         if (h1!=NODE_Z(node)) h2=NODE_Z(node);
280  i++;
281 }
282  return getMINIMUM(h2,h1);
283 }
284 real getNode_Z2 (cell_t c, Thread *ct)
285 { /* Z2 =The Z coordinate of current cell
286 |----------|Z2
287 |   CELL   |
288 |----------|Z1 */
289         int n, i; real h1,h2;Node *node; i=0;
290 h1=h2=0.;
291 c_node_loop(c, ct, n)
292 {node = C_NODE(c,ct,n);
293     if (i==0) h1=NODE_Z(node);
294         if (h1!=NODE_Z(node)) h2=NODE_Z(node);
295  i++;
296 }
297  return getMAXIMUM(h2,h1);
298 }
299
300 /* ################################### */
301 real getCell_height_X(cell_t c, Thread *ct)
302 {/*For Hexa-Mesh*/
303 int n, i; real height, h1,h2;
304 Node *node;
305 i=0;
306 h1=h2=0.;
307 c_node_loop(c, ct, n)
308 {node = C_NODE(c,ct,n);
309  if (i==0) h1=NODE_X(node);
310  if (h1!=NODE_X(node)) h2=NODE_X(node);
311  /*Looping through all the nodes in an order am not sure of
312   Avoid a situation where the two nodes will be on the same x
313   Only two (different) points make a straight line
314  */
315  i++;
316 }
317  height=fabs(h2-h1);
318  return getGoodNumber(height);
319 }
320 real getCell_height_Y(cell_t c, Thread *ct)
321 {/*For Hexa-Mesh*/
322 int n, i; real height, h1,h2;
323 Node *node;
324 i=0;
325 h1=h2=0.;
326 c_node_loop(c, ct, n)
327 {node = C_NODE(c,ct,n);
328  if (i==0) h1=NODE_Y(node);
329  if (h1!=NODE_Y(node)) h2=NODE_Y(node);
330  /*Looping through all the nodes in an order am not sure of
331   Avoid a situation where the two nodes will be on the same x
332   Only two (different) points make a straight line
333  */
334  i++;
```

/otherfunctions.h 7

```
335  }
336   height=fabs(h2-h1);
337  return getGoodNumber(height);
338
339  }
340  real getCell_height_Z(cell_t c, Thread *ct)
341  {/*For Hexa-Mesh*/
342  int n, i; real height, h1,h2;
343  Node *node;
344  i=0;
345  h1=h2=0.;
346  c_node_loop(c, ct, n)
347  {node = C_NODE(c,ct,n);
348   if (i==0) h1=NODE_Z(node);
349   if (h1!=NODE_Z(node)) h2=NODE_Z(node);
350   /*Looping through all the nodes in an order am not sure of
351    Avoid a situation where the two nodes will be on the same x
352    Only two (different) points make a straight line
353   */
354   i++;
355  }
356   height=fabs(h2-h1);
357   return getGoodNumber(height);
358
359  }
360  /* function taken to .c file 22/01/2013 to scan instead of using constant h
361  real getFilmThickness()
362
363  {*/ /*########################################*/
364
365    /*########################################*/
366   /*This is film thickness relative to the impacting droplet h*=h/d
367     Assumming h*=0.8 for test case...read film thickness and divide by droplet dia
368   */
369  /*
370      return 800./1000.;
371  }
372  */
373  real getMagnitude(real *V)
374  {
375     return pow(V[0]*V[0]+V[1]*V[1]+V[2]*V[2],0.5);
376  }
377
378  int approximately_equal_to(real number1, real number2)
379  {/* Checking if specified number1 is close to number2
380    eg 400.1 is close to 399 or 401
381   */
382   int result; real max_margin_percent=1./100.;
383   result=No;
384   if ((number1-number2)>0.){if ((number1-number2)<=max_margin_percent*number1) {
     result=Yes;}}
385   if ((number1-number2)<0.){if ((number2-number1)<=max_margin_percent*number2) {
     result=Yes;}}
386   if (number1==number2) {result=Yes;}
387   return result;
388  }
```

/otherfunctions.h 8

```
389
390  int IsMyNeighbour(cell_t c, Thread *ct, cell_t *c_n, Thread **ct_n, int num)
391  { /* IsMyNeighbour(c,ct,c_n,ct_n,num)
392      c,ct is me, c_n,ct_n is the neighbour num is the face number
393     */
394  face_t f; Thread *tf;
395       f = C_FACE(c,ct,num);
396       tf = C_FACE_THREAD(c,ct,num);
397  if (THREAD_TYPE(tf) != THREAD_F_WALL) /*!BOUNDARY_FACE_THREAD_P(tf))*/
398   {  (*c_n) = F_C0(f,tf);
399        if((*c_n) == c)
400           {  (*c_n) = F_C1(f,tf);
401             (*ct_n) = F_C1_THREAD(f,tf);
402            }
403        else
404           {
405             (*ct_n) = F_C0_THREAD(f,tf);
406            } return Yes;
407   } return No;
408  }
409  /* ************************July 2012*****************************************/
410  real within_360(real theta)
411  { return  theta-360.*floor(theta/360.);
412   }
413  int radial_pointer(real theta,int V_axis)
414  {
415  /*Creates a radial pointing vector...
416          DEBUG: outwards from impact center */
417
418   int outward_sign=0;
419   theta=within_360(theta);
420
421   if (V_axis==Axis_x) /* V_x-axis*/
422      {
423      if(theta>  0.    && theta< 90. ) outward_sign= 1;
424       if(theta> 90.   && theta<270. ) outward_sign=-1;
425       if(theta>270.   && theta<360. ) outward_sign= 1;
426       if(theta==  0.  || theta==360.) outward_sign= 1;
427       if(theta== 90.  || theta==270.) outward_sign= 0;
428      }
429    if (V_axis==Axis_y)
430      {
431      outward_sign=1;
432      }
433    if (V_axis==Axis_z)
434      {
435       if(theta>  0.  && theta< 180. ) outward_sign= 1;
436       if(theta>180.  && theta< 360. ) outward_sign=-1;
437       if(theta==  0. || theta==180. || theta==360.) outward_sign= 0;
438      }
439  return outward_sign;
440  }
441  int find_substring(char *needle, char *haystack)
442  { int h_index,n_index,matched_counts,ret;  /*char *p, *p2;*/
443   matched_counts=0; ret=No;
444    for(h_index=0; h_index<sizeof(haystack); h_index++)
```

/otherfunctions.h 9

```
445     { for(n_index=0; n_index<sizeof(needle); n_index++)
446         { if(needle[n_index]==haystack[h_index+n_index])
447             matched_counts++;
448         }
449         if (matched_counts==sizeof(needle))
450            {ret=Yes;
451           /* CX_Message("Needle=%s Hay=%s\n", needle,haystack);*/
452            }
453         matched_counts=0;
454     }
455 
456     return ret;
457 }
458 
459 void echo(char texts[100])
460 {/*
461 CX_Message("*-*-*-*-*-*-*-*-*---::::::: >> ");
462  CX_Message(texts);
463  CX_Message("\n");*/}
464 
465 void freeup_All_Injectors()
466 {int i;
467 /*LIQ_RHO=999.;debug */
468 
469 /* Set the children injection start to 1 micro seconds after current timestep */
470 childrenInjectionStarts=CURRENT_TIME+VOF_FLOW_TIME_STEPS;
471 
472 CX_Message("INFO. ONLY: Children injection can only start after %g
    micro-seconds\n"
473             ,1000000.*childrenInjectionStarts);
474 
475 for (i=0;i<MAX_NUMBER_OF_CHILD_INJECTORS;i++)
476    {  child_injector[i].ID=i;
477       child_injector[i].MotherID=-1;
478       child_injector[i].free=Yes;
479       child_injector[i].number_of_droplets=1;
480       child_injector[i].mass_flow_rate=SMALLEST_NUMBER;
481       child_injector[i].diam=1.;
482       child_injector[i].u=0.;
483       child_injector[i].v=0.;
484       child_injector[i].w=0.;
485       child_injector[i].x=0.;
486       child_injector[i].y=0.;
487       child_injector[i].z=0.;
488           child_injector[i].Temp=300.;
489           child_injector[i].Rho=LIQ_RHO;
490     }
491 }
492 void freeup_Injector(int ID)
493 { if(ID>-1)
494    {  child_injector[ID].free=Yes;
495       child_injector[ID].MotherID=-1;
496       child_injector[ID].number_of_droplets=1;
497       child_injector[ID].mass_flow_rate=SMALLEST_NUMBER;
498       child_injector[ID].diam=1.;
499       child_injector[ID].u=0.;
```

/otherfunctions.h 10

```
500         child_injector[ID].v=0.;
501         child_injector[ID].w=0.;
502         child_injector[ID].x=0.;
503         child_injector[ID].y=0.;
504         child_injector[ID].z=0.;
505       }
506   }
507   int get_Injector_ID_Waiting()
508   {int ID,i;
509   ID=-1;
510     /* Search for the next DPM waiting to inject */
511    for (i=0;i<MAX_NUMBER_OF_CHILD_INJECTORS;i++)
512     { if(child_injector[i].free==No)
513        {/*A child injection found waiting*/
514         return i;
515        }
516     }
517   return ID;
518   }
519
520   int NextInjectorID()
521   {int ID,i;
522   ID=-1;
523    for (i=0;i<MAX_NUMBER_OF_CHILD_INJECTORS;i++)
524     { if(child_injector[i].free==Yes)
525        {/*A child injection free for use*/
526         return i;
527        }
528     }
529   return ID;
530   }
531
532   void initInjectors()
533   {/* int i;*/
534       freeup_All_Injectors();
535       CX_Message ("\n\n WARNING: Liquid Phase Density= %g kg/m3\nChange in
      globalvars.h\n!----Initialisation Complete\n\n",LIQ_RHO);
536   }
537
538   real liq_source(real foo)
539   {   if(counter<200 && foo!=0.)
540        /* Print Source Terms on screen 200X only */
541           {CX_Message("--***Run Water MASS Source %E\n", foo);counter++; }
542       if (Not_A_Number(foo)==Yes) /*IF NOT A NUMBER eg INFINITY*/
543            {foo=0.;
544             if(counter<20) echo("WARNING:NAN Zeroed LiquidSrce");
545            }
546       if (foo>9.*pow(10,18)) /*Bound Input*/
547         {if (foo!=0.) CX_Message("WARNING: Mass Source %E>9e+018 IGNORED\n\n",foo);
548          foo=0.;
549         }
550       return foo;
551   }
552
553   real gas_source(real foo)
554   {real LiqPhaseRho;
```

/otherfunctions.h 11

```
555    LiqPhaseRho =LIQ_RHO; /* DEBUG: Do not Hardcode*/
556                    foo = foo/LiqPhaseRho;
557      if(counter<20 && foo!=0.)
558       {CX_Message("--***Run Air MASS Source %E\n", -foo);counter++; }
559    if (Not_A_Number(foo)==Yes) /*IF NOT A NUMBER eg INFINITY*/
560        {foo=0.;
561         if(counter<20) echo("WARNING:NAN Zeroed GasSource");
562        }
563
564   /*  if(foo!=0.) {CX_Message("*-*-*- Mass Source: %E\n",foo);counter++;}*/
565       if (foo>9.*pow(10,18)) /*Bound Input*/
566         {if (foo!=0.)
567            if(counter<20) CX_Message("!!WARNING Air MASS Source %E >-9e+018
              IGNORED\n\n",-foo);
568            foo=0.;
569          }
570   return -foo;
571   }
572   real energy_source(real foo)
573   {if(foo!=0. && counter_erg<2000)
574     {CX_Message(" *-*-*-Mass Averaged Temp: %g\n",foo);counter_erg++;}
575   /* edit 26/Nov/2012
576    Energy source used to be passed: Now Mass Averaged temp is set
577     if (foo>9.*pow(10,18))
578      {if (foo!=0.)CX_Message("----->>> ENERGY Source %E > 9e18 is Ignored\n",foo);
579        foo=0.;
580      }*/
581   return 0.; /* foo;*/
582   }
583
584   /*Functions 27/Nov/2012 */
585   void computeNormal(cell_t c, Thread *ct, real *Normal_N)
586   {/* Normal=gradPhi/|gradPhi| by definition */
587   real dot;
588   /* Reconstructed VoF Grad :use either better use this*/
589       Normal_N[Axis_x] =C_UDMI(c,ct,VOF_R_GRADIENT_x);
590       Normal_N[Axis_y] =C_UDMI(c,ct,VOF_R_GRADIENT_y);
591       Normal_N[Axis_z] =C_UDMI(c,ct,VOF_R_GRADIENT_z);
592           dot = NV_MAG(Normal_N);
593                   if(dot<=0.) dot=1.;
594                       /*Compute Normal in the cell*/
595                       Normal_N[Axis_x]/=dot;  Normal_N[Axis_y]/=dot; Normal_N[
                        Axis_z]/=dot;
596   if (counter!=250){CX_Message("\n----------------\nImpact Normal:
      (%gi+%gj+%gk)\n"
597                           ,Normal_N[Axis_x],Normal_N[Axis_y],Normal_N[Axis_z]);
                            counter++;}
598   }
599
600   #endif
601
```

A.2 .c file

/dpmvof.c 1

```
#include "udf.h"
#include "sourceterms.h"

/* Prototypes */
 /* moved to otherfunctions.h */
/*Global variables
 child_injector_t  */
int ndrops=0;
real xVelocityRelaxation =1.;
real yVelocityRelaxation =1.;
real zVelocityRelaxation =1.;
int MotherIDUsed=-1;
int counter,K;  real sums;
real sum_mass; /*DEBUG: Remove these later*/
real dry_wall_vof_after_impact;
int once=1;
/* -=-=-=-=-=-=-=-=-=-=-=-=-=-=-=-=-=-=-=-=-=-=-=-=-=-=-=-=-=-=-=-=-=-=-=-
   END DECLARATIONS AND PROTOTYPING
   -=-=-=-=-=-=-=-=-=-=-=-=-=-=-=-=-=-=-=-=-=-=-=-=-=-=-=-=-=-=-=-=-=-=-=-
  */
real getFilmThickness(real *ScanZONE)
{ /*##########################################*/

real SR_Max; /* Max. region to scan hstar=1.1 */
real hstar,R_new_scan_distance;
int dummy;
real dp;
real xc[ND_ND];
int n; cell_t c; Thread *ct,*f_thread; /* face_t face; */
Domain *subdomain;


 /*Scan around the spread sphere range for film
 if impact is at a wall, it is a dry wall
 if it is at a free surface, it is a thin film...but scan further till h*=1,
 if there is film within h*>1, it is a droplet approaching a thick film

 if (VERBOSE==1) CX_Message("ScanZONE x%E,y%E,z%E, R%E,wall%d \n",
                         ScanZONE[Axis_x],
                         ScanZONE[Axis_y],
                         ScanZONE[Axis_z],
                         ScanZONE[Rscan],
                         ScanZONE[itsWall]

                         );*/
subdomain  =Get_Domain(LIQUID_PHASE_ID);
      dummy=1;
        dp =ScanZONE[Rscan]*2.; /*Rscan comes with particle radius */

if(ScanZONE[itsWall]==Yes)
     {hstar=0.; /* This is a dry wall: Call from Wall BC enables is_wall=Yes*/
     }
else
     { /*  */
SR_Max=dp*SR_STAR_MAX;
hstar=SMALLEST_NUMBER;
```

/dpmvof.c 2

```
57
58          thread_loop_c(ct,subdomain)
59           { begin_c_loop (c,ct)
60               { C_CENTROID(xc,c,ct);
61                /* The Spherical SCAN range */
62                R_new_scan_distance=ScanRange(xc,ScanZONE);
63                if (R_new_scan_distance<=SR_Max)
64                  { /*If any cell has vof>0,5 it has fluid */
65                  if(C_VOF(c,ct)>=interface_vof1)
66                      {/*still in thin film  */
67                        hstar=getMAXIMUM(R_new_scan_distance,hstar);
68                      /* if (VERBOSE==1) CX_Message("Current depth Scan Radius
                        =%3.2f mm  VoF =%3.2f\n",1000*hstar,C_VOF(c,ct));
69                    */
70                    /*If any wall BC is found when R<SR_Max it is a thin film */
71                      /*Check face thread only in the film range */
72                       c_face_loop(c,ct,n)
73                         {   /* face = C_FACE(c,ct,n);*/
74                          f_thread = C_FACE_THREAD(c,ct,n);
75                          if (THREAD_TYPE(f_thread) == THREAD_F_WALL)
76                            {/*This cell is at a wall*/
77                            dummy=0;
78                            }
79                          }
80                      }
81                  }
82               }end_c_loop(c,ct)
83           }
84       }
85  /* if (VERBOSE==1) CX_Message("h* =%E  SR_Max =%E
    dummy=%d\n",hstar,SR_Max,dummy); */
86   if(dp<0.) {dp=1.;hstar=0.;} /*dont crash */
87       hstar/=dp; /*relative film thickness */
88    /*if(dummy==0) hstar=hstar_THIN_FILM; */
89
90  if(dummy>0)
91  {/*Did not hit a wall*/
92    if(hstar>SMALLEST_NUMBER)
93      { /*Film is still away..must be a thick film
94        If mesh is coarse, it might not be able to scan far
95         thus predicting a thin film in error
96         */
97       if(hstar<1) /*Correct this*/
98         hstar=SR_STAR_MAX;
99      }
100 }
101
102 if(hstar<1.)
103   {/*if(dummy==0)
104     echo("Droplet hits dry wall");
105       else*/
106     echo("Droplet approaching THIN film");
107   }
108 else
109   echo("Droplet approaching THICK film");
110
```

/dpmvof.c 3

```
111     return hstar;
112   }
113   real ScanRange(real *xc,real *ScanZONE)
114   {
115   return    sqrt(ND_SUM(pow(xc[Axis_x] - ScanZONE[Axis_x],2.),
116                         pow(xc[Axis_y] - ScanZONE[Axis_y],2.),
117                         pow(xc[Axis_z] - ScanZONE[Axis_z],2.)
118                 ));
119   }
120   real SphericalRange(real *xc,real *SpreadSphere)
121   {/*Returns the Length of two Points
122      This is used to know if the points
123      lie in the spherical domain to mark
124      xc is the Centroid of the Cell
125      SpreadSphere is the point marked*/
126      return sqrt(ND_SUM(pow(xc[Axis_x] - SpreadSphere[Axis_x],2.),
127                         pow(xc[Axis_y] - SpreadSphere[Axis_y],2.),
128                         pow(xc[Axis_z] - SpreadSphere[Axis_z],2.)
129                 ));
130   /*  return sqrt(ND_SUM(pow(xc[Axis_x] - SpreadSphere[Axis_x],2.),
131                         pow(xc[Axis_y] -
132                         (SpreadSphere[Axis_y]+0.1*SpreadSphere[Axis_z+1]),2.),
133                         pow(xc[Axis_z] - SpreadSphere[Axis_z],2.)
134                 ));  0.1*SpreadSphere[Axis_z+1] =10% Spread Radius?
135     */
136   }
137   void SpreadMassSource(real *SpreadSphere )
138   {/*SpreadSphere (x,y,z,R,M)
139      Centre (x,y,z):   R= Radius: M= Total Mass Source:kg/m3s */
140   /*Declaring Variables*/
141       int i,phase_domain_index;
142       int CentreChecked;
143   /* n,real Prant; real NU_selt;
144   real Ap; real mp;
145   real Dp; real HTC;
146   real tcond, Miu; */
147    cell_t c,c_home;
148    Thread *ct,*ct_home;
149      real R_range,xc[ND_ND],massadded;
150      real R_range_smallest;
151      real Rmin,RminNew,dummy,massadded_toThisCell;
152      real countCells;
153      real Tf;
154   /*face_t f; Thread *ft;*/
155   Domain *mixture_domain,*subdomain;
156
157   /*End Variable Declarations*/
158        phase_domain_index  =0;
159                countCells  =0.;
160                      Rmin  =LARGEST_NUMBER;
161                    RminNew  =0.;
162          R_range_smallest  =LARGEST_NUMBER;
163            mixture_domain  =Get_Domain(1);
164                 subdomain  =Get_Domain(LIQUID_PHASE_ID);
165   /* Loop to Mark the Cell Thread for Mass Source */
166
```

/dpmvof.c 4

```
167  /*
168  MARKING:
169   The Spherical Droplet is enclosed within a Box
170  (1) Loop over all cells in the domain
171      and Mark Cells in the Sphere
172      -Slow? Note: The call to this loop is from
173      DPM drag (Memory can cause issues?)
174  (2) Alternative using CX_Find_Cell_With_Point()
175      not working but looks nice
176  (3) Loop over cell Neighbours radially outwards
177      to get cell within the box.
178      Problem is the complex structure and
179      multiple marking of same cell
180
181  Clip to the Box Inside
182  */
183                  i  =0;
184           massadded  =SpreadSphere[M];
185               dummy  =0.;
186       CentreChecked  =No;
187  /*Spread the Mass sources
188    in ratio of volume of cell
189    to total sphere vol
190  VolSphere=PI*pow(2.*SpreadSphere[R],3.)/6.;*/
191  /*Is Counting first Not EFFICIENT??
192  No. It is better, as cells to be spread to might be wall
193  bounded and less than the diam to spread to.
194  COUNT: How many cells to add */
195  if (SpreadSphere[M]>0)
196  {
197  thread_loop_c(ct,subdomain)
198   {/*if (VERBOSE==1) CX_Message("*********Thread Counter %d\n", i+10000);*/
199   begin_c_loop (c,ct)
200   { C_CENTROID(xc,c,ct);
201    /* The Spherical Domain range to mark */
202    R_range=SphericalRange(xc,SpreadSphere);
203    if (R_range<=R_range_smallest)
204      { R_range_smallest=R_range;
205        c_home=c; ct_home=ct;
206      }
207
208    if (R_range<=SpreadSphere[R])countCells+=1.;
209   }end_c_loop(c,ct)
210  }
211  /* if countCells<=0, the DPM is so small
212     that it can pass inside the cell and not close to the centroid
213     in this case, check this cell and dump the mass there
214     :The Current Cell has the closest range
215  */
216  if(countCells<=0 && R_range_smallest!=LARGEST_NUMBER)
217  { /*Dump in current cell */
218    c  = c_home;  ct = ct_home;  countCells=1;
219    echo("DPM dumped in the current cell ONLY, NO SPREADING REQUIRED");
220                   massadded_toThisCell =    SpreadSphere[M]/(C_VOLUME(c,ct));
221                  C_VOF_DPM_M_SRC(c,ct) =    massadded_toThisCell;
222              C_VOF_DPM_MOM_SRC_X(c,ct) =    massadded_toThisCell*SpreadSphere[
```

/dpmvof.c 5

```
            xVel];
223         C_VOF_DPM_MOM_SRC_Y(c,ct) =    massadded_toThisCell*SpreadSphere[
            yVel];
224         C_VOF_DPM_MOM_SRC_Z(c,ct) =    massadded_toThisCell*SpreadSphere[
            zVel];
225       if(fabs(C_VOF_DPM_H_SRC(c,ct))<=0.) /* Mass average once on 1 dpm
          impact*/
226         {       Tf=C_T(c,ct); dummy=C_VOF(c,ct);
227                 if (Tf>=MIN_TEMPERATURE || Tf<=MAX_TEMPERATURE)Tf=
                    MIN_TEMPERATURE;
228                 if (dummy<0.1) dummy=0.5; dummy*=LIQ_RHO;
229         /* Mass Averaged expected temperature */
230         C_VOF_DPM_H_SRC(c,ct) = ( dummy*Tf+massadded_toThisCell*SpreadSphere
            [TEMP2])
231                                             /(dummy+massadded_toThisCell);
232         }
233       if (once<20){if (VERBOSE==1) CX_Message("*********Source Mass %g MomY
          %g Temp=%g \n",
234       C_VOF_DPM_M_SRC(c,ct) ,C_VOF_DPM_MOM_SRC_Y(c,ct),C_VOF_DPM_H_SRC(c,ct));
235                   once++;
236                 }
237 }/*end Dump in current cell */
238 else
239 {
240         /* Spread Mass Source EQUALLY in the Cell */
241   thread_loop_c(ct,subdomain)
242     {/*if (VERBOSE==1) CX_Message("*********Mass Sphere %E \n",
      SpreadSphere[M]); */
243       begin_c_loop (c,ct)
244         { /*if (VERBOSE==1) CX_Message("Count Domain Loop: %d\n",i++);*/
245         C_CENTROID(xc,c,ct);
246         /* The Spherical Domain range to mark */
247           R_range=SphericalRange(xc,SpreadSphere);
248        if (R_range<=SpreadSphere[R])
249           /* This means the DPM is bigger than the cell!
250            The Distribution of Mass/Momentum and HT
251            goes to the cells in the R_range region  */
252         { /* MASS SOURCE   C_VOF(c,ct)=interface_vof;*/
253             /* Keep the Left over mass for the centre*/
254         massadded_toThisCell  =  SpreadSphere[M]/(C_VOLUME(c,ct)*countCells
            );
255             C_VOF_DPM_M_SRC(c,ct)  =    massadded_toThisCell;
256         C_VOF_DPM_MOM_SRC_X(c,ct)  =    massadded_toThisCell*SpreadSphere[
            xVel];
257         C_VOF_DPM_MOM_SRC_Y(c,ct)  =    massadded_toThisCell*SpreadSphere[
            yVel];
258         C_VOF_DPM_MOM_SRC_Z(c,ct)  =    massadded_toThisCell*SpreadSphere[
            zVel];
259
260         if(fabs(C_VOF_DPM_H_SRC(c,ct))<=0.) /* Mass average once on 1 dpm
            impact*/
261                {  Tf=C_T(c,ct); dummy=C_VOF(c,ct);
262                 if (Tf>=MIN_TEMPERATURE || Tf<=MAX_TEMPERATURE)Tf=
                    MIN_TEMPERATURE;
263                 if (dummy<0.1) dummy=0.5; dummy*=LIQ_RHO;
264
```

/dpmvof.c 6

```
265                          /* Mass Averaged expected temperature */
266                         C_VOF_DPM_H_SRC(c,ct) =
267                                    ( dummy*Tf+massadded_toThisCell*SpreadSphere
                                       [TEMP2])
268                                              /(dummy+massadded_toThisCell);
269
270                       }
271              if (once<20){
272      if (VERBOSE==1)
273      CX_Message("*********Source Mass %g MomY %g Temp=%g \n",
274                  C_VOF_DPM_M_SRC(c,ct) ,C_VOF_DPM_MOM_SRC_Y(c,ct),
                    C_VOF_DPM_H_SRC(c,ct));
275                           once++;
276                          }
277
278              }
279          }end_c_loop(c,ct)
280
281      }     once=0;
282  }
283  }
284
285   if (VERBOSE==1) CX_Message ("****Mass of Droplet Sphere=%E\n Spread to %g
     Cells\n\n",
286                  SpreadSphere[M],countCells);
287   /*return void;*/
288  }
289
290  int add_tracked_particle_to_vof(Tracked_Particle *p, face_t c, Thread *ct,int
     is_wall,real VOF)
291  { /*########################################*/
292    /*########################################*/
293  /*Declaring Variables */
294  /*
295    cell_t c_n;  Thread *ct_n; */
296    /*Neighbour cells*/
297    /* face_t f;  Thread *tf; */
298    real foo,We,Re,film_thickness;  real l_scale;/*mass_src_increment,*/
299    real Miu, Rho,surface_tension, L,Vp,V_fluid; /*,x,y, JetLength;*/
300    real Vel[3],v_cont[3]; int droplet_impact_outcome,no_faces,no_cells_to_add;
301    real massadded,mass_fraction_absorbed,dry_wall_factor;
302    real Dp,Oh;  real mass_vof_patch;
303    real Beta,percent_others,percent;
304    real WeCrown,Vcrown;
305    real SpreadSphere[8+2];
306    real ScanZONE[DIM_SCANNER]; /*Droplet impact point */
307    real secondary_drop_temp;
308       int R,M;
309       int xVel,yVel,zVel,Cp,TEMP;
310    /* unused variables to be removed DEBUG
311    int i,
312    real ds;
313    */     /* Diam. and no. of secondary droplets*/
314   /*Ending Variable Declarations*/
315  /*Don't do anything for a Dead particle */
316   droplet_impact_outcome=DROP_STICKS; /* Default */
```

/dpmvof.c 7

```
317     WeCrown=Vcrown=0.;    no_cells_to_add       =0;
318           no_faces=0;             percent_others=percent=0.;
319      Beta=1;R=Axis_z+1;M=R+1;xVel=M+1;yVel=M+2;zVel=M+3;Cp=zVel+1;TEMP=Cp+1;
320   foo=1.;
321   if(P_FLOW_RATE(p)<=SMALLEST_NUMBER)
322   {foo=0.;if (VERBOSE==1) CX_Message("\n\n----Droplet Dead---Continue(Yes/No?)
      Yes Selected \n");
323      /*return DROP_DEAD; */
324   }
325   /* ################### */
326   massadded=0.;mass_vof_patch=0.;dry_wall_factor=1.;
327   mass_fraction_absorbed=1.;
328   /* Since Stick is default: 100% absorbed*/
329   /*Velocity of DPM particles*/
330   Vel[Axis_x]= P_VEL(p)[Axis_x];  Vel[Axis_y]= P_VEL(p)[Axis_y]; Vel[Axis_z]=
      P_VEL(p)[Axis_z];
331   /*Velocity of Eulerian Phase*/ v_cont[Axis_x]=C_U(c,ct);    v_cont[Axis_y]=C_V(c
      ,ct);    v_cont[Axis_z]=getGoodNumber(C_W(c,ct));
332   Vp = getMagnitude(Vel);
333         surface_tension=getMAXIMUM(DPM_SURFTEN(p),surf_ten);
334         Rho=P_RHO(p);
335         Dp= L=P_DIAM(p);
336
337        /*Miu= getMAXIMUM (SMALLEST_NUMBER,C_MU_EFF(c,ct));*/
338         Miu= getMAXIMUM (SMALLEST_NUMBER,LIQ_MU);
339         V_fluid=getMagnitude(v_cont);
340
341
342         ScanZONE[Axis_x]=p->state.pos[Axis_x];
343         ScanZONE[Axis_y]=p->state.pos[Axis_y];
344         ScanZONE[Axis_z]=p->state.pos[Axis_z];
345         ScanZONE[Rscan]=0.5*Dp;
346         ScanZONE[itsWall]=is_wall;
347
348
349         film_thickness=getFilmThickness(ScanZONE);
350         l_scale=getCell_height_Y(c,ct);
351   /*################### Mass Source ######################*/
352    P_MASS(p)= massadded= (Rho*M_PI*pow(Dp,3)/6.);
353   massadded = foo*massadded/CURRENT_TIMESTEP;
354               /*
355               foo*P_MASS(p)/CURRENT_TIMESTEP;
356               P_MASS(p)/CURRENT_TIMESTEP same as P_FLOW_RATE(p); but better for
                  variable time step*/  /*/(C_VOLUME(c,ct));*/
357
358   /*      ------------------------- */
359                 We=foo*getMAXIMUM(getWeber(Rho,Vp,L,surface_tension),
                    SMALLEST_NUMBER );
360                 Re=foo*getReynolds(Rho,Vp,V_fluid,L,Miu);
361                 Oh=Ohnesorg(Dp);
362                if (VERBOSE==DEBUG)
363                       CX_Message("=+=+We=%E Re=%E Vp=%g V_fluid=%g Miu=%E\n",We,Re
                          ,Vp,V_fluid,Miu);
364    /* ########################################*/
365   /*Debug Here*/
366   if (massadded!=0. && Re>0.)
```

/dpmvof.c 8

```
367  {if (is_wall!=Yes)
368  droplet_impact_outcome=drop_impact_outcome(We,Re,film_thickness,Oh);
369   /*DEBUG: Testing Mass Transfer...DO NOT SPLASH...Just STICK ALL
370          droplet_impact_outcome=DROP_STICKS;
371     End Debug
372
373       Crown Velocity */ /* WeCrown=getCrownWeber(Re,We);
374           Vcrown=pow(WeCrown*surface_tension/(Rho*L),0.5); Vp x 0.55; 55 percent
              */
375          /* ds=4.23*2*L/WeCrown;  second. drop diam Rayleigh Taylor*/
376    if (is_wall==Yes)
377    {droplet_impact_outcome=drop_impact_outcome(We,Re,0.,Oh);
378     /* Film is at a wall bounded Cell*/
379      if (VERBOSE==1) CX_Message("\n**-*-*-Droplet Impacting Cell Wall -DPM-VOF\n"
       );
380      switch (droplet_impact_outcome)
381         {  case DROP_STICKS:
382               { /* Stop Particle tracking */
383               echo("Droplet STICKS to WALL x89779854f");
384                 mass_fraction_absorbed=1.; /* 100% absorbed */
385                 /*Create Source Terms
386                   :Distribute to Neighbour Cells
387                    within the
388                       1. One Cell ONLY?
389                       2. Spherical/Hemispherical range
390                           Using Petudo/Marengo/Tropea
                            correlations?
391
392                 CreateSourceTerms(SpreadRadius);
393                 dD*\dT* =+xVelocityRelaxation=zVelocityRelaxation
394                 dY*\dT* =+zVelocityRelaxation
395                 */
396                   SpreadSphere[Axis_x]=p->state.pos[Axis_x];
397                   SpreadSphere[Axis_y]=p->state.pos[Axis_y];
398                   SpreadSphere[Axis_z]=p->state.pos[Axis_z];
399
400                   SpreadSphere[xVel]=xVelocityRelaxation=1.;
401                   SpreadSphere[yVel]=yVelocityRelaxation=1.;
402                   SpreadSphere[zVel]=zVelocityRelaxation=1.;
403                   SpreadSphere[xVel]*=p->state.V[Axis_x];
404                   SpreadSphere[yVel]*=p->state.V[Axis_y];
405                   SpreadSphere[zVel]*=p->state.V[Axis_z];
406
407                   SpreadSphere[R]=getSpreadRadiusCorrelation(0.5*P_DIAM(p));
408                   SpreadSphere[M]=massadded;
409                   SpreadSphere[Cp]=DPM_SPECIFIC_HEAT(p,p->state.temp);
410                    SpreadSphere[TEMP2]=p->state.temp;
411                 if (VERBOSE==1) CX_Message(">>>>>>>Sp. Heat Capacity of DPM: %E
                    Ave. Temp %3.4f\n"
412                                 ,SpreadSphere[Cp],SpreadSphere[TEMP2]);
413
414                       SpreadMassSource(SpreadSphere);
415                         Kill_DPM(p,ct,massadded);
416
417
418                          break;
```

/dpmvof.c 9

```
419                         }
420                    case DROP_SPLASHES:
421                         {  /*Make a splash:: Debug and create correct splash*/
422                           /* 0.65; DEBUG HERE: Assuming the droplet creates a
                              splash 35% of its size*/
423                            /*secondary_drop_temp=420.; Debug:
424                            mass_fraction_absorbed
425                              =create_splashed_drops_old(p,secondary_drop_temp);*/
426                 echo("====Drop Splashing WALL...xg08887hf");
427                          /*-----------------SPLASH HANDLE*/
428                            /*Make a splash:: Debug and create correct splash
429                          0.65;*/
430                          secondary_drop_temp=C_T(c,ct); /*Debug: */
431
432                    /* Reduce momentum */
433                     SpreadSphere[Axis_x]=p->state.pos[Axis_x];
434                     SpreadSphere[Axis_y]=p->state.pos[Axis_y];
435                     SpreadSphere[Axis_z]=p->state.pos[Axis_z];
436                          /*DEBUG reducing impact momentum*/
437                         /*reduce by normal component*/
438                          xVelocityRelaxation=1.;
439                          yVelocityRelaxation=1.-Secondary_Drop_Mean_Velocity(1.);
440                          zVelocityRelaxation=1.;
441                     SpreadSphere[xVel]=xVelocityRelaxation;
442                     SpreadSphere[yVel]=yVelocityRelaxation;
443                     SpreadSphere[zVel]=zVelocityRelaxation;
444
445                     SpreadSphere[xVel]*=p->state.V[Axis_x];
446                     SpreadSphere[yVel]*=p->state.V[Axis_y];
447                     SpreadSphere[zVel]*=p->state.V[Axis_z];
448                           /*DEBUG reduce spread now*/
449                     SpreadSphere[R]=getSpreadRadiusCorrelation(0.5*P_DIAM(p));
450                     SpreadSphere[M]=mass_fraction_absorbed*massadded;
451                      SpreadSphere[Cp]=DPM_SPECIFIC_HEAT(p,p->state.temp);
452                      SpreadSphere[TEMP2]= p->state.temp;
453                   mass_fraction_absorbed
454                          =create_splashed_drops_old(p,secondary_drop_temp);
455                           SpreadMassSource(SpreadSphere);
456                    Kill_DPM(p,ct,massadded);
457
458
459                              break;
460                         }
461                    case DROP_BOUNCES:
462                         {   echo("Droplet bounces xh8999056");
463                             mass_fraction_absorbed=0.; /* 100% absorbed*/
464                              break;
465                         }
466                    case DROP_SPREADS:
467                         {  echo("Droplet sticks xhh08909h");
468                            mass_fraction_absorbed=1.; /* 100% absorbed*/
469                            break;
470                         }
471
472                  } /*end switch*/
473               } /*end if is_wall*/
```

/dpmvof.c 10

```
474       /*ELSE---> Film is not attached to a wall FILM IS FLOATING IN SPACE
          ---DEBUG*/
475        /* else
476             {
477                switch (droplet_impact_outcome)
478                  {
479                   case DROP_STICKS_NON_WALL:
480                         {*/
481                         /* Stop Particle tracking */
482                               /*if (Beta<=0) Kill_DPM(p,ct);*/
483                               /*if (VERBOSE==1) CX_Message("DPM killed and
                                  sticked as vof to NON-WALL-FILM \n");
484                          */
485                          /*
486                             break;
487                         }
488                    case DROP_SPLASHES_NON_WALL:
489                         { break;}
490                    case DROP_BOUNCES_NON_WALL:
491                         { break;}
492                    case DROP_SPREADS_NON_WALL:
493                         { break;}
494                   }
495             }
496           */
497   /* The code below should run at film interface Not at the wall Cell
498     ...Need to put in the if iswall case above
499     ...this is just simplified now to forge ahead and fast
500   ------------------------------------FILM INTERFACE -------------
501   */
502   if (is_wall==No)
503             {
504           if (droplet_impact_outcome==DROP_SPLASHES)
505             {/*Running Splashing Action */
506                 echo("====Drop Splashing...xh00988");
507                          /*-----------------SPLASH HANDLE*/
508                            /*Make a splash:: Debug and create correct splash
509                          0.65;*/
510                          secondary_drop_temp=C_T(c,ct); /*Debug: */
511
512                    /* Reduce momentum */
513                     SpreadSphere[Axis_x]=p->state.pos[Axis_x];
514                     SpreadSphere[Axis_y]=p->state.pos[Axis_y];
515                     SpreadSphere[Axis_z]=p->state.pos[Axis_z];
516                          /*DEBUG reducing impact momentum*/
517                         /*reduce by normal component*/
518                          xVelocityRelaxation=1.;
519                          yVelocityRelaxation=1.-Secondary_Drop_Mean_Velocity(1.);
520                          zVelocityRelaxation=1.;
521                     SpreadSphere[xVel]=xVelocityRelaxation;
522                     SpreadSphere[yVel]=yVelocityRelaxation;
523                     SpreadSphere[zVel]=zVelocityRelaxation;
524
525                     SpreadSphere[xVel]*=p->state.V[Axis_x];
526                     SpreadSphere[yVel]*=p->state.V[Axis_y];
527                     SpreadSphere[zVel]*=p->state.V[Axis_z];
```

/dpmvof.c 11

```
528                         /*DEBUG reduce spread now*/
529                   SpreadSphere[R]=getSpreadRadiusCorrelation(0.5*P_DIAM(p));
530                   SpreadSphere[M]=mass_fraction_absorbed*massadded;
531                    SpreadSphere[Cp]=DPM_SPECIFIC_HEAT(p,p->state.temp);
532                    SpreadSphere[TEMP2]= p->state.temp ;
533                mass_fraction_absorbed
534                       =create_splashed_drops_old(p,secondary_drop_temp);
535                        SpreadMassSource(SpreadSphere);
536                Kill_DPM(p,ct,massadded);
537
538                    } /*-----------------End Splash Handle*/
539          if (droplet_impact_outcome==DROP_SPREADS)
540                    {/*Running Spreading Action*/
541                      mass_fraction_absorbed=1.; /* 100% absorbed*/
542                      echo("=========Droplet Spreading x0000f");
543                      /*if (Beta<=0) Kill_DPM(p,ct);*/
544                    }
545          if (droplet_impact_outcome==DROP_STICKS)
546                     {/*Running Droplet Sticking*/
547                     echo("Droplet sticks xx8900077");
548                     /*if (VERBOSE==1) CX_Message("\n---------Drop Sticks
                       Non-Wall CELL\n");*/
549                         mass_fraction_absorbed=1.;
550                         /* 100% absorbed
551                         CreateSourceTerms(SpreadRadius);*/
552                   SpreadSphere[Axis_x]=p->state.pos[Axis_x];
553                   SpreadSphere[Axis_y]=p->state.pos[Axis_y];
554                   SpreadSphere[Axis_z]=p->state.pos[Axis_z];
555
556                    /* CreateSourceTerms(SpreadRadius);
557                  dD*\dT* =+xVelocityRelaxation=zVelocityRelaxation
558                  dY*\dT* =+zVelocityRelaxation
559                  */
560                   SpreadSphere[xVel]=xVelocityRelaxation;
561                   SpreadSphere[yVel]=yVelocityRelaxation;
562                   SpreadSphere[zVel]=zVelocityRelaxation;
563
564                   SpreadSphere[xVel]*=p->state.V[Axis_x];
565                   SpreadSphere[yVel]*=p->state.V[Axis_y];
566                   SpreadSphere[zVel]*=p->state.V[Axis_z];
567
568                    SpreadSphere[R]=getSpreadRadiusCorrelation(0.5*P_DIAM(p));
569                    SpreadSphere[M]=massadded;
570                   SpreadSphere[Cp]=DPM_SPECIFIC_HEAT(p,p->state.temp);
571                   SpreadSphere[TEMP2]= p->state.temp ;
572
573          if (VERBOSE==1) CX_Message(">>>>>>>Sp.Heat Capacity of DPM: %E Average
                 Temp %3.4f\n"
574                                    ,SpreadSphere[Cp],SpreadSphere[TEMP2]);
575
576                         SpreadMassSource(SpreadSphere);
577                         Kill_DPM(p,ct,massadded);
578                      }
579
580             } /*End of no is wall*/
581
```

/dpmvof.c 12

```
582  }/*End if mass added*/
583
584  return droplet_impact_outcome;
585   }
586  int drop_impact_outcome(real We, real Re, real film_thickness, real Oh)
587  { /*########################################*/
588      int outcome; real K;
589      /*outcome=DROP_SPLASHES;*/
590      outcome=DROP_STICKS;
591      /*return DROP_SPLASHES;*/
592
593  /*return outcome;
594  Default Droplet outcome is STICK
595
596  outcome=DROP_STICKS;
597  return outcome;  STICK ALL DROPS - DEBUG HERE*/
598  /*
599  There are 4 Ranges based on h*=h/d
600             Source/Author
601  0.00-0.08  Assumed to Splash/May depend on Wall Roughness not included in this
     work
602  0.08-0.14  Yarin et al 2006
603  0.14-1.00  Cossali et al 1997
604  1.00++     Assumed based on K
605  */
606  /*if (Re!=0){Oh=pow(We,0.5)/Re;} else {Oh=0.;}Division by zero not allowed*/
607
608  K=We * pow(Oh,-2./5.);
609  if (film_thickness<0.08)
610   {/*Very Very Thin film AND Dry walls
611     if (VERBOSE==1) CX_Message("*-*-*-> h=%E K=%E/n",film_thickness,K);*/
612     if (K<400) outcome=DROP_STICKS; else outcome=DROP_SPLASHES;
613   }
614
615   if (film_thickness>=0.08 && film_thickness<0.14)
616       {/* Yarin 2006 : Very Thin film*/
617        if(approximately_equal_to(400.,K)==Yes) {outcome=DROP_SPLASHES;}
618        else outcome=DROP_STICKS;
619       }
620  if (film_thickness>=0.14 && film_thickness<1.0)
621       {/* Cossali 1997 :Thin film*/
622          K=(We * pow(Oh,-.4))/(2100. +5880. * pow(film_thickness,1.44));
623        if (K<=1.) {outcome=DROP_STICKS;} else {outcome=DROP_SPLASHES;}
624
625       }
626  if (film_thickness>=1.0)
627      { /*Assumed :Thick film, No correlations */
628        K=(2100. +5880. * pow(film_thickness,1.44));
629        if (K<5000.) {outcome=DROP_STICKS;} else {outcome=DROP_SPLASHES;}
630
631      }
632
633    /*if (VERBOSE==1) CX_Message("*-*-*-> h=%E K=%E\n",film_thickness,K);*/
634    return outcome;
635  }
636
```

/dpmvof.c 13

```
637
638  real create_splashed_drops_old(Tracked_Particle *p,real secondary_drop_temp )
639  {/*Splash is created as new DPM Particle*/
640     /* Signature:       film_mass = Mass of film turning to droplets     */
641
642  cell_t c;  Thread *ct;
643  /*Node *node;*/
644
645  /*real x[ND_ND];*/
646
647  int i,ID,MotherID,N_Children;
648  int isThisANormalSplash, AxisNormal;
649  real JetLength,K,mass_fraction_absorbed;
650  real secondary_drop_diam; /*n,real secondary_drop_temp;*/
651  real secondary_drop_x,secondary_drop_y,secondary_drop_z; /*Each drop position */
652  real NV_VEC(A),NV_VEC(B);
653
654  /*real NV_VEC(Phi);,NV_VEC(gradPhi) Level Set Variable */
655
656
657  real NV_VEC(secondary_drop_Pos);/*Position vector holding center of children
     crown, P2 */
658  real NV_VEC(impact_point);      /*Position vector holding impact location P1 */
659  /*P2=P1-|JetLength|UnitVector(Vsecondary) */
660
661  real NV_VEC(Vsecondary);    /*Velocity vector of children crown center=Vs */
662  real NV_VEC(VsecondaryBar); /*Unit Vector of Vsecondary Vsbar*/
663
664  real NV_VEC(Vprimary);    /*Velocity vector of the impact droplet=Vp*/
665
666  real NV_VEC(VprimaryBar);/* Unit vector of Vp*/
667  real NV_VEC(Normal_1); /*Normal at the impact surface*/
668  real secondary_drop_Vx , secondary_drop_Vy, secondary_drop_Vz;
669                   /*Individual secondary droplet */
670  real dot,foo;
671  real secondary_drop_velocity_magnitude,impact_magnitude;
672  real secondary_drop_mass_flow_rate; real CrownDiam;
673
674  real ring_start_angle, ring_theta,ring_theta_rad;
675  real theta_exit,sin_theta_exit, cos_theta_exit;
676
677  real ds,Oh,We;
678  /*-------------------------------------------------------------*/
679  isThisANormalSplash=No; /* Default */
680  AxisNormal =-20;
681  /*&& once<=1*/
682    if(LIQ_RHO<=0.) initInjectors(); /*DEBUG */
683    MotherID=p->part_id;
684          if(MotherID<=-1) return 1.;
685      /*Returns mass fraction absorbed =100% as there was no Droplet to splash*/
686
687         NV_D(A,=,0.,0.,0.);          NV_D(B,=,0.,0.,0.);
688         ring_start_angle =getMIN(90,cheap_uniform_random()*90);
689  /* The children are ejected as a ring
690  The angle between each child drop is ring_theta,
691  The start is randomised from 0-90 deg*/
```

/dpmvof.c 14

```
692
693       Vprimary[Axis_x]       =p->state.V[Axis_x];
694       Vprimary[Axis_y]       =p->state.V[Axis_y];
695       Vprimary[Axis_z]       =p->state.V[Axis_z];
696   impact_magnitude = NV_MAG(Vprimary);
697           if(impact_magnitude<=0. || impact_magnitude>MAX_DROPLET_SPEED)
698                   return 1.; /*NO IMPACT? impact_magnitude=1.;*/
699       VprimaryBar[Axis_x]=Vprimary[Axis_x]/impact_magnitude;
700       VprimaryBar[Axis_y]=Vprimary[Axis_y]/impact_magnitude;
701       VprimaryBar[Axis_z]=Vprimary[Axis_z]/impact_magnitude;
702
703
704       impact_point[Axis_x] = p->state.pos[Axis_x];
705       impact_point[Axis_y] = p->state.pos[Axis_y];
706       impact_point[Axis_z] = p->state.pos[Axis_z];
707   /*Compute surface normal at the impact point */
708
709   c  = P_CELL(p);
710   ct = THREAD_SUB_THREAD(P_CELL_THREAD(p), PHASE_DOMAIN_INDEX(Get_Domain(
      LIQUID_PHASE_ID)));
711   computeNormal(c,ct,Normal_1);
712   /*if (VERBOSE==1) CX_Message ("\n\n*****Normal =%gi +%gj+ %gk \n",
713                Normal_1[Axis_x],Normal_1[Axis_y],Normal_1[Axis_z]
714               );
715   */
716
717   i=0;
718
719   /*Vector Vs Vsecondary=Vprimary-2.*dot*Normal_1;*/
720   dot=NV_DOT(Vprimary,Normal_1);
721   Vsecondary[Axis_x]=Vprimary[Axis_x]-2.*dot*Normal_1[Axis_x];
722   Vsecondary[Axis_y]=Vprimary[Axis_y]-2.*dot*Normal_1[Axis_y];
723   Vsecondary[Axis_z]=Vprimary[Axis_z]-2.*dot*Normal_1[Axis_z];
724   secondary_drop_velocity_magnitude=NV_MAG(Vsecondary);
725   /*Dont crash by dividing zero! */
726    if(secondary_drop_velocity_magnitude<=0.)secondary_drop_velocity_magnitude=1.;
727       VsecondaryBar[Axis_x]=Vsecondary[Axis_x]/secondary_drop_velocity_magnitude;
728       VsecondaryBar[Axis_y]=Vsecondary[Axis_y]/secondary_drop_velocity_magnitude;
729       VsecondaryBar[Axis_z]=Vsecondary[Axis_z]/secondary_drop_velocity_magnitude;
730   if(secondary_drop_velocity_magnitude>MAX_DROPLET_SPEED)
731              {echo ("Ballistic overshoot of sec. droplet, ignored"); return 1.;}
732              CrownDiam      =5.*P_DIAM(p)  ; /*DEBUG:*/
733             JetLength       =CrownDiam*0.57; /*Yarin */
734             /*Jet_Length(CrownDiam);  JetLength=2./4.; */
735
736   secondary_drop_Pos[Axis_x]=impact_point[Axis_x]+JetLength*VsecondaryBar[Axis_x];
737   secondary_drop_Pos[Axis_y]=impact_point[Axis_y]+JetLength*VsecondaryBar[Axis_y];
738   secondary_drop_Pos[Axis_z]=impact_point[Axis_z]+JetLength*VsecondaryBar[Axis_z];
739
740
741
742
743
744
745       /*  Using correlations  */
746   ds=Oh=P_DIAM(p)+0.;    ds =Secondary_Drop_Size(ds);
```

/dpmvof.c 15

```
747  Oh =Ohnesorg(Oh);
748  We =getMAXIMUM(getWeber(LIQ_RHO,impact_magnitude,
749                          P_DIAM(p),surf_ten),SMALLEST_NUMBER );
750  K =We*pow(Oh,-0.4);
751  N_Children =Number_of_Children(K);
752  /* Quit if bad splash */
753  if(N_Children<=0||N_Children>MAX_NO_OF_DROPS_PER_SPLASH)
754     {echo("Bad Splash! Ignored: Trapped all mass"); return 1.;}
755
756  theta_exit =Ejection_Angle(K);/*DEBUG: Why not a distribution */
757  if(theta_exit<=0||theta_exit>90.)
758     {echo("Bad Splash angle! Continue (Y/N)? Yes selected"); theta_exit=0.;}
759
760        cos_theta_exit      =cos(theta_exit*M_PI/180.);
761        sin_theta_exit      =sin(theta_exit*M_PI/180.);
762  secondary_drop_velocity_magnitude=Secondary_Drop_Mean_Velocity(impact_magnitude
     );
763  mass_fraction_absorbed=1.-Mass_Fraction_Ejected(P_DIAM(p),ds,N_Children);
764
765  if (VERBOSE==1) CX_Message("Impact created %d secondary drops\n",N_Children);
766  if (VERBOSE==1) CX_Message("We = %E Impact=%gm/s d=%Emicrons\n",We,
     impact_magnitude,1000000.*ds);/* */
767  if (VERBOSE==1) CX_Message("K = %E\n\n",K);/**/
768  if (VERBOSE==1) CX_Message("P1= %3.4fi+%3.4fj+%3.4fk\n",
769                    impact_point[Axis_x],impact_point[Axis_y],
770                    impact_point[Axis_z]);
771  if (VERBOSE==1) CX_Message("Vp= %3.4fi+%3.4fj+%3.4fk\n",
772         Vprimary[Axis_x],Vprimary[Axis_y]
773         ,Vprimary[Axis_z]);
774
775  if (VERBOSE==1) CX_Message("...Ps= %3.4fi+%3.4fj+%3.4fk\n",secondary_drop_Pos[
     Axis_x],
776                                     secondary_drop_Pos[Axis_y],
777                                     secondary_drop_Pos[Axis_z]);
778  if (VERBOSE==1) CX_Message("...Vs= %3.4fi+%3.4fj+%3.4fk\n",
779                      Vsecondary[Axis_x],Vsecondary[Axis_y]
780                      ,Vsecondary[Axis_z]);
781
782  if (VERBOSE==1) CX_Message("\n\nJetLength =%gmicrons\n",
783                JetLength*1000000.);
784  /*Parametric definition of a 3D circle in X,Y,Z cordinates
785      X(thetha)=C1+Radius(A1*cos(thetha)+B1*sin(thetha))
786      Y(thetha)=C2+Radius(A2*cos(thetha)+B2*sin(thetha))
787      Z(thetha)=C3+Radius(A3*cos(thetha)+B3*sin(thetha))
788  C=secondary_drop_Pos, A=Vsbar cross N1, B=A cross N1
789      */
790  NV_CROSS(A,Vsecondary,Normal_1);
791     foo=NV_MAG(A); if (foo<=0.)foo=1.;
792            A[Axis_x]/=foo;A[Axis_y]/=foo;A[Axis_z]/=foo;
793                                  /*Projected Radius on Unit vector*/
794  NV_CROSS(B,Normal_1,A);
795     foo=NV_MAG(B); if (foo<=0.)foo=1.;
796            B[Axis_x]/=foo;B[Axis_y]/=foo;B[Axis_z]/=foo;
797                                  /*Projected Radius on Unit vector*/
798  /*
799  if (VERBOSE==1) CX_Message("A= %3.4fi+%3.4fj+%3.4fk\n",
```

/dpmvof.c 16

```
800                     A[Axis_x],A[Axis_y],A[Axis_z]);
801   if (VERBOSE==1) CX_Message("B= %3.4fi+%3.4fj+%3.4fk\n",
802                     B[Axis_x],B[Axis_y],B[Axis_z]);
803     if (VERBOSE==1) CX_Message("Impact Created %d Droplets\nMother ID =%d Used
        =%d\n"
804     ,N_Children,MotherID,MotherIDUsed);*/
805
806
807   if(impact_magnitude>0. && MotherID>MotherIDUsed)
808   {/*There is a droplet impacting*/
809     MotherIDUsed=MotherID;
810   /*ASSUMPTIONS:
811         All secondary droplets have roughly the same flow rate
812         Secondary droplets may have a distribution (Assumed LINEAR HERE)
813    */
814       secondary_drop_diam           =                          ds;
815       secondary_drop_mass_flow_rate  =             P_FLOW_RATE(p);
816       secondary_drop_mass_flow_rate *=(1.0-mass_fraction_absorbed);
817       secondary_drop_mass_flow_rate /=                 N_Children;
818
819      if (VERBOSE==1) CX_Message("@@@********** Mass Rate Sec=%g kg/s\n",
        secondary_drop_mass_flow_rate);
820
821   ring_theta=0.+ring_start_angle;
822   for(i=0;i<N_Children;i++)
823    {
824    /* The mother Particle ID should be checked
825       if this is a case of iteration and only over-write
826       instead of getting a new injection*/
827      ID =NextInjectorID();
828      if (ID==-1)
829       {echo ("WARNING!!! Too many secondary droplets...Ignoring this 1");}
830      else
831      {
832       /*DEBUG: Use Normals to compute */
833         ring_theta+=(360./N_Children);
834            ring_theta_rad=within_360(ring_theta);
835          /* if (VERBOSE==1) CX_Message("*******Ring %d =%g\n",i,ring_theta_rad);*/
836           ring_theta_rad=M_PI*ring_theta_rad/180.;
837   /*
838         secondary_drop_x =impact_point[Axis_x]+0.5*CrownDiam*cos(ring_theta_rad);
839         secondary_drop_y =impact_point[Axis_y]+    JetLength;
840         secondary_drop_z =impact_point[Axis_z]+0.5*CrownDiam*sin(ring_theta_rad);;
841   */
842         secondary_drop_x = secondary_drop_Pos[Axis_x]
843                            + 0.5*CrownDiam
844                              *( A[Axis_x]*cos(ring_theta_rad)
845                                +B[Axis_x]*sin(ring_theta_rad)
846                               );
847
848         secondary_drop_y = secondary_drop_Pos[Axis_y]
849                            + 0.5*CrownDiam
850                              *( A[Axis_y]*cos(ring_theta_rad)
851                                +B[Axis_y]*sin(ring_theta_rad)
852                               );
853
```

/dpmvof.c 17

```
854         secondary_drop_z = secondary_drop_Pos[Axis_z]
855                                + 0.5*CrownDiam
856                                  *( A[Axis_z]*cos(ring_theta_rad)
857                                    +B[Axis_z]*sin(ring_theta_rad)
858                                   );
859
860
861         if (VERBOSE==1) CX_Message("Droplet ID=%d Marked @ X(%g,%g,%g)mm\n",
862                         child_injector[i].injector_name,
863                         1000.*secondary_drop_x,
864                         1000.*secondary_drop_y,
865                         1000.*secondary_drop_z);
866    /*DEBUG Direction cosine of Normal pointing out   */
867     /*Treat the Normal splash velocity differently */
868
869
870    /* ACADEMIC TESTS for single droplet on plane film */
871       if( fabs(Normal_1[Axis_x])   >=0.99
872        && fabs(VprimaryBar[Axis_x])>=0.99
873          )
874            {AxisNormal=Axis_x; isThisANormalSplash=Yes;}
875
876       if( fabs(Normal_1[Axis_y])   >=0.99
877        && fabs(VprimaryBar[Axis_y])>=0.99
878          )
879            {AxisNormal=Axis_y; isThisANormalSplash=Yes;}
880
881       if( fabs(Normal_1[Axis_z])   >=0.99
882        && fabs(VprimaryBar[Axis_z])>=0.99
883          )
884            {AxisNormal=Axis_z; isThisANormalSplash=Yes;}
885    /*if (VERBOSE==1) CX_Message ("\n\n*****Normal =%gi +%gj+ %gk \n   VpBar =%gi
       +%gj+ %gk \n",
886                  Normal_1[Axis_x],Normal_1[Axis_y],Normal_1[Axis_z],
887                  VprimaryBar[Axis_z],VprimaryBar[Axis_y],VprimaryBar[Axis_z]
888                 ); */
889
890
891
892     if(isThisANormalSplash==Yes)
893     {echo ("Splash on a plane x-y, x-z or y-z");
894     /* Use reflection as default */
895      secondary_drop_Vx = VsecondaryBar[Axis_x]*secondary_drop_velocity_magnitude;
896      secondary_drop_Vy =VsecondaryBar[Axis_y]*secondary_drop_velocity_magnitude;
897      secondary_drop_Vz=VsecondaryBar[Axis_z]*secondary_drop_velocity_magnitude;
898          switch (AxisNormal)
899           {case Axis_x:
900            {secondary_drop_Vy = fabs(secondary_drop_velocity_magnitude*
              cos_theta_exit*cos(ring_theta_rad))
901                                  *radial_pointer(ring_theta,Axis_x);
902
903             secondary_drop_Vz =fabs(secondary_drop_velocity_magnitude*
              cos_theta_exit*sin(ring_theta_rad))
904                                  *radial_pointer(ring_theta,Axis_z);
905
906             secondary_drop_Vx= -1.*secondary_drop_velocity_magnitude
```

/dpmvof.c 18

```
907                                 *signOf(Vprimary[Axis_x])
908                                 *sin_theta_exit;
909
910
911           break;
912           }
913          case Axis_y:
914           {
915
916            secondary_drop_Vx = 0.-fabs(secondary_drop_velocity_magnitude*
              cos_theta_exit*cos(ring_theta_rad))
917                                 *radial_pointer(ring_theta,Axis_x);
918
919            secondary_drop_Vz = fabs(secondary_drop_velocity_magnitude*
              cos_theta_exit*sin(ring_theta_rad))
920                                 *radial_pointer(ring_theta,Axis_z);
921
922            secondary_drop_Vy= -1.*secondary_drop_velocity_magnitude
923                                 *signOf(Vprimary[Axis_y])
924                                 *sin_theta_exit;
925
926
927           break;
928           }
929          case Axis_z:
930           {
931            secondary_drop_Vx = fabs(secondary_drop_velocity_magnitude*
              cos_theta_exit*cos(ring_theta_rad))
932                                 *radial_pointer(ring_theta,Axis_x);
933
934            secondary_drop_Vy =fabs(secondary_drop_velocity_magnitude*
              cos_theta_exit*sin(ring_theta_rad))
935                                 *radial_pointer(ring_theta,Axis_z);
936
937            secondary_drop_Vz= -1.*secondary_drop_velocity_magnitude
938                                 *signOf(Vprimary[Axis_z])
939                                 *sin_theta_exit;
940
941           break;
942           }
943           }
944
945
946
947     }
948     else
949     {    secondary_drop_Vx = VsecondaryBar[Axis_x]*
       secondary_drop_velocity_magnitude;
950                               /* *cos_theta_exit*fabs(cos(ring_theta_rad))*
951                                    radial_pointer(ring_theta,Axis_x); */
952
953          secondary_drop_Vy =VsecondaryBar[Axis_y]*
             secondary_drop_velocity_magnitude;
954                             /*secondary_drop_velocity_magnitude*
955                                   cos_theta_exit*fabs(sin(ring_theta_rad))*
956                                    radial_pointer(ring_theta,Axis_z);*/
```

/dpmvof.c 19

```
957
958       secondary_drop_Vz=VsecondaryBar[Axis_z]*secondary_drop_velocity_magnitude;
959                         /* -1.*signOf(impact_direction_cosine[Axis_y]);
960          secondary_drop_Vy *=secondary_drop_velocity_magnitude*sin_theta_exit; */
961     }
962
963          child_injector[ID].number_of_droplets  =1;      /* Single Injector Used*/
964          child_injector[ID].free                =No;  /*Assigned a droplet */
965          child_injector[ID].injection_kind      =1;   /*INJECTOR_SINGLE  */
966          child_injector[ID].Rho                 =LIQ_RHO;
967               child_injector[ID].mass_flow_rate =secondary_drop_mass_flow_rate;
968               child_injector[ID].diam           =secondary_drop_diam;
969               child_injector[ID].u              =secondary_drop_Vx;
970               child_injector[ID].v              =secondary_drop_Vy;
971               child_injector[ID].w              =secondary_drop_Vz;
972               child_injector[ID].x              =secondary_drop_x;
973               child_injector[ID].y              =secondary_drop_y;
974               child_injector[ID].z              =secondary_drop_z;
975               child_injector[ID].Temp           =secondary_drop_temp;
976
977               if (VERBOSE==1) CX_Message("**AXES=%d Vel. of particle %d %g   %g
                  %g \ncos_theta_exit=%g stX %g rth %g \n",
978                           AxisNormal,i,secondary_drop_Vx,secondary_drop_Vy,
                              secondary_drop_Vz,
979                           cos_theta_exit,sin_theta_exit,ring_theta);
980       }
981    }
982    }
983
984
985
986   return mass_fraction_absorbed;}
987
988   /*====================DRAG================================================*/
989   DEFINE_DPM_DRAG(dpm_drag_virtual,Re,p)
990   {     cell_t c;  Thread *ct;
991         real Cd,drag,k;
992         real NV_VEC(Vp);
993         int outcome;  int is_wall=No;
994   /*Particle is in this cell*/
995     c  = P_CELL(p);
996     ct = THREAD_SUB_THREAD(P_CELL_THREAD(p),
997                            PHASE_DOMAIN_INDEX
998                           (Get_Domain(LIQUID_PHASE_ID)));
999
1000    Vp[Axis_x]=p->state.V[Axis_x];
1001    Vp[Axis_y]=p->state.V[Axis_y];
1002    Vp[Axis_z]=p->state.V[Axis_z];
1003     k =Cd =1.;
1004     /* Stop balistic overshoot of droplets */
1005    if(   fabs(Vp[Axis_x])>MAX_DROPLET_SPEED
1006        ||fabs(Vp[Axis_y])>MAX_DROPLET_SPEED
1007        ||fabs(Vp[Axis_z])>MAX_DROPLET_SPEED)
1008       {
1009       echo ("Ballistic Overshoot of Droplet---Removed!!");
1010       if (VERBOSE==1) CX_Message("Velocity=%3.3fi +%3.3fj +%3.3fk\n",p->state.V[
```

```
        Axis_x],p->state.V[Axis_y],p->state.V[Axis_z]);
1011    Kill_DPM(p,ct,0.);
1012    return 1E-30;
1013    }
1014
1015  if(P_FLOW_RATE(p)<=SMALLEST_NUMBER||P_MASS(p)<=SMALLEST_NUMBER ||Re<=0.)
1016    {/*
1017    if (VERBOSE==1) CX_Message("\n\nDead particle in DRAG--Re %E %Ekg %Ekg/s
        %Em %gm/s\n\n",
1018            Re,P_MASS(p),P_FLOW_RATE(p),P_DIAM(p),p->state.V[Axis_y]);*/
1019    Kill_DPM(p,ct,0.);
1020    return 1E-30;
1021    }
1022    /*
1023  if(Cd==1)
1024
         Re=getReynolds(P_RHO(p),getMagnitude(Vp),getMagnitude(v_cont),P_DIAM(p),GAS_
         MU);
1025   if (VERBOSE==1) CX_Message("Re=%g D=%g Vp=%g
       Vy=%g\n",Re,P_DIAM(p),p->state.V[Axis_y],C_V(c,ct));
1026    --------------------------------*/
1027    /*Compute Drag Coefficient
1028  *********************************
1029  Schiller-Naumann 1933 and Newton Drag Correlations
1030  *********************************
1031    if (Re <= 1000.)
1032      { Cd=(24./Re)*(1.+0.15*pow(Re,0.687));}
1033    else
1034      { Cd= 0.44;}
1035
1036  *********************************
1037  from Mingjun et al 2011
1038  *********************************
1039  */
1040  /*Compute Drag everywhere but only exchange mass at interface and Boundary*/
1041  if (Re>0. && Re <= 1.)
1042      { Cd=(24./Re);}
1043    else if (Re > 1. && Re < 1000.)
1044       { Cd=(24./Re)*(1.+ 0.15*pow(Re,0.68));}
1045    else if (Re >= 1000. && Re < 350000.)
1046      { Cd = 0.45;}
1047  /* Special Case Re=0*/
1048    if (Re<=0.) Cd=0.;
1049  drag=18.0*Cd*Re/24.0;
1050
1051
1052
1053   /*At the interface */
1054   if(ForceTrap==No)
1055  {
1056      if (((C_VOF(c,ct) >=interface_vof)||is_wall==Yes) && (P_FLOW_RATE(p)>
        SMALLEST_NUMBER))
1057            { outcome = add_tracked_particle_to_vof(p, c, ct,is_wall,C_VOF(c,ct));
1058              drag=SMALLEST_NUMBER; k=SMALLEST_NUMBER;
1059              Re=SMALLEST_NUMBER;
1060            }
```

/dpmvof.c 21

```
1061
1062  }
1063  else
1064  {
1065          if (p->state.pos[Axis_x]<=x_dpmTrap &&
1066              p->state.pos[Axis_y]<=y_dpmTrap &&
1067              p->state.pos[Axis_z]<=z_dpmTrap
1068              )
1069                { outcome = add_tracked_particle_to_vof(p, c, ct,is_wall,C_VOF(c,
                    ct));
1070                  drag=SMALLEST_NUMBER; k=SMALLEST_NUMBER;
1071                  Re=SMALLEST_NUMBER;
1072                }
1073  }
1074
1075
1076  /*Caping Momentum Exchange */
1077  if (drag>1E18 || (Not_A_Number(drag)==Yes))
1078  {if (VERBOSE==1) CX_Message ("*****WARNING:Drag=%E IGNORED\n",drag); drag=
      SMALLEST_NUMBER;}
1079  return (drag*k);
1080  }
1081
1082  /* ************************************************************************ */
1083  /*====================BOUNDARY CONDITION
      DPM================================================*/
1084  DEFINE_DPM_BC(vof_dpm_trap, p, ft, f, norm, dim)
1085  {cell_t c;  Thread *ct;  int vfo,is_wall=Yes;
1086    c  = P_CELL(p); /*Particle is in this cell*/
1087    ct = THREAD_SUB_THREAD(P_CELL_THREAD(p), PHASE_DOMAIN_INDEX(Get_Domain(
      LIQUID_PHASE_ID)));
1088  if (VERBOSE==1) CX_Message("*************Running Wall DPM_BC\n\n");
1089  vfo=add_tracked_particle_to_vof(p, c, ct,is_wall,0.99); /* returns impact
      outcome */
1090  switch (vfo)
1091    {case DROP_BOUNCES:
1092      { /*Do not kill/end this path for this one */
1093              if (VERBOSE==1) CX_Message("*************Droplet BOUNCED >>>Running
                  Wall DPM_BC\n");
1094          return PATH_ACTIVE;
1095          break;
1096      }
1097      case DROP_DEAD:
1098          {/*Dead Particle: Do what?*/
1099              if (VERBOSE==1) CX_Message("----Dead Particle running BC\n");
1100              return PATH_END;
1101          break;
1102          }
1103     }
1104     /* Kill_DPM(p,ct,0.); */ /* test exit
1105     P_DIAM(p)*=5.6; This Particles are not really DEAD--So I set Diam to zero at
        death!
1106     if (VERBOSE==1) CX_Message("This particle is supposed to be DEAD!
        Diam:%E\n", P_DIAM(p));
1107       */
1108    /* Case else eg STICK, SPREAD etc*/
```

/dpmvof.c 22

```
1109            if (!dpm_par.unsteady_tracking) add_to_dpm_summary(p,FATE_ESCAPED,ft);
1110                return PATH_END;
1111        /*   PATH_ACTIVE PATH_END,,, Was PATH_ABORT but that is for emergencies
                (lost particles) */
1112    }
1113
1114    /* ************************************************************************ */
1115    /*====================MOMENTUM=================================================*/
1116    /*====================z-MOMENTUM===============================================*
        /
1117    DEFINE_SOURCE(vof_dpm_Z_momentum, c, ct, dS, eqn)
1118    {real foo=C_VOF_DPM_MOM_SRC_Z(c,ct);
1119    if(foo!=0. && counter<20) {if (VERBOSE==1) CX_Message("*-*-*- Mom z Source:
        %E\n",foo);counter++;}
1120    if (foo>9.*pow(10,18))
1121       {if (foo!=0.)if (VERBOSE==1) CX_Message("-*-* * -->>> Z-Momentum Source %E >
           9e18 is Ignored\n",foo);
1122          foo=0.;
1123       }
1124    dS[eqn]=0.;
1125    return foo;
1126    }
1127    /* ************************************************************************ */
1128    /*====================x-MOMENTUM===============================================*
        /
1129    DEFINE_SOURCE(vof_dpm_X_momentum, c, ct, dS, eqn)
1130    {real foo=C_VOF_DPM_MOM_SRC_X(c,ct);
1131    if(foo!=0. && counter<20) {if (VERBOSE==1) CX_Message("*-*-*- Mom x: %E\n",foo);
        counter++;}
1132    if (foo>9.*pow(10,18))
1133       {if (foo!=0.)if (VERBOSE==1) CX_Message("-*-* * -->>> X-Momentum Source %E >
           9e18 is Ignored\n",foo);
1134          foo=0.;
1135       }
1136    dS[eqn]=0.;
1137    return foo;
1138    }
1139    /* ************************************************************************ */
1140    /*====================y-MOMENTUM===============================================*
        /
1141    DEFINE_SOURCE(vof_dpm_Y_momentum, c, ct, dS, eqn)
1142    {real foo=C_VOF_DPM_MOM_SRC_Y(c,ct);
1143    if(foo!=0. && counter<500) {if (VERBOSE==1) CX_Message("*-*-*- Mom y Source:
        %E\n",foo);counter++;}
1144    if (foo>9.*pow(10,18))
1145       {if (foo!=0.)if (VERBOSE==1) CX_Message("----->>> Y-Momentum Source %E >
           9e18 is Ignored\n",foo);
1146          foo=0.;
1147       }
1148    dS[eqn]=0.;
1149    return foo;}
1150
1151    /* ====================ENERGY SOURCE=================================*/
1152    DEFINE_SOURCE(vof_dpm_Energy, c, ct, dS, eqn)
1153    {real foo=C_VOF_DPM_H_SRC(c,ct);
1154      dS[eqn]=0.;
```

/dpmvof.c 23

```
1155  return energy_source(foo);
1156  }
1157  /* ************************************************************************** */
1158  /*====================MASS
      SOURCES================================================*/
1159  DEFINE_SOURCE(vof_liquid_src, c, ct, dS, eqn)
1160  {real foo=fabs(C_VOF_DPM_M_SRC(c,ct));
1161   dS[eqn]=0.;
1162   return liq_source(foo);
1163   }
1164  /*====================AIR MASS
      SOURCES================================================*/
1165  DEFINE_SOURCE(vof_gas_src, c, ct, dS, eqn)
1166  { real foo = fabs(C_VOF_DPM_M_SRC(c,ct));
1167    dS[eqn]=0.;
1168  return gas_source(foo);
1169  }
1170  /*====================PROPERTIES=============================================*
      /
1171  DEFINE_DPM_PROPERTY(dpm_surface_tension,c,t,p)
1172  {/*Debug here for correct surface tension characteristics*/
1173  return surf_ten;
1174  }
1175
1176
1177  /* DROPLET INSTANTANEOUS INJECTION */
1178  DEFINE_DPM_INJECTION_INIT(dpmCHILDREN,I)
1179  { /* Variables */
1180    int remove,ID;
1181    real theta,x,y,Vx,Vy;
1182    Particle *p;
1183    /*real dummy; real t;
1184    ,N_To_Inject
1185    ,N_Injectors,N_Max_Droplets,N_InjectedDrops
1186    */
1187
1188    /*unused variables to be removed DEBUG
1189    Thread *ct;cell_t c; i,
1190    */
1191    /*End variables
1192    t=CURRENT_TIME;*/
1193    ID=-1;remove=Yes; theta=0.;
1194    x=y=Vx=Vy=0;
1195  /*echo("Attempting to Inject Droplet");
1196   Single Injections from the Injectors
1197      Number of Injectors  = N_Injectors  =20 eg
1198     Number of Injections  = N_Injections =5 droplets
1199             N_Injections <= N_Injectors
1200      Injector Names:
1201                      child-01
1202                      child-02
1203                      ...
1204                      child-99
1205      FLUENT is set to inject from all injectors every time step
1206       The CleanUp Module in this UDF removes unwanted injections
1207   */
```

/dpmvof.c 24

```
1208  /*For the Mother Injector ONLY =Can use "injection" or "mother" in the names */
1209  /*RELEASE_STEP=5000.e-6;55.e-6;*/
1210  /*if(find_substring("mother",I->name)==Yes)*/
1211  if(memcmp("mother",I->name,5)== 0 || memcmp("injection",I->name,8)== 0)
1212      { I->unsteady_start  +=  RELEASE_STEP;
1213       if (VERBOSE==1) CX_Message("************\n %s Attempting in %g sec of the
          FLOW\n",I->name,I->unsteady_start);
1214      }
1215  else
1216      {   I->unsteady_start  =  childrenInjectionStarts;
1217  /*Secondary droplets can be waiting
1218  every timestep so try inject always*/
1219      }
1220
1221   if (VERBOSE==1) CX_Message("%s \n",I->name);
1222
1223  /* Model of the RID injector */
1224  if (SHAFT_SPEED>0.){
1225  if(memcmp("mother",I->name,5)== 0 || memcmp("injection",I->name,8)== 0)
1226  {
1227  loop(p,I->p_init)
1228    {
1229    /* Move the injector position with the RID injector shaft */
1230    theta= 2.*M_PI*SHAFT_SPEED*(childrenInjectionStarts-CURRENT_TIME)/60.;
      /*Injector moves with shaft speed*/
1231
1232      /*Initial position as defined in the injection file*/
1233            x= p->state.pos[Axis_x] ;
1234            y= p->state.pos[Axis_y] ;
1235         /*  p->state.pos[Axis_z] ;  The Axial axis is Z */
1236
1237             Vx=p->state.V[Axis_x] ;
1238             Vy=p->state.V[Axis_y] ;
1239         /*  p->state.V[Axis_z]  */
1240    p->state.pos[Axis_x] =x*cos(theta)+y*sin(theta);
1241    p->state.pos[Axis_y] =y*cos(theta)-x*sin(theta);
1242
1243    /*Rotation vector */
1244    p->state.V[Axis_x] =(Vx*cos(theta)+Vy*sin(theta));
1245    p->state.V[Axis_y] =(0.-Vx*sin(theta)+Vy*cos(theta));
1246    if (VERBOSE==1) CX_Message ("Po(%3.2g,%3.2g) \n...Pn(%3.2g,%3.2g)
      Vo(%3.2g,%3.2g) \n...Vn(%3.2g,%3.2g) \n",
1247    x,p->state.pos[Axis_x],
1248    y,p->state.pos[Axis_y],
1249    Vx,p->state.V[Axis_x],
1250    Vy,p->state.V[Axis_y]);
1251
1252    }
1253   }
1254   }
1255
1256
1257
1258  if(memcmp("child",I->name,5)== 0)
1259  {
1260  loop(p,I->p_init)
```

/dpmvof.c 25

```
1261    {/*Loop thru the say 10 "child" injectors only*/
1262       { remove =Yes; ID =get_Injector_ID_Waiting();
1263         /*Returns ID of Injector Store Next() */
1264
1265     if(ID>-1) /* Inject the Child */
1266       {if (VERBOSE==1) CX_Message("sec. drop-> %d waiting\n",ID);
1267       if(child_injector[ID].diam<1. && child_injector[ID].diam>0.)
1268            {remove=No;
1269             echo("CHILD DROPLET INITIALISING");
1270             /*Load Properties*/
1271              p->state.pos[Axis_x]=child_injector[ID].x;
1272              p->state.pos[Axis_y]=child_injector[ID].y;
1273              p->state.pos[Axis_z]=child_injector[ID].z;
1274              p->state.V[Axis_x]  =child_injector[ID].u;
1275              p->state.V[Axis_y]  =child_injector[ID].v;
1276              p->state.V[Axis_z]  =child_injector[ID].w;
1277                           P_T(p) =child_injector[ID].Temp;
1278                      P_DIAM(p) =child_injector[ID].diam;
1279                       P_RHO(p) =child_injector[ID].Rho;
1280                      P_MASS(p) =P_RHO(p)*M_PI*pow(P_DIAM(p),3.0)/6.0;
1281                 P_FLOW_RATE(p) =P_MASS(p)/CURRENT_TIMESTEP;
1282
1283      if (VERBOSE==1) CX_Message("%s\n %E(m) %Ekg\n %Ekg/s\n",I->name,
1284                                              P_DIAM(p),
1285                                              P_MASS(p),
1286                                               P_FLOW_RATE(p)
1287                                          );
1288              freeup_Injector(ID);
1289             }
1290      }
1291     else
1292       {
1293       {P_RHO(p)=1.;P_DIAM(p)=SMALLEST_NUMBER; P_FLOW_RATE(p) =SMALLEST_NUMBER;
1294
1295            MARK_PARTICLE(p, P_FL_REMOVED);
1296                     /*p->stream_index = -1;  */
1297            P_MASS(p) = 0.;     NV_S(P_VEL(p),=,0.);
1298              /* add_to_dpm_summary(p,FATE_ESCAPED,ct);*/
1299          echo("Blank Injection -For CLEAN UP");
1300           }
1301         }
1302    }
1303   }
1304
1305    if (VERBOSE==1) CX_Message("End Drop Injection attempt @%s\n-----\n", I->name);
1306  }
1307
1308  }
1309  DEFINE_ADJUST(Cleanup_DPM,d)
1310  {
1311  }
1312  /*-----------------------------INITIALISE SOLUTION----------------- */
1313  DEFINE_INIT(Init_Child_Injectors,d)
1314  { initInjectors();
1315   }
1316
```

/dpmvof.c 26

```
1317  /*--------------- Create Gradients to use for Interface Normal Computation
      -------*/
1318  DEFINE_ADJUST(interfaceNormals, domain)
1319  { Thread *ct; Thread **pt;  cell_t c;
1320  int phase_domain_index = 0.;
1321  Domain *pDomain = DOMAIN_SUB_DOMAIN(domain,phase_domain_index);
1322      Alloc_Storage_Vars(pDomain,SV_VOF_RG,SV_VOF_G,SV_NULL);
1323       Scalar_Reconstruction(pDomain, SV_VOF,-1,SV_VOF_RG,NULL);
1324       Scalar_Derivatives(pDomain,SV_VOF,-1,SV_VOF_G,SV_VOF_RG,
       Vof_Deriv_Accumulate);
1325
1326  mp_thread_loop_c (ct,domain,pt)
1327   if (FLUID_THREAD_P(ct))
1328    { Thread *ppt = pt[phase_domain_index];
1329        begin_c_loop (c,ct)
1330            { /*Can use VoF Grad */
1331              C_UDMI(c,ct,VOF_GRADIENT_x) = C_VOF_G(c,ppt)[Axis_x];
1332              C_UDMI(c,ct,VOF_GRADIENT_y) = C_VOF_G(c,ppt)[Axis_y];
1333              C_UDMI(c,ct,VOF_GRADIENT_z) = C_VOF_G(c,ppt)[Axis_z];
1334              /*or Reconstructed VoF Grad */
1335              C_UDMI(c,ct,VOF_R_GRADIENT_x) = C_VOF_RG(c,ppt)[Axis_x];
1336              C_UDMI(c,ct,VOF_R_GRADIENT_y) = C_VOF_RG(c,ppt)[Axis_y];
1337              C_UDMI(c,ct,VOF_R_GRADIENT_z) = C_VOF_RG(c,ppt)[Axis_z];
1338              /* Level Set Grad Function
1339              C_UDMI(c,ct,LS_GRADIENT_x) = NODE_PHI_G(c,ppt)[Axis_x];
1340              C_UDMI(c,ct,LS_GRADIENT_y) = NODE_PHI_G(c,ppt)[Axis_y];
1341              C_UDMI(c,ct,LS_GRADIENT_z) = NODE_PHI_G(c,ppt)[Axis_z];*/
1342
1343              }
1344        end_c_loop (c,ct)
1345  }
1346  Free_Storage_Vars(pDomain,SV_VOF_RG,SV_VOF_G,SV_NULL);
1347  }
1348
1349
1350   /* ------------------------------------ RESET THE
       VARIABLES-------------------- */
1351  DEFINE_EXECUTE_AT_END(src_reseter)
1352  { Domain *d;  Thread *ct; cell_t c;
1353      int noDPM;
1354  int  i=0;
1355  /*unused variables to be removed DEBUG
1356  Tracked_Particle *tp;real t; Particle *p;
1357   Injection *I;, *IList
1358  */
1359  d = Get_Domain(1);
1360  noDPM=0;
1361  thread_loop_c(ct,d)
1362    {begin_c_loop (c,ct)
1363
1364    /* Reset Source Terms */
1365                C_VOF_DPM_M_SRC(c,ct)=0.;
1366            C_VOF_DPM_MOM_SRC_X(c,ct)=0.;
1367            C_VOF_DPM_MOM_SRC_Y(c,ct)=0.;
1368            C_VOF_DPM_MOM_SRC_Z(c,ct)=0.;
1369
```

/dpmvof.c 27

```
1370
1371            /*Dont set the cell temp to zero ie no DPM-VoF action*/
1372            if(fabs(C_VOF_DPM_H_SRC(c,ct))>0.)
1373                {
1374        if (VERBOSE==1)
1375    CX_Message (" Cell Temp. was : %3.2f now: %3.2f K\n", C_T(c,ct), C_VOF_DPM_H_SRC
        (c,ct));
1376                C_T(c,ct) = C_VOF_DPM_H_SRC(c,ct);
1377                 C_VOF_DPM_H_SRC(c,ct)=0.;
1378                   }
1379
1380              /*  C_UDMI(c,ct,VOF_GRADIENT_x) = 0.;
1381                C_UDMI(c,ct,VOF_GRADIENT_y) = 0.;
1382                C_UDMI(c,ct,VOF_GRADIENT_z) = 0.;
1383                or Reconstructed VoF Grad
1384                C_UDMI(c,ct,VOF_R_GRADIENT_x) = 0.;
1385                C_UDMI(c,ct,VOF_R_GRADIENT_y) = 0.;
1386                C_UDMI(c,ct,VOF_R_GRADIENT_z) = 0.;*/
1387
1388    }end_c_loop (c,ct)
1389    /* How many outstanding carried over to next timestep? */
1390    for (i=0;i<MAX_NUMBER_OF_CHILD_INJECTORS;i++)
1391        if(child_injector[i].free==No && child_injector[i].diam<1.) noDPM++;
1392     if (VERBOSE==1) CX_Message("*-*->>%d Injections leftover till Next
        Timestep\n",noDPM);
1393     if (VERBOSE==1) CX_Message("\n*****************End of Time Step T=%E\n",
        CURRENT_TIME);
1394  }
1395
1396
1397
1398
1399
1400
1401
1402  /*Reset Injectors every time a case is read or new data is read */
1403  DEFINE_EXECUTE_AFTER_CASE(NewCaseResetInjectors,libraryname)
1404  {
1405  initInjectors();
1406  echo ("READ CASE and Prepared the Children Injectors: Complete");
1407
1408  }
1409  DEFINE_EXECUTE_AFTER_DATA(NewDataResetInjectors,libraryname)
1410  {
1411  initInjectors();
1412  echo ("READ DATA and Prepared the Children Injectors: Complete");
1413  }
1414
1415
1416
1417
1418
1419
1420
1421
1422
```

/dpmvof.c 28

```
1423
1424
1425
1426  /* ************************************************************************ */
1427  /*                    CORRELATIONS                                          */
1428  real Ohnesorg(real Dp)
1429  {/*Oh  (K=We*Oh-0.4) */
1430   if (VERBOSE==1) CX_Message("Oh=%E, rho:%E st=%E Mu=%E dp=%E\n",
1431   LIQ_MU/pow(surf_ten*LIQ_RHO*Dp,0.5),
1432   LIQ_RHO,surf_ten,LIQ_MU,Dp
1433   );
1434   if(Dp<0)
1435    return 1.;
1436   else
1437   return LIQ_MU/pow(surf_ten*LIQ_RHO*Dp,0.5);
1438  }
1439  int Number_of_Children(real K)
1440  {/*Experiment: Davide et al(2012), Okawa 2006, ?????
1441           K=We*Oh^-0.4        N=0.0085246*K-14.02 */
1442   if (K<=14.02/0.0085246)
1443     return 0;
1444   else
1445     return getMIN(0.0085246*K-14.02,MAX_NO_OF_DROPS_PER_SPLASH);
1446  }
1447  real Ejection_Angle(real K)
1448  {/*Experiment: Davide et al(2012)
1449     Alpha=0.0015*K+12 (K=We*Oh-0.4)
1450  */
1451  real ang=0.0015*K+12;
1452      if (ang<0.||ang>90.) ang=12.;
1453       /*Bound unphysical result when K diverging eg K>52,000 */
1454  return ang;
1455  }
1456  real Mass_Fraction_Ejected_2(real Oh, real We)
1457  {/* Experiment showing Em=0.02 to 0.1 */
1458   return 0.04;
1459  }
1460  real Mass_Fraction_Ejected(real dp, real ds, int N_Drops)
1461  {/*The total mass of droplets ejected
1462     as a fraction of the impacting droplet.
1463     Mass Conservation
1464     Mass_sec  = N_Drops*LIQ_RHO*M_PI*pow(ds,3.0)/6.0;
1465     Mass_prim =   LIQ_RHO*M_PI*pow(dp,3.0)/6.0; */
1466     real mf=N_Drops*pow(ds/dp,3.0);
1467     /*if (VERBOSE==1) CX_Message("**********Ns=%d ds=%E dp=%E
        M.Ejected=%E\n",N_Drops,ds,dp,mf);*/
1468    return mf;
1469  }
1470  real Secondary_Drop_Size(real Primary_Drop_Size)
1471  {/* Okawa et al 2006, Davide et al 2012
1472    Ds=0.1*Dp constant 0<K<12000 for Water
1473    Some distribution exists for high viscous
1474    fluid like Water-Glycerine and dependent on K
1475    if (VERBOSE==1) CX_Message("Prim. drop size %E\n",Primary_Drop_Size);*/
1476   return 0.1*Primary_Drop_Size;
1477  }
```

/dpmvof.c 29

```
1478  real Jet_Length(real CrownDiam)
1479  {real foo;/*dhc/drc=0.57 Yarin & Weiss 1995 by A.L. Yarin 2006*/
1480     foo=0.57*CrownDiam*0.5;
1481     if (VERBOSE==1) CX_Message("Sec. drop Jet Length. %E\n",foo);
1482  return foo;
1483  }
1484  real Secondary_Drop_Mean_Velocity(real Impact_Velocity)
1485  {/*Davide et al (2012) Vol. mean, Okawa et al (2006)
1486     based on 80% distribution
1487     if (VERBOSE==1) CX_Message("Sec. drop Vel. %E\n", 0.52*Impact_Velocity);*/
1488      return 0.52*Impact_Velocity;
1489  }
1490  real getSpreadRadiusCorrelation(real foo)
1491  {/* The Crown Dynamics corretion from Published Articles
1492      to determine the source term coordinates
1493      DEBUG: Now using Radius of DPM (foo)
1494  Spread Mass source to the Radius*/
1495  /*if (VERBOSE==1) CX_Message("Radius: Corr. %E\n",foo);*/
1496      if(foo>=LARGEST_NUMBER)
1497          return SMALLEST_NUMBER;
1498      else
1499          return foo;
1500  }
1501
```

```
/* End of UDF codes */
```